UNIVERSIDADE FEDERAL DE SANTA CATARINA
PROGRAMA DE PÓS-GRADUAÇÃO EM
ENGENHARIA MECÂNICA

William D'Andrea Fonseca

Beamforming considerando difração acústica em superfícies cilíndricas

Florianópolis

2013

UNIVERSIDADE FEDERAL DE SANTA CATARINA
PROGRAMA DE PÓS-GRADUAÇÃO EM
ENGENHARIA MECÂNICA

William D'Andrea Fonseca

BEAMFORMING CONSIDERANDO DIFRAÇÃO ACÚSTICA EM SUPERFÍCIES CILÍNDRICAS

Tese submetida ao Programa de Pós-Graduação em Engenharia Mecânica da Universidade Federal de Santa Catarina para a obtenção do grau de Doutor em Engenharia Mecânica.

Orientador:
Prof. Ph.D. Samir Nagi Yoursi Gerges

Co-orientador:
Prof. Dr. rer. nat. Michael Vorländer

Co-orientador:
Prof. Ph. D. Arcanjo Lenzi

Florianópolis

2013

Fonseca, William D'Andrea
Beamforming Considering Acoustic Diffraction over Cylindrical Surfaces [tese] / William D'Andrea Fonseca ; orientador, Samir Nagi Yoursi Gerges ; co-orientador, Michael Vorländer; co-orientador, Arcanjo Lenzi.
- Florianópolis, SC, 2013. 340 p.

Tese (doutorado) - Universidade Federal de Santa Catarina, Centro Tecnológico. Programa de Pós-Graduação em Engenharia Mecânica.

Inclui referências

1. Engenharia Mecânica. 2. acústica. 3. beamforming. 4. difração. 5. processamento de sinais. I. Gerges, Samir Nagi Yoursi. II. Vorländer, Michael. III. Lenzi, Arcanjo
IV. Universidade Federal de Santa Catarina. Programa de Pós-Graduação em Engenharia Mecânica. V. Título.

Beamforming Considering Acoustic Diffraction over Cylindrical Surfaces

A dissertation presented

by

William D'Andrea Fonseca

to

The Graduate Program in
Mechanical Engineering

in partial fulfillment of the requirements
for the degree of
Doctor of Engineering
in the subject of
Vibration and Acoustics

Federal University of Santa Catarina
Florianópolis, SC, Brazil

May, 2013

William D'Andrea Fonseca

BEAMFORMING CONSIDERANDO DIFRAÇÃO ACÚSTICA EM SUPERFÍCIES CILÍNDRICAS

Esta Tese foi julgada adequada para obtenção do Título de Doutor em Engenharia Mecânica e aprovada em sua forma final pelo Programa de Pós-Graduação em Engenharia Mecânica da Universidade Federal de Santa Catarina, Florianópolis, 2 de maio de 2013.

Albertazzi

Armando Albertazzi Gonçalves Jr., Dr. Eng.
Coordenador do Curso

Banca Examinadora:

Samir Nagi Yoursi Gerges, Ph. D.
Orientador

Michael Vorländer, Dr. rer. nat.
Co-orientador

Arcanjo Lenzi

Arcanjo Lenzi, Ph. D.
Co-orientador

Jose Roberto de França Arruda, Dr. Eng.

Pieter Sijtsma, Dr. Ir.

Júlio Apolinário Cordioli, Dr. Eng.

Hans Helmut Zürn

Hans Helmut Zürn, Ph. D.

Marcio Henrique de Avelar Gomes, Dr. Eng.

William D'Andrea Fonseca

BEAMFORMING CONSIDERING ACOUSTIC DIFFRACTION OVER CYLINDRICAL SURFACES

This dissertation was judged adequate for obtaining title Doctor of Engineering in the subject of Vibration and Acoustics and is approved in its final form by the Graduate Program in Mechanical Engineering of the Federal University of Santa Catarina, Florianópolis, May the 2nd 2013.

Examining Committee:

Prof. Samir Nagi Yoursi Gerges, Ph. D.
Laboratory of Acoustics and Vibration
Department of Mechanical Engineering
Federal University of Santa Catarina, Brazil
Advisor

Prof. Michael Vorländer, Dr. rer. nat.
Institute of Technical Acoustics
Faculty of Electrical Engineering and Information Technology
RWTH Aachen University, Germany
Co-Advisor

Prof. Arcanjo Lenzi, Ph. D.
Laboratory of Acoustics and Vibration
Department of Mechanical Engineering
Federal University of Santa Catarina, Brazil
Co-Advisor

Prof. Jose Roberto de França Arruda, Dr. Eng.
Vibroacoustics Laboratory
Department of Computational Mechanics
State University of Campinas, Brazil

Pieter Sijtsma, Dr. Ir.
Department of Helicopters and Aeroacoustics
National Aerospace Laboratory - NLR, Netherlands

Prof. Júlio Apolinário Cordioli, Dr. Eng.
Laboratory of Acoustics and Vibration
Department of Mechanical Engineering
Federal University of Santa Catarina, Brazil

Prof. Hans Helmut Zürn, Ph. D.
Power Systems Laboratory
Department of Electrical Engineering
Federal University of Santa Catarina, Brazil

Prof. Marcio Henrique de Avelar Gomes, Dr. Eng.
Academic Department of Mechanics
Federal University of Technology, Paraná, Brazil

À meus pais Clarice e Carlos por seu amor, apoio, dedicação e exemplo de honestidade e perseverança.

To my parents Carlos and Clarice for their love, support, dedication and example of honesty and perseverance.

Agradecimentos

À minha família Carlos, Clarice e Priscila Fonseca pelo apoio incondicional, acreditando no meu sucesso e sempre me fornecendo o essencial, o amor.

Ao meu orientador Samir N. Y. Gerges por proporcionar a possibilidade de prosseguir com o tema e abrir portas para projetos.

A Pieter Sijtsma, uma pessoa que trouxe grande inspiração para o desenvolvimento do tema de beamforming. Agradeço por ter sido o tutor durante o período de estudos no Laboratório Aeroespacial da Holanda (NLR), orientando parte deste projeto e sempre contribuindo com ideias e conselhos.

Ao amigo e fiel escudeiro João Paulo Ristow pela ajuda e empenho nos desenvolvimentos de códigos, medições e ideias sobre o tema, sobretudo nas modelagens de GA.

Ao professor Michael Vorländer pela orientação e oportunidade de trabalhar no Instituto Técnico de Acústica (ITA) da RWTH Aachen.

Ao professor Arcanjo Lenzi pela orientação, amizade, e conselhos acerta de acústica.

Ao Eric Brandão, amigo de tantas horas e prosas sobre a vida. Alguém em que posso confiar uma ampla faixa dinâmica de temas, das discussões sobre cervejas a transformadas de Fourier.

Ao Bruno Masiero pela amizade e ajuda em Aachen, sempre alguém que pude contar seja para descomplicar algo em alemão ou para trocar algumas ideias.

À Karol Crespi pelo carinho e compreensão nos minutos em que escrever a tese consumia todo o tempo. Um obrigado especial também à Vera Crespi para com a ajuda na impressão do documento.

Aos professores do Laboratório de Vibrações e Acústica da UFSC (LVA), Júlio Cordioli e Roberto Jordan, pelos ensinamentos e por sempre estarem abertos a ideias.

Ainda no laboratório, quero lembrar dos colegas que contribuíram para o trabalho de alguma forma, e que pude também atuar como co-orientador, Diogo Sanches, Vinicius Corassa, Flávia Ferreira e Jean Métailler.

Quero também lembrar dos amigos que compartilharam vários momentos, seja por um almoço, um churrasco, ou mesmo discussões sobre a vida e tudo mais, Marcelo Portela, Yuri Ribeiro, Alexandre Montenegro, Rafael Pereira, Thiago Gasparino, Bia Gobbi, Jeanine Caminha, Gabi Paz, Cássia Wust, Nadja Klecks, Paulo Mareze, Alexandre Teixeira, entre outros. E ainda a Vanessa Bortucan pela paciência e apoio dedicado nos primeiros anos deste trabalho.

No ITA, em Aachen, também quero lembrar dos colegas que ajudaram nessa jornada dentre a cultura alemã, Pascal Dietricht, Martin Pollow, Johannes Klein, Markus Müller-Trapet e Christian Haar.

No NLR, em Flevoland, gostaria de lembrar dos colegas Stefan Oerlemans, Martien Oppeneer, Henk van der Wal, Marino Beenhakker e Marthijn Tuinstra, pelas proveitosas caminhadas e discussões durante o almoço.

Ao Robert Dougherty pelas discussões e ideias acerca de beamforming nos primeiros anos do trabalho.

Ao Stepahn Paul, pelo apoio e discussões acerca de acústica, INAD e Latex.

À Embraer pela oportunidade de trabalhar no Projeto Aeronave Silenciosa nos primeiros anos do trabalho.

Ao professor Sylvio Bistafa, coordenador do Projeto Probral, que apoiou minha missão de estudos de doutorado sanduíche e à CAPES pelo apoio financeiro neste período.

Ao CNPq, pelo apoio financeiro.

Tenho certeza de que outras pessoas também contribuíram, deixo este espaço para o seu nome ____________________ e lhe agradeço da mesma forma!

Acknowledgements

To my family Carlos, Clarice and Priscila Fonseca for their unconditional support, for believing in my success and always providing that which is most essential, love.

To my advisor Samir N. Y. Gerges for providing the opportunity to continue research within this topic and for opening doors for other projects.

To Pieter Sijtsma, the person who provided a great inspiration concerning the beamforming theme. Thank you for being my tutor during my studies at the Netherlands Aerospace Laboratory (NLR), guiding part of this project and constantly contributing with ideas and advice.

To my friend and tireless colleague João Paulo Ristow for all the help and commitment above and beyond the call of duty in developing codes, measurements and ideas, especially in the GA modelling.

To Professor Michael Vorländer for the support and opportunity to work at the Technical Institute of Acoustics (ITA), RWTH Aachen.

To Professor Arcanjo Lenzi for guidance, friendship, and advice regarding acoustics.

To Eric Brandão a true friend indeed. Someone I can count on over a wide dynamic range of topics, from *life and everything*, through analyses about beer to the Fourier transforms.

To Bruno Masiero for his friendship and help in Aachen, someone I could always count on to uncomplicate the German language, and to exchange ideas.

To Karol Crespi for her support and understanding during the time when the dissertation writing was consuming all the time. Also a special thanks to Vera Crespi for her help in organizing the printing of the document.

To the Laboratory of Acoustics and Vibrations of UFSC (LVA) professors Julio Cordioli and Roberto Jordam, for their teaching and willingness for discussion.

I would also like to remember other LVA colleagues who contributed to this work in different ways, and for whom I had the opportunity to co-advise, Diogo Sanches, Vinicius Corassa, Flávia Ferreira and Jean Métailler.

I also want to remember the friends who were there for me, whether for a lunch, a barbecue, or even discussions about life, Marcelo Portela, Yuri Ribeiro, Alexandre Montenegro, Rafael Pereira, Thiago Gasparino, Bia Gobbi, Jeanine Caminha, Gabi Paz, Cassia Wust, Nadja Klecks, Paulo Mareze, Alexandre Teixeira, among others. And also, Vanessa Bortucan for her patience and support in the early years of this work.

In the ITA, in Aachen, I also want to thank the colleagues who helped on this journey concerning German culture, Pascal Dietricht, Martin Pollow, Johannes Klein, Markus Müller-Trapet and Christian Haar.

In NLR, in Flevoland, I want to remember colleagues Stefan Oerlemans, Martien Oppeneer, Henk van der Wal, Marino Beenhakker and Marthijn Tuinstra, for fruitful discussions during lunch time walks in the woods.

To Robert Dougherty for discussions and ideas regarding beamforming in the early years of this work.

To Stephan Paul for support and discussions about acoustics, INAD and Latex.

To Embraer for the opportunity to work on the Silent Aircraft Project during the early years of the work.

To Professor Sylvio Bistafa, Probral Project Coordinator, who supported my study mission abroad and CAPES for financial support during this period.

To CNPq for the financial support.

As many other people also contributed, I then want to leave this space for your name ______________________ thank you!

"Só se vê bem com o coração, o essencial é
invisível aos olhos."

"It is only with the heart that one can see rightly;
what is essential is invisible to the eye."

Antoine de Saint-Exupéry

Abstract

Beamforming is a signal processing technique recognized for its applications in antennas and radio astronomy. It is essentially a technique to locate sources based on the conformation of wave beams from a given direction or region in space. Its application in acoustics originated rudimentarily during World War I. However, the advances that have led to the creation of acoustic images date from the early seventies.

The present work proposes the application this technique considering the sensors are over a rigid cylindrical surface with the external field as the object of interest. Thus, sound sources anywhere around the cylinder become detectable and subject to viewing. For this purpose not only the free-field is considered, but also the diffraction acoustic field created by the cylinder. The problem's analytical modelling is developed and adapted in order to apply the beamforming algorithm. This is one of the contributions of this research since in most applications only the incident field is considered in post-processing. In addition, measurements were carried out in an anechoic environment for one of the geometries studied to compare the results with the analytical and numerical simulations.

Other numerical methods are also employed on two fronts, to confirm the physical meaning and discuss the results; and to search for a more suitable geometry. The Boundary Element Method (BEM) is used to generically review the problem, since the great majority of structures can be modelled in its domain. The objective is to calculate the same diffraction situations in the analytical model and the BEM for comparison. The work then presents a study on the mesh of the 3D model used correlated with beamforming sound source map location errors. Subsequently, an optimisation method based on the Genetic Algorithm (GA) is developed to place the sensors over the cylinder's surface in order to prevent sidelobes, grating lobes, and to maximize the dynamic range.

↪

The application of the methods studied together with beamforming has created new aspects in array design. This document then discusses and points out the improvements and problems with respect to sound source location performance. Finally, there is a summary concerning the research contributions and some thoughts for future work.

Keywords: beamforming, acoustics, diffraction, acoustic imaging, signal processing, optimisation, cylindrical surface, boundary element method.

Resumo

Beamforming é uma técnica de processamento de sinais já conhecida por suas aplicações em antenas e radioastronomia. É essencialmente uma técnica de localização de fontes baseada na conformação de feixes de onda de uma dada direção ou região no espaço. Sua aplicação em acústica foi iniciada de forma rústica na primeira grande guerra. Todavia, os avanços que propiciaram a criação das imagens acústicas são datados a partir dos anos setenta.

Este trabalho propõe a aplicação desta técnica considerando que os sensores estão posicionados na superfície de uma estrutura rígida e cilíndrica, sendo que o campo externo é o objeto de interesse. Deste modo, fontes sonoras ao redor do cilindro serão detectáveis e passíveis de visualização. Para este propósito, diferente do comumente aplicado, não somente o campo livre é considerado, mas também o campo de difração que é criado pelo cilindro. A modelagem analítica do problema é desenvolvida e adaptada para a aplicação do algoritmo de *beamforming*. Esta é uma das contribuições desta pesquisa, visto que na maioria das aplicações somente o campo incidente é considerado no pós-processamento. Além disso, para uma das geometrias estudadas, medições foram realizadas em ambiente anecóico para comparar os resultados com as simulações analítica e numérica.

Outros métodos numéricos foram também empregados em duas frentes: para confirmar o significado físico e discutir resultados, e para encontrar uma geometria mais adequada. O Método de Elementos de Contorno (MEC ou BEM) é utilizado para avaliação do problema de maneira genérica, visto que quase todos os tipos de estruturas podem ser modelados em seu domínio. O objetivo é calcular as mesmas situações de difração com o modelo analítico e com o MEC e compará-las. O trabalho então apresenta um estudo correlacionando à malha do modelo 3D com os erros de localização nos mapas criados pelo *beamforming*. Em conseguinte, um método de otimização baseado em Algoritmo Genético (GA) é desenvolvido para posicionar os sensores na superfície do cilindro de modo a prevenir lóbulos laterais, lóbulos espelho e maximizar a faixa dinâmica.

↪

A aplicação dos métodos estudados junto ao beamforming criou novos aspectos em design de *arrays*. Ao longo do documento as discussões apontam os aprimoramentos e problemas relacionados ao desempenho na localização de fontes sonoras. Ao final, há um sumário acerca das contribuições da pesquisa e algumas ideias para trabalhos futuros.

Palavras-chave: beamforming, acústica, difração, imagem acústica, processamento de sinais, otimização, superfície cilíndrica, método de elementos de contorno.

Table of Contents

List of Figures

List of Tables

Nomenclature

General Symbols

$\vec{r}$	Position vector in space, $\vec{r} = (x,y,z) \in \mathbb{R}^3$, eq. (2.1), page 11.
$\vec{C}$	*Cross-Power Matrix*, eq. (3.33), page 37.
$\vec{g}$	*Steering vector*, it contains all the $g_m = G(\vec{x}_m, \vec{x}_s, f)$ steering functions at the microphone locations, eq. (3.31), page 36.
$\vec{n}_y$	Unit normal to the surface point $\vec{y}$ (pointed into the fluid domain) (BEM), eq. (5.1), page 141.
$\vec{p}$	Vector containing all the M microphone pressures, eq. (3.30), page 36.
$\vec{r}, r$	r is the length of the vector $\vec{r}$ that is directed from the source point $\vec{y}$ to the field point $\vec{x}$, $r = \|\vec{x} - \vec{y}\|$ (BEM), eq. (5.1), page 141.
$\vec{x}$	Spatial position vector, $\vec{x} = (x, y, z)$, eq. (3.2), page 28.
$\vec{x}$	*Field point* or *evaluation point* in the fluid domain (BEM), eq. (5.1), page 141.
$\vec{x}_m$	Microphone position in space, $\vec{x}_m = (x_m, y_m, z_m)$, eq. (3.2), page 28.
$\vec{x}_s$	Sound source position in space, eq. (3.4), page 29.

$\vec{y}$	*Data point* located on the boundary surface S (BEM), eq. (5.1), page 141.
A	Estimated source auto-powers, eq. (3.36), page 39.
a	Complex amplitudes of sources located in $\vec{x}_p$, eq. (3.34), page 37.
a	Fraction of opening angle, $a = {}^{O}/2$ (GA), page 172.
a	Geometry-factor for sampled aperture, or for continuous aperture, dependent on the chosen criterion, eq. (3.51), page 48.
A, B	Influence matrices in DBEM, eq. (5.3), page 142.
$b'(\vec{x}_p, f)$	DSB in alternative notation for focus point $\vec{x}_p$ and frequency f, eq. (3.21), page 34.
$B(\omega)$, $P_m(\omega)$	Fourier transformed signals of $b(t)$ and $p_m(t)$; $B(\omega)$ is the frequency domain DSB, eq. (3.16), page 33.
$b(t)$	DSB *estimated source signal*, eq. (3.7), page 29.
$b_{\mathrm{pw}}(t)$	Time domain version of beamforming for plane waves; the frequency domain is denoted by $B_{\mathrm{pw}}\left(-\vec{\zeta}, \omega\right)$, eq. (3.42), page 41.
B_w	Spatial window factor, page 56.
c	Sound speed $\left[\frac{\mathrm{m}}{\mathrm{s}}\right]$, eq. (2.1), page 11.
$C_{mn}(f)$, $C_{mm}(f)$	*Cross-powers* and *Auto-powers*, respectively, eq. (3.32), page 37.
D	Geometrically intrinsic distance, normally the array diameter, eq. (3.51), page 48.
d	Perpendicular distance from the source plane to the point where the incident field is evaluated (DBEM), eq. (5.13), page 164.
d	Sampling microphone interval, eq. (3.69), page 59.

d_z	Distance between the array and the scanning plane, eq. (3.51), page 48.
f	Frequency [Hz], eq. (2.14), page 15.
f_s	ADC sampling frequency, page 63.
$f_{\max}$	The maximum frequency of analysis (in the calculation of the *mesh size*), eq. (5.6), page 143.
$G(r)$	Green's function representing the response of the inhomogeneous Helmholtz Differential Equation to a Dirac pulse in space, eq. (5.2), page 141.
G_{array}	Array gain, eq. (3.65), page 55.
$H_{mp}(f)$	$H(\vec{x}_m, \vec{x}_p, f) = H_{mp}(f)$ is the source-receiver transfer function $\left[p_m(\vec{x}_m, \vec{x}_p, f) \rightleftharpoons G(\vec{x}_m, \vec{x}_p, f)\right]$, eq. (3.17), page 33.
k	Total number of angles (GA), eq. (5.28), page 189.
k	Wave number, $k = \frac{\omega}{c} = \frac{2\pi f}{c}$. It is related to the case of plane wave propagating in fluid, where the *wavelength* is $\lambda = 2\pi/k$ and so k is the number of waves per 2π units of length, eq. (2.7), page 13.
L_{arr}	Largest array dimension, eq. (3.1), page 24.
N	Total number of focus points contained in the scanning grid, page 25.
n	Integer that selects the grating lobe, eq. (3.77), page 60.
n	Number of elements per dimension (BEM), page 140.
n_i, n'_i	Number of times that each individual is placed in the roulette wheel list and scaled values (GA), eq. (5.23), page 175.
$n_m(t)$	Uncorrelated zero-mean random noise component, eq. (3.60), page 54.

n_{total}	Total number of elements of the surface S (BEM), page 140.
N_{FFT}	Number of points in a FFT block, page 63.
$O, O_{.5}, O_{\mathfrak{c}}$	Open angle for symmetry evaluation, half the open angle ($O/2$), and open angle times a constant ($O * \mathfrak{c}$) (GA), page 172.
p	Acoustic pressure, primary variable in DBEM, page 139.
p	Vector of nodal pressures on the BEM surface, eq. (5.3), page 142.
$p(\vec{r}, t)$	Sound pressure with the vector in space $\mathbb{R}^3$ and time, eq. (2.1), page 11.
$p(\vec{x}, t)$	Sound pressure at focus point $\vec{x}$ and t time due to a monopole excitation, eq. (3.5), page 29.
$p(r_m, t)$, $p_m(t)$	Signal received at the m^{th} microphone, eq. (3.6), page 29.
$p^{\text{in}}(\vec{x})$	Incident acoustic wave (BEM), eq. (5.1), page 141.
p_0	Reference sound pressure $p_0 = 20\mu$ Pa which is approximately the human hearing threshold in mid-frequencies, eq. (2.19), page 17.
P_k	Position of the main lobe peak in the PSF, page 172.
$P_n(O)$	Geometrical evaluation point for a given O angle, eq. (5.17), page 172.
p_t, p_i, p_s	Total sound field, incident field (or free-field pressure) and scattered field, respectively (DBEM), eq. (5.12), page 163.
p_{rms}	"Root mean square" sound pressure, eq. (2.19), page 17.
$P_{\vec{x}}$	Pressure at an arbitrary field point $\vec{x}$, eq. (5.4), page 142.
P_{pn}, P_{pk}	Pressure value (in Pa) for the geometrical point $P_n(O)$, and for P_k, eq. (5.17), page 173.

R	Distance from the source to the point where the incident field is evaluated (DBEM), eq. (5.14), page 165.
$R(\vartheta)$	Spatial resolution for a given ϑ wave incident angle, eq. (3.67), page 56.
r_m	Distance from the source to the m^{th} sensor, $r_m = \lvert \vec{x}_m - \vec{x}_s \rvert$, eq. (3.6), page 29.
r_p, r'_m	Distances between a focus point $\vec{x}_p$ and the array's centre; and the m^{th} microphone, respectively, eq. (3.12), page 31.
r_s	Distance between the source and the origin (DSB), eq. (3.8), page 30.
R_{ff}	Minimum distance to consider the array's far-field, eq. (3.1), page 24.
$r_{\vec{x}}$	Distance from the source to the field point $\vec{x}$, $r_{\vec{x}} = \lvert \vec{x} - \vec{x}_s \rvert$, eq. (3.5), page 29.
r_{sp}	Distance between the supposed source (focus point) and the receiver (in this case m^{th} sensor), eq. (3.20), page 34.
$S(\omega)$	Source signal spectrum, eq. (3.47), page 43.
$s(t)$	Arbitrary sound source signal, eq. (3.4), page 29.
S_{DR}, S_{BW}, S_{Sy}	Dynamic range, beamwidth and symmetry scores, respectively (GA), eq. (5.16), page 171.
t	Time [s], eq. (2.1), page 11.
T_0	Constant, eq. (3.15), page 33.
u	Particle velocity, page 77.
V	Constant depending on the computer's memory for the calculation of L_{size} (GA), eq. (5.25), page 175.
v	Acoustic velocity, primary variable in DBEM, page 139.

V, X	Frequency vectors of *numerical simulations*, *analytical simulations*, and *input angle* depending on the case, eq. (5.10), page 151.
v_n	Vector of normal velocities on the BEM surface, eq. (5.3), page 142.
v_{snd}	Sound Speed in the medium $\left[\frac{\text{m}}{\text{s}}\right]$, eq. (5.6), page 143.
$W(\cdot)$	Array pattern, eq. (3.47), page 43.
$W_{\text{DR}}, W_{\text{BW}}, W_{\text{Sy}}$	Dynamic range, beamwidth and symmetry weights, respectively (GA), eq. (5.16), page 171.
$y(t), Y(\omega)$	Pairs of the Fourier Transform, eq. (3.15), page 33.
Z	Acoustic impedance, page 77.
z_i	Coordinate for the i^{th} microphone, eq. (5.26), page 179.
Z_{limit}	Border of the cylinder, eq. (5.26), page 179.
BW_{axis}	Beamwidth on the z-axis, eq. (3.51), page 48.
BW_{null}	Beamwidth considering when the mainlobe falls into a null, page 62.
J	Solution for the minimization problem $J = \mid \vec{p} - a\vec{g} \mid^2$, eq. (3.34), page 37.
L_{size}	Length of the desired roulette wheel list (GA), eq. (5.24), page 175.
$\mathfrak{c}$	Constant for producing an angle proportional to the open angle O (GA), page 172.
w_m	Weighting factor for the m^{th} sensor, eq. (3.7), page 29.
(r, θ, z)	Cylindrical coordinates, radius, azimuth and height (or elevation), respectively, eq. (2.4), page 12.

(r, φ, θ)	Spherical coordinates, radius, polar angle (or inclination) and azimuth, respectively , eq. (2.5), page 12.
(x, y, z)	Cartesian coordinates, eq. (2.3), page 12.

Greek Symbols

$\alpha(\vec{x})$	Geometry related coefficient (BEM), eq. (5.1), page 141.
α_n	Weight factor for a given frequency f_n (GA), eq. (5.15), page 171.
$\delta \mathrm{d}p$	Difference in the normal gradient, or *jump of velocity* - primary variable in IBEM, page 139.
Δf	Resolution in terms of frequency, page 63.
δp	Difference in pressure, *jump of pressure* - primary variable in IBEM, page 139.
Δt	Resolution in terms of time, page 63.
$\Delta t_{\vec{x}}$	Emission time delay at focus point $\vec{x}$, $\Delta t_{\vec{x}} = r_{\vec{x}}/c$, eq. (3.5), page 29.
Δ_m	DSB microphone-dependent emission time delay for a focal point $\vec{x}_p$, eq. (3.7), page 29.
η	Arbitrary constant used in the truncation of Equation (4.31) , page 263.
λ	Wavelength $[\mathrm{m}]$, eq. (2.14), page 15.
ρ_0	Air density $\left[\mathrm{kg} * \mathrm{m}^{-3}\right]$, eq. (2.2), page 11.
σ	Intrinsic characteristic dimension of an object, page 18.
τ	Time delay between consecutive sensors, eq. (3.69), page 59.
θ	Incident wave angle, eq. (3.69), page 59.
σ	Standard deviation, page 186.

ϑ	Wave incident angle, eq. (3.67), page 56.
$\vec{\alpha}$	Slowness vector, $\vec{\alpha}_s = \vec{\zeta}_s / c$, eq. (3.37), page 40.
$\vec{\zeta}_s$	Unit-length vector pointing in the direction of propagation (the negative of the direction of aim), eq. (3.38), page 40.
μ	Mean value for a given distribution, page 186.
ω	Circular frequency, $\omega = 2\pi f$, eq. (2.12), page 15.

Mathematical Operators and Conventions

$(\cdot)^*$	Complex conjugate operator, eq. (3.32), page 37.
$(\cdot)^\dagger$	Hermitian operator, complex conjugate transpose, eq. (3.33), page 37.
Δ	Laplacian, $\Delta = \nabla^{\mathrm{T}}\nabla$. Cartesian coordinates (x, y, z): $\Delta = \frac{\partial^2}{\partial x^2} + \frac{\partial^2}{\partial y^2} + \frac{\partial^2}{\partial z^2}.$ Cylindrical coordinates (r, θ, z): $\Delta = \frac{1}{r}\frac{\partial}{\partial r}\left(r\frac{\partial}{\partial r}\right) + \frac{1}{r^2}\frac{\partial^2}{\partial \theta^2} + \frac{\partial^2}{\partial z^2}.$ Spherical (or polar) coordinates (r, φ, θ): $\Delta = \frac{1}{r^2}\left(\frac{\partial}{\partial r}\left(r^2\frac{\partial}{\partial r}\right) + \frac{1}{\sin\varphi}\frac{\partial}{\partial \varphi}\left(\sin\varphi\frac{\partial}{\partial \varphi}\right) + \frac{1}{\sin^2\varphi}\frac{\partial^2}{\partial \theta^2}\right),$ eq. (2.1), page 11.
$\delta(\cdot)$	Dirac-delta function, eq. (3.4), page 29.
$\mathrm{E}[\cdot]$	Expected value of a random variable, eq. (3.60), page 54.
$\mathrm{e}^{(\cdot)}$ $\exp(\cdot)$	Exponential function, where $\mathrm{e}^{(1)}$ is approximately 2,7182, eq. (2.6), page 13.
$\int \cdot$	Integral, eq. (2.12), page 15.

j	$\sqrt{-1}$, imaginary operator, eq. (2.6), page 13.
$\langle \cdot \rangle$	Averaging, eq. (3.36), page 39.
$\log(\cdot)$	Common base-ten logarithm, eq. (2.20), page 17.
∇	Gradient, $\nabla = \partial/\partial\vec{r}$, eq. (2.2), page 11.
∂	Partial derivative operator, eq. (2.1), page 11.
$\mathrm{Re}(\cdot)$	Returns the real part of a number, eq. (2.6), page 13.
$\max(\cdot)$	Function that returns the element with the maximum value for a sequence of numbers, or for a vector, eq. (5.18), page 173.
$\min(\cdot)$	Function that returns the element with the minimum value for a sequence of numbers, or for a vector, eq. (5.18), page 173.
$\{\cdot\}^t$	Transpose matrix, eq. (5.4), page 142.
$\{\cdot:\cdot:\cdot\}$	Vector in which the first value represents the starting point, the second the interval, and the third the last. For example, $f = \{500:5:5000\}$, eq. (E.2), page 263.
i	Imaginary operator just for Section 4.2, $i = \sqrt{-1}$, eq. (4.5), page 75.
$\lvert\cdot\rvert$	Absolute value, page 17.
$\mathrm{d}\cdot$	Derivative, eq. (2.12), page 15.
dB	Decibel scale, used for Sound Pressure Level $\mathrm{SPL} = 20\log\left(\frac{p_{\mathrm{rms}}}{p_0}\right)$, eq. (2.19), page 17.
OR	The OR operator returns logical 1 (or true) if either input, or both, evaluate to true, and logical 0 (or false) if they do not., page 269.
$\mathrm{size}(\cdot)$	Return the number of elements of a vector or matrix, eq. (5.10), page 151.

Acronyms

AC/DC	Alternating current and Direct Current in electric circuits field, eq. (2.20), page 17.
ADC	Analogic-to-digital converter, page 63.
ASL	Average sidelobe level, page 49.
BEM	Boundary Element Method, page 137.
BIE	Boundary Integral Equations, page 138.
BW	Beamwidth, page 48.
CB	Conventional beamforming, page 36.
CCD	Charge-Coupled Device, page 3.
CHB	Circular Harmonics Beamforming, page 66.
CPOW	Cross-Power Matrix, page 37.
CSM	Cross-Spectral Matrix, page 37.
CSR	Crossover Rate (GA), page 179.
D+F, D+FF	Diffraction plus Free-Field, page 95.
DAS	Delay-and-Sum beamforming, page 24.
dB	Decibel, pseudo-unit for Sound Pressure Level, usually ref. $p_0 = 20$ µPa, page 17.
DBEM	Direct Boundary Element Method, page 139.
DPI	Dots-per-inch (or pixels-per-inch for video devices), page 63.
DR	Dynamic range, page 50.
DSB	Delay-and-Sum beamforming, page 24.
EAA	Equally Angled Array, page 69.

ELR	Elitism Rate (GA), page 179.
FEM	Finite Element Method, page 138.
FF	Fitness Function (GA), page 171.
FFT	Fast Fourier Transform, page 63.
FS	Fitness Score (GA), page 171.
FvB	Frequency *vs.* Beampattern plot, page 52.
FWHM	*Full-width, half-maximum*, page 48.
GA	Genetic Algorithm, page 137.
GP	Genetic Programming (GA), page 168.
HGA	Hybrid Genetic Algorithm (GA), page 178.
HIE	Helmholtz Integral Equation, page 140.
HSV	*Hue*, *saturation*, and *value* colour scale, page 83.
IBEM	Indirect Boundary Element Method, page 139.
KHIE	Kirchhoff-Helmholtz Integral Equation, page 141.
LD	Loudspeaker Set, page 119.
LTI	Linear time-invariant systems, page 43.
MEC	*Método de Elementos de Contorno*, page 137.
MR	*Mesh refinement* coefficient, page 143.
MRA	Maximum response axis, page 47.
MSL	Maximum sidelobe levels, page 50.
MUR	Mutation Rate (GA), page 179.
NGEN	Number of Generations (GA), page 178.

nsqc	*Next square corner*, eq. (5.18), page 173.
OR	The OR operator returns logical 1 (or true) if either input, or both, evaluate to true, and logical 0 (or false) if they do not., page 269.
PDE	Partial Differential Equation, page 138.
PSF	Point Spread Function, page 43.
PWB	Plane wave beamforming, page 40.
RAM	Random Access Memory, page 159.
RH	Relative humidity, page 124.
rms	Root Mean Square, page 16.
SEA	Statistical Energy Analysis, page 138.
SGA	Simple Genetic Algorithm (GA), page 169.
SNR	Signal-to-noise ratio, page 52.
SOA	Solid opening angle, page 56.
SPL	Sound Pressure Level, page 17.
SPOP	Size of Population (GA), page 178.
STC	Stop Criteria of $J'_m\left(kr\sin(\phi)\right)$, page 263.
UAV	Unmanned Aerial Vehicle, page 5.
UCA	Uniform circular array, page 68.
ULA	Uniform linear array, page 58.
VANT	Veículo Aéreo Não Tripulado, page 206.
VLA	Very Large Array, page 2.
WT	Weather station, page 124.

1

Introduction

Sound is undeniable part of life. It can be faced as just another type of wave or with more joy, such as pleasant music. Beyond its nature as a wave, there is the key point that living beings are continuously and unconsciously under its effects. Such effects can provide useful information, like a fire alarm or inherent consequences of use, like an aircraft's turbine [1]. High intensity sounds can damage the human ears, leading to changes in perception and cause other side effects like stress and irritation. For this reason, acoustics is an important point of concern to modern human life.

Governments and communities[1] have efforts to regulate and mitigate the sounds which can cause health problems and/or those considered disturbing. Nevertheless, it is difficult to clearly identify the sources of sound, this is the point where the acoustic imaging techniques play an important role. That is, they help in source localization and, with more sophisticated instrumentation, they can create maps of the sound.

The necessary efforts to use such techniques become clear when human limitations (psychophysics) are presented [3]. The typical human ranges of vision and hearing are in truth very restricted, Figure 1.1. Beyond recovering source directions, the idea behind these techniques is to extend the understanding of an unknown event and/or sound source by crossing both information domains. Visual information has proved to clarify a situation that otherwise requires several lines of text to describe. Moreover, the analysis of a raw sound information, without the acoustic image and

---

[1] The International Noise Awareness Day (INAD) is one of the campaigns to create knowledge and awareness [2]. More details about the Brazilian branch can be found at `http://www.inadbrasil.org`.

performed by an human, would be influenced by the his/her previous knowledge and sometimes by his/her creativity.

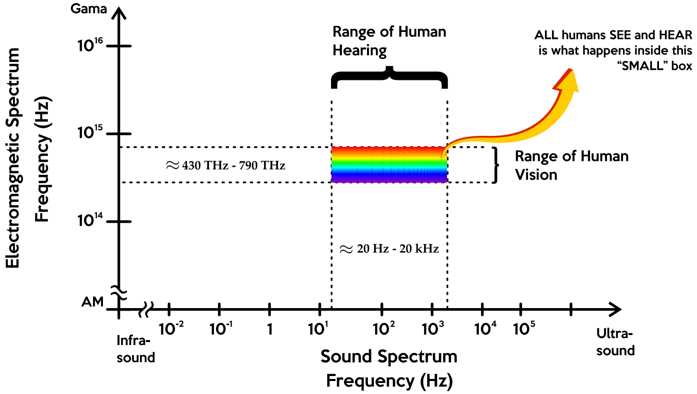

Figure 1.1: Typical human range of vision and hearing.

In this study, one of these techniques, Beamforming, is put into practice together with other concepts to improve its performance. It is a known signal enhancement technique which has been applied also in other fields such as astronomy, sonar, and seismic detection. With signal processing, the array is the main tool behind the technique, because the it is responsible for sampling the time-space domain with distributed receivers to extract signals which incide upon it.

The Very Large Array (VLA) in New Mexico, USA, is one of the most famous arrays built in the 20th Century, Figure 1.2. Its proposition to see great distances into the sky makes it one of the great tools in the field of radio astronomy [4].

The beamforming principle is quite simple. It basically samples the sound field with an array of sensors. The correct summation of these signals will render a reinforcement of the recorded sound for a chosen direction in space. In addition, processing a set of possible incoming directions enables the creation of sound maps. Figure 1.3 exemplifies the difference between an omnidirectional beampattern and a focused beampattern created by a set of microphones.

Figure 1.2: Very Large Array (VLA) antennas of the radio telescope beamforming in New Mexico, USA (photo by Kim Jew [5]).

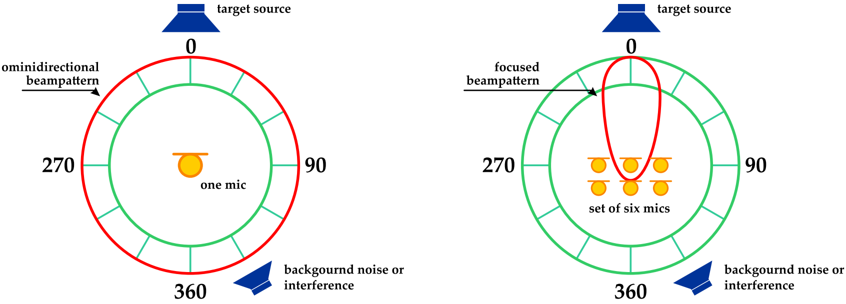

(a) Omnidirectional response

(b) Directional response

Figure 1.3: Response pattern differences between single and multiple sensors.

In practice, the reader might imagine that beamforming functions similarly to a digital camera. Inside a digital camera there is a CCD microchip which has an array of photon (or light) sensitive points . After an acquisition of photons through the lens, there is a post-processor that delivers the final photo to the user. In acoustics, the sensitive parts involved are the microphones, also disposed in an array, and the result of the post-processing is the acoustic map or acoustic image. These acoustic images (with a distinct comparison) are similar to pictures from thermal cameras. There is a colourmap and usually the spots in red colour represent points of high intensity while the blue regions are those with less energy. Chapter 3 formally describes the physics involved in this process.

The second important phenomenon considered in this study is sound diffraction. Although the mathematics to describe it involves a great deal of physics, its nature is rather intuitive. It is because of diffraction that one can comfortably listen to music outside a room where the sound source is located. The waves "bend over" surfaces and propagate to the listener. It is also because of diffraction (together with other effects) that humans can localise the origin of sound sources. The acoustic "shadow" that the head creates between the ears helps brain processing in estimating the sound's original direction. Chapter 4 offers the descriptions of the diffraction model applied here.

In summary, the important points of array processing are[2]:

a. the sensors' placement, or array geometry;

b. the post-processing technique employed; and

c. the wavenumber-frequency resolution.

These three items are strongly connected since any change in one will in turn affect the others. Geometry determines the wavenumber-frequency response of the array, which together with post-processing is the essence of the applied strategy. Issues with the geometry can possibly fall into an unpleasant spatial undersampling condition or other pitfalls. In this document, the two most important geometries are extensively discussed. The first one is the most basic as it is simply a circumference. The second one is the fruit of a genetic algorithm (GA) simulation.

GA is part of family of the evolutionary techniques which are based on the concepts initially developed by Charles Darwin. The principle is simple: the individuals which best fit surrounding conditions will survive and perpetuate their genes. This optimization and search technique is adapted to the context of geometry modelling to suit the problem proposed - the fundamentals are described in Section 5.3.

With methods clarified, analytical simulations are carried out to discuss and comment on the principles presented herein. Subsequently, Bboundary Element Method (BEM) simulations are collated with the beamforming processing. The BEM is used as a supplementary numerical method to predict diffraction effects from a general to specific perspective.

---

[2] They are amply described in Sections 3.2 and 3.3.

1.1 Motivation and Problem Description

Science's quest to describe events and behaviours is a continuous process. When a research topic emerges there are always several problems or questions surrounding it. It is important to organize related ideas and analyse possible steps from the starting point to the still unknown final result. Given a defined block of time for the execution, the scope has to be defined and tangible work must proceed. The science is then the work on gathering information based on observations and previous knowledge towards the extraction of new conclusions.

It is usual that acoustical engineers state that one array is acoustically transparent for a determined range of frequencies. However, what would be the real diffraction effects that impact upon the measurements? When questions like this arise the role of the researcher is to investigate methods to estimate a way to the target. This work has strong motivations that have come from the author's previous experience with related techniques combined with the will to solve open questions and doubts.

The object of study on which this dissertation is based is a cylinder. The properties of basic volume can serve as raw-material for applications over a broad spectrum. The proposed problem is accounting diffraction over a cylindrical surface, placing sensors over that surface, and beamforming the sensors' outputs.

To exemplify one application, consider the aeroacoustics field, in which the beamforming technique is widely applied and in diverse kinds of fronts, e.g., fly-over testing, wind-tunnel testing, jet noise, etc. However, the concepts presented in this dissertation can feed a distinct application: the use of beamforming as an auxiliary system in localizing sound emitting obstacles. The cylinder shape is similar to a fuselage, thus, their behaviour should be alike. For example, the Unmanned Aerial Vehicle (UAV) - an aircraft without human pilot or crew - could be an aircraft that would have improved sensory systems through the use of beamforming, Figure 1.4. It is evident that in this application the researcher in question will have to connect the effects of motion and fluid to the aspects shown here.

Different applications can also be considered in fields like sound monitoring, naval practices, and environmental noise, among others. It is just a matter of using the knowledge presented here as previous knowledge. Besides the shape of the volume, the discussion about diffraction combined with beamforming can inspire, or contribute, to other research areas or projects. Although the GA and BEM are not the main theme of this work, they are used as powerful tools to achieve improved results.

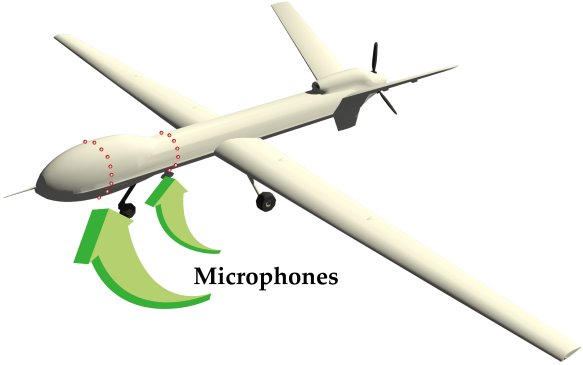

Figure 1.4: UAV (Unmanned Aerial Vehicle) with sensors on the surface.

1.2 Research Objectives and Contributions

This study aims to develop the beamforming technique within the field of acoustics. As its main contribution, the condition of diffraction is included in the proposed problem. Its derivations are demonstrated and the conjecture that this addition leads to improvements is presented and discussed.

The project has a multidisciplinary nature which can be seen throughout the document, in dealing with acoustics; beamforming; diffraction; signal processing; analytical and numerical methods; measurements and instrumentation; optimization; computer science; and others. Furthermore, it also has a conceptual aspect as the basic problem can be extended to other dimensions, and the results discussed can be applied to other beamforming problems.

In an objective way, the goals and contributions are:

1. Implementation of the diffraction on the beamforming technique for the acoustically hard[3] cylinder problem. Besides the analytical derivations, simulations were realised discussing the array performance

---

[3] It means the surfaces are considered acoustically rigid, i.e. not soft.

for the two geometries considered. Furthermore, experimental results were compared against the analytical;

2. A method of geometry optimization based on genetic algorithm is developed adapting evolutionary concepts into the “array domain”. In this application, the array is projected in cylindrical coordinates to fit over a surface of any radius;

3. The Boundary Element Method (BEM) is used as an alternative tool to confirm and discuss the diffraction effects. In addition, this section lists details concerning the relationship between source localisation and the refinement of the 3D model;

4. A solid revision about beamforming concepts, including equations and figures, while minimising possible misconceptions;

5. Construction of original processing tools (software), integrating all the different aspects contained in this research.

1.3 Document Outline

The document is organised in six chapters. The first three introduce bases for a good understanding of the discussions in the last three. They are:

Chapter 1. Introduction
It comprises the initial thoughts, objectives, and an introduction to contextualize the reader with the topics outlined in this research.

Chapter 2. Acoustical Formulations
It introduces the formal mathematics that sustain the bases of modern acoustics.

Chapter 3. Beamforming
This chapter provides a solid review of the basic beamforming methods and the description of the parameters to estimate performance in array processing.

Chapter 4. Diffraction and Cylinder

This chapter initiates with the basics about diffraction, following with derivations for the cylinder case. At the end of the first part the beamforming is contextualized. The subsequent sections discuss the simulations for the two types of arrays. For one of these arrays, measurements were carried out in anechoic environment. This chapter is of fundamental importance since it sews the knowledge produced with the theories presented.

Chapter 5. Numerical Methods

This chapter is split in two main sections, the BEM and the GA. In each part there is a basic review of the respective techniques and following with discussions concerning the results achieved. It contributes in the sense that some aspects of these themes are mashed-up with beamforming.

Chapter 6. Conclusions

It comprises the final considerations and comments on the development of this research. At the end, there are recommendations for future studies.

Elements after the main chapters:

I. After the chapters written in English, Chapters 1 and 2 are presented in Portuguese.

II. The List of References follows, starting on page 217.

III. The Appendices complement the content of the main chapters. In particular, Appendix B contains the abstract in the foreign languages: Dutch, German, French, Spanish and Italian.

IV. The Annexes include additional information related to the instrumentation employed.

V. The Alphabetical Index is intended to help in finding terms and their context.

1.3.1 Electronic Version

Besides the printed version of this dissertation, Appendix A includes the electronic PDF version of the document. During the research, care was taken to use high definition and vector figures at the maximum number of plots. This enables the reader to perform successive zooming and better observe and understand the details.

2

Acoustical Formulations

This chapter describes a series of basic formulations in acoustics which are fundamental for a better understanding of the subsequent chapters. The basic formulations described herein are restricted to homogeneous and isotropic fluids in which the speed of sound c is constant throughout.

2.1 The Wave Equation

Considering lossless medium[1], the linear wave equation can be derived as follows (the complete derivations can be consulted in Kuttruff [6] or Kinsler *et al.* [7]). The wave equation for the time-domain sound pressure $p(\vec{r},t)$ and the Euler equation for the particle velocity $v(\vec{r},t)$ can be written as

$$\Delta p(\vec{r},t) = \frac{1}{c^2}\frac{\partial^2 p(\vec{r},t)}{\partial t^2}\,, \tag{2.1}$$

$$\rho_0 \frac{\partial \vec{v}(\vec{r},t)}{\partial t} = -\nabla p(\vec{r},t)\,, \tag{2.2}$$

where $\vec{r} = (x,y,z)$ is the position vector in space $\mathbb{R}^3$, t the time variable, c the speed of sound, $\nabla = \partial/\partial\vec{r}$ is the gradient, Δ is the Laplacian[2], and ρ_0 is the air density. The Laplace[3] operator ($\Delta = \nabla^{\mathrm{T}}\nabla$), or spatial differential

---

[1] This implies that viscous and thermal effects are neglected.

[2] The Laplacian operator is also found with ∇^2 notation, e.g., Helmholtz equation.

[3] Pierre-Simon Laplace (1749-1827) was a French mathematician who is considered one of the great influences among French scientists in history. He excelled in the fields of Physics, Astronomy, and Mathematics [8]. He also pioneered the Laplace transform and the Laplacian differential operator, widely used in math and engineering.

operator, ensures three dimensional extension in Cartesian coordinates (x, y, z)

$$\Delta = \frac{\partial^2}{\partial x^2} + \frac{\partial^2}{\partial y^2} + \frac{\partial^2}{\partial z^2}\,, \tag{2.3}$$

in cylindrical coordinates (r, θ, z),

$$\Delta = \frac{1}{r}\frac{\partial}{\partial r}\left(r\frac{\partial}{\partial r}\right) + \frac{1}{r^2}\frac{\partial^2}{\partial \theta^2} + \frac{\partial^2}{\partial z^2}\,, \tag{2.4}$$

or in spherical coordinates (r, φ, θ),

$$\Delta = \frac{1}{r^2}\left(\frac{\partial}{\partial r}\left(r^2\frac{\partial}{\partial r}\right) + \frac{1}{\sin\varphi}\frac{\partial}{\partial \varphi}\left(\sin\varphi\frac{\partial}{\partial \varphi}\right) + \frac{1}{\sin^2\varphi}\frac{\partial^2}{\partial \theta^2}\right). \tag{2.5}$$

In spherical polar coordinates, the coordinate r is the distance of some point from the origin. The other coordinates are two angles defining the direction of the line connecting that point with the origin. Namely, they are the polar angle (φ), which is the angle between the fixed axis *zenith* and the line segment OP, and the azimuth angle (θ), which is the signed angle measured from the azimuth reference direction to the orthogonal projection of the line segment OP on the reference plane [6], Figure 2.1.

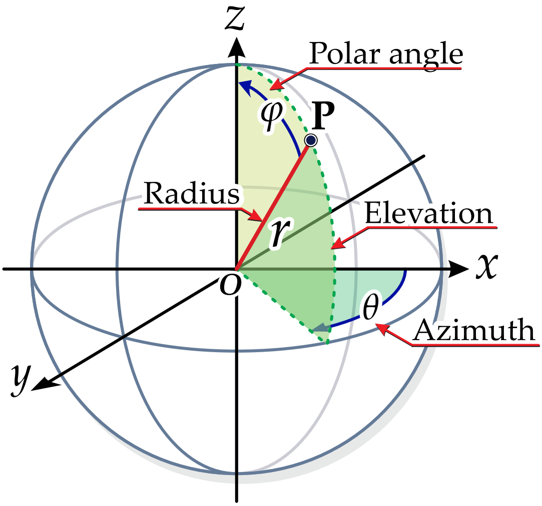

Figure 2.1: Polar coordinates: distance r; polar angle (or inclination) φ and azimuth angle θ.

Equation (2.1) is linear and has particular solutions that are periodic in time. If the time dependence is a harmonic function of *circular frequency* ω, it is possible to write[4]

$$p(\vec{r},t) = \mathrm{Re}(\mathrm{e}^{+\mathrm{j}\omega t}\,\psi(\vec{r}))\,, \tag{2.6}$$

where $\psi(\vec{r})$ is a complex scalar function defined at a spatial point $\vec{r} = (x,y,z) \in \mathbb{R}^3$ and "j" is the complex operator, i.e., $\mathrm{j} = \sqrt{-1}$. Substituting Equation (2.6) into Equation (2.1) yields the Helmholtz[5] Equation [11]

$$\nabla^2\psi(\vec{r}) + k^2\psi(\vec{r}) = 0, \qquad k = \frac{\omega}{c}\,, \tag{2.7}$$

where k is the wave number[6] with a dimension of $1/\mathrm{m}$.

Naturally, by comparing Equations (2.7) and (2.1), the Helmholtz equation can be rewritten for the frequency ω as

$$\nabla^2 p(\vec{r},t) + \left(\frac{\omega}{c}\right)^2 p(\vec{r},t) = 0\,, \tag{2.8}$$

and the general spherically symmetric solution is [12, 7]

$$p(\vec{r},t) = \underbrace{\frac{1}{r}\,f_1(ct-r)}_{\mathbf{A}} + \underbrace{\frac{1}{r}\,f_2(ct+r)}_{\mathbf{B}}\,, \tag{2.9}$$

for any $r > 0$. Part **A** represents a spherical wave diverging from the origin and part **B** represents a wave converging towards the origin. For the causality case (backward-travelling wave) part **B** is not a suitable solution, hence, Equation (2.9) simplifies to:

$$p(\vec{r},t) = \frac{f_1(ct-r)}{r} = \frac{f_1(t-r/c)}{r}\,, \tag{2.10}$$

where $1/r$ represents the spherical spreading effect (Figure 2.2) and r/c is the time needed for the wave to travel to point P (r distant) in space.

---

[4] The time dependence $\mathrm{e}^{+\mathrm{j}\omega t}$ in Equation (2.6) is traditional among acousticians. The sign ± is a convention related to the phasor direction assumed [6, 9].

[5] Hermann von Helmholtz (1821-1894), the famous German physiologist and empiricist, whose impact on acoustics, hydrodynamics, and electromagnetism is of great magnitude [10, 11].

[6] The *wave number* is related to the case of a plane wave propagating through the fluid, where the wavelength is $\lambda = 2\pi/k$. Thus, k is the number of waves per 2π units of length [11].

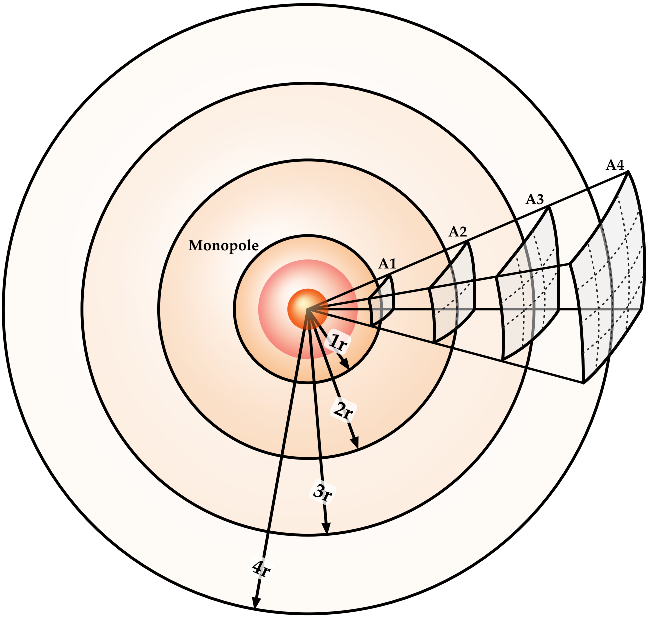

Figure 2.2: Sound divergence.

Figure 2.2 shows that the same sound energy is distributed over spherical surfaces of increasing areas as the radius r increases. The intensity of sound is inversely proportional to the square of the distance from the point source.

The complex representation is usually used, thus, for a divergent, symmetric, and harmonic wave, Equation (2.10) becomes

$$p(\vec{r},t) = \frac{\tilde{p}}{r}\,\mathrm{e}^{j\omega(t-r/c)} = \frac{\tilde{p}}{r}\,\mathrm{e}^{j(\omega t-kr)}\,, \tag{2.11}$$

where $\tilde{p}$ is a complex constant, dependant on the boundary conditions; r is the distance to the observation point; and k is the wave number.

The Helmholtz equation, therefore, stands for monochromatic waves, or waves of some given frequency ω. For polychromatic waves, or sums of waves of different frequencies, it is possible to sum solutions with different ω values. Thus, the *Forward Fourier*[7] *Transform* with respect to the

---

[7] Jean Baptiste Joseph Fourier (1768-1830) was a French mathematician and physicist best known for the developments produced by his Fourier Transform and Series in diverse scientific fields, such as heat transfer and acoustics [13].

temporal variable is performed as follows [14]:

$$p(\vec{r},\omega) = \int_{-\infty}^{+\infty} p(\vec{r},t)\,\mathrm{e}^{\,-\mathrm{j}\omega t}\,\mathrm{d}t\,, \tag{2.12}$$

where $\omega = 2\pi f$ is the *circular frequency*. Thereupon, it is also possible to determine the solution of the wave equation using the *Inverse Fourier Transform*[8] [16, 17]:

$$p(\vec{r},t) = \frac{1}{2\pi}\int_{-\infty}^{+\infty} p(\vec{r},\omega)\,\mathrm{e}^{\mathrm{j}\omega t}\,\mathrm{d}\omega\,, \tag{2.13}$$

$$\omega = ck \qquad \text{or} \qquad k = \frac{\omega}{c} = \frac{2\pi f}{c} = \frac{2\pi}{\lambda}\,, \tag{2.14}$$

where k is the *wave number* and is real for real ω values; λ is the *wavelength* and f is the frequency.

2.2 Plane Wave

The plane wave (Figure 2.3) can be interpreted as a special solution of the general wave equation. Considering a plane wave that travels along the x-axis, Equation (2.1) can be reduced to a one-dimensional form as follows [6]

$$\frac{\partial^2 p}{\partial x^2} = \frac{1}{c^2}\frac{\partial^2 p}{\partial t^2}\,, \tag{2.15}$$

where $p = p(x,t)$. Its characteristic property is that each acoustic variable has constant amplitude and phase on any plane perpendicular to the direction of propagation [7]. That is to say, they are compressed or dilated to the same degree.

A direct comparison shows that the mathematical development is similar and can be applied here without repetition. Hence the general solution reads:

$$p(x,t) = \underbrace{f_1(x-ct)}_{\mathbf{A}} + \underbrace{f_2(x+ct)}_{\mathbf{B}}\,. \tag{2.16}$$

---

[8] Other authors and scientists may define the Fourier Transform pairs differently. A discussion about it can be consulted in Cohen [15].

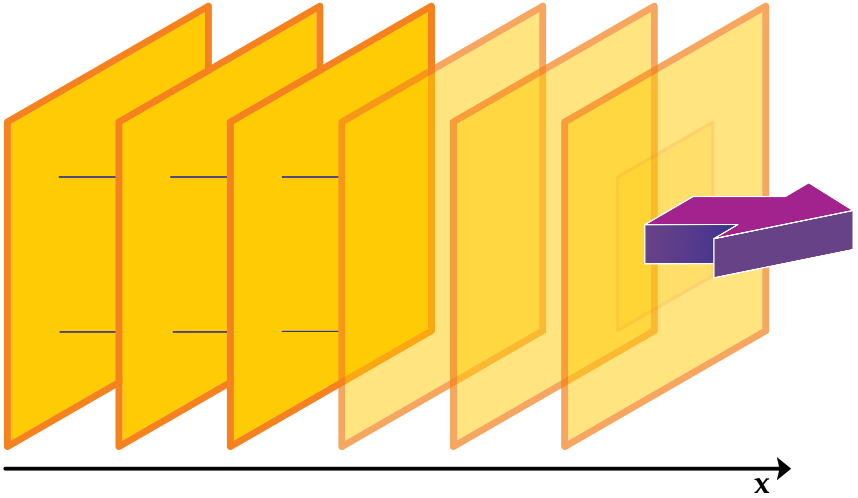

Figure 2.3: Plane wave.

The former term **A** describes the propagation of the local state of sound pressure $p(x,t)$ in space and time in the positive x direction and the latter term **B** describes such propagation in the negative x direction. For harmonic time dependence,

$$p(x,t) = D\cos(\omega t - kx - \phi_1) + E\cos(\omega t + kx - \phi_2)\,, \tag{2.17}$$

where D, E, ϕ_1, and ϕ_2 are constants. Considering a plane wave proceeding in the x-direction with the sound pressure varying according to a harmonic time law, the constant E is set to zero and Equation (2.17) in complex notation reads

$$p(x,t) = \hat{p}\,\mathrm{e}^{-jk(x-ct)} = \hat{p}\,\mathrm{e}^{j(\omega t - kx)}\,, \tag{2.18}$$

where $\hat{p}$ is the complex pressure amplitude[9], ω is the angular frequency, kx is the phase angle, and k is the wave number, Figure 2.4.

---

[9] Some authors use a slightly different notation, for example, Beranek in his book, Acoustics [12]. Instead $|\hat{p}|$ he uses the notation $\sqrt{2}p_+$ to express the peak value (assuming p as the magnitude rms value) for a diverging wave.

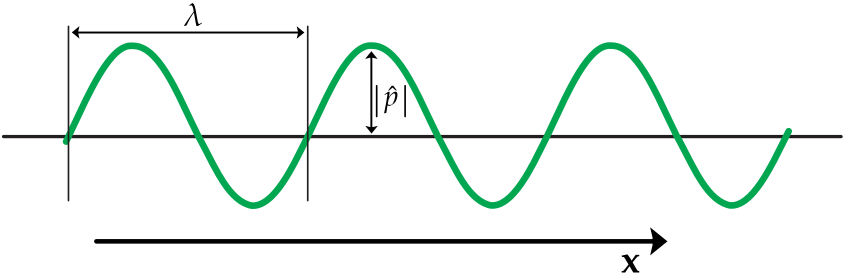

Figure 2.4: Spatial pressure distribution for a plane harmonic wave.

2.3 Sound Pressure Level

Sound consists of small disturbances (compression and rarefaction) as deviations from the quiescent pressure value (or atmospheric pressure). The human ear can detect a wide range of sound pressures [3, 18], which implies difficult representation. The decibel (dB) is then a convenient way for expressing the ratio of a wide range of orders of magnitude. Therefore, the Sound Pressure Level (SPL) is defined as

$$\mathrm{SPL} = 10 \log \left(\frac{p_{\mathrm{rms}}}{p_0} \right)^2 = 20 \log \left(\frac{p_{\mathrm{rms}}}{p_0} \right) \ \mathrm{dB}\ [\text{Pa ref. } p_0]\,, \tag{2.19}$$

with

$$p_{\mathrm{rms}} = \sqrt{\frac{1}{T} \int_0^T p^2(t)\, \mathrm{d}t}\ , \tag{2.20}$$

where p_{rms} is the "root mean square[10] "

sound pressure; p is sound pressure (in Pa); log is the common base-ten logarithm; and p_0 is the reference sound pressure, p_0 = 20 µPa. This constant p_0 is approximately the human hearing threshold in mid-frequencies. In daily acoustics, the range mapped by the logarithmic scale ranges approximately from 0 dB to 130 dB.

---

[10] The *root mean square* (rms or *quadratic mean*) is the equivalent steady (constant) value. To better understand, consider the electric circuits field. The DC value delivers the same amount of *power* to a load in a circuit as the AC signal does over its cycle. For example, for sine waves of amplitude a, $y = a\sin(2\pi f t)$, its rms value is $a/\sqrt{2}$.

2.4 Frequency Domain

The frequency domain (f or Fourier domain) results from the transformation of the time domain in seconds (s), via the Fourier Transform [19] into a domain where signal representation is given in Hertz (or s^{-1}). In acoustics, the range of frequencies generally of most interest is between 20 Hz and 20 kHz. This is approximately the range a human can perceive as sound.

When approaching a problem in acoustics, in addition to the human frequency range it is possible to determine the low, medium, and high frequency regions related to the object of study. This can be explained if one compares the dimension of importance to the wavelength that this measurement can render, see Figure 2.5.

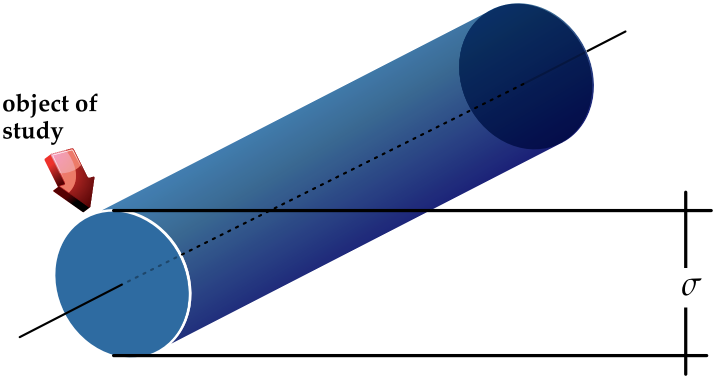

Figure 2.5: Dimension of importance on the object of study.

Given σ as an intrinsic characteristic (diameter in this example), a dimensionless wave number $k\sigma$ can be computed whose frequency ranges rely on the following ratios:

1. if wavelength λ is significantly larger than σ, i.e. $\lambda \gg \sigma$, or $k\sigma \ll 2\pi$, the problem is referred to as low frequency;

2. dually if wavelength λ is significantly smaller than σ, i.e. $\lambda \ll \sigma$, or $k\sigma \gg 2\pi$, the problem is referred to as high frequency;

3. and if wavelength λ has approximately the same size as σ, i.e. $\lambda \approx \sigma$, or $k\sigma \approx 2\pi$, the problem is referred to as medium frequency.

Understanding the frequency ranges as such (and for linear acoustics), results calculated for one model size can be extrapolated for a model of different size. This application is typical in the field of aeroacoustics [20, 21] where scale models are measured and later on the full scale is recovered using the ratios

$$f_{\text{full}} = \text{Scale Factor} \cdot f_{\text{measured}}\,, \tag{2.21}$$

where the "Scale Factor" is a ratio between the scale and the real model.

2.4.1 Acoustic Fields

When dealing with any type of acoustic simulation or measurement some care must be taken concerning the sound field. To begin, one must take into account two factors

(a) the acoustic field in terms of frequency, that is, *far-field*, *near-field* or *transition-field* [9]; and

(b) the acoustic field in terms of *reverberation* or *anechoicity* [22].

2.4.1.1 Near and Far Fields

The acoustic field in terms of frequency is defined with respect to the observation point. The transition from the near- to far-field regions occurs when $r \sim \lambda/2\pi$, where r is the distance from the source to the observation point and λ is the wavelength. Usually, a dimensionless parameter kr is used to define these fields.

In the near-field (see Equation (2.11)) the velocity and pressure differ in phase by an amount that depends on the distance from the source and the frequency. Close to the source, $kr \ll 1$, the pressure and the induced velocity are out of phase[11]. This difference depends on the type of sound source and/or problem. Therefore, this uncertainty is depicted as an area in Figure 2.6. The fluctuations (red line) seen in this figure exemplify the dominance of the reactive component in the acoustic energy. The near-field region[12] is usually within 1/4-wavelength of a given sound source (or large reflective surface) [9].

---

[11] If the pressure and the particle velocity have 90° (1/4 of their period) of phase difference (as in the red line in the near field region of Figure 2.6) they are in *phase quadrature*.

[12] This value may differ among books and standards, but the range is mostly (1/4 ⇔ 1/1)-wavelength [23].

On the other hand, beyond the near-field, in the far-field, $kr \gg 1$, the pressure is in phase with the particle velocity and the sound radiation varies in intensity as $1/r^2$ (or 6 dB per distance doubled). The far-field region is recommended for recording sound pressure level, per Figure 2.6.

2.4.1.2 Free and Reverberant Fields

Different acoustics environments exist in all types of rooms or spaces. In the far-field there are two special regions, the free- and reverberant field.

The free-field[13] conditions exist in large open outdoor spaces or in rooms having highly absorptive surfaces. The effectiveness in absorbing acoustic waves is called anechoicity. In the free-field, one always considers the direct path between emitter and receiver.

In the lower limit of the free-field constant decay, the sound pressure drops to a relatively constant level. At this point, the sound field is considered diffuse, and its size is determined by the amount of reflected sound within a room. In the reverberant field, sound pressures are similar independent of location, Figure 2.6.

Another way of thinking of this would be to place distinct observers in both fields. For the observer in the free-field the direct sound predominates over the diffuse, hence the reverberant field (green dashed line) is not noticeable, per Figure 2.6. The same analogy can be used for an observer in the reverberant field.

To perform acoustic measurements special rooms are constructed to reproduce the sound fields described above. It is also important to say that the room characteristics depend on its size and materials on the walls.

---

[13] The *free-field* is also referred to as the *direct-field*.

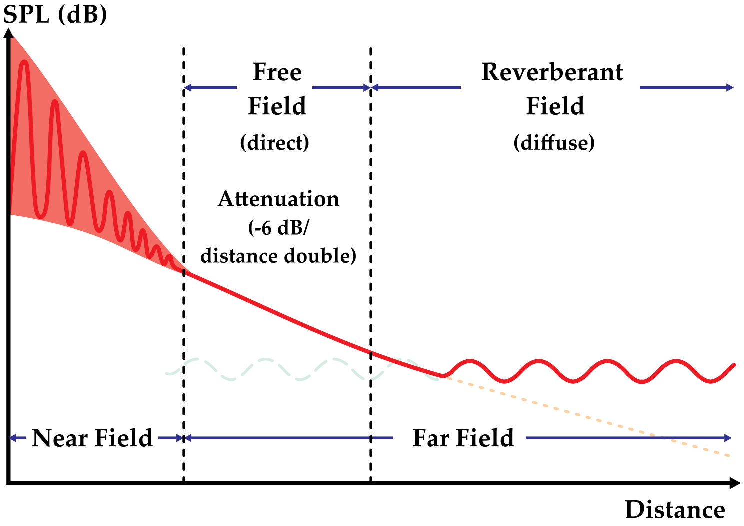

Figure 2.6: Sound fields in enclosed space [9].

3

Beamforming

When dealing with sound sources, the one of interest is usually contaminated by the soundscape. Therefore, signal processing methods can be used to focus on, separate, and map the desired signals. For propagating signals in space, spatiotemporal filtering must be used to extract the directions of propagation and frequency content. The set of algorithms that focus to a point or direction is commonly referred to as beamforming.

Its principles have been applied to a diverse research fields such as astronomy, sonar, and seismology. It has been applied rudimentarily since the beginning of the 20th century as a technique to identify travelling aircrafts [24]. Nevertheless, modern advances during the 1970's made it possible to record and post-process the time data [25].

This chapter will describe beamforming fundamentals and array performance, as well as demonstrate how sound sources can be located using a microphone array.

3.1 Acoustic Imaging

There are three well known techniques for acoustic imaging: beamforming [26], holography [27], and intensimetry [28]. Among them, beamforming is the only one that can be measured in the far-field . Also, its processing time is relatively faster with respect to the others.

Of course beamforming has its limitations, usually related to the number of microphones, the array's geometry, the source model, and/or distance to the sound source. These themes will be discussed throughout this dissertation. In Michel (2006) [29] it is possible to consult a historical review about beamforming.

3.2 Fundamentals

This section provides a summary of the basic beamforming techniques, as well as a description of the source model. Although Conventional Beamforming for plane waves is the algorithm most applied in this dissertation, basic delay-and-sum beamforming introduces the technique to better comprehend the concepts involved.

At first, it is important to consider the frequency range of the application at hand and what the expected source position in space is. These parameters will define in which acoustic field the array is immersed. If the sources are in the array far-field[1], the wavefronts become planar and the incident field is modelled as a sum of plane waves (with incident direction $\vec{\zeta}$). Otherwise, when the source is close to the array the wave fronts are curved; thus it is considered near-field. As a consequence, the incident field is modelled as a sum of monopoles. An approximate rule to define the *array-field* is given by

$$|R_{\text{ff}}| = \frac{2 \cdot L_{\text{arr}}^2}{\lambda} \tag{3.1}$$

where R_{ff} is the minimum distance to consider the array's far-field, L_{arr} is the largest array dimension and λ is the acoustic wavelength. Mailloux [30] states that although R_{ff} is sufficient to consider far-field, in order to have lower sidelobes $10L_{\text{arr}}^2/\lambda$ or more may be necessary [31, 32].

3.2.1 Delay-and-Sum Beamforming

The Delay-and-Sum[2] (DSB) is one of the simplest array processing techniques but still offers a robust approach. The idea of DSB is based on first sampling the sound field by an array of microphones, and then the signals are delayed and added together. This process will render a reinforced signal with respect to background noise and waves propagating from different directions.

The basic concepts of DSB will first be explained with an example. Following, there are the equations that describe the steps involved.

---

[1] In acoustics, these two regions can also be found as Fraunhofer region (far-field), and Fresnel region (near-field). They are references to the physicists who contributed significantly to wave optics theory; Joseph Fraunhofer (1787 - 1826) and Augustin-Jean Fresnel (1788 - 1827).

[2] The delay-and-sum beamforming is also referred to as *classical* beamforming or DAS in literature.

1. First, a scanning plane where the source is expected is defined. This plane is meshed into a grid of N points, Figure 3.1;

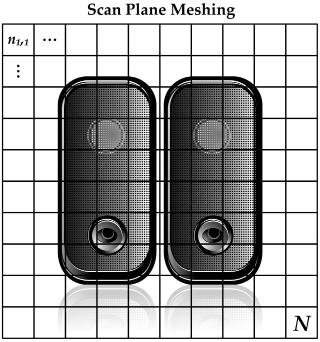

Figure 3.1: Scanning plane with $N = 10x10$ grid points for the loudspeaker measurement example.

2. For each cell of the grid, the sensor's signals are delayed by an amount proportional to the difference between the time it takes from the N^{th} grid point to the m^{th} microphone, Figures 3.2, 3.3, and 3.4;

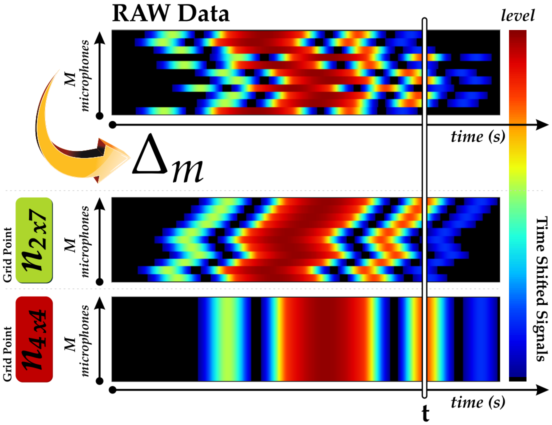

Figure 3.2: Delay correction in DSB for the grid points n_{2x7} and n_{4x4}.

   (a) If the analysed focus point does not have properly a source, the algorithm will attribute a value less than one to that cell, Figure 3.3;
   (b) If the analysed focus point coincides with the source position, the algorithm will attribute a value closer to one to that cell, Figure 3.4;

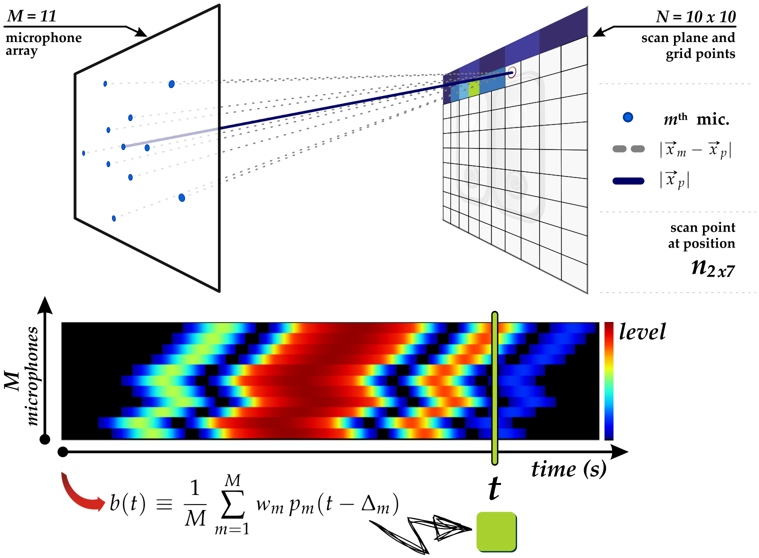

Figure 3.3: DSB scanning the n_{2x7} grid point. Green colour assigned, no sound source found.

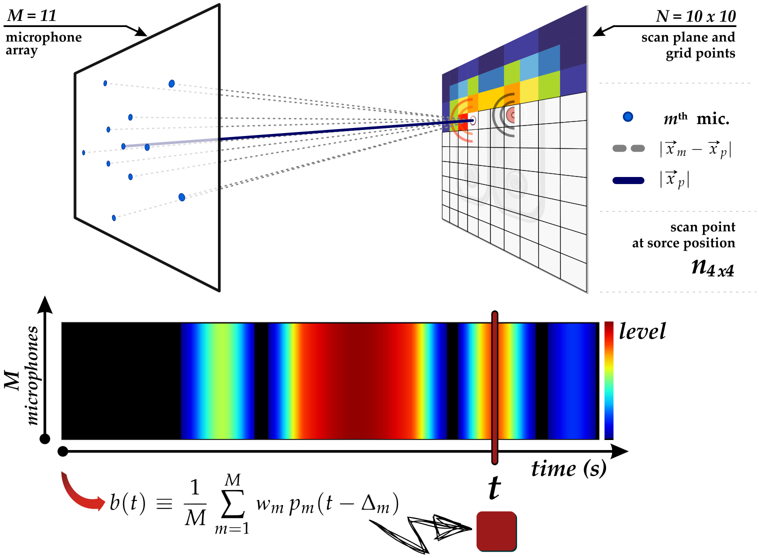

Figure 3.4: DSB scanning the n_{4x4} grid point. Red colour assigned, sound source localisation.

3. The amplitudes are corrected to account the distance between the N^{th} grid point to the m^{th} microphone;
4. The signals of all M microphones are added and weighted by the number of microphones;
5. The resulting acoustic pressures build the matrix, which is later encoded as a colour spectrum;
6. With the pressure matrix created, the acoustic and photo images are *overlaid*, Figure 3.5;

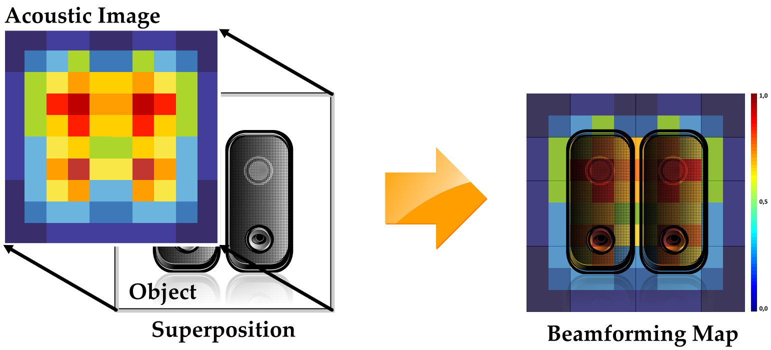

Figure 3.5: DSB, the acoustic and photo images are *overlaid*.

7. Finally, the beamforming acoustic map (for a given frequency) is created, Figure 3.6.

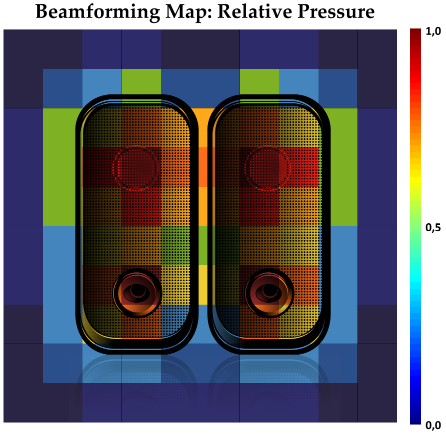

Figure 3.6: Beamforming map.

Figure 3.7 summarizes the basic steps described above. Although some examples are given for linear or 2D arrays in this document, the equations described in this chapter are extendable to two- and three-dimensional arrays.

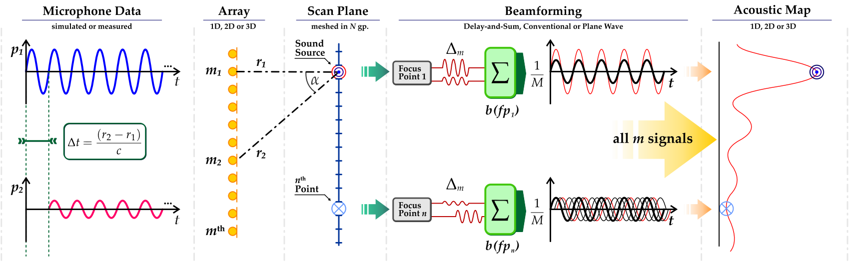

Figure 3.7: Summary of beamforming processing.

3.2.1.1 DSB in Time Domain

Consider an array of M omnidirectional microphones whose locations are given by

$$\vec{x}_m = (x_m, y_m, z_m), \quad \text{with} \quad m = 1,2,3,\cdots,M, \tag{3.2}$$

in free space, where $\vec{x} = (x, y, z)$ is a spatial position vector. Let the origin of the coordinate system be the array's centre

$$\vec{x}_0 = \sum_{m=1}^{M} \vec{x}_m = \vec{0}\,, \tag{3.3}$$

where $\vec{x}_m$ denotes the location of the m^{th} microphone and $\vec{x}_0$ is the origin. Now consider a monopole source (point source with uniform directivity) with a signal $s(t)$ located at an unknown location $\vec{x}_s$. From the wave equation, Equation (2.1),

$$\frac{1}{c^2}\frac{\partial^2 p(\vec{r},t)}{\partial t^2} - \Delta p(\vec{r},t) = s(t) * \delta(\vec{x} - \vec{x}_s)\,. \tag{3.4}$$

where $\delta(\cdot)$ is the Dirac-delta[3] function.

Accordingly, the signal at some arbitrary point $\vec{x}$, descendent of the spherical solution for outward propagation is given by

$$p(\vec{x},t) = \frac{s(t - |\vec{x} - \vec{x}_s|/c)}{|\vec{x} - \vec{x}_s|} \Rightarrow \frac{s(t - \Delta t_{\vec{x}})}{r_{\vec{x}}}, \tag{3.5}$$

where $s(t)$ is emitted source signal as a function of time; $\Delta t_{\vec{x}} = r_{\vec{x}}/c$ is the emission time delay; $r_{\vec{x}} = |\vec{x} - \vec{x}_s|$ is the distance from the source to the field point $\vec{x}$; and c is the speed of sound. Equation (3.5) shows that the amplitude is inversely proportional to the distance.

The signal received at the m^{th} microphone is

$$p(r_m,t) = \frac{s(t - r_m/c)}{r_m}, \tag{3.6}$$

where $r_m = |\vec{x}_m - \vec{x}_s|$ is the distance from the source to the m^{th} sensor. For the sake of simplicity, $p(r_m,t)$ is just called $p_m(t)$ from now on.

In DSB the signal from a potential source S (in some scan plane position) is estimated as a weighted linear sum of time shifted signals,

$$b(t) \equiv \frac{1}{M} \sum_{m=1}^{M} w_m \, p_m(t - \Delta_m), \tag{3.7}$$

where $b(t)$ is the *estimated source signal*; w_m is a weighting factor[4] and Δ_m is the microphone-dependent emission time delay for a focal point $\vec{x}_p$.

The Δ_m are selected so the signals captured by the M microphones reinforce each other, i.e., the delays are adjusted to focus the array's beam on signals propagating from a particular point in space (also known as co-phasing[5]), Figure 3.8.

---

[3] Paul Adrien Maurice Dirac (1902 - 1984) was an English electrical engineer and theoretical physicist who developed important research in the field of quantum mechanics. In his book, *Principles of Quantum Mechanics* [33], he introduced the currently well known Dirac-delta function.

[4] The amplitude weighting is also found in literature as an array's *shading* or *taper*.

[5] Co-phasing is coadunation of more than one antenna to be used together in one system. The advantage is to modify the radiation pattern such that it is concentrated in a particular direction.

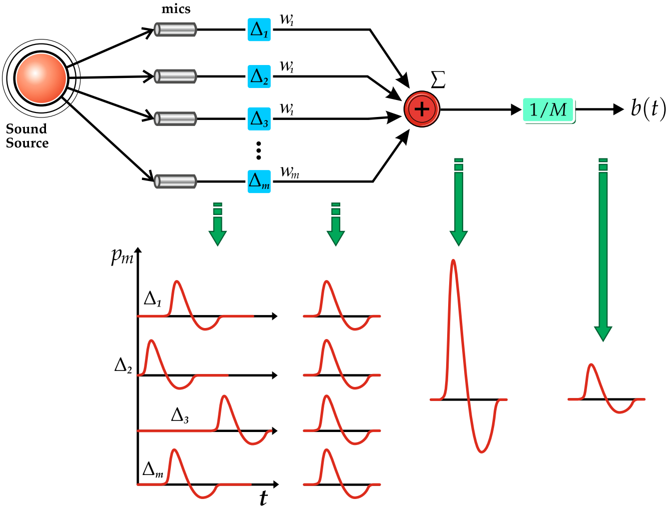

Figure 3.8: Delay-and-Sum beamforming principle.

Focusing on the Source

To effectively synchronize (Δ_m) and focus on the source position, the signals must be delayed by a value which is equal to the difference between the time it takes from the source to the origin and from the source to the microphone,

$$\Delta_m = \frac{r_s - r_m}{c} = \frac{|\vec{x}_s| - |\vec{x}_m - \vec{x}_s|}{c}, \tag{3.8}$$

where r_s is the distance between the source and the origin. A positive delay is applied to the microphones closer to the source than to the origin, while a negative delay (forward time shift) is applied to those further away. To compensate for the spherical spreading (see page 14), the weighting for the m^{th} is given by

$$w_m = \frac{r_m}{r_s} = \frac{|\vec{x}_m - \vec{x}_s|}{|\vec{x}_s|}. \tag{3.9}$$

Substituting Equations (3.8) and (3.9) in Equation (3.7)

$$\begin{aligned} b(t) &= \frac{1}{M}\sum_{m=1}^{M} w_m \frac{1}{r_m} s\left(t - \frac{r_m}{c} - \Delta_m\right), \\ &= \frac{1}{M}\sum_{m=1}^{M} \frac{r_m}{r_s}\frac{1}{r_m} s\left(t - \frac{r_m}{c} - \frac{r_s - r_m}{c}\right), \qquad (3.10) \\ &= \frac{1}{M}\sum_{m=1}^{M} \frac{1}{r_s} s\left(t - \frac{r_s}{c}\right), \\ &= \frac{1}{M}\left[M\, s_0(t)\right]. \qquad (3.11) \end{aligned}$$

All the microphones are correctly scaled and time-shifted, thus, the beamforming reduces to the signal received at the array's centre. The factor $1/M$ prevents that $s_0(t)$ is amplified by the number of microphones, Equation (3.11).

Focusing on Any Grid Point

The point $\vec{x}_s$ is assumed to be in a defined scanning plane. Thus, in a generic sense, the weights and delays should be calculated to focus to an arbitrary point $\vec{x}$ in the grid. Therefore,

$$\Delta_m = \frac{r_p - r'_m}{c} = \frac{|\vec{x}_p| - |\vec{x}_m - \vec{x}_p|}{c}, \qquad (3.12)$$

where r_p and r'_m are the distances between a focus point $\vec{x}_p$ and the array's centre; and the m^{th} microphone, respectively (Figure 3.9). And

$$w_m = \frac{r'_m}{r_p} = \frac{|\vec{x}_m - \vec{x}_p|}{|\vec{x}_p|}, \qquad (3.13)$$

are the respectively weights.

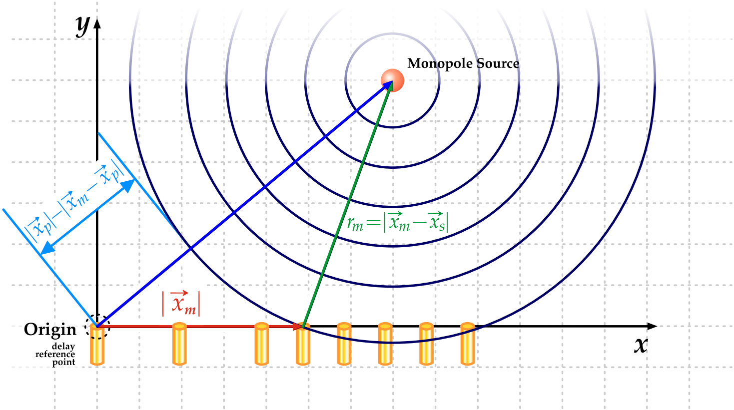

Figure 3.9: Δ_m calculation in DSB.

Accordingly, the beamforming output will be

$$\begin{aligned} b(t) &= \frac{1}{M}\sum_{m=1}^{M} w_m \frac{1}{r_m} s\left(t - \frac{r_m}{c} - \Delta_m\right), \\ &= \frac{1}{M}\sum_{m=1}^{M} \frac{r'_m}{r_p}\frac{1}{r_m} s\left(t - \frac{r_m}{c} - \frac{r_p - r'_m}{c}\right), \\ &= \frac{1}{M}\sum_{m=1}^{M} \frac{r'_m}{r_p}\frac{1}{r_m} s\left(t - \frac{r_p - (r'_m - r_m)}{c}\right). \qquad (3.14) \end{aligned}$$

In Equation (3.14) it is possible to see that w_m and Δ_m do not cancel each other as in Equation (3.10) (though it still will happen when the focus point coincides with the source location). Thus, Equations (3.12) and (3.13) are the general delays and weights for an arbitrary focus point.

Weighting Factor - w_m

The weighting factor w_m is associated with each microphone and can be considered as a spatial window. Several applications in beamforming use weighting factors. Some examples are: frequency-dependant weights applied for coherence loss correction [34, 35]; effective aperture correction [36]; microphone density corrections [37]; main lobe width control [38]; or just spherical spreading compensation, as described in this section.

3.2.1.2 DSB Frequency Domain

The frequency domain DSB is based on the Fourier Transform property that a change in time (in time domain) corresponds to a phase shift in the frequency domain

$$y(t - T_0) \Longleftrightarrow Y(\omega)\, \mathrm{e}^{-j\omega T_0}\,, \tag{3.15}$$

where $y(t)$ and $Y(\omega)$ are the pairs of the Fourier Transform, and T_0 is a constant. Consequently, Equation (3.7) can be rewritten as

$$B(\omega) \equiv \frac{1}{M} \sum_{m=1}^{M} w_m\, P_m(\omega)\, \mathrm{e}^{-j\omega\Delta_m}\,, \tag{3.16}$$

where $B(\omega)$ and $P_m(\omega)$ are the Fourier transformed signals.

If time history is not needed, the frequency domain DSB can offer some advantages over the time domain like post-processing in frequency bands, the use of techniques to decrease the sidelobes, techniques to reduce self- and spurious noise, and so forth.

Since the frequency domain post-processing is usually faster and permits matrix manipulation (see Section 3.2.2), in practice, most applications (simulated and measured) use frequency domain.

3.2.1.3 DSB Alternative Notation

Considering beamforming as a spatio-temporal filter, it is possible to estimate a source-receiver transfer function. In frequency domain this relation can be modelled as

$$p_m(\vec{x}_m, \vec{x}_p, f) = H(\vec{x}_m, \vec{x}_p, f) \cdot G(\vec{x}_m, \vec{x}_p, f)\,, \tag{3.17}$$

where $p_m(\vec{x}_m, \vec{x}_p, f)$ is the sound pressure at the m^{th} microphone; $H(\vec{x}_m, \vec{x}_p, f)$ is the source-receiver transfer function; and $G(\vec{x}_m, \vec{x}_p, f)$ is Green's function for acoustical free-field.

This $H(\vec{x}_m, \vec{x}_p, f) = H_{mp}(f)$ relates the measured pressure at the microphone position with a monopole radiation at the same point. The comparison of the amplitudes and phases (included in this function) will later render a matrix of correlation between the pressure at the m^{th} microphone and the assumption that there is a point source at the estimated focus point, i.e.

$$H_{mp}(f) = \frac{p_m(\vec{x}_m, \vec{x}_p, f)}{G(\vec{x}_m, \vec{x}_p, f)} \, . \tag{3.18}$$

The Equation (3.18) can be faced as a different interpretation of Equation (3.7). If the weighting factors to compensate propagation delay and attenuations are pondered as

$$w_m = \frac{1}{G(\vec{x}_m, \vec{x}_p, f)} \, , \tag{3.19}$$

where the $G(\vec{x}_m, \vec{x}_p, f)^6$ represents the symmetrical full free-field Green's function (and also solution of Equation (3.4))

$$G(\vec{x}_m, \vec{x}_p, f) = \frac{\mathrm{e}^{-jk|\vec{x}_m - \vec{x}_p|}}{4\pi|\vec{x}_m - \vec{x}_p|} \, , \tag{3.20}$$

where $k = 2\pi f/c$ is the wave number and $r_{sp} = |\vec{x}_m - \vec{x}_p|$ is the distance between the supposed source and the receiver (in this case m^{th} sensor).

The frequency domain DSB can be denoted as

$$b'(\vec{x}_p, f) = \frac{1}{M} \sum_{m=1}^{M} \frac{p_m(f)}{G(\vec{x}_m, \vec{x}_p, f)} \, , \tag{3.21}$$

thus,

$$b'(\vec{x}_p, f) = \frac{1}{M} \sum_{m=1}^{M} p_m(f) \left[\mathrm{e}^{+jk|\vec{x}_m - \vec{x}_p|}\right] 4\pi \, |\vec{x}_m - \vec{x}_p| \, . \tag{3.22}$$

Using the inverse Fourier transform, Equation (3.22) can be written as

$$b'(\vec{x}_p, t) = \frac{1}{M} \sum_{m=1}^{M} 4\pi|\vec{x}_m - \vec{x}_p| \, p_m(t + \Delta'_m) \, , \tag{3.23}$$

---

[6] The $G(\vec{x}_m, \vec{x}_s, f)$ or simply g_m is also known as *steering function*.

where

$$\Delta'_m = \frac{|\vec{x}_m - \vec{x}_p|}{c}\,. \tag{3.24}$$

The free space Green's function G_0 is the acoustical field generated at the observer's position $\vec{x}$ at time t by a pulse $\delta(\vec{x} - \vec{x}_s)\delta(t - \tau)$ released in $\vec{x}_s$ at time τ. From Equation (3.4) it is possible to derive the equation[7]

$$G_0 = \frac{1}{4\pi r}\delta\left(t - \tau - \frac{r}{c}\right), \tag{3.25}$$

integrating the wave equation over a compact sphere positioned in $\vec{x}_s$, where $r = |\vec{x} - \vec{x}_s|$, as demonstrated in references [39, 40]. Now considering $\tau = 0$, the monopole is emitting a signal $s_g(t)$ and the focus point at $\vec{x}_m$, Equation (3.25) turns into

$$p_{m_{s_g}}(r_m, t) = \frac{1}{4\pi r_m} s_g\left(t - \frac{r_m}{c}\right), \tag{3.26}$$

which is similar to Equation (3.6). In fact, sometimes the 4π is neglected due to array's calibration procedures that can take care of this constant.

Substituting of the actual (but unknown) pressure field Equation (3.26) into Equation (3.23), produces

$$b'(\vec{x}_p, t) = \frac{1}{M}\sum_{m=1}^{M} \frac{|\vec{x}_m - \vec{x}_p|}{|\vec{x}_m - \vec{x}_s|} s_g\left(t + \frac{|\vec{x}_m - \vec{x}_p| - |\vec{x}_m - \vec{x}_s|}{c}\right). \tag{3.27}$$

By examining Equation (3.27), it is easy to perceive that when the focus point $\vec{x}_p$ coincides with the source location $\vec{x}_s$, the output beamforming will be $b'(\vec{x}_p, t) = p_m(t)$. And for other potential focus points ($\vec{x}_p \neq \vec{x}_s$), the beamformer output will produce $|b'(\vec{x}_p, t)| < |p_m(t)|$.

---

[7] Equation (3.25) is the time domain version of Equation (3.20) and here represents the "measured" pressure.

To have this approach completely analogous with Section 3.2.1.1, compare Equation (3.19) and Equation (3.13), and consider

$$|G| = \frac{1}{|x_p|} \, , \qquad |H| = \frac{|x_p|}{|x_m - x_p|} \tag{3.28}$$

and,

$$w_m = \frac{1}{|H|} = \frac{|x_m - x_p|}{|x_p|} \, , \tag{3.29}$$

or swap G and H.

3.2.2 Conventional Beamforming and Matrix Notation

This section will describe Conventional Beamforming (CB) [41] together with the matrix notation used in this work. CB will only be delineated in terms of frequency - which is mainly used in this work. Thus, the "f" is suppressed in the M-dimensional vectors and matrices notations.

Consider M microphone pressures

$$\vec{p} = \begin{pmatrix} p_1 \\ \vdots \\ p_M \end{pmatrix} . \tag{3.30}$$

The *steering vector*[8] $\vec{g}$ contains all the $g_m = G(\vec{x}_m, \vec{x}_s, f)$ steering functions[9] at the microphone locations,

$$\vec{g} = \begin{pmatrix} g_1 \\ \vdots \\ g_M \end{pmatrix} = \begin{pmatrix} G(\vec{x}_1, \vec{x}_p) \\ \vdots \\ G(\vec{x}_M, \vec{x}_p) \end{pmatrix} . \tag{3.31}$$

The *Cross-powers* $C_{mn}(f)$ and *Auto-powers* $C_{mm}(f)$ are defined as

$$C_{mn}(f) = \frac{1}{2} \left[p_m(f) \, p_n^*(f) \right] , \tag{3.32}$$

---

[8] Contains the weighting factors and phase shifts to be applied.

[9] In this example, it is just the free field. However, the application of this research uses the combined free-field plus diffraction field.

where p_m is the pressure for the m^{th} microphone, p_n is the pressure for the n^{th} microphone, and $(\cdot)^*$ is the complex conjugate operator. Then, the *Cross-Spectral Matrix* $\vec{C}$ (CSM or *Cross-Power Matrix*, CPOW) is given by

$$\vec{C} = \frac{1}{2}\,\vec{p}\,\vec{p}^{\dagger} = \frac{1}{2}\begin{pmatrix} p_1 \\ \vdots \\ p_M \end{pmatrix}\begin{pmatrix} p_1^* & \cdots & p_M^* \end{pmatrix} \tag{3.33a}$$

$$\vec{C} = \frac{1}{2}\begin{pmatrix} p_1 p_1^* & p_1 p_2^* & \cdots & p_1 p_M^* \\ p_2 p_1^* & p_2 p_2^* & \cdots & p_2 p_M^* \\ \vdots & \vdots & \ddots & \vdots \\ p_M p_1^* & p_M p_2^* & \cdots & p_M p_M^* \end{pmatrix} \tag{3.33b}$$

where $(\cdot)^{\dagger}$ is the Hermitian operator (complex conjugate transpose). The CSM is an $M \times M$ complex matrix that contains the auto-spectral and cross-spectral components. It has all the relative magnitude and phase relations between pairs of microphones, summarizing then all the information needed to compute a signal's direction of propagation.

As previously stated, the beamforming algorithm "compares" two set of information to determine the source strength. In CB this process is interpreted as a minimisation problem. The differences between the measured pressures ($\vec{p}$) and the steering vector[10] ($a\,\vec{g}$) for a given position $\vec{x}_p$ can be written as

$$J = \left|\vec{p} - a\,\vec{g}\right|^2, \tag{3.34}$$

where (a) represents the complex amplitudes of sources located in $\vec{x}_p$. The cost function J is minimised by choosing (a) in such way that $\vec{p} - a\,\vec{g}$ is perpendicular to ($\vec{g}$), Figure 3.10.

---

[10] Considering a source model $p(\vec{x}) = ag(\vec{x})$.

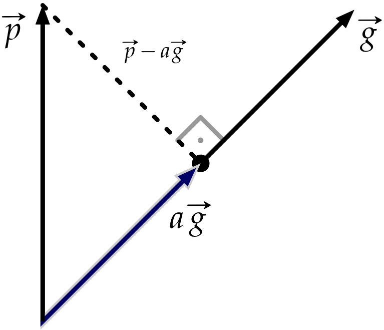

Figure 3.10: J is minimised by choosing (a) in such way that $\vec{p} - a\vec{g}$ is perpendicular to ($\vec{g}$).

The solution of the problem yields

$$a = \frac{\vec{g}^{\dagger}\vec{p}}{|\vec{g}|^2}, \tag{3.35a}$$

$$a = \frac{\sum\limits_{m=1}^{M} g_m^* p_m}{\sum\limits_{m=1}^{M} g_m^* g_m}, \tag{3.35b}$$

where $|\vec{g}|^2$ will be the normalization.

For broadband noise processing makes no sense in averaging (a) since magnitude and phase varies with time (or each block of samples), and the average of a tends to zero. Therefore, it is more convenient to consider estimated source auto-powers

$$A = \frac{1}{2}|a|^2 = \frac{1}{2}aa^{\dagger} = \frac{1}{2}\frac{\vec{g}^{\dagger}\vec{p}}{|\vec{g}|^2}\left(\frac{\vec{g}^{\dagger}\vec{p}}{|\vec{g}|^2}\right)^{\dagger}, \tag{3.36a}$$

$$A = \frac{1}{2}\frac{\vec{g}^{\dagger}\vec{p}\,\vec{p}^{\dagger}\vec{g}}{|\vec{g}|^4} = \frac{\vec{g}^{\dagger}\,1/2\langle\vec{p}\,\vec{p}^{\dagger}\rangle\,\vec{g}}{|\vec{g}|^4} = \frac{\vec{g}^{\dagger}\vec{C}\,\vec{g}}{|\vec{g}|^4}, \tag{3.36b}$$

$$A = |B(\omega)|^2 = \frac{\sum_{m=1}^{M} \sum_{n=1}^{M} g_m^\dagger C_{mn} g_n}{\sum_{m=1}^{M} \sum_{n=1}^{M} |g_m|^2 |g_n|^2}, \tag{3.36c}$$

where $\vec{C}$ is the CSM and can be averaged. The A value can be also found in literature as *array power response*, and its square root as *array pressure response*. Equation (3.36c) is known as Conventional Beamforming (Figure 3.11) and is the frequency-domain equivalent to the *Least Squares Beamforming*, as cited by Sijtsma in [42].

The main difference between DSB and CB relies on the weighting factor of the microphone signals. In DSB, the signals are multiplied by a factor proportional to the distance $r_{sp} = |\vec{x}_m - \vec{x}_s|$ while in CB they are divided by r_{sp} (on multiplying with $\vec{g}^\dagger$). That means the sensors that are closer to the focus point contribute more to the final result than outlying ones. For large distances between the array and the scan plane both techniques are equivalent. This happens because the differences in r_{sp} become smaller.

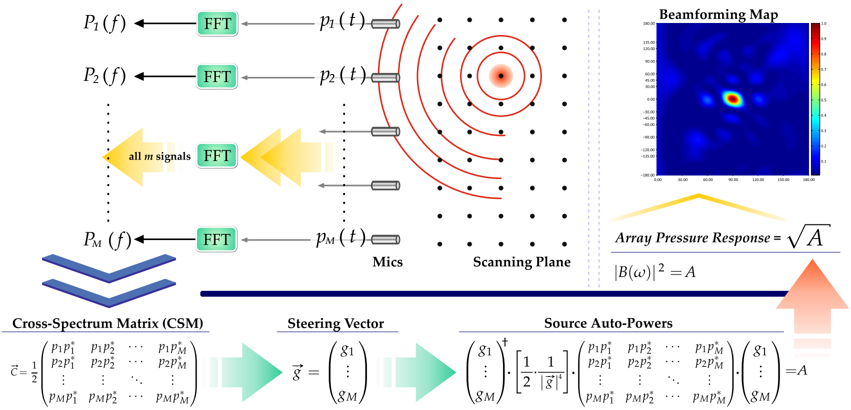

Figure 3.11: Conventional Beamforming flow chart.

3.2.3 Plane Wave Beamforming

Plane wave beamforming (PWB) can be used when sources are in the array's far-field[11]. Instead of points in a scan plane, in PWB the array looks for potential sound directions. The direction of an array's aim is usually the opposite of a signal's propagation direction, as in Figure 3.12.

Assuming a plane waveform $s(t)$ propagating across an array of M sensors, the wavefield[12] can be expressed by

$$f(\vec{x},t) = s(t - \vec{\alpha}_s \cdot \vec{x}) = \exp\left[j\omega_s(t - \vec{\alpha}_s \cdot \vec{x})\right], \tag{3.37}$$

where the *slowness vector* is defined by

$$\vec{\alpha}_s = \frac{\vec{\zeta}_s}{c}. \tag{3.38}$$

where $\vec{\zeta}_s$ is a unit-length vector pointing in the direction of propagation (the negative of the aim direction) and $\vec{k}_s = \omega_s \cdot \vec{\alpha}_s$.

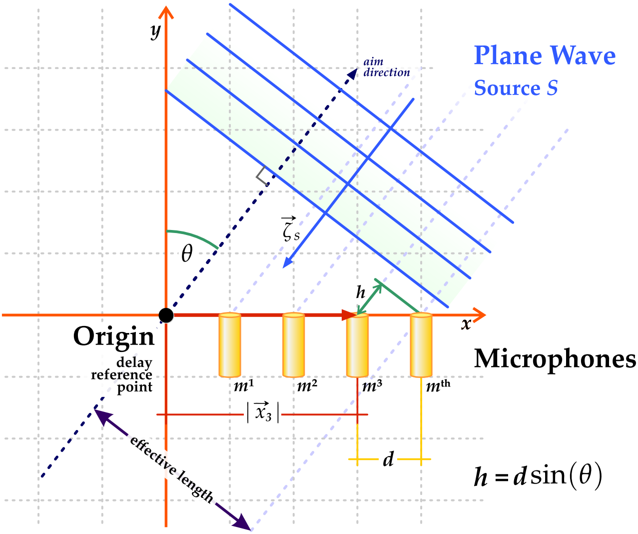

Figure 3.12: Plane wave with linear array example.

---

[11] Some authors consider *infinite focus distance*.

[12] See Section 2.2 for further details on plane wave derivation.

The m^{th} microphone will measure

$$p_m(t) = s(t - \vec{\alpha}_s \cdot \vec{x}_m), \tag{3.39}$$

thus, analogously to Equation (3.7), the DSB for plane waves become

$$b_{\text{pw}}(t) = \sum_{m=1}^{M} w_m s(t - \Delta_m - \vec{\alpha}_s \cdot \vec{x}_m). \tag{3.40}$$

If the Δ_m delays are chosen for the propagating direction

$$\Delta_m = -\vec{\alpha}_s \cdot \vec{x}_m = \frac{-\vec{\zeta}_s \cdot \vec{x}_m}{c}. \tag{3.41}$$

the signal processing delays compensate for the propagation delays and the waveforms are added constructively, recovering the signal back

$$b_{\text{pw}}(t) = \sum_{m=1}^{M} w_m s(t) = s(t) \left[\sum_{m=1}^{M} w_m \right], \tag{3.42}$$

as the original signal times a constant. In the case of perfect focus, the output is amplified by the number of sensors. For this reason $b_{\text{pw}}(t)$ is usually also normalised by M.

More generally, steering the array to an assumed propagation direction $\vec{\zeta}$

$$\Delta_m = -\vec{\alpha} \cdot \vec{x}_m = \frac{-\vec{\zeta} \cdot \vec{x}_m}{c}. \tag{3.43}$$

where the slowness vector $\vec{\alpha}$ corresponds to the assumed propagation direction as $\vec{\zeta}/c$. The beamforming output for a plane wave propagating in the $\vec{\zeta}_s$ direction will be

$$b_{\text{pw}}(t) = \sum_{m=1}^{M} w_m s(t + (\vec{\alpha} - \vec{\alpha}_s) \cdot \vec{x}_m). \tag{3.44}$$

The frequency domain version of Equation (3.44) is

$$B_{\mathrm{pw}}\left(-\vec{\zeta},\omega\right) = \sum_{m=1}^{M} w_m\, P_m(\omega)\, \mathrm{e}^{\left\{-j\omega\,\Delta_m(-\vec{\zeta})\right\}}\,, \tag{3.45}$$

and if $w_m = 1$, the *array pattern* depends only on the array geometry. Other considerations concerning the plane wave approach can be found in Hald & Christensen [43] , and in Johnson & Dudgeon [38].

3.2.4 Advanced Techniques

Some advanced techniques regarding improving beamforming maps have been developed over the years. From very simple ones, like the removing the main diagonal of the CSM [44, 45], enhanced resolution [46], to the more sophisticated ones such as DAMAS [47, 48, 49], CLEAN-SC [50], TIDY [46], MUSIC [51, 52], ESPRIT [53], orthogonal [54, 55], inverse methods [56, 57], and robust adaptive [58, 59], among others. They are not applied in this work, but they are suggested for further research.

3.3 Array Parameters and Performance

The evaluation of array performance is carried out throughout the estimation of some parameters. They are basically taken from a Point Spread Function (PSF), which is a unique response for a given geometry.

3.3.1 Point Spread Function - PSF

The beamformer's response to a single frequency wave is often called an *array pattern*[13]. That is, the beamformer output spectrum equals to the source signal spectrum $S(\omega)$ multiplied by a factor that depends on the array pattern $W(\cdot)$, i. e., $B(\omega) = S(\omega)W(\cdot)$. The array pattern for plane waves is

$$W(\vec{k}) = \sum_{m=1}^{M} w_m \exp\left(j\vec{k} \cdot \vec{x}_m\right) , \tag{3.46}$$

and for spherical waves is

$$W(\vec{k}, \vec{x}_p, \vec{x}_s) = \sum_{m=1}^{M} w_m \frac{r_s}{r_m} \exp\left\{ jk\Big[\left(r_s - r_p\right) - \left(r_m - r'_m\right)\Big]\right\} . \tag{3.47}$$

It is evident that these functions relate frequency, source position, focus point, and microphone position. Johnson & Dudgeon [38] provide the complete derivations of these equations.

A linear time-invariant system (LTI) is characterized by examining its frequency response. Similar to this, the array pattern corresponds to the wavenumber-frequency response[14] (spatial and time domain) of a spatiotemporal filter [38]. This can be interpreted as the array's response to a monopole, in the same way an impulse response represents the response to a LTI. These concepts can be better understood by viewing the processing domains flowchart in Figure 3.13.

The *point spread function* nomenclature is most used in optics, telescopy and imaging systems. But fundamentally, it has the same

---

[13] Also found as *aperture smoothing function* - it also determines the array's directivity pattern [38]. The array pattern $W(\cdot)$ can be subdivided into *element factor* and *array factor*, since it is essentially the summation of individual element fields. The element pattern signifies the radiation behaviour of an individual element and the array factor depends on the array architecture [60].

[14] It is also referred to as $k-\omega$ response.

meaning as the wavenumber-frequency response. That is, the PSF is the irradiance distribution when a point source is present at scan point and no other sources are present. The point source is positioned on the *boresight* (z-axis) of the array, and the map representation is usually a two-dimensional (xy-axis and normalized to the maximum) distribution, as depicted in the example of Figure 3.14.

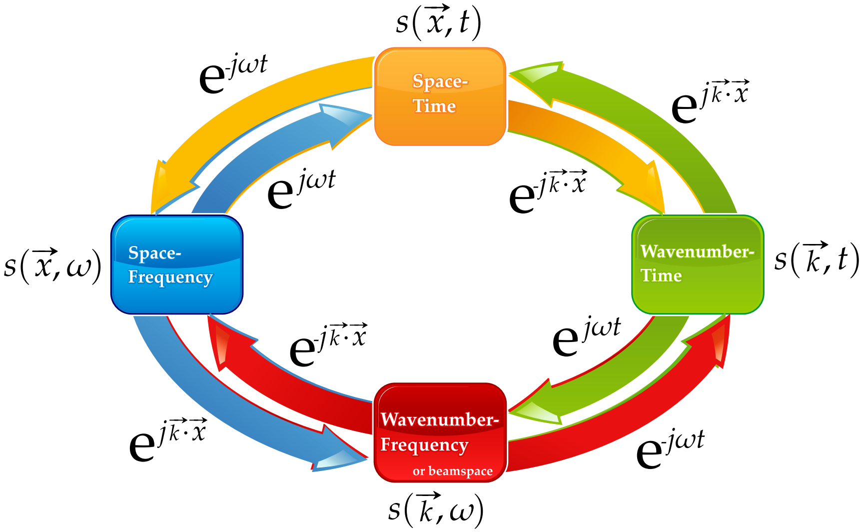

Figure 3.13: Processing domains flowchart .

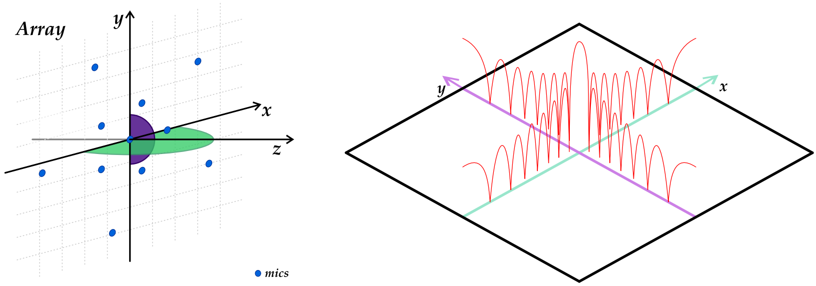

(a) Array

(b) PSF xy-axis sketch

Figure 3.14: Relation between array and PSF.

Formally, consider a unit source in the scan point $\vec{x}_j$ which induces [50]

$$\vec{C}_j = \vec{g}_j \vec{g}_j^{\dagger} \, , \tag{3.48}$$

where

$$\vec{g}_j = \begin{pmatrix} G(\vec{x}_1, \vec{x}_j) \\ \vdots \\ G(\vec{x}_M, \vec{x}_j) \end{pmatrix} . \tag{3.49}$$

Following the CB method (Section 3.2.2), the source auto powers for a given scan point $\vec{x}_p$ is

$$|B_{jp}(\omega)|^2 = A_{jp} = \frac{\vec{g}_p^{\dagger} \, \vec{C}_j \, \vec{g}_p}{|\, \vec{g}_p \,|^4} = \frac{\vec{g}_p^{\dagger} \, \overline{\left[\vec{g}_j \, \vec{g}_j^{\dagger} \right]} \, \vec{g}_p}{|\, \vec{g}_p \,|^4} \, . \tag{3.50}$$

Theoretically $B_{jp} = 1$ for $j = p$, and $B_{jp} = 0$ for $j \neq p$, however, since the array aperture is discretized in M points, these ratios cannot hold. In Figures 3.15 to 3.20, there are examples of free-field simulated PSFs of commonly used geometries in beamforming: spiral, regular, circle, cross, random, and line. In these graphics there are the geometry and the PSF plotted in 3D and 2D.

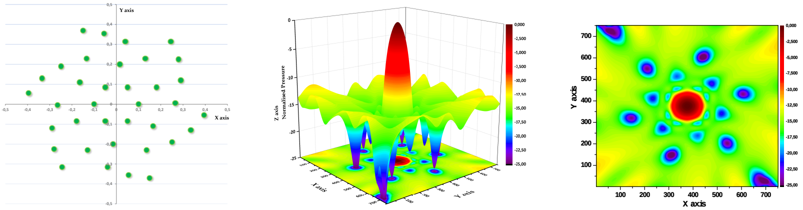

(a) Geometry (b) 3D PSF (c) 2D PSF

Figure 3.15: Spiral array, 36 sensors, min. radius 0,1 m, max. radius 0,4 m, 6 mics per circle, 6 circles, spiral angle 3 rad (the modelling equations are described in [61]). PSF, monopole, 2 kHz, 1/3 oct. band, 1,5 m away, 30° solid angle aperture.

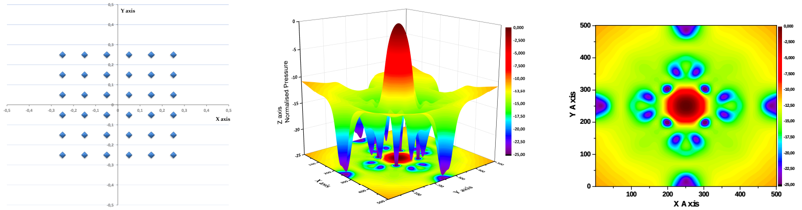

(a) Geometry (b) 3D PSF (c) 2D PSF

Figure 3.16: Regular 2D array, 36 sensors, 6*x*6, mic. interval 0,1 m, size 0,5 m *x* 0,5 m. PSF, monopole, 2 kHz, 1/3 oct. band, 1,5 m away, 30° solid angle aperture.

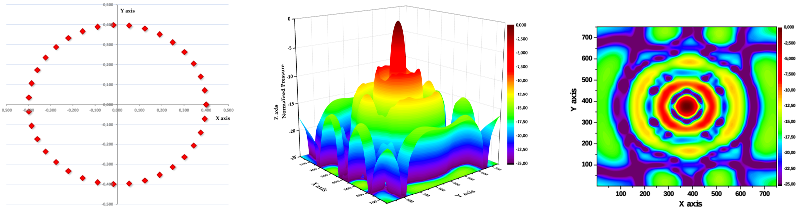

(a) Geometry (b) 3D PSF (c) 2D PSF

Figure 3.17: Circular 2D array, 36 sensors, diameter 0,4 m. PSF, monopole, 2 kHz, 1/3 oct. band, 1,5 m away, 30° solid angle aperture.

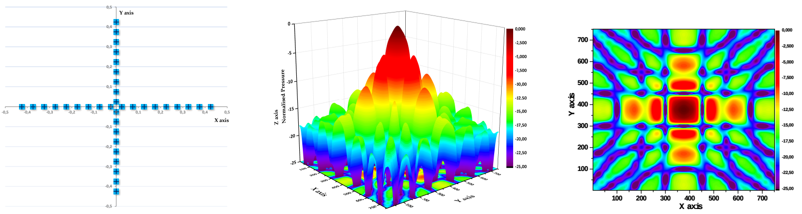

(a) Geometry (b) 3D PSF (c) 2D PSF

Figure 3.18: Cross 2D array, 36 sensors, mic interval 0,05 m, 18*x*18. PSF, monopole, 2 kHz, 1/3 oct. band, 1,5 m away, 30° solid angle aperture.

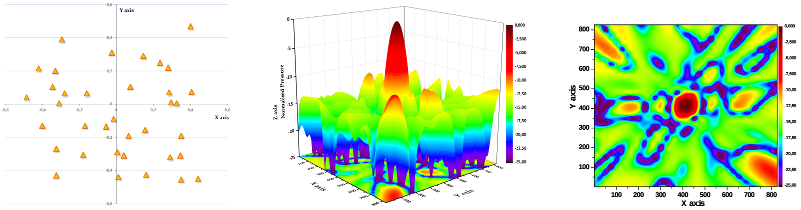

(a) Geometry (b) 3D PSF (c) 2D PSF

Figure 3.19: Random 2D array, 36 sensors. PSF, monopole, 2 kHz, 1/3 oct. band, 1,5 m away, 30° solid angle aperture.

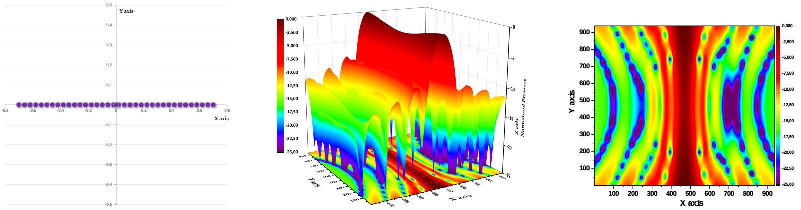

(a) Geometry (b) 3D PSF (c) 2D PSF

Figure 3.20: Linear 1D array, 36 sensors, mic spacing 0,04 m. PSF, monopole, 2 kHz, 1/3 oct. band, 1,5 m away, 30° solid angle aperture.

3.3.2 Beamwidth, Sidelobes and Dynamic Range

The PSF allows the derivation of the beamformer response to an arbitrary wavefield. Accordingly, it is primary used in evaluating arrays and algorithms. Generally, the central slice in the PSF in referred to as the beampattern[15], Figure 3.21. Assuming that the array looks for signals originating from a given direction, the beampattern delivers the information concerning how the output is disturbed by signals different from those under focus.

In the beampattern there is typically a mainlobe on the maximum response axis (MRA) (in which the array is steered to) and the sidelobes. These sidelobes can be either waves from undesired directions, background noise, electrical noise, or spatial aliasing, among other effects.

---

[15] For one-dimensional arrays it is the most common plot. Sometimes it is also referred as the complete PSF.

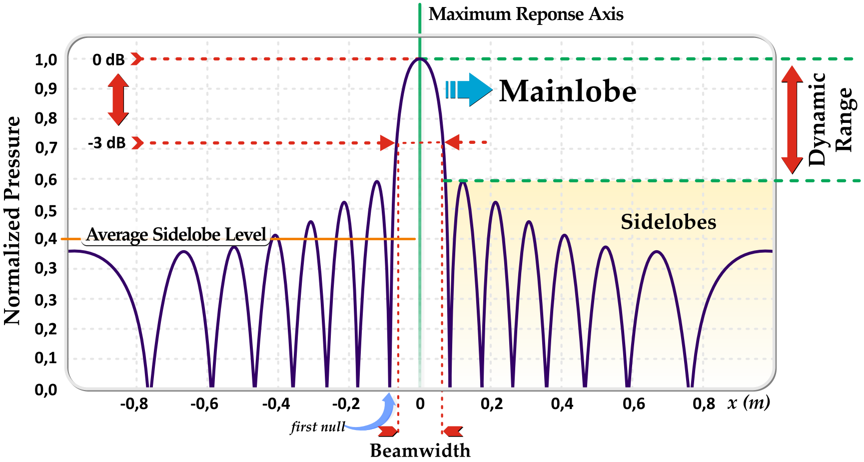

Figure 3.21: Beampattern and some response characteristics.

The width of the mainlobe is known as the *beamwidth* (BW), the most used criterion defines it as the space (or angle) where the mainlobe is reduced to $1/\sqrt{2}$, Figure 3.21. That is, it is half-power[16] (or -3 dB) of the mainlobe and a interesting measure of the array's ability to resolve signal sources with similar directions of arrival. The BW on the z-axis [62, 43] is given by

$$\mathrm{BW}_{\mathrm{axis}} = a \cdot \frac{d_z}{D} \cdot \lambda \,, \tag{3.51}$$

where d_z is the distance between the array and the scanning plane, D is a geometrically intrinsic distance, normally the array diameter, λ is the wavelength of the incident wave, and a can be:

(a) for continuous aperture, dependent on the chosen criterion. That is, $(a = 1)$ for *linear aperture*; and for *circular aperture*, $(a = 1.22)$ for *Rayleigh criterion*, $(a = 1.03)$ for *3-dB criterion*, and $(a = 1.41)$ for *6-dB criterion*.

(b) for sampled aperture, it is the so called *geometry-factor* [45], since its empirical[17] determination can only be obtained for a fixed geometrical disposition.

---

[16] It is also referred to as *full-width, half-maximum* (FWHM) in the literature.

[17] This linearisation of the BW sometimes do not hold, thus, further studies are recommended to use a distinct model instead of just a constant. An application of this linearisation can be found in Fonseca [61] and Silva [63].

Although in this work the *3-dB criterion* is most used, the *Rayleigh criterion* is explained in the next section. The *6-dB criterion* [64] is usually applied for problems when there are two sources and they are coherent.

The beamwidth is narrower[18] for high frequencies, as shown in the example of Figure 3.22 - the black line is the 3 dB down position. Usually, for higher frequencies, the mesh (N cells) of the scanning plane is finer, so the main and sidelobes can have a better definition.

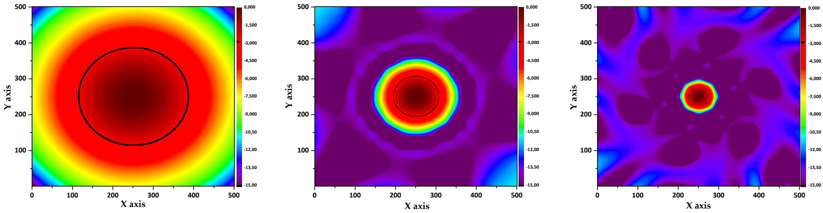

(a) 500 Hz (b) 1 kHz (c) 2 kHz

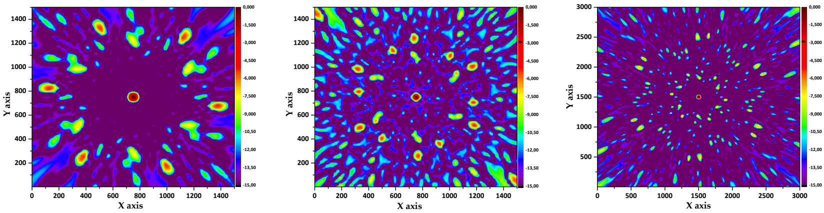

(d) 6 kHz (e) 12 kHz (f) 15 kHz

Figure 3.22: PSFs of the spiral array of Figure 3.15 (a) for several frequencies. Beamwidth (-3 dB) detail in black line.

The power density of the sidelobes is generally much smaller than the mainlobe. The foregoing theory regarding arrays indicates the *average sidelobe level*[19] (ASL) as one criterion of performance. The number of microphones is the key parameter in determining the ASL [65] and is given by:

$$\mathrm{ASL} = 10 \log \left(\frac{1}{M} \right) . \tag{3.52}$$

---

[18] Some weighting factor techniques can be applied to attempt to keep the mainlobe constant along the frequencies.

[19] In fact, some authors consider this parameter as a first impression of the array's "general" dynamic range.

For a fixed frequency, one can also estimate the *maximum sidelobe levels* (MSL), which are more related to the solid angle that the array is sampling the space. Basically, when the mainlobe falls into a null, a line is traced following the sidelobe shape. At the sidelobe maximum, the value holds until it finds a higher sidelobe (see Figure 3.23 for a better understanding). Further information about this parameter can be found in Christensen & Hald [43].

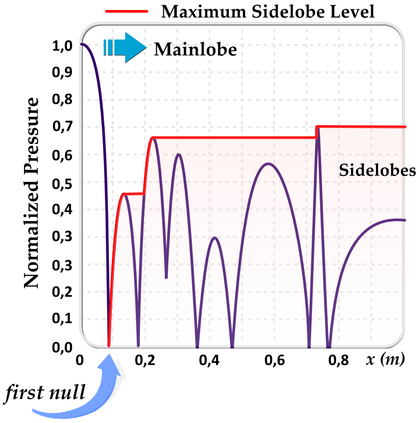

Figure 3.23: Max. Sidelobe Level.

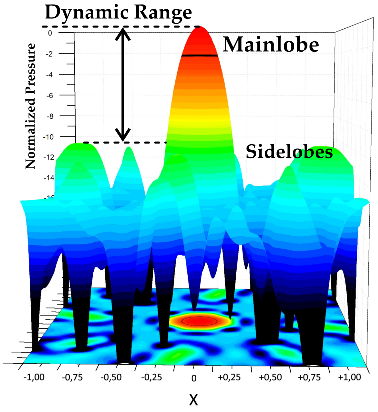

Figure 3.24: Dynamic Range.

The *dynamic range* (DR) of an array is the difference between the mainlobe and the highest sidelobe, as depicted in Figures 3.21 and 3.24. It is strongly dependent on the array architecture, hence it is frequency-dependent. Since sidelobes generally create false peaks/sources (or *ghost images*) on the map, an ideal array would have a large dynamic range and a small beamwidth. However, there is a drawback in maximizing these two important parameters which happens because they work in opposite directions. That is, if a geometry is maximized for DR the BW will be certainly wider, and the same is true in the opposite direction. In summary, an optimum compromise must be found between BW and DR.

Formally, consider a matrix $M_{m \times n}$, where $m > n$, representing a PSF. A bi-dimensional linear interpolation is carried out to transform this $m \times n$ matrix into a square matrix ($m \times m$), thus creating a new equivalent matrix $M'_{m \times m}$. The process investigates the peaks in the columns and rows of this $M'_{m \times m}$ matrix. Later, a final matrix $X_{m \times m}$ is created with all possible PSF peaks. First, the columns of M' are treated as single vectors, as follows

$$\vec{A}_{\mathrm{cols},\,1\times m} = \begin{bmatrix} \vec{a}_{\mathrm{c\,\#1}} & \vec{a}_{\mathrm{c\,\#2}} & \cdots & \vec{a}_{\mathrm{c\,\#m}} \end{bmatrix}, \tag{3.53}$$

where $\vec{A}_{\mathrm{cols}}$ is a $1 \times m$ vector, and its elements $\vec{a}_{\mathrm{c\,\#m}}$ are $m \times 1$ vectors containing the original elements of M', see Figure 3.25 (a). To avoid misunderstanding, sub-index c stands for columns and l for lines of matrix M'.

Each $\vec{a}_{\mathrm{c\,\#m}}$ passes through a peak detector which returns

$$\vec{a}_{\mathrm{c\,\#m}}(c) = \begin{cases} M'|_{(c,l)} & \text{if } (c,l) \text{ is a peak of } \vec{a}_{\mathrm{c\,\#m}} \\ 0 & \text{if } (c,l) \text{ is not a peak} \end{cases}, \tag{3.54}$$

with $c = \{1,2,\ldots,m\}$. The same process is used to evaluate the lines,

$$\vec{B}_{\mathrm{lines},\,m\times 1} = \begin{bmatrix} \vec{b}_{\mathrm{l\,\#1}} \\ \vec{b}_{\mathrm{l\,\#2}} \\ \vdots \\ \vec{b}_{\mathrm{l\,\#m}} \end{bmatrix}, \tag{3.55}$$

where $\vec{B}_{\mathrm{lines}}$ is a $m \times 1$ vector, and its elements $\vec{b}_{\mathrm{l\,\#m}}$ are $1 \times m$ vectors containing the original elements of M', see Figure 3.25 (b). In the same way, the peak detector returns

$$\vec{b}_{\mathrm{l\,\#m}}(l) = \begin{cases} M'|_{(c,l)} & \text{if } (c,l) \text{ is a peak of } \vec{b}_{\mathrm{l\,\#m}} \\ 0 & \text{if } (c,l) \text{ is not a peak} \end{cases}, \tag{3.56}$$

with $l = \{1,2,\ldots,m\}$.

Properly equipped with $A_{m\times m} = \vec{A}_{\mathrm{cols}}$ (matrix with column peaks) and $B_{m\times m} = \vec{B}_{\mathrm{lines}}$ (matrix with line peaks), a global matrix of peaks is created by performing the product element by element (or *entrywise product*[20]) as

$$X_{m\times m} = \sqrt{(A \circ B)_{m\times m}}\ . \tag{3.57}$$

---

[20] The *entrywise product* (also known as the Schur product or the Hadamard product) is an operation that takes two matrices of the same dimensions, and produces another matrix where each element ij is the product of elements ij of the original two matrices.

This new $X_{m \times m}$ matrix will have the values of the peaks in the cells that are global peaks and zeros in all other cells, as in Figure 3.25. To find the dynamic range (DR), the matrix $X_{m \times m}$ is converted into a one dimensional vector $\vec{Z}_{(m \cdot m)}$ containing all the cells of the matrix. The vector is then ordered from highest to lowest value and the DR is estimated as

$$\mathrm{DR}(f) = Z_0 - Z_s \,, \tag{3.58}$$

where Z_0 is the highest value and is in the first position of the vector. The s represents the number of expected point sources (for PSF evaluation, i.e. monopole, $s = 1$).

Another common plot in the beamforming field is the Frequency *vs.* Beampattern (FvB). Built with the central lines (or source position lines) of each PSF, this type of graph gives information on how the parameters behave with respect to frequency. Some researchers consider the extraction of the BW and DR from this plot, nevertheless estimations from this type of plot will differ from the PSF (as shown in Section 4.3). If the mainlobe is not a "regular circumference", the BW estimation from the PSF will bring different xy sizes via radial scan. Whereas, with just one line out of the beampattern a single value is found. The DR estimation from the PSF considers possible sidelobes in all the "field of vision". On the other hand, the DR extracted from the beampattern contains only the sidelobe information of the chosen frequency line.

3.3.3 Signal-to-Noise Ratio and Array Gain

One of advantages in using multiple microphones is to improve the signal-to-noise ratio (SNR) in contrast to just a single sensor. The array gain estimates the enhancement obtained by a given set of M sensors.

To derive a general ratio for SNR and array gain, consider an array of M microphones steered to a point source $s(t)$. At each m^{th} microphone the sound pressure will be

$$p_m(t - \Delta_m) = s(t) + n_m(t) \,. \tag{3.59}$$

where each signal has the same deterministic component $s(t)$, and an uncorrelated zero-mean random noise component $n_m(t)$. This noise component could be an adverse effect such as self-noise, wind noise,

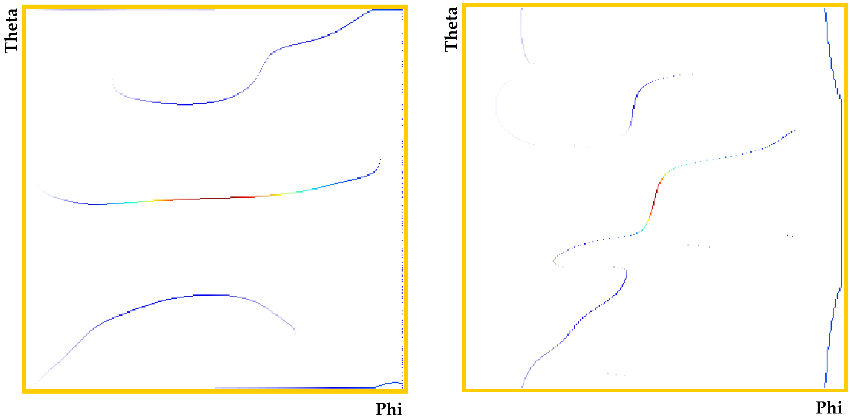

(a) Columns Peaks, $A_{m \times m}$ (b) Lines Peaks, $B_{m \times m}$

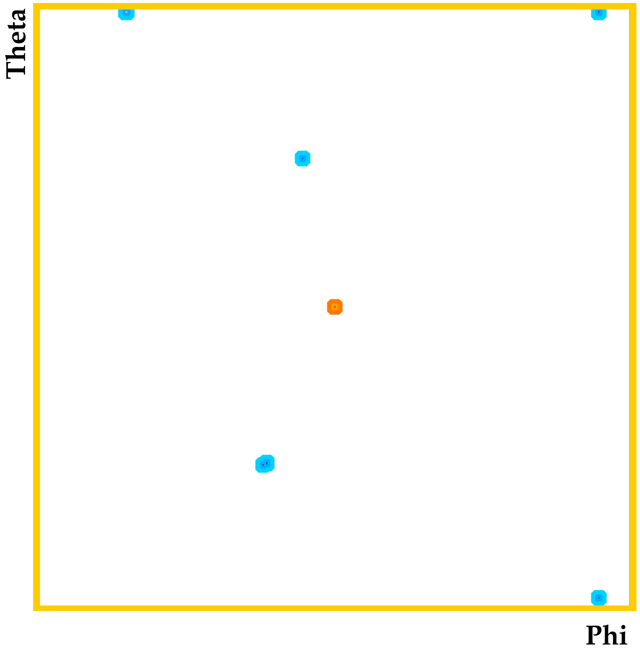

(c) Global Peaks, $X_{m \times m}$

Figure 3.25: Dynamic range estimation process depicted.

electrical interference, background noise and etc. The SNR for a single sensor is the ratio of power between the signal and the noise,

$$\mathrm{SNR}_{\mathrm{sensor}} = \frac{\mathrm{E}\left[\, s^2(t)\right]}{\mathrm{E}\left[n^2(t)\right]}\,, \tag{3.60}$$

where $\mathrm{E}\left[\cdot\right]$ is the expected value of a random variable. The beamforming output given by Equation (3.7) reads

$$\begin{aligned} b(t) &= \frac{1}{M}\sum_{m=1}^{M} w_m\, p_m(t-\Delta_m)\,, \\ &= \frac{1}{M}\sum_{m=1}^{M} w_m\left[s(t) + n_m(t)\right] \\ &= \frac{1}{M}\sum_{m=1}^{M} w_m\, s(t) + \frac{1}{M}\sum_{m=1}^{M} w_m\, n_m(t)\,. \end{aligned} \tag{3.61}$$

Now, computing the array's SNR and considering[21] $w_m = 1$,

$$\mathrm{SNR}_{\mathrm{array}} = \frac{\mathrm{E}\left[\left(\frac{1}{M}\sum_{m=1}^{M} w_m\, s(t)\right)^2\right]}{\mathrm{E}\left[\left(\frac{1}{M}\sum_{m=1}^{M} w_m\, n_m(t)\right)^2\right]} = \frac{\mathrm{E}\left[s^2(t)\right]}{\mathrm{E}\left[\left(\frac{1}{M}\sum_{m=1}^{M} n_m(t)\right)^2\right]}\,, \tag{3.62}$$

$$\mathrm{SNR}_{\mathrm{array}} = \frac{\mathrm{E}\left[s^2(t)\right]}{\frac{1}{M^2}\sum_{m_1=1}^{M}\sum_{m_2=1}^{M}\mathrm{E}\left[n_{m_1}(t)\, n_{m_2}(t)\right]}\,. \tag{3.63}$$

---

[21] If the array size is small compared to the point source location, $r_m \approx r_s$, and the weighting factors w_m will be approximately one (see Equation (3.9)).

Assuming that noise is uncorrelated from sensor to sensor [66],

$$\mathrm{E}\Big[n_{m_1}(t)\,n_{m_2}(t)\Big] = \begin{cases} 0, & m_1 \neq m_2 \\ n_m^2(t), & m_1 = m_2 \end{cases} ,$$

then,

$$\mathrm{SNR}_{\mathrm{array}} = \frac{\mathrm{E}\Big[s^2(t)\Big]}{\dfrac{1}{M^2}\, E\Bigg[\sum_{m=1}^{M} n_m^2(t)\Bigg]} = M\,\frac{\mathrm{E}\,[\,s^2(t)]}{\mathrm{E}\,[\,n^2(t)]} = M \cdot \mathrm{SNR}_{\mathrm{sensor}}\,, \tag{3.64}$$

and in consequence the array gain is given by

$$G_{\mathrm{array}} \equiv \frac{\mathrm{SNR}_{\mathrm{array}}}{\mathrm{SNR}_{\mathrm{sensor}}} = M\,. \tag{3.65}$$

It is possible to see that the G_{array} is predominantly influenced by the number of microphones M and by the weighting factors w_m. In this example case, the improvement is M, and if expressed in dB

$$G_{\mathrm{array.dB}} = 10\,\log_{10}\Big(M\Big)\,. \tag{3.66}$$

In this case, the output of Equation (3.66) and Equation (3.52) will only differ with respect to the sign. For example, for 36 sensors $G_{\mathrm{array}} \approx$ +15,5 and ASL $\approx$ -15,5; that is, it is just a matter of reference.

3.3.4 Spatial Resolution

The term *resolution*[22] is connected to the angular resolution of the array, and is directly related to its constructive factors and frequency of analysis.

According to the *Rayleigh criterion*, two point sources are just separable when the peak of the first source coincides with the first null of the second source, see Figure 3.26 - more details and the complete derivation can be found in [38, 43]. Thus, mathematically, the calculation

---

[22] There is a discussion on the *resolution* nomenclature in the end of this section.

using this criterion results in the expression[23]:

$$R(\vartheta) = a \cdot \frac{d_z}{D} \cdot \lambda \cdot \frac{1}{\cos(\vartheta)^3}\,, \tag{3.67}$$

where ϑ is the wave incident angle. In the post-processing, a solid opening angle (SOA) is usually considered, the limit angle of the SOA is usually determined by the use of Equation (3.68), see Figure 3.28. Analogous to optics, a is a factor that is associated with the type of the lens *opening angle* (or *viewing angle*). For a lens with a circular aperture, for example, the analytical value is $a = 1.22$ (as cited in page 48).

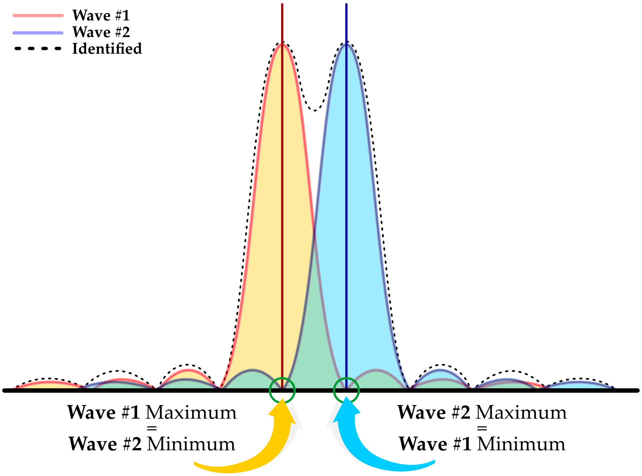

Figure 3.26: *Rayleigh criterion*: two sources are just separable when the peak of the first source coincides with the first null of the second source.

Equation (3.67) is mainly used

(a) for a sampled aperture (and if a is known), to estimate the expected resolution for a given angle ϑ; and

(b) for an initial calculation of the N total cells in the scanning plane.

Theoretically, for any type of array it is possible to calculate an empirical a. The lower the value of $R(\vartheta)$, the better is the ability of the array to separate closely spaced sources. This can be verified with the example

---

[23] Some authors also include a spatial window (B_w) factor in Equation (3.67), see Boone [67] and Mast [68] for details.

of Figure 3.27. There are plots for the array of Figure 3.15 (a), with 36 mics and $D = 0{,}8\,\mathrm{m}$, and for another spiral array with 64 mics and $D = 1{,}6\,\mathrm{m}$. It is possible to see in the array with 36 mics that the sources cannot be separated, whereas with 64 mics it is possible to perceive two sources.

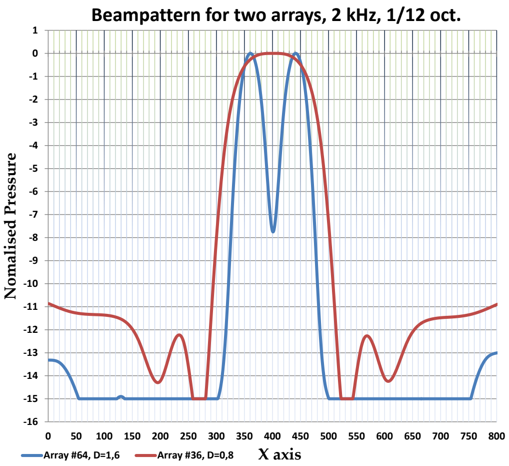

(a) Beampattern, arrays with #36 and #64 mics.

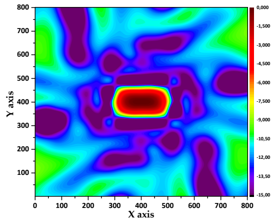

(b) PSF, Array #36 mics

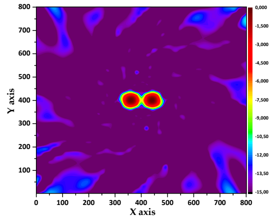

(c) PSF, Array #64 mics

Figure 3.27: PSFs of two different arrays for spatial resolution comparison.

If the angle ϑ is zero, then Equation (3.26) equals Equation (3.52) and thus $R(0) = R_{\text{axis}} = \text{BW}_{\text{axis}}$. Thus, it is possible to estimate the ratio between off-axis and on-axis resolution by doing $R(\vartheta)/R_{\text{axis}}$, then

$$\frac{R(\vartheta)}{R_{\text{axis}}} = \frac{1}{\cos(\vartheta)^3}\,, \tag{3.68}$$

the ratio above is depicted in the graphic of Figure 3.28 (b).

In Figure 3.28 one can observe that for angles over $\vartheta = 30^\circ$ the resolution is degraded more than 50%. For this reason the solid angle is restricted in the applications. In practice, the resolution may be compared to the resolution of a camera[24], since in its functioning there is also dependence on the diameter of the lens and the distance to the object.

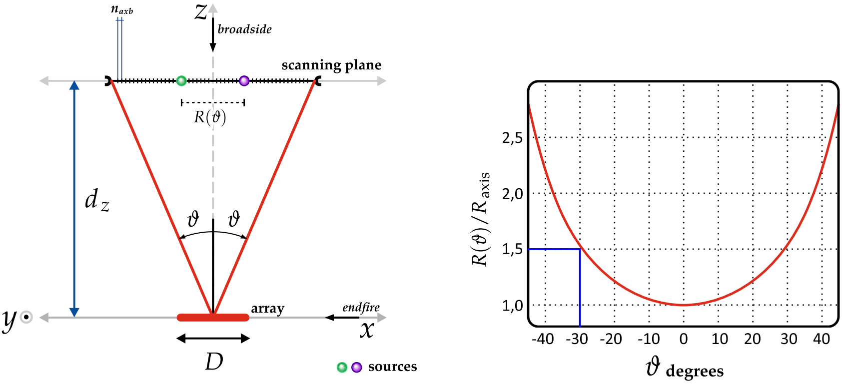

(a) Equation (3.67) depicted

(b) $R(\vartheta)/R_{\text{axis}}$

Figure 3.28: Rayleigh criterion.

3.3.4.1 Spatial Aliasing and Ambiguity

The inter-element spacing is very important in array processing because it determines the *spatial aliasing*. It is an inconvenient side effect of spatially undersampling the aperture of an array. It is also analogue to the time domain effect, while temporal undersampling results in the inability to differentiate between frequency components, spatial undersampling (with discrete sensors) yields the inability to distinguish between multiple directions of propagation. The *aliases* (or mainlobe replicas or mirrors) are called *grating lobes* (see Figure 3.30).

As in the temporal domain, the Nyquist[25] rate [70, 17] is utilized. In the spatial domain, the same concept can also be applied. Consider - for the sake of simplicity - the uniform linear array (ULA) of Figure 3.29. The additional distance that the wave takes between sensors is $d\sin(\theta)$. Thus, the time delay between consecutive sensors τ is given by:

---

[24] In fact, some authors have already referred beamforming applications as *acoustic telescope* [25] and *acoustic camera* [69].

[25] Harry Nyquist (1889 - 1976) was a Swedish engineer/physicist who made important contributions to information theory. His work in transmission [70] generated what is nowadays known as the *Nyquist sampling theorem*.

$$\tau = \frac{d}{c}\sin(\theta)\,, \tag{3.69}$$

where θ is the incident wave angle and d is the sampling microphone interval.

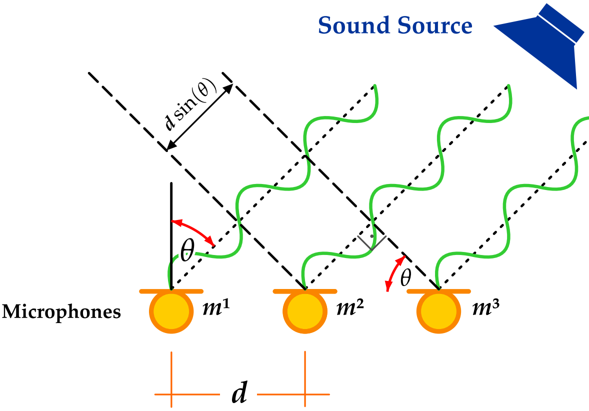

Figure 3.29: Uniform linear array.

The steering range for a ULA is $0 \le \theta \le \pi$; thus, to avoid spatial aliasing the phase differences must be limited to π. Considering a source signal $s(t) = \cos(2\pi f_{\max} t_0)$ the following condition is assumed

$$2\pi f_{\max}\tau \le \pi\,, \tag{3.70}$$

Now, substituting Equation (3.69) and considering the worst case for an *endfire* condition $\theta = 90^\circ$,

$$d \le \frac{c}{2f_{\max}}\,, \tag{3.71}$$

which is equivalent to

$$d \le \frac{\lambda_{\min}}{2}\,, \tag{3.72}$$

where $\lambda_{\min} = {}^{c}/_{f_{\max}}$. Another way to derive this expression is by the direct use of the *Nyquist sampling theorem* in the space domain. If so,

$$f_s \geq 2 \cdot f_{\max} \,, \tag{3.73}$$

in space,

$$k_s \geq 2 \cdot k_{\max} \,. \tag{3.74}$$

If the sampling interval is equal to d, then the spatial Nyquist wave number $k_{\max} = \pi / d$, with a period length equal to $2d$ and $\lambda_{\min} = 2d$. Therefore, the Equation (3.72) is recovered by the expression

$$f_{\max} = \frac{c}{\lambda_{\min}} \,. \tag{3.75}$$

When $\lambda = d \sin(\theta)$, the grating lobes are present and can be calculated (for ULA) as

$$\sin(\theta) = \frac{\lambda}{d} \,, \tag{3.76}$$

then

$$\theta = \sin^{-1}\left(\frac{n\,c}{f\,d}\right) \,, \tag{3.77}$$

where f is the signal frequency and n is an integer that selects the grating lobe. The table below demonstrates the respective grating lobe positions for the ULA example.

Table 3.1: Grating lobe positions considering the example of Figure 3.29 for $d = 0{,}2$ m, $c = 340$ m/s, $f = 6$ kHz.

n	**angle °**
0	0,00
1	16,46
2	34,52
3	58,21

Although exemplified with a linear array, these effects stand for all kinds of discrete arrays. There is an example for a regular 2D array in Figure 3.30. A complete review on this subject can be consulted in Dmochowski *et al.* [71] and Doron *et al.* [72].

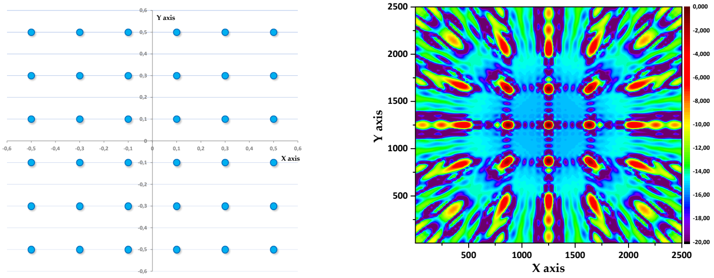

(a) Array (b) PSF

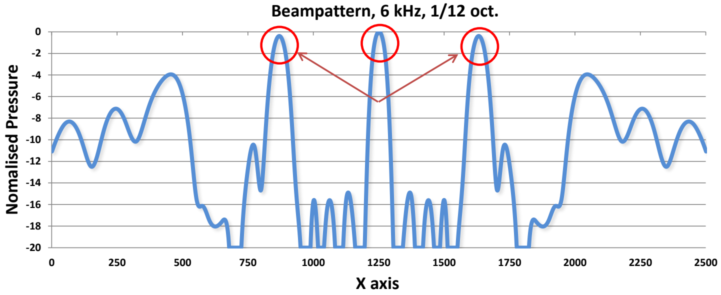

(c) Beampattern, *grating lobes* in detail

Figure 3.30: Spatial aliasing yields grating lobes.
Regular 2D array, 36 mics, 0,2 m inter-element spacing.

A problem regarding acoustically transparent arrays is the incapability to distinguish between front and back sides (or above/below). This is easily explained by looking the example of Figure 3.31. For this reason, in practical measurements, it is strongly recommended to avoid sources (or reflectors) behind the array. Otherwise they will appear in the maps as sources located in front of the array.

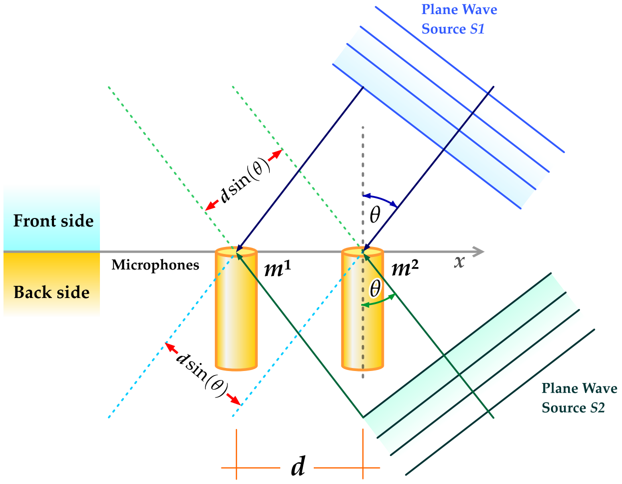

Figure 3.31: Ambiguity problem with front and back side of the array.

3.3.4.2 Resolution?

The term "resolution" is employed in several points related to array processing. However, it sometimes means different things. In order to clarify ambiguities, a summary is presented below.

1. **Beamwidth**

   Since the beamwidth estimates the 3 dB down of the mainlobe, in a certain way it also estimates the capability to resolve closely spaced waves. For this reason, it is also called *resolution* by some authors. Nevertheless, others [38] classify it as *mainlobe width*, which is different than the *resolution* term (see Section 3.3.2).

2. **Rayleigh criterion**

   As explained in this section, it establishes the limit where two waves are resolvable. Sometimes it is also found as $\mathrm{BW}_{\mathrm{null}}$ (or *peak-to-zero distance*) since it estimates the points where the mainlobe falls into a null. As a consequence, it is also referred to as *Rayleigh resolution*, *spatial resolution* or just *resolution* (see Section 3.3.4).

3. **Wavenumber** [§]

   Wavenumber resolution summarizes a beamfomer's ability to localize a propagating wave in wavenumber. This localization could be in direction of propagation, in wavelength, or both. The mainlobe width determines wavenumber resolution. Because wavenumber-frequency response and array pattern are equivalent for the delay-and-sum beamformer, width of the array pattern's mainlobe defines resolution. Because the array pattern depends on wavenumber, wavenumber is the natural variable on which to base resolution performance.

4. **Time**

   The *time resolution* is usually related to measurements. In the time domain, the Δt is the time between two consecutive samples. The sampling frequency of an analogue-to-digital converter (ADC) is commonly set to $f_s = 1/\Delta t$.

5. **Bit**

   The *bit resolution* is also related to measurements and indicates the number of discrete values that a device can produce over the range of analogue values. For example, an ADC with a resolution of 24 bits can encode an analogue input into 2^{24} = 16.777.216 different levels.

6. **Frequency**

   The *frequency resolution* is related to the number of points in each block of the Fast Fourier Transform (FFT). The number of points could be any, but usually is power of two based, e.g., $2^{12} = 4096$. For example, if f_s = 44.1 kHz and $N_{\text{FFT}} = 4096$, then $\Delta f = f_s / N_{\text{FFT}} \Rightarrow \Delta f \approx 10\,\text{Hz}$.

7. **Photo**

   The *photo resolution*, is the resolution of the picture that goes under the acoustic image layer. It is usually given in dots-per-inch (DPI, or pixels-per-inch for video devices). For a lossless picture at least 300 DPI is suggested (see Section 3.2.1).

[§] Excerpt extracted from *Array Signal Processing: Concepts and Techniques*, Dudgeon & Johnson, page 143 [38].

8. **Acoustic Image**

   The *acoustic image resolution* is the basically determined by the number of cells in the scanning plane. Fox example, in this dissertation the acoustic images have one cell per 1° (for the swept angles).

3.3.5 Geometry

The geometry of an array will determine its response since it samples the space in M points at specific positions. In general, arrays can be classified in two ways, concerning the dimensional span, i. e., one-, two- or three-dimensional; and concerning the *acoustical transparency*.

A structure or material is called *acoustically transparent* when its characteristics do not have any influence over the propagating acoustic field. The term influence here summarizes some known effects such as absorption, reflection, diffraction, transmission loss, etc. For example, many types of fabrics are considered acoustically transparent up to some frequency (determined by its mesh). That is, an object can be considered transparent if its properties and dimensions do not cause disturbance in the sound field for the chosen frequency.

As discussed in Section 2.4, the frequency range of an object under study can be determined based on its dimensions. The acoustical transparency concept falls into exactly the same idea. That is, if one given dimension is comparable (or closer) to the wavelength of a given wave, the object is considered an obstacle and cannot be acoustically transparent.

3.3.5.1 Planar Arrays

Planar arrays are those with one or two dimensions. There are infinite types of geometrical shapes, which means a suitable one must be chosen according to the proposed application.

Linear Arrays

The linear arrays are the most basic, and have been applied in acoustics since the early 1970's [73]. Some examples are given throughout this document (Figures 3.20, 3.29 and 3.31) and further information can be consulted in Kummer [74] and Möser *et al.* [75].

Two-Dimensional Arrays

The 2D arrays are largely applied in acoustics because they yield easily understandable maps. Figures 3.15 to 3.19 show the PSFs for the most commonly employed geometries. In practice, the spiral array is one of the best solutions for broad band noise applications [76].

In Figure 3.32 there is an example of a beamforming map in the applied to a 2D array for pass-by noise testing. It is possible to see sources on the ground that possibly are effects of the engine knocking and exhaust system output.

Figure 3.32: Example of beamforming map in the application of one 2D array for pass-by noise testing [61].

Apart from the knowledge shown in this dissertation, some other discussions concerning 2D array performance can be found in the references [38, 61, 43, 76, 77]. Also, several other applications in topics like pass-by noise testing [61, 78], auralization [79], psychoacoustics [64], MEMS [80], fly-over testing [35, 81], jet noise [82], and wind-tunnel measurements [83], wind turbines [84], among others use 2D arrays.

3.3.5.2 Three-Dimensional Arrays

The 3D arrays can also be classified[27] as transparent and solid arrays. Therefore, some authors [87] use the nomenclature *unbaffled*, for transparent (or free-field), and *baffled* for solid rigid surface or solid

---

[27] There are also the *special applications* 3D arrays, which they work in strictly specific conditions such as in-duct beamforming [85] or nozzle measurements [86], for example.

absorbent surface. The most commonly used shapes are the sphere and the cylinder. Considering those shapes, several authors have employed different techniques to turn them into good spatial sampling devices. That means that not only the DSB or CB are used, but also other domains like spherical harmonics [88] or circular harmonics (CHB) [89]. In Figure 3.33 there are examples of transparent and rigid sphere arrays.

(a) Transparent array

(b) Rigid array

Figure 3.33: Commercial sphere arrays from GFai [90] and B&K [91].

Cylinder Array

As previously cited in Section 1.2, the target of this work is the beamforming application for a cylinder array. This process comprises the simulations, measurements, and discussion. All the array parameters discussed until this point are completely compatible for the cylinder application.

Although the complete derivations will be described in Section 4.2, the angles θ and ϕ that will build the PSFs are presented here in Figures 3.34 and 3.35. The θ angle (azimuth) is swept from 0° to 360°; and the ϕ angle is only swept from 0° to 180°, since the problem is *a priori* symmetric. The cylinder surface is considered acoustically solid and rigid, and the sensors are positioned “inside” the cylinder (or flush to the surface) and always “looking” outside into space - also, no imperfections on the surface are considered.

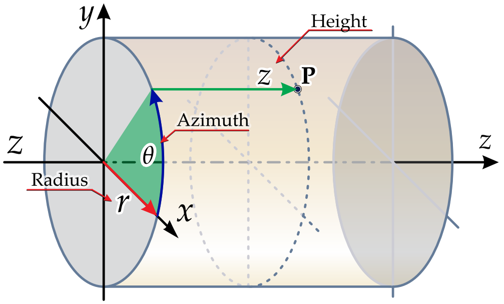

(a) sweep angle $\Rightarrow\ \theta$

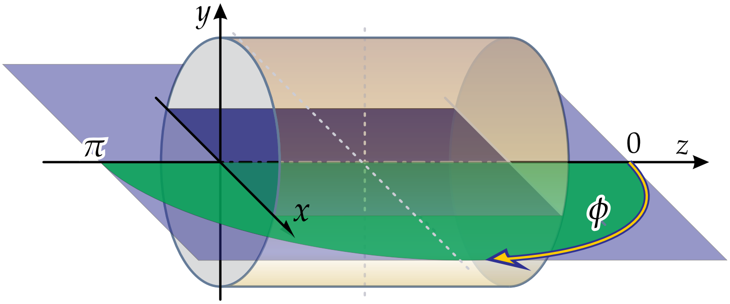

(b) sweep angle $\Rightarrow\ \phi$

Figure 3.34: Angles swept to build the PSF.

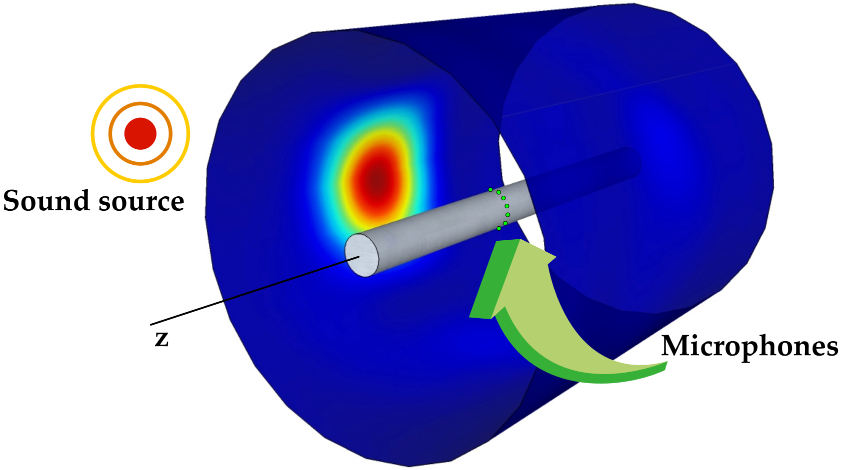

Figure 3.35: Example of PSF in the cylindrical coordinates for the swept angles θ and ϕ.

3.4 Array Design

Besides the possibility of using a scale factor model, the array design also must involve its construction aspects. The cylinder diameter was chosen considering two important aspects:

1. measurements, a real size tube has to be used. Thus, it must not be big, so it fits in the anechoic chamber, and also it must have enough space along the radius for 32 microphones;
2. BEM simulations, if the radius is large, there will be thousands of elements and thus the numerical simulations could take a great deal of time.

For these reasons, the diameter chosen was $\varnothing = 0{,}25\,\mathrm{m}$, which for the frequency of $2{,}2\,\mathrm{kHz}$ renders a $kr \approx 5$. In Appendix C the coordinates of both geometries can be consulted.

3.4.1 Equally Angled Array

Let M omnidirectional sensors equispaced on a circle of radius r around the circumference of a cylinder, with the array's centre located at the origin of coordinates. The transducers positions[28] in Cartesian coordinates are given by

$$\vec{x}_m = \Big[r \cdot \cos(\theta_m),\, r \cdot \sin(\theta_m),\, 0 \Big]^T, \qquad m = 0, 1, 2, 3, \ldots, M-1, \tag{3.78}$$

where the azimuth angle of each sensor is

$$\theta_m = m \left(\frac{2\pi}{M} \right). \tag{3.79}$$

The inter-element spacing is

$$d_{\text{chord}} = 2r \sin\left(\frac{\pi}{M} \right), \tag{3.80}$$

considering the chord and the arc is

---

[28] This array is also found in the references as *uniform circular array* (UCA).

$$d_{\text{arc}} = r \cdot \theta_1 = r \cdot \left(\frac{2\pi}{M} \right). \tag{3.81}$$

Consequently, the maximum analysis frequency is $f_{\max} = {}^{c}/_{2d}$ (Equation 3.75) . For 32 microphones Equations (3.80) and (3.81) yield approximately the same results, and thus theoretically the maximum frequency is $f_{\max} \approx 6{,}9\,\text{kHz}$ to avoid spatial aliasing.

Figure 3.36 depicts the EAA array described, this array will be widely discussed in this document. Furthermore, there will be the GA geometry to overcome some EAA inconvenient issues.

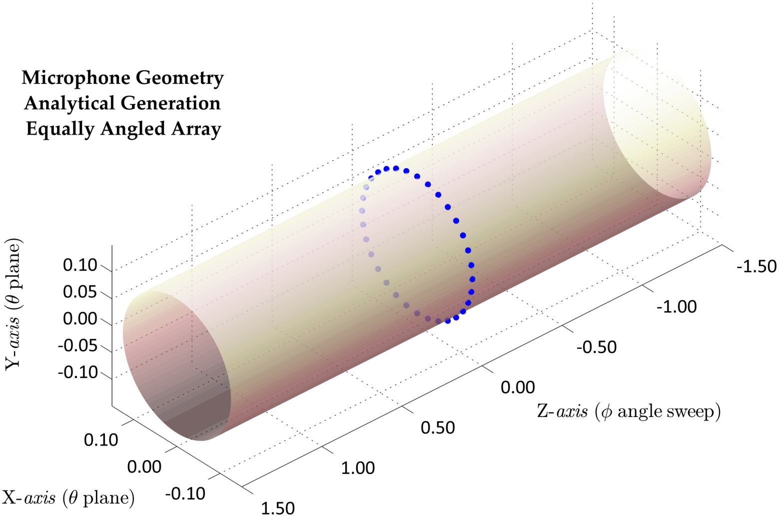

Figure 3.36: Equally Angled Array (EAA).

3.4.2 Genetic Algorithm Array

The Genetic Algorithm Array (GA), Figure 3.37, is fruit of the search and optimisation process discussed in their entirety in Section 5.3.

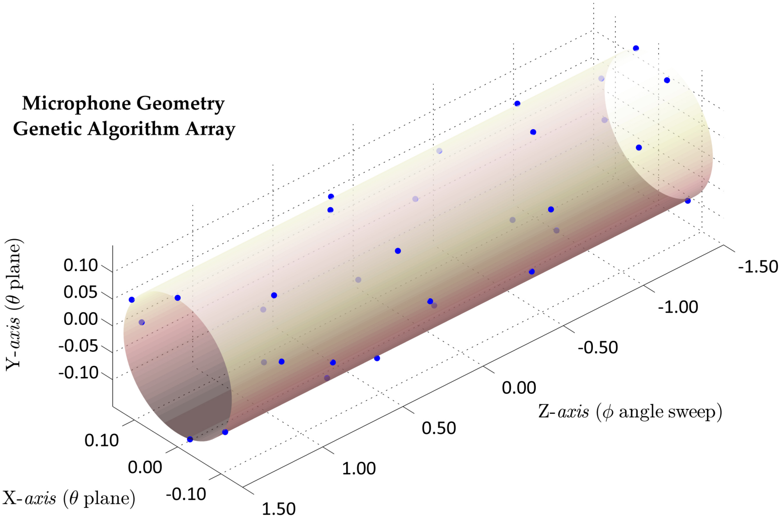

Figure 3.37: Genetic Algorithm Array (GA).

4

Diffraction of Plane Acoustic Waves

This chapter will enclose the diffraction effects applied to the case of an acoustically rigid cylinder. The derived *non-free-field* pressure is then used in the beamforming process, and analytical simulations are carried out to estimate the behaviour for different parameters (for two array geometries).

4.1 Diffraction

As cited in the previous chapter, the cylinder is considered solid and rigid. Pondering this hypothesis, two acoustic effects[1] emerge, reflection and diffraction. These two concepts are applicable when a propagating wave encounters an obstacle (of any shape). The treatment concerning which is the better choice is based on the relative wavelength size compared to the object size.

If the cylinder diameter is much larger than the wavelength of the incident sound (high frequency), the reflection law is applied to "each ray of sound", as depicted in Figure 4.1 (specular reflection). On the opposite side of the cylinder there will exist a *shadow region*, theoretically free of sound. However, if the wavelength is comparable to d, the sound rays are meaningless and the cylinder - in addition to the incident field - becomes a generator of secondary waves [6] (which will superimpose the incoming sound field). Moreover, the waves with longer wavelengths will *bend around* the cylinder "creating" sound in the shadow region. This phenomenon is called diffraction[2].

---

[1] The *refraction* effect will also exist if the cylinder is not acoustically rigid [92].

[2] For a historical review, the reader may consult the book *Origins in Acoustics* [93].

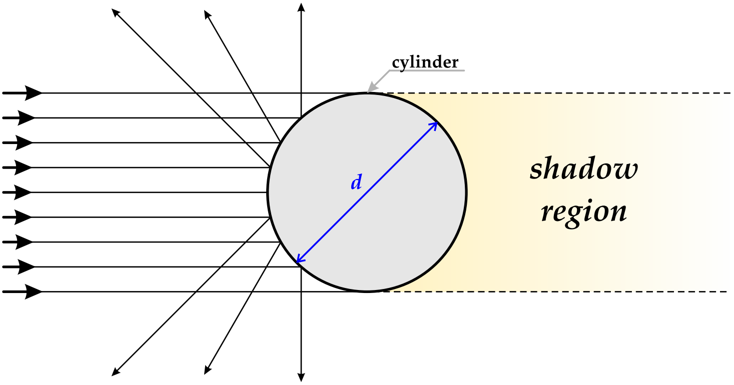

Figure 4.1: Specular reflection occurs when $d \gg \lambda$.

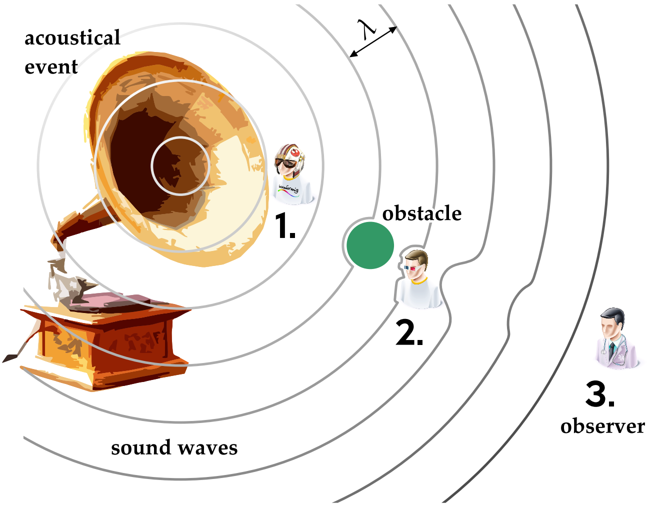

Figure 4.2: Acoustical event, obstacle and observers #1, #2, and #3.

The diffraction[3] phenomena are most known by *contouring* objects and/or by passing small slits and spreading the sound. Consider the illustrative example of Figure 4.2. First, discard air absorption effects, then, an acoustical event (containing the entire audible frequency rage) emits sound waves at a given position,

---

[3] Some authors [18] distinguish *diffraction* and *scattering*, in the sense that scattering is "just" a modification caused by a small object. Since they have the same physical meaning no distinction is made in this document.

- observer #1 will listen to the sound “brightly” and without interference,
- observer #2 will listen to the sound, but it probably lacks of high frequency content due to the obstacle in front of him/her, and
- observer #3, several wavelengths away of observer #2, will listen to the sound different than the others, but he/she is not able to infer that there is an obstacle ahead - from the nature of the sound approaching him/her.

Another experience with diffraction similar to beamforming in a certain way is the human sense of the direction of sound. A significant part of the brain “post-processing” considers the shadow and delay between the ears. Thus, there also the confusion or difficulty in distinguishing whether the waves are coming from the front or back [94]. The easiest and most instinctive way to solve this problem is to move the head to a distinct position.

Following the idea presented in these examples, it is possible to perceive that diffraction effects depend on the shape of the wavefronts that reach the surfaces. For interaction among curved wavefronts (near-field), the effect is called *Fresnel diffraction*. On the other hand, for planar wavefronts interaction (far-field) it is called *Fraunhofer diffraction*. Since the wavefield can be considered far-field after a few wavelengths apart from the cylinder, the derivations and hypothesis used in this dissertation are all for plane waves. Further reading about acoustic rays and detailed derivations for diffraction can be consulted in Rossing *et al.* [9].

Although the diffraction concept is easy to understand, its analytical calculation for complicated surfaces is hard to predict [95, 96]. For more geometrically simple obstacles like the sphere, the disc, or the cylinder the degree of difficulty is not as pronounced and can be carried out accordingly. Nevertheless, numerical methods such as BEM or FEM are normally used for other generic shapes.

4.2 Rigid Cylinder Diffraction

The derivations shown in this section consider the case of an infinite cylinder. Consider the cylindrical coordinates (r,θ,z) and a rigid cylinder as depicted in Figure 4.3:

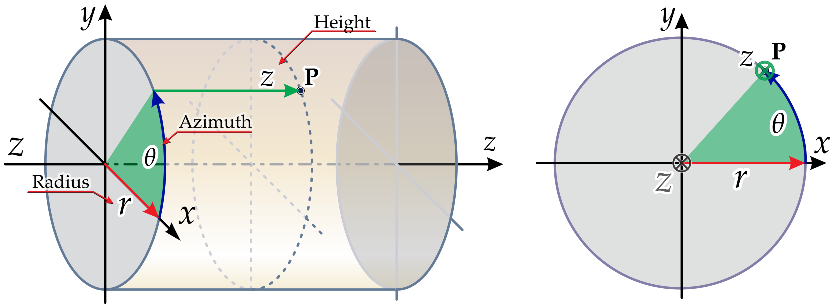

(a) (b)

Figure 4.3: Cylindrical coordinates (r,θ,z). (a) 3D sketch; (b) xy plane.

It is possible to decompose the coordinates in

$$\begin{cases} x = r\cos(\theta), \\ y = r\sin(\theta), \end{cases} \quad \text{and} \quad r = \sqrt{x^2+y^2}, \tag{4.1}$$

with $0 \leq \theta \leq 2\pi$, and

$$\theta = \begin{cases} 0 & \text{if } x = 0 \text{ and } y = 0 \\ \arcsin(\frac{y}{r}) & \text{if } x \geq 0 \\ -\arcsin(\frac{y}{r}) + \pi & \text{if } x < 0 \end{cases} . \tag{4.2}$$

The Helmholtz equation (presented previously as Equation (2.7))

$$\nabla^2\psi(\vec{x}) + k^2\psi(\vec{x}) = 0 \tag{4.3}$$

can be used to describe a sound field. In cylindrical coordinates it reads

$$\frac{1}{r}\frac{\partial}{\partial r}\left(r\frac{\partial p}{\partial r}\right) + \frac{1}{r^2}\frac{\partial^2 p}{\partial\theta^2} + \frac{\partial^2 p}{\partial z^2} + k^2 p = 0, \tag{4.4}$$

with $k = 2\pi f/c$ as the wave length.

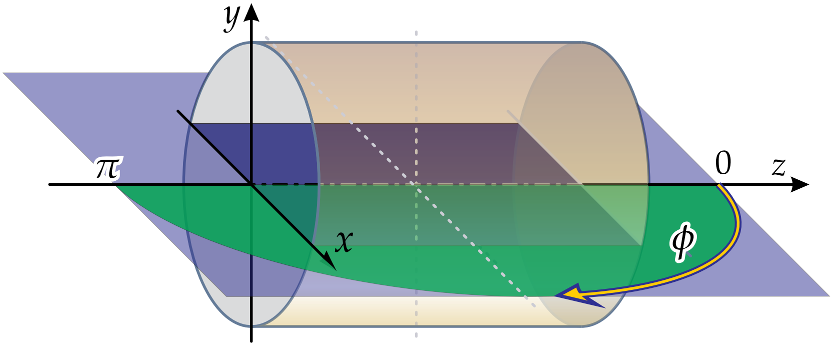

Figure 4.4: Polar angle ϕ.

Now, consider the solutions for a fixed polar angle ϕ (see Figure 4.4) and

$$p = p(r,\theta)\,\exp\Big(ikz\cos(\phi)\Big)\,, \tag{4.5}$$

with $0 \leq \phi \leq \pi$, since the problem is symmetrical. Exclusively in this section $i = \sqrt{-1}$ (and not j) to avoid later confusion. Then substituting p from Equation (4.5) into Equation (4.4)

$$\frac{1}{r}\frac{\partial}{\partial r}\left(r\,\frac{\partial p}{\partial r}\right) + \frac{1}{r^2}\frac{\partial^2 p}{\partial \theta^2} + k^2\sin^2(\phi)\,p = 0\,\cdot \tag{4.6}$$

Applying the *separation of variables*[4]:

$$p(r,\theta) = F(r)\,G(\theta)\,, \tag{4.7}$$

gives

$$\frac{r\frac{\partial}{\partial r}\left(r\frac{\partial F}{\partial r}\right)}{F} + k^2 r^2\sin^2(\phi) = -\frac{\left(\frac{\partial^2 G}{\partial\theta^2}\right)}{G}\,\cdot \tag{4.8}$$

The left and right hand sides of Equation (4.8) are constant, say B, this gives

$$\frac{1}{r}\frac{\mathrm{d}}{\mathrm{d}r}\left(r\,\frac{\mathrm{d}F}{\mathrm{d}r}\right) + \left(k^2\sin^2(\phi) - \frac{B}{r^2}\right)F = 0\,, \tag{4.9}$$

---

[4] The method is also found as *Fourier method* or *product method*. A reading in the textbook *Advanced Engineering Mathematics* [97] may elucidate all the steps involved.

$$\frac{\mathrm{d}^2 G}{\mathrm{d}\theta^2} + BG = 0 \cdot \tag{4.10}$$

Differential equation in the azimuthal coordinate

Non-trivial periodical solutions for Equation (4.10) are found for

$$B = m^2 , \qquad \text{with} \qquad m = \{0,1,2,\ldots\} . \tag{4.11}$$

The solutions of Equation (4.10) with (4.11) are

$$G(\theta) = G_m(\theta) = \exp\left(im\theta\right) . \tag{4.12}$$

Differential equation in the radial coordinate

Equation (4.11) substituted in Equation (4.9) gives

$$\frac{1}{r}\frac{\mathrm{d}}{\mathrm{d}r}\left(r\frac{\mathrm{d}F_m}{\mathrm{d}r}\right) + \left(k^2\sin^2(\phi) - \frac{m^2}{r^2}\right)F_m = 0 . \tag{4.13}$$

The outward radiating solution of Equation (4.13) is

$$F_m(r) = H_m^{(2)}\left(kr\sin(\phi)\right) , \tag{4.14}$$

where $H_m^{(2)}$ is the m-th order Hankel[5] function of the second kind [99, 100].

Full solution

From the foregoing - combining Equations (4.5), (4.7), (4.12) and (4.14) - it follows that the full outward radiating solution can be written as

$$p(r,\theta,z) = \sum_{m=-\infty}^{\infty} C_m H_m^{(2)}\left(kr\sin(\phi)\right) \exp\left[i\left(m\theta + kz\cos(\phi)\right)\right] \cdot \tag{4.15}$$

---

[5] Hermann Hankel (1839 - 1873) was a German mathematician who worked on the theory of functions and the theory of complex numbers. His study with the functions nowadays called *Hankel functions* are published in the *Mathematische Annalen* Journal [98].

Incident plane wave on a rigid cylinder

Suppose an incident plane wave

$$p_{\text{in}}(r,\theta,z) = \exp\left[i\left(kr\sin(\phi_{\text{in}})\cos(\theta-\theta_{\text{in}}) + kz\cos(\phi_{\text{in}})\right)\right]\cdot \tag{4.16}$$

For acoustically rigid cylinder the impedance Z tends to infinite. Thus, the particle velocity $u \to 0^+$, which means $u_s + u_{\text{in}} = 0$ at $r = r_0$, where the subscript "s" stands for scattered and "in" for incident plane wave. Then from the momentum equation follows

$$\frac{\partial p_s}{\partial r} + \frac{\partial p_{\text{in}}}{\partial r} = 0\cdot \tag{4.17}$$

Thus, omitting the subscript "s" and considering $r = r_0$:

$$\frac{\partial p}{\partial r} = -\frac{\partial p_{\text{in}}}{\partial r}\cdot \tag{4.18}$$

Substituting Equations (4.15) and (4.16) it follows that $\phi = \phi_{\text{in}}$ and, furthermore,

$$\begin{aligned}\sum_{m=-\infty}^{\infty} C_m H_m^{(2)\prime}\left(kr_0\sin(\phi_{\text{in}})\right)\exp\left(im\theta\right) &= \\ -i\cos(\theta-\theta_{\text{in}})\exp&\left[ikr_0\sin(\phi_{\text{in}})\cos(\theta-\theta_{\text{in}})\right]\cdot\end{aligned} \tag{4.19}$$

Consider a temporary change of variables on the left side of Equation (4.19) from $m \to \mu$

$$\begin{aligned}\sum_{\mu=-\infty}^{\infty} C_\mu H_\mu^{(2)\prime}\left(kr_0\sin(\phi_{\text{in}})\right)\exp\left(i\mu\theta\right) &= \\ -i\cos(\theta-\theta_{\text{in}})\exp&\left[ikr_0\sin(\phi_{\text{in}})\cos(\theta-\theta_{\text{in}})\right]\cdot\end{aligned} \tag{4.20}$$

Both sides of Equation (4.20) are multiplied by $\exp(-im\theta)$ and integrated over θ between 0 and 2π

$$\sum_{\mu=-\infty}^{\infty} C_\mu H_\mu^{(2)'}\left(kr_0 \sin(\phi_{\text{in}})\right) \int_0^{2\pi} \exp\left[i(\mu-m)\theta\right] \mathrm{d}\theta \ = \\ \int_0^{2\pi} -i\cos(\theta-\theta_{\text{in}}) \exp\Big[ikr_0 \sin(\phi_{\text{in}}) \cos(\theta-\theta_{\text{in}}) - m\theta\Big] \mathrm{d}\theta \cdot \quad (4.21)$$

It follows that in the left side of Equation (4.22)

$$\int_0^{2\pi} \exp\left[i(\mu-m)\theta\right] \mathrm{d}\theta = \begin{cases} 0 & \text{for } m \neq \mu \\ 2\pi & \text{for } m = \mu \end{cases} ,$$

thus,

$$\sum_{m=-\infty}^{\infty} C_m H_m^{(2)'}\left(kr_0 \sin(\phi_{\text{in}})\right) 2\pi \ = \\ \int_0^{2\pi} -i\cos(\theta-\theta_{\text{in}}) \exp\Big[ikr_0 \sin(\phi_{\text{in}}) \cos(\theta-\theta_{\text{in}}) - m\theta\Big] \mathrm{d}\theta \cdot \quad (4.22)$$

After the change of integral variable $\theta \to (\theta-\theta_{\text{in}})$, the coefficients C_m follow from

$$C_m = \frac{-i\exp(-im\theta_{\text{in}})}{2\pi\, H_m^{(2)'}\left(kr_0 \sin(\phi_{\text{in}})\right)} \int_0^{2\pi} \cos(\theta) \exp\Big[i\left(kr_0 \sin(\phi_{\text{in}}) \cos(\theta) - m\theta\right)\Big] \mathrm{d}\theta \,. \quad (4.23)$$

The diffracted solution can be rewritten as

$$p(r,\theta,z) = \sum_{m=-\infty}^{\infty} C_m \frac{H_m^{(2)}\left(kr \ \sin(\phi_{\text{in}})\right)}{H_m^{(2)'}\left(kr_0 \sin(\phi_{\text{in}})\right)} \exp\Big[i\left(m(\theta-\theta_{\text{in}}) + kz\cos(\phi_{\text{in}})\right)\Big], \quad (4.24)$$

with

$$C_m = \frac{-i}{2\pi} \int_0^{2\pi} \cos(\theta) \exp\Big[i\left(kr_0 \sin(\phi_{\text{in}}) \cos(\theta) - m\theta\right)\Big] \mathrm{d}\theta \cdot \quad (4.25)$$

These coefficients can be evaluated quickly using FFT; since $C_m = C_{-m}$, Equation (4.24) can be written as

$$p(r,\theta,z) = \Bigg\{ C_0 \, \frac{H_0^{(2)}\Big(kr \, \sin(\phi_{\text{in}})\Big)}{H_0^{(2)\prime}\Big(kr_0 \sin(\phi_{\text{in}})\Big)}$$

$$+ 2 \sum_{m=1}^{\infty} C_m \frac{H_m^{(2)}\Big(kr \, \sin(\phi_{\text{in}})\Big)}{H_m^{(2)\prime}\Big(kr_0 \sin(\phi_{\text{in}})\Big)} \cos\Big(m(\theta - \theta_{\text{in}})\Big) \Bigg\} \exp\Big(ikz \cos(\phi_{\text{in}})\Big) . \tag{4.26}$$

Consider temporarily $x = kr_0 \sin(\phi_{\text{in}})$, the coefficients of Equation (4.25) can also be evaluated analytically, because

$$\frac{-i}{2\pi} \int_0^{2\pi} \cos(\theta) \exp\Big[i\,(x \cos(\theta) - m\theta)\Big] \mathrm{d}\theta = \frac{-1}{2\pi} \frac{\mathrm{d}}{\mathrm{d}x} \int_0^{2\pi} \exp\Big[i\,(x \cos(\theta) - m\theta)\Big] \mathrm{d}\theta$$

$$= \frac{-1}{2\pi} \frac{\mathrm{d}}{\mathrm{d}x} \int_0^{2\pi} \exp\left[i\left(x \cos\left(\theta - \frac{\pi}{2}\right) - m\left(\theta - \frac{\pi}{2}\right)\right)\right] \mathrm{d}\theta$$

$$= \frac{-1}{2\pi} \, i^m \, \frac{\mathrm{d}}{\mathrm{d}x} \int_0^{2\pi} \exp\Big[i\,\Big(x \sin(\theta) - m\theta\Big)\Big] \mathrm{d}\theta$$

$$= \frac{-1}{\pi} \, i^m \, \frac{\mathrm{d}}{\mathrm{d}x} \int_0^{\pi} \cos\Big(x \sin(\theta) - m\theta\Big) \mathrm{d}\theta$$

$$= -i^m \frac{\mathrm{d}}{\mathrm{d}x} J_m(x) \ , \tag{4.27}$$

where $J_m(x)$ is an m order Bessel[6] function [102], for positive integer values of m. Hence,

$$C_m = -i^m J_m'\Big(kr_0 \sin(\phi_{\text{in}})\Big) \ , \tag{4.28}$$

---

[6] Friedrich Wilhelm Bessel (1784 - 1846) was a German astronomer and mathematician who is considered the founder of the German school of practical astronomy [101]. His study about perturbation in planetary system yielded what is now known as the *Bessel function*.

and

$$p(r,\theta,z) = \Bigg\{ -J_0' \left(kr_0 \sin(\phi_{\text{in}})\right) \frac{H_0^{(2)}\left(kr\ \sin(\phi_{\text{in}})\right)}{H_0^{(2)\prime}\left(kr_0 \sin(\phi_{\text{in}})\right)} - 2\sum_{m=1}^{\infty} i^m J_m' \left(kr_0 \sin(\phi_{\text{in}})\right) \frac{H_m^{(2)}\left(kr\ \sin(\phi_{\text{in}})\right)}{H_m^{(2)\prime}\left(kr_0 \sin(\phi_{\text{in}})\right)} \cos\left(m(\theta-\theta_{\text{in}})\right) \Bigg\} \exp\left(ikz\cos(\phi_{\text{in}})\right) . \quad (4.29)$$

4.2.1 Phased Array on the Cylinder

On the cylinder ($r = r_0$), the incident pressure is (see Eq. Equation (4.16))

$$p_{\text{in}}(r_0,\theta,z) = \exp\left[i\left(kr_0 \sin(\phi_{\text{in}})\cos(\theta-\theta_{\text{in}}) + kz\cos(\phi_{\text{in}})\right)\right] . \quad (4.30)$$

and the diffracted-reflected pressure[7] is (see Eq. Equation (4.29))

$$p(r,\theta,z) = \Bigg\{ -J_0' \left(kr_0 \sin(\phi_{\text{in}})\right) \frac{H_0^{(2)}\left(kr_0 \sin(\phi_{\text{in}})\right)}{H_0^{(2)\prime}\left(kr_0 \sin(\phi_{\text{in}})\right)} - 2\sum_{m=1}^{\infty} i^m J_m' \left(kr_0 \sin(\phi_{\text{in}})\right) \frac{H_m^{(2)}\left(kr_0 \sin(\phi_{\text{in}})\right)}{H_m^{(2)\prime}\left(kr_0 \sin(\phi_{\text{in}})\right)} \cos\left(m(\theta-\theta_{\text{in}})\right) \Bigg\} \exp\left(ikz\cos(\phi_{\text{in}})\right) . \quad (4.31)$$

The total pressure is the sum of Equation (4.30) and Equation (4.31). Supposing there are microphones on the cylinder surface, located[8] at $\vec{x}_n = (r_0, \theta_n, z_n)$. The pressures measured by these microphones are

---

[7] The truncation criteria of Equation (4.31) is described in Appendix E.

[8] Only in this section n means the n^{th} microphone and N is the total number of mics. This is to avoid confusion with the m of the Hankel and Bessel functions.

$$p_n(\phi_{\text{in}},\theta_{\text{in}},z_n) \;=\; p_{\text{in}}(r_0,\theta_n,z_n) + p(r_0,\theta_n,z_n)$$

$$= \Bigg\{ \exp\Big(ikr_0\sin(\phi_{\text{in}})\cos(\theta_n-\theta_{\text{in}})\Big) - J_0'\Big(kr_0\sin(\phi_{\text{in}})\Big)\frac{H_0^{(2)}\Big(kr_0\sin(\phi_{\text{in}})\Big)}{H_0^{(2)'}\Big(kr_0\sin(\phi_{\text{in}})\Big)}$$

$$-2\sum_{m=1}^{\infty} i^m J_m'\Big(kr_0\sin(\phi_{\text{in}})\Big)\frac{H_m^{(2)}\Big(kr_0\sin(\phi_{\text{in}})\Big)}{H_m^{(2)'}\Big(kr_0\sin(\phi_{\text{in}})\Big)}\cos\Big(m\,(\theta_n-\theta_{\text{in}})\Big)\Bigg\}$$

$$\exp\Big(ikz_n\cos(\phi_{\text{in}})\Big). \qquad (4.32)$$

Now suppose beamforming is applied to the (ϕ,θ)-plane, that is, it scans for plane waves from all possible directions. Then steering vector values can be applied as follows.

Free-field:

$$g_n(\phi,\theta) = \exp\Big(ikr_0\sin(\phi)\cos(\theta_n-\theta)\Big)\exp\Big(ikz_n\cos(\phi)\Big). \qquad (4.33)$$

Adjusted for diffraction:

$$g_n(\phi,\theta) =$$

$$\Bigg\{ \exp\Big(ikr_0\sin(\phi)\cos(\theta_n-\theta)\Big) - J_0'\Big(kr_0\sin(\phi)\Big)\frac{H_0^{(2)}\Big(kr_0\sin(\phi_{\text{in}})\Big)}{H_0^{(2)'}\Big(kr_0\sin(\phi_{\text{in}})\Big)}$$

$$-2\sum_{m=1}^{\infty} i^m J_m'\Big(kr_0\sin(\phi)\Big)\frac{H_m^{(2)}\Big(kr_0\sin(\phi_{\text{in}})\Big)}{H_m^{(2)'}\Big(kr_0\sin(\phi_{\text{in}})\Big)}\cos\Big(m\,(\theta_n-\theta)\Big)\Bigg\}$$

$$\exp\Big(ikz_n\cos(\phi)\Big). \qquad (4.34)$$

Now, recalling the equations of Section 3.2.2, it is possible to write the “measured pressures” and the steering values in vector notation as (Equations (3.30) and (3.31)):

$$\vec{p} = \begin{pmatrix} p_1 \\ \vdots \\ p_N \end{pmatrix}, \qquad \vec{g} = \begin{pmatrix} g_1 \\ \vdots \\ g_N \end{pmatrix}, \tag{4.35}$$

and conventional beamforming can be performed as usual:

$$a = \frac{\vec{g}^{\dagger}\vec{p}}{|\vec{g}|^2}, \tag{4.36}$$

for the source amplitude, or

$$A = \frac{1}{2}|a|^2 = \frac{\vec{g}^{\dagger}\vec{C}\,\vec{g}}{|\vec{g}|^4}, \tag{4.37}$$

for the power. For simulations, it is convenient to use Equation (4.36) written out as

$$a(\phi,\theta) = \frac{\sum_{n=1}^{N} g_n^{\dagger}(\phi,\theta)\, p_n(\phi_{\text{in}},\theta_{\text{in}})}{\sum_{n=1}^{N} \left| g_n(\phi,\theta) \right|^2}. \tag{4.38}$$

In the following there will be simulations discussing the models presented here.

4.3 Analytical Simulations

The analytical[9] simulations have two parts. The former presents the behaviour of the sound waves that strike the cylinder in polar plots. The latter provides the simulations for the beamforming processing.

As derived in the previous section, the frequency determines what constitutes an obstacle. Typical simulations to estimate diffraction are plotted as polar plots with the dimensionless parameter kr. Figure 4.5

---

[9] Some scientists also would call it the numerical evaluation of the analytical models.

depicts the diffraction over cylinders of different radii for several *kr* values. In the plots the diffraction plus free-field curves are in HSV colour scale, the pink lines signifying higher frequencies and the light blue lower frequencies. The frequency range extends from 50 Hz to 3,2 kHz with steps of df=50 Hz, and $\phi_{in} = 90°$.

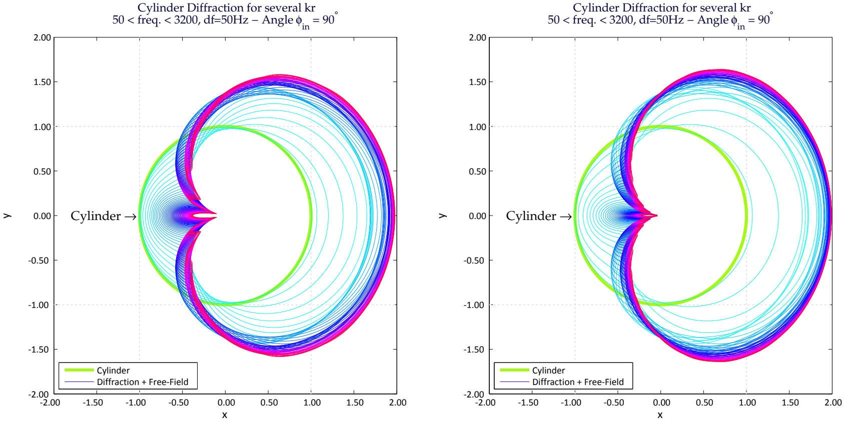

(a) $r = 0,1250$ m (b) $r = 0,2500$ m

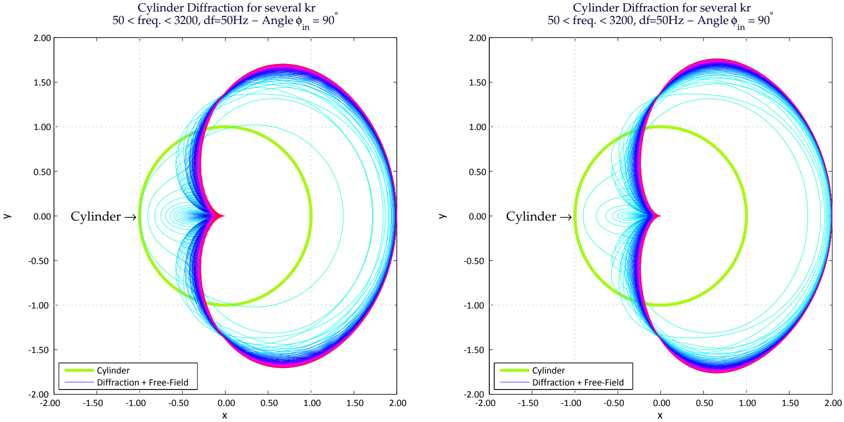

(c) $r = 0,5000$ m (d) $r = 1,0000$ m

Figure 4.5: Polar plots of acoustic pressure over the cylinder for different radii. The frequency range extends from 50 Hz to 3,2 kHz with df=50 Hz, and polar angle of $\phi_{in} = 90°$.

It is possible to observe that the *shadow* effects are more pronounced for wider diameters. On the other hand, for high *kr* values the acoustic pressure is doubled, as can also be seen Figure 4.6.

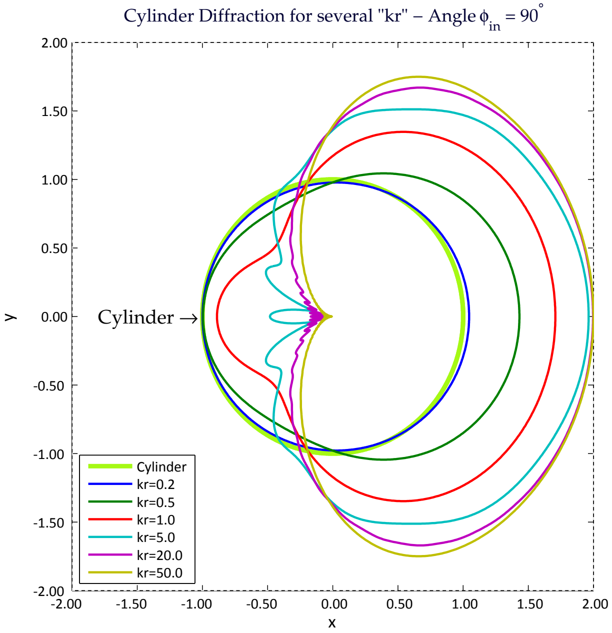

Figure 4.6: Diffraction on a rigid cylinder for a discrete number of *kr* ($r =$0,1250 m).

Since the experimental measurements and BEM simulations have 0,1250 m radius cylinder, most simulations throughout this chapter will consider this dimension. To promote a better understanding of the sound field behaviour, in Figure 4.7, there are 4 sub-plots. The first three separate the frequency range into three regions and the last shows the full sweep up to the frequency of 10 kHz. These plots were constructed with a thousand points along the θ-axis, which is comparable to a case in which 1000 microphones could be placed on the surface (for the EAA). However, if only 32 microphones are sampling the space, as shown[10] in Figure 4.8, the “perceived“ diffraction field is different. The natural conclusion is that the greater the number of microphones present, the better the sound field representation will be.

---

[10] Similar simulations for other radii (as Figure 4.5) and other numbers of sampling points (as Figure 4.8) can be found in Appendix F.

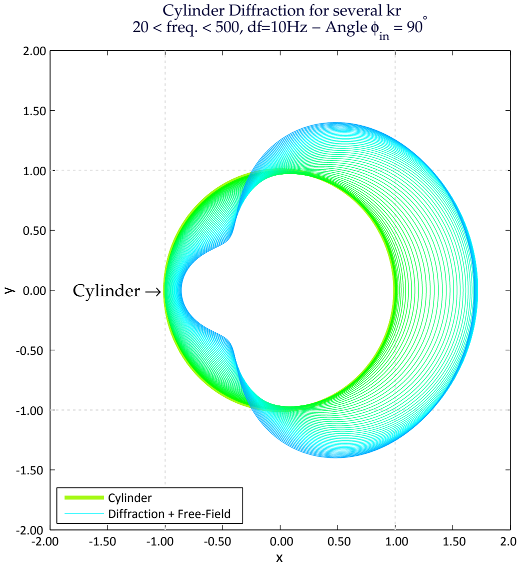

(a) $20 < f < 500$ Hz, df=10 Hz

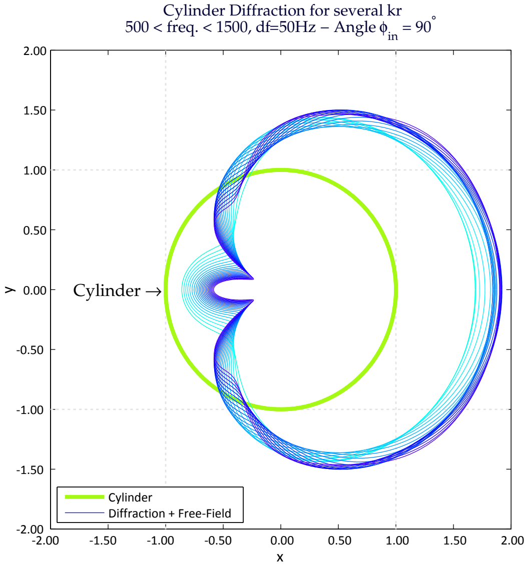

(b) $500 < f < 1500$ Hz, df=50 Hz

Figure 4.7: Polar plots of acoustic pressure on the cylinder, diffraction + free-field. Cylinder radius $r = 0,1250$ m and $\phi_{in} = 90°$.

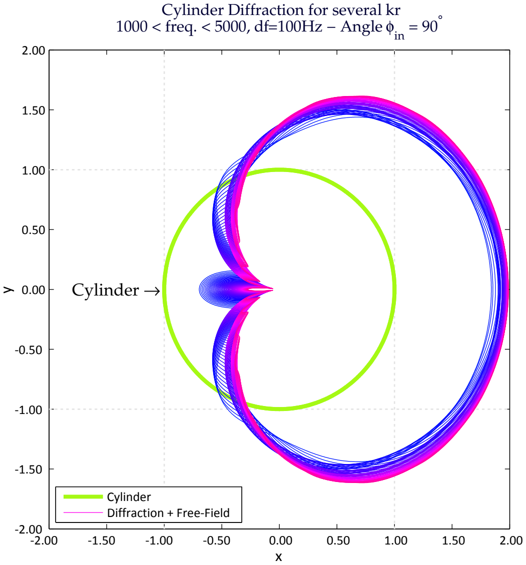

(c) $1000 < f < 5000$ Hz, df=100 Hz

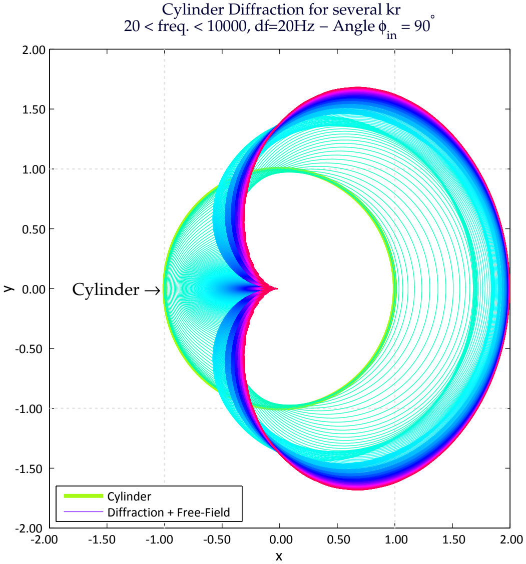

(d) $20 < f < 10000$ Hz, df=10 Hz

Figure 4.7: Polar plots of acoustic pressure on the cylinder, diffraction + free-field. Cylinder radius $r = 0,1250$ m and $\phi_{in} = 90°$.

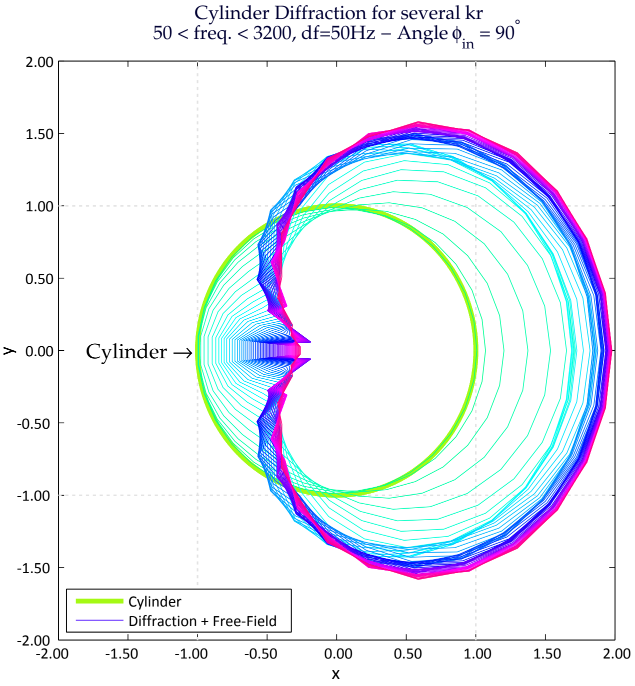

Figure 4.8: Diffraction on a rigid cylinder perceived by 32 points on a circumference (50 Hz<f<3,2 kHz with df=50 Hz, $\phi_{in} = 90°$ and $r = 0,1250$ m).

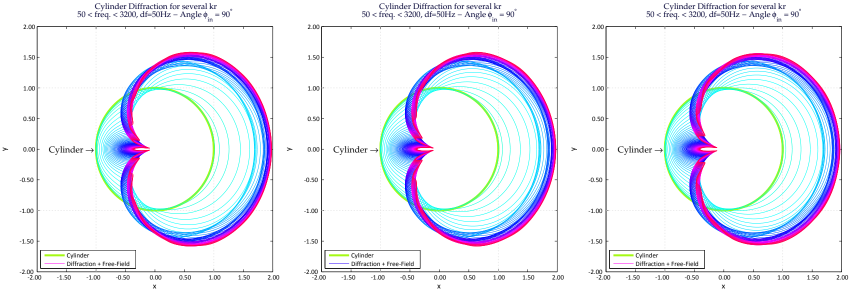

(a) $c = 306\ ^{m}/_{s}$ (b) $c = 340\ ^{m}/_{s}$ (c) $c = 374\ ^{m}/_{s}$

Figure 4.9: Diffraction field varying the sound speed at ±10% of $c = 340\ ^{m}/_{s}$.

A simulation was carried out varying the sound speed at ±10% of $c = 340\ {}^{m}/_{s}$, but as can be seen in Figure 4.9, visually there is not a great impact. Throughout this document the sound speed is considered $c = 340\ {}^{m}/_{s}$. However, further research is suggested to better investigate the variations of the sound speed and atmospheric absorption that may impact the results.

There is a symmetry centred in $\phi_{in} = 90^{\circ}$. The consequence of this is that supplementary angles will render the same results, as shown in Figure 4.10 for the angles of $\phi_{in} = 45^{\circ}$ or 135° (plots for other angles can be consulted in Appendix F).

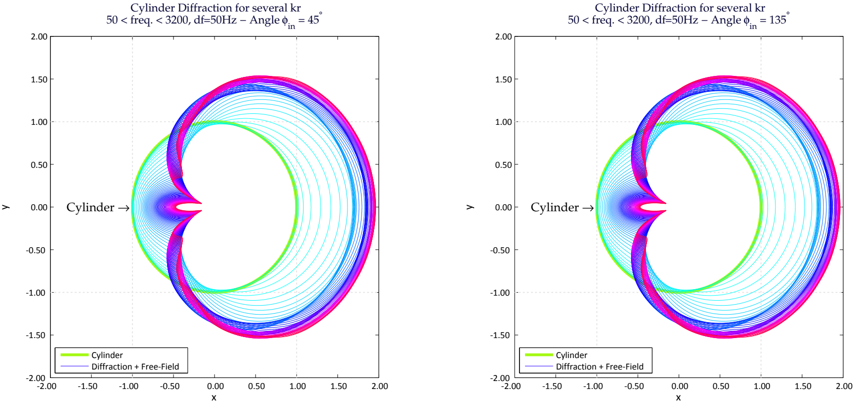

(a) $\phi_{in} = 45^{\circ}$ (b) $\phi_{in} = 135^{\circ}$

Figure 4.10: Polar plots of acoustic pressure on the cylinder for supplementary ϕ_{in} angles.

4.3.1 Beamforming processing

In the beamforming processing the concepts described in the Section 3.3 are applied. Thus, the following graphs are plotted and evaluated

(a) PSF;

(b) Frequency vs. Beampattern (FvB);

(c) Dynamic Range (DR);

(d) Beamwidth (BW).

The analysis shown in this section comprises the EAA and the array out of GA.

The PSF plots are plotted in a square area (as usual), and for this reason some spots seems to be stretched. In fact, this is a side effect of plotting dimensions of different lengths. This can be verified by comparing Figures 4.11 and 4.12 with their equivalent Figures 4.17 (b) and 4.29 (b). It is also important to explain that all the PSF and FvB figures are plotted relatively to the maximum value, and for simplicity $1 \sim 94$ dB (ref. 20 µPa).

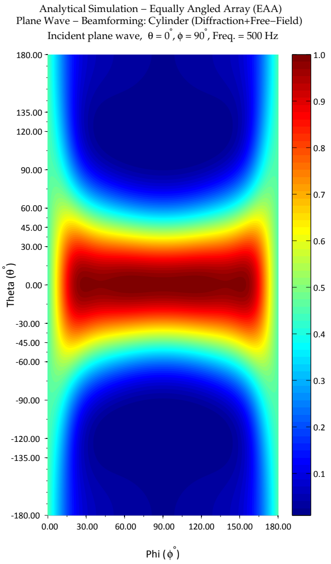

Figure 4.11: EAA: 360 x 180 angles.

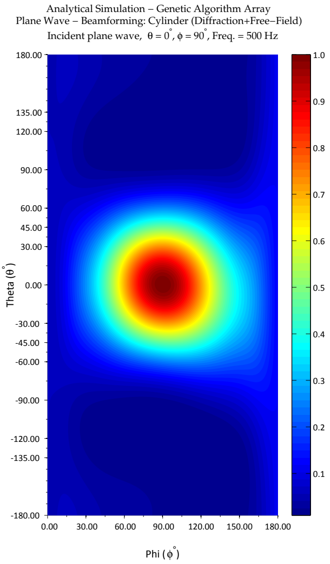

Figure 4.12: GA: 360 x 180 angles.

4.3.1.1 EAA

To represent the EAA response many angles and frequencies were simulated, with a few of them presented in this section. Figure 4.13 depicts the EAA's PSF for three angles of ϕ_{in}, it is possible to notice that there is a mirror source. This occurs because the EAA perceives the source and the mirror with the same phase, i.e., the array cannot distinguish between a source and its mirror, and both will be "detected". Considering Equation (4.29), if the incident wave is at $\phi = \phi_0$, then the reflected wave is at $\phi = \pi/2 - \phi_0$. Consequently, since $\sin(\phi_0) = \sin(\pi/2 - \phi_0)$, the expression between brackets is equal. The expression outside the brackets, $\exp(jkz\cos(\phi))$, is constant for the EAA (z is constant), and therefore has no influence on the beamforming process. That is, not even increasing the number of mics to 1000 would vanish the mirror lobe.

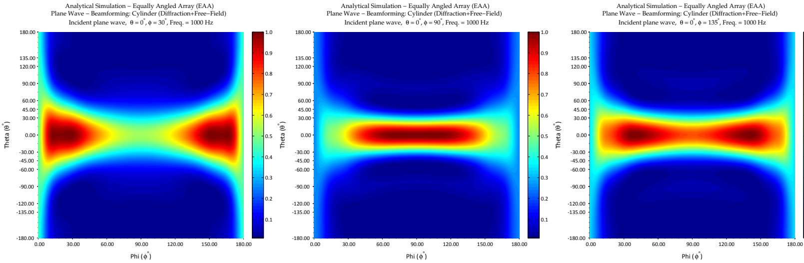

(a) $\phi_{in} = 30^\circ$ (b) $\phi_{in} = 90^\circ$ (c) $\phi_{in} = 135^\circ$

Figure 4.13: PSFs for different angles and frequency of 1 kHz.

Other authors such Parthy *et al.* [103], Tiana-Roig *et al.* [89], and Teutsch & Kellermann [87] also have studied the application of cylindrical arrays with beamforming. Nevertheless, in their applications, they only consider normal incidence. Therefore, they don't observe the lobe replica shown here.

The consequence of the mainlobe replica is that there is no DR - since the lobes have the same energy - and the BW loses meaning. Even for $\phi_{in} = 90^\circ$, at first there seems to be one lobe, but in truth it is a "joined lobe". Thus, with the considered post-processing, the EAA would be safely used for just the half of ϕ-axis. To extend its use, the signals could be processed with weighting factors, and/or also a change of microphone positions[11] should be considered.

In order to continue the EAA study some restrictions are made:

a. the BW estimation is carried out just along half of the ϕ-axis;

b. and for $\phi_{in} = 90^\circ$ the analysis is carried out as if it were just one lobe.

Considering these aspects, the processing is carried out and the plots are shown in Figures 4.14, 4.15, 4.16, and 4.17. Evaluation of $\phi_{in} = 70^\circ$ was not possible since the lobes start to "stick" to each other as the ϕ_{in} gets closer to 90°- this is shown in Figure 4.14 (b). Also, the DR cannot be calculated for half of the ϕ-axis because without sidelobes the result would be infinite, as in Figure 4.14.

---

[11] The strategy proposed to solve this issue is the GA array. Its plots are shown in the next section and its modelling can be consulted in Section 5.3.

Since the BW curves are similar to a log curve, it is convenient to plot both axes in log scale[12] to get a better view of the differences between the free-field and the diffraction plus the free-field. Figure 4.15 depicts the BW for the angles of $\phi_{in} = 30°$, $90°$ and $135°$. The black line (around the mainlobe) present in the PSF and FvB figures represents the 3 dB down in which BW is usually estimated. For the EAA it is hard to understand the BW plots if no other information is given. However, with the help of the FvB (Figure 4.16) and PSF (Figure 4.17) plots, the behaviour can be better inferred.

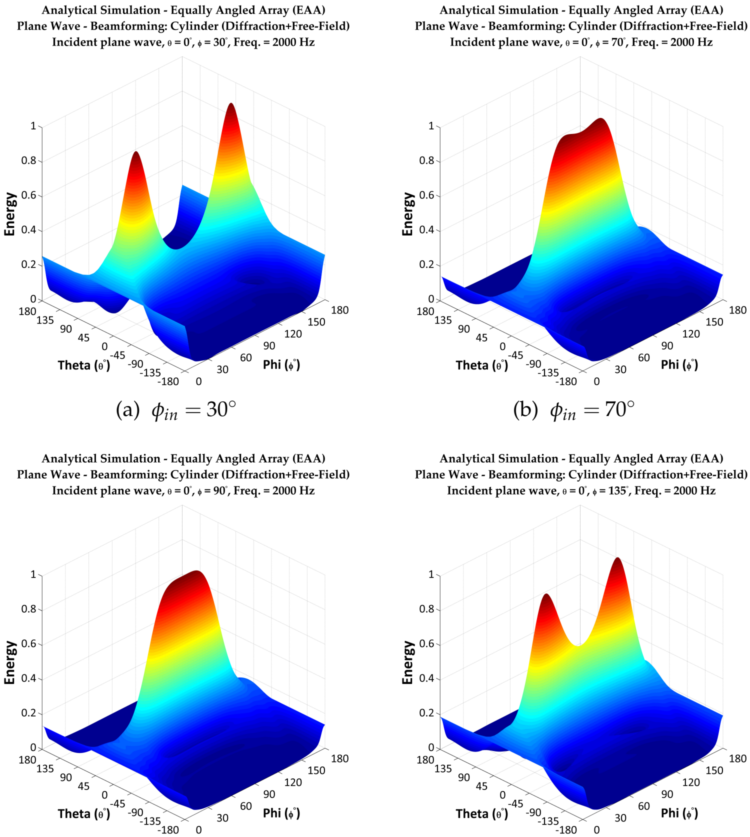

(a) $\phi_{in} = 30°$ (b) $\phi_{in} = 70°$

(c) $\phi_{in} = 90°$ (d) $\phi_{in} = 135°$

Figure 4.14: PSF 3D plots of the EAA for $\phi_{in} = 30°, 70°, 90°$ and $135°$, frequency of 2 kHz.

---

[12] The linear plots can be consulted in Appendix F.1

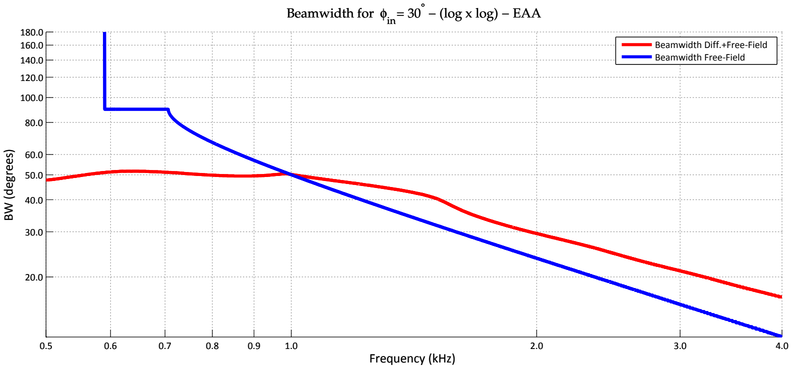

(a) $\phi_{in} = 30°$, log x log

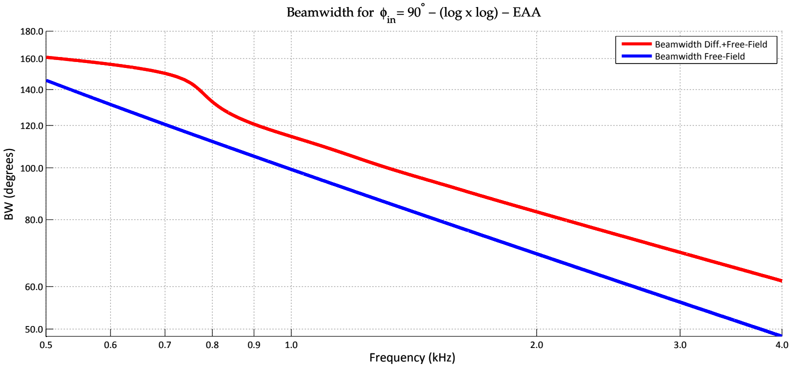

(b) $\phi_{in} = 90°$, log x log

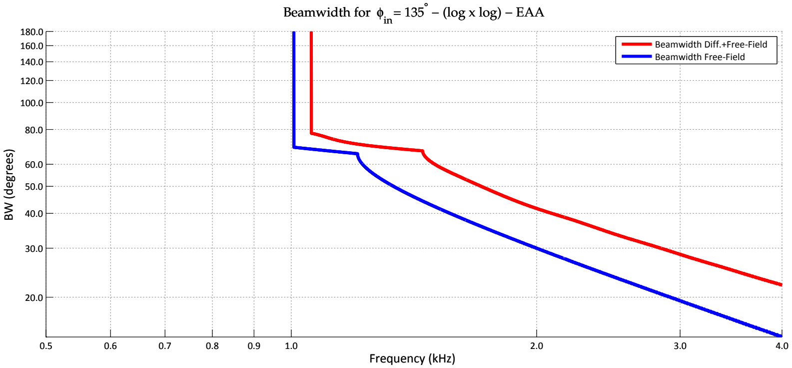

(c) $\phi_{in} = 135°$, log x log

Figure 4.15: BW plots of the EAA for $\phi_{in} = 30°, 90°$ and $135°$ (log x log plots, half ϕ-axis, FvB extraction).

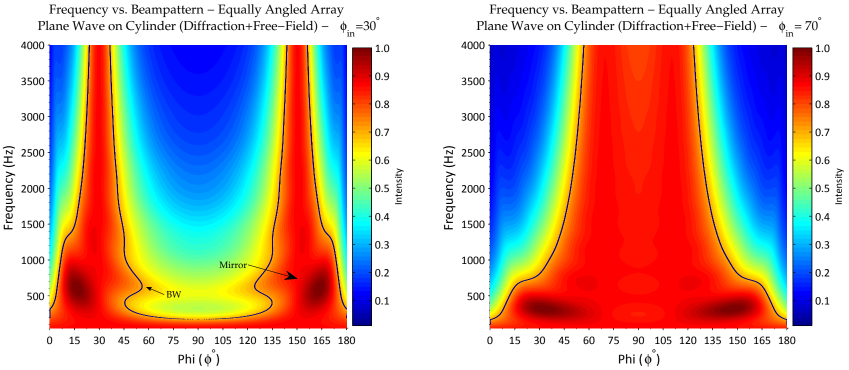

(a) D+FF, $\phi_{in} = 30°$ (b) D+FF, $\phi_{in} = 70°$

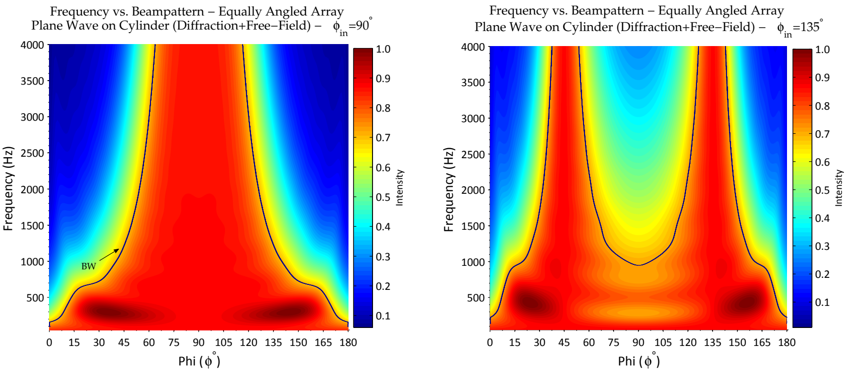

(c) D+FF, $\phi_{in} = 90°$ (d) D+FF, $\phi_{in} = 135°$

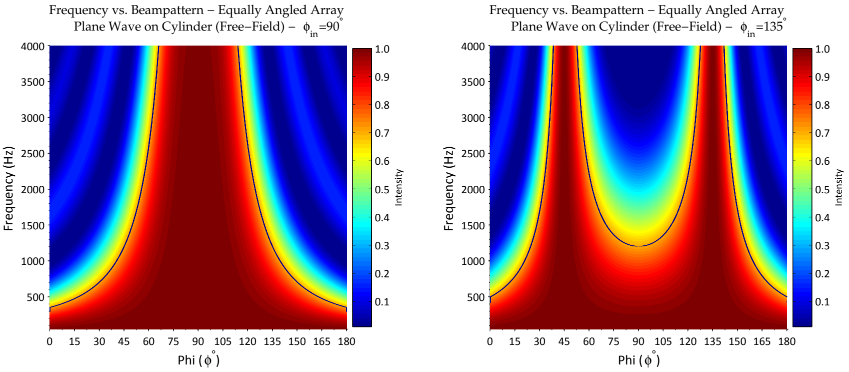

(e) Free-Field, $\phi_{in} = 90°$ (f) Free-Field, $\phi_{in} = 135°$

Figure 4.16: FvB plots of the EAA for $\phi_{in} = 30°, 70°, 90°$ and $135°$; 4 kHz> freq. >50 Hz (BW detail in black line).

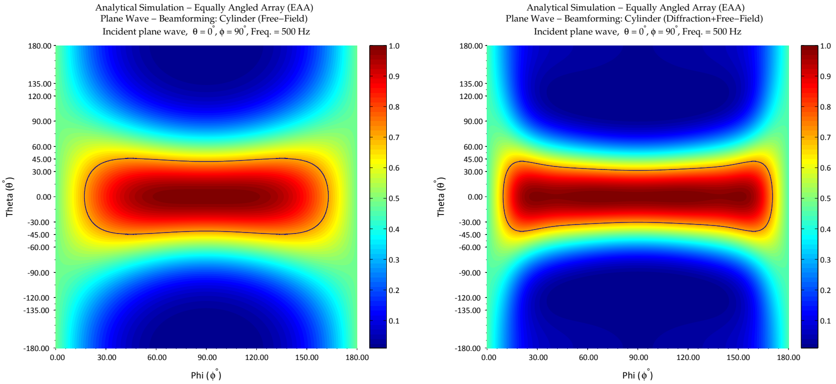

(a) Free-Field, $\phi_{in} = 90^\circ$, 500 Hz (b) Diffraction+FF, $\phi_{in} = 90^\circ$, 500 Hz

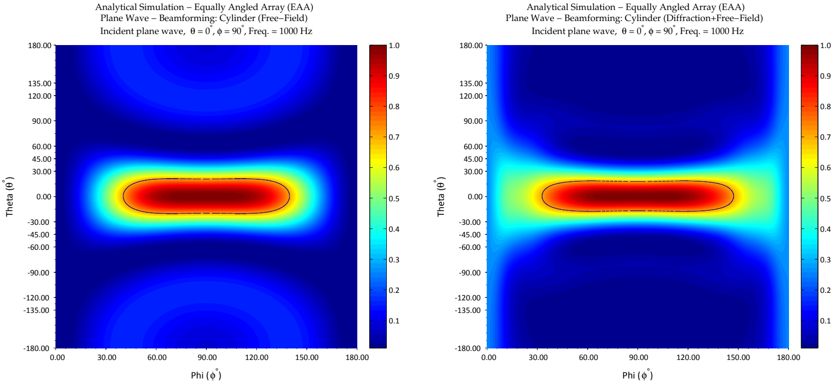

(c) Free-Field, $\phi_{in} = 90^\circ$, 1000 Hz (d) Diffraction+FF, $\phi_{in} = 90^\circ$, 1000 Hz

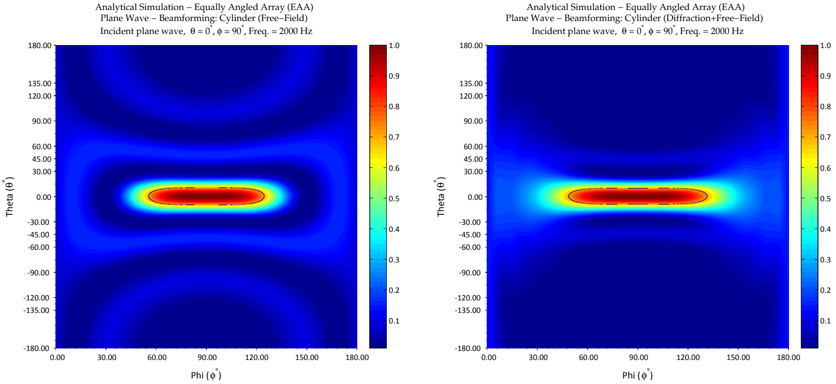

(e) Free-Field, $\phi_{in} = 90^\circ$, 2000 Hz (f) Diffraction+FF, $\phi_{in} = 90^\circ$, 2000 Hz

Figure 4.17: PSF plots of the EAA for $\phi_{in} = 90^\circ$ and frequencies of 500, 1 k and 2 k Hz (BW detail in black line).

In Figure 4.16 (a) there is the indication of the BW line (plotted also for the mirror) as well as the indication of the mirror source position. The analysis of Figure 4.16 demonstrates that the mirror effect is inherent to free-field response and the addition of the diffraction field only modifies it. In addition, for the plotted frequencies, it can be seen that diffraction has decreased the sidelobes, per Figures 4.16 and 4.17.

As previously commented, for lower frequencies the cylinder tends to be acoustically transparent. This is evidenced by observing Figure 4.16 for frequencies up to 1 kHz, where the shape of the mainlobe is clearly distinct to the trend of the other frequencies. In Figure 4.18, this is explicitly shown:

1. for 800 Hz the localization is completely wrong in the ϕ-axis but correct in θ-axis, Figures 4.18 (a) and 4.18 (d);

2. for frequencies near 1 kHz ($kr = 2,30$) there is a transition region where "two peaks" are found, Figures 4.18 (b) and 4.18 (e);

3. for higher frequencies the source direction is perfectly recovered, Figures 4.18 (c) and 4.18 (f).

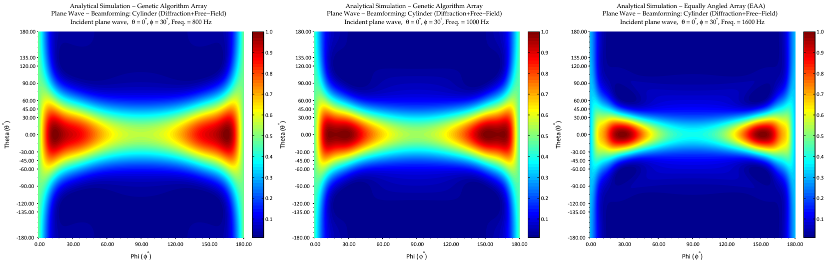

(a) $\phi_{in} = 30°$, f= 800 Hz (b) $\phi_{in} = 30°$, f= 1000 Hz (c) $\phi_{in} = 30°$, f= 1600 Hz

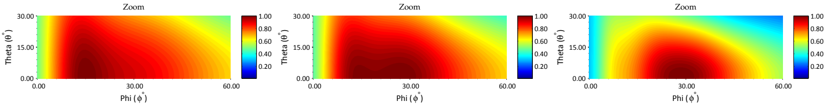

(d) $\phi_{in} = 30°$, f= 800 Hz (e) $\phi_{in} = 30°$, f= 1000 Hz (f) $\phi_{in} = 30°$, f= 1600 Hz

Figure 4.18: PSFs for $\phi_{in} = 30°$ showing the transition of source localisation considering the addition of the diffraction field.

4.3.1.2 GA Array

The GA array simulations shown in this section are the fruit of the geometry found by the modelling discussed in Section 5.4.2. Similar to the EAA, a series of simulations were carried out and just a part of them is presented here. The array used here does not have a mirror lobe, see Figure 4.19 in contrast to Figure 4.14, hence no special care is needed for the analysis.

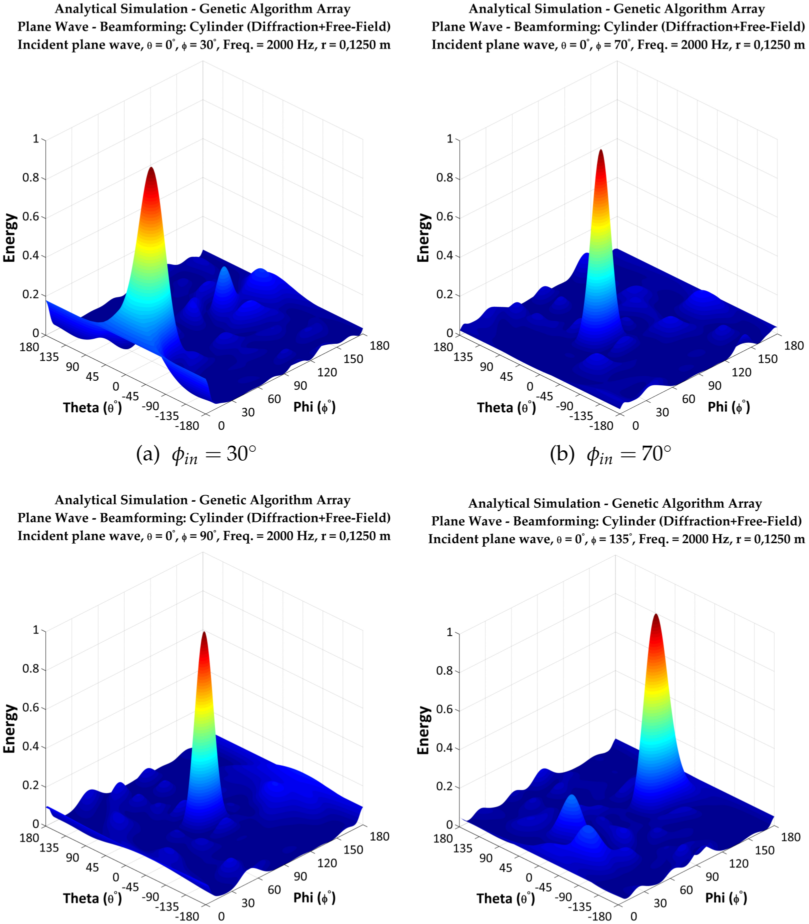

Analytical Simulation - Genetic Algorithm Array
Plane Wave - Beamforming: Cylinder (Diffraction+Free-Field)
Incident plane wave, θ = 0°, ϕ = 30°, Freq. = 2000 Hz, r = 0,1250 m

Analytical Simulation - Genetic Algorithm Array
Plane Wave - Beamforming: Cylinder (Diffraction+Free-Field)
Incident plane wave, θ = 0°, ϕ = 70°, Freq. = 2000 Hz, r = 0,1250 m

Analytical Simulation - Genetic Algorithm Array
Plane Wave - Beamforming: Cylinder (Diffraction+Free-Field)
Incident plane wave, θ = 0°, ϕ = 90°, Freq. = 2000 Hz, r = 0,1250 m

Analytical Simulation - Genetic Algorithm Array
Plane Wave - Beamforming: Cylinder (Diffraction+Free-Field)
Incident plane wave, θ = 0°, ϕ = 135°, Freq. = 2000 Hz, r = 0,1250 m

(a) $\phi_{in} = 30°$

(b) $\phi_{in} = 70°$

(c) $\phi_{in} = 90°$

(d) $\phi_{in} = 135°$

Figure 4.19: PSF 3D plots of the GA array for $\phi_{in} = 30°, 70°, 90°$, and $135°$, frequency of 2 kHz.

The BW plots[13] for $\phi_{in} = 30^\circ$, 70°, 90° and 135° are depicted in Figure 4.20. Now, it is possible to better evaluate the modifications imposed by the inclusion of diffraction over the free-field. By analysing sub-plots of Figure 4.20 it is possible to observe that the BW is frequency-ϕ-dependant; with the addition of the diffraction the changes in the BW ranges from a slight improvement for $\phi_{in} = 90^\circ$ to a worsening for $\phi_{in} = 30^\circ$.

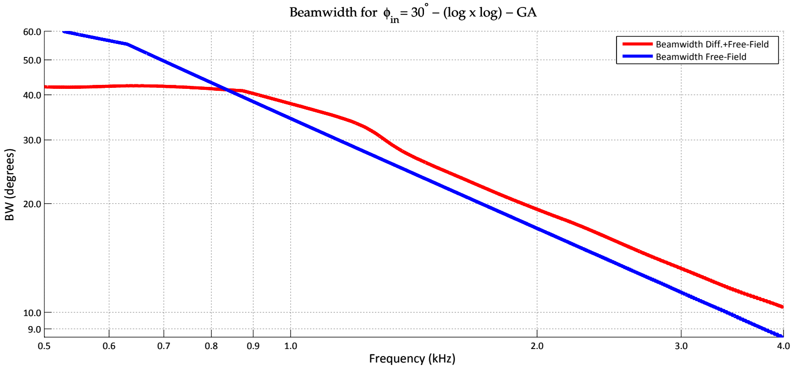

(a) $\phi_{in} = 30^\circ$, log x log

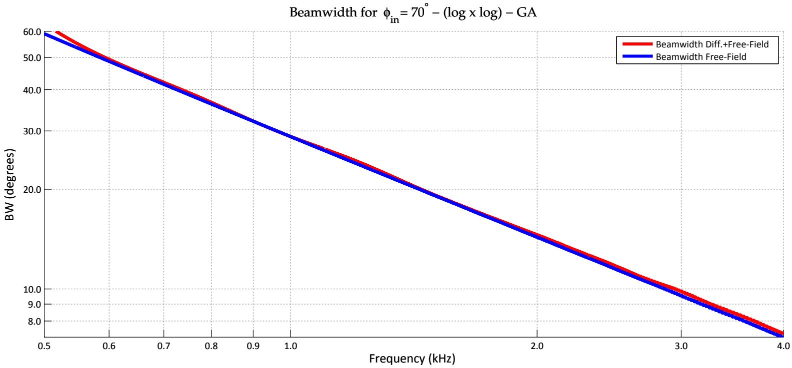

(b) $\phi_{in} = 70^\circ$, log x log

Figure 4.20: BW plots of the GA array for $\phi_{in} = 30^\circ$ and $\phi_{in} = 70^\circ$ (log x log plots, FvB extraction).

---

[13] The linear plots can be consulted in Appendix F.1

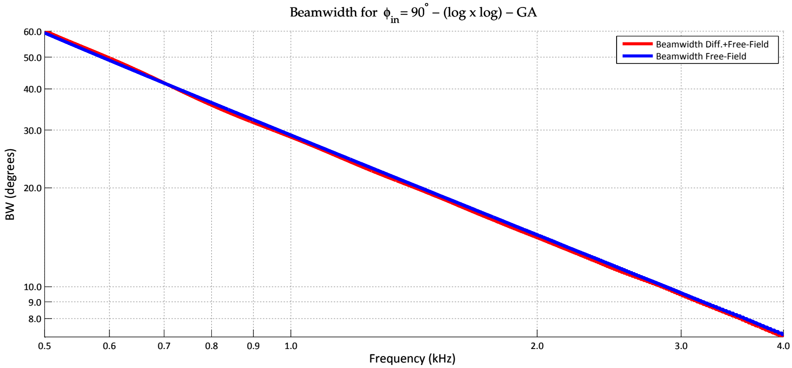

(c) $\phi_{in} = 90°$, log x log

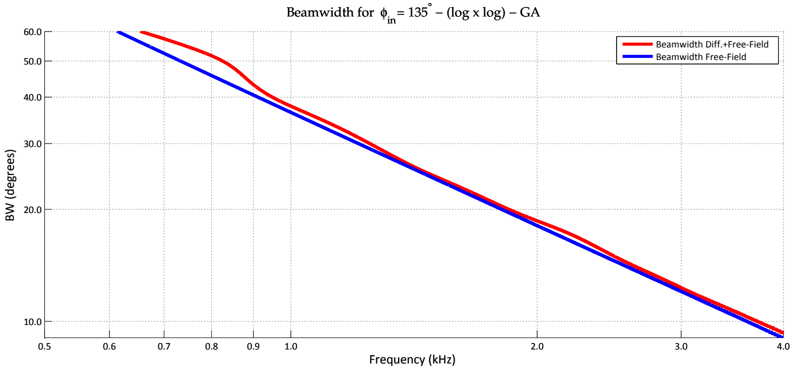

(d) $\phi_{in} = 135°$, log x log

Figure 4.20: BW plots of the GA array for 90° and 135° (log x log plots, FvB extraction).

The narrower the mainlobe the better is the separation of waves coming from closely spaced directions. Additionally, if the array does not have the microphone positions distributed so the PSF response has a uniform omnidirectional pattern, the BW will have different sizes along the $\theta\phi$-plane. The Figure 4.21 demonstrates the BW response extracted from the PSF[14], consider the ϕ-axis (in green) and the θ-axis (in orange). As can be seen even with the efforts to keep the mainlobe symmetrical[15], the BW is different. For example, in Figure 4.21, for 1 kHz,

---

[14] Figures 4.15, 4.20 and 4.24 were extracted from the Frequency *vs.* Beampattern plot (FvB).

[15] This is explained in Section 5.3.1.2, page 171.

BW(ϕ-axis) ≈ 28,62° and BW(θ-axis) ≈ 34,94°- see also Figure 4.21 (b). If one dimension (say ϕ-axis) of the mainlobe is enough to characterize a given array or problem, the extraction of BW through the PSF is basically the same as the beampattern extraction - yielding the same results.

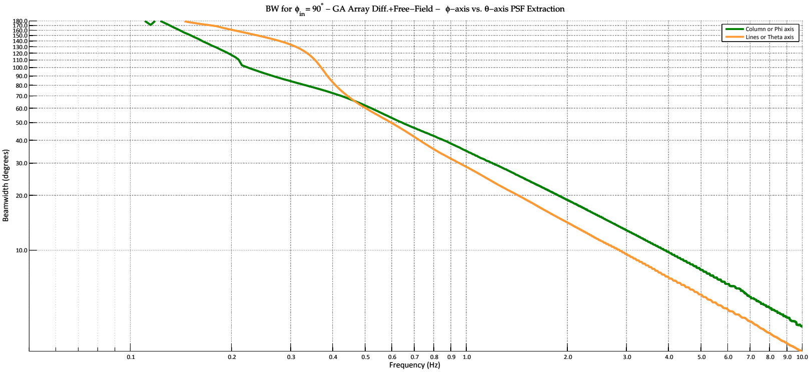

(a) BW PSF extraction: {Column or Phi} vs. {Row or Theta}, 50 Hz - 10 kHz

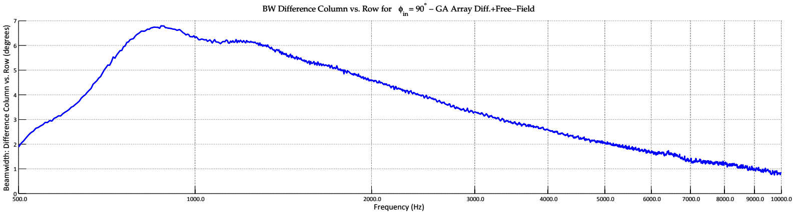

(b) Difference (Column - Row), 500 Hz - 10 kHz

Figure 4.21: Beamwidth (BW) for PSF extraction in ϕ-axis (in green) and the θ-axis (in orange) - GA array.

The DR plots of the GA array are depicted from Figure 4.22 to 4.26, the lines in blue are the DR for just the free-field and the lines in red represent the diffraction plus free-field. The dashed lines represent mean values for a certain frequency range (or kr range). For example, in most DR plots the mean is taken from 500 Hz up to 4 kHz. In some plots below 500 Hz the lines go to the infinite; in such cases the mainlobe is so wide that the DR cannot be calculated due to the absence of sidelobes.

For the DR there are also differences if the extraction is made through the PSF or the FvB. Figure 4.22 (a) depicts the same case with both methods of extraction. As expected, in the beampattern extraction the results seems to be better than the PSF extraction, which happens because the PSF extraction considers all the visible area, computing sidelobes over all the $\theta\phi$-plane and not just for one row (or column) of one axis. Therefore, this is an important point of concern because one of these estimations can lead to results that mask the reality.

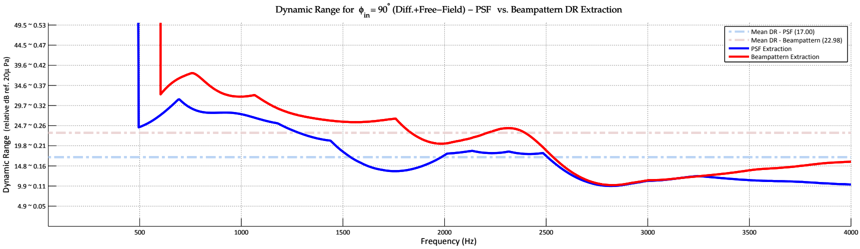

(a) FvB vs. PSF estimation, Diff.+Free-Field, 50 Hz < freq. < 4 kHz, $\phi_{in} = 90°$

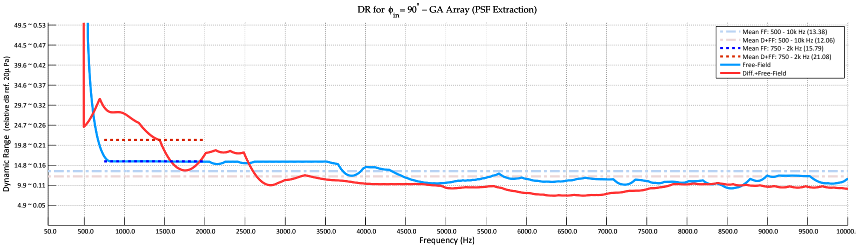

(b) PSF estimation, Free-field and Diff.+Free-Field, 50 Hz < freq. < 10 kHz, $\phi_{in} = 90°$

Figure 4.22: DR (GA array) difference between FvB and PSF estimation; and extension of the frequency range.

Evaluating the relative mean values in the frequency range of 750 Hz to 2 kHz (or $1{,}7 \lessapprox kr \lessapprox 4{,}6$), it is possible to quickly estimate the improvement brought by the diffraction field in this range, see Table 4.1 and the dotted lines in Figure 4.22 (b) (this can also be noticed by inspecting the sidelobes in the PSFs of Figure 4.29).

Figure 4.23 shows the DRs with PSF extraction and Figure 4.24 shows the same results for the beampattern extraction. Comparing these two, it is clear that Figure 4.24 gives the wrong impression since in almost all frequencies the diffraction field is the worst case. In Figure 4.23 it can be noticed that the diffraction field has most improved the DR in frequencies ranging from 500 Hz to 2,5 kHz (for the exposed angles). Thus, it demonstrates that the improvement is dependent upon ϕ and frequency.

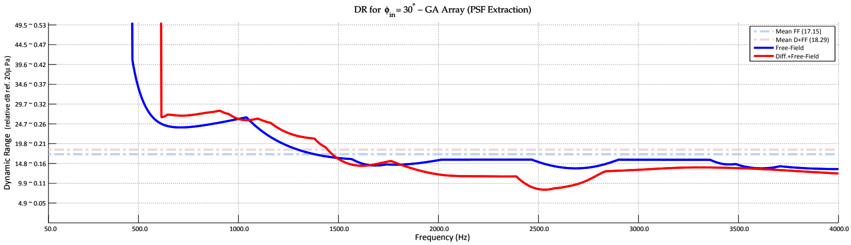

(a) $\phi_{in} = 30°$

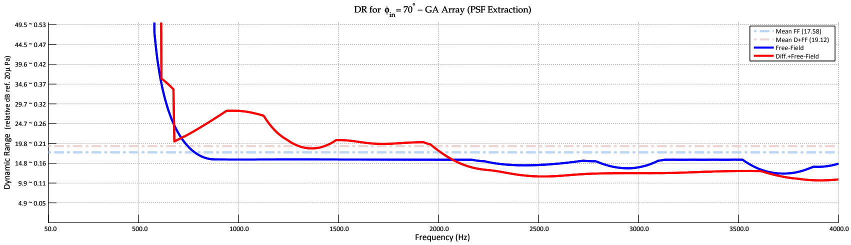

(b) $\phi_{in} = 70°$

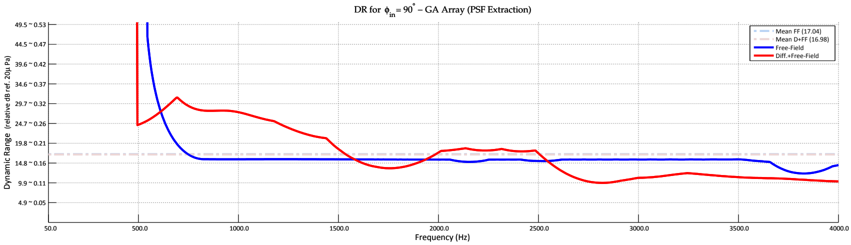

(c) $\phi_{in} = 90°$

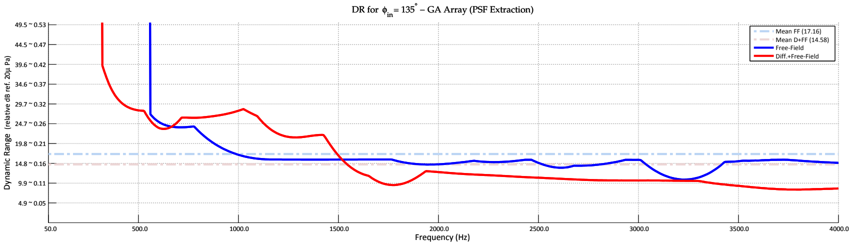

(d) $\phi_{in} = 135°$

Figure 4.23: DR plots of the GA array for $\phi_{in} = 30°, 70°, 90°$ and $135°$ (PSF extraction).

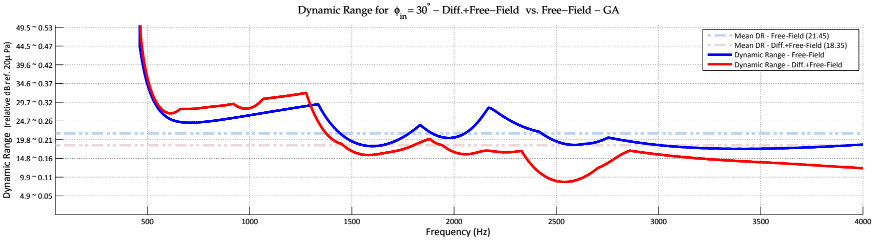

(a) $\phi_{in} = 30°$

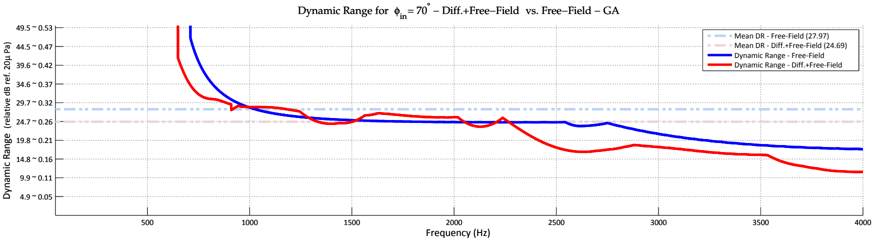

(b) $\phi_{in} = 70°$

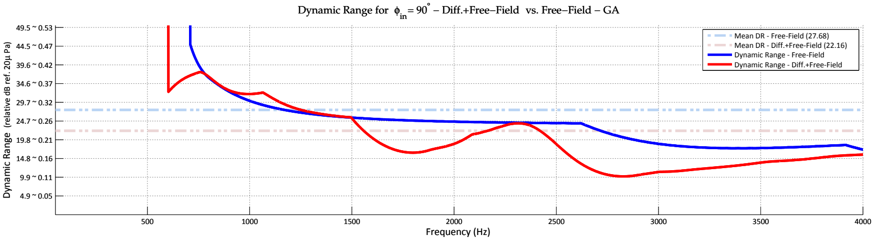

(c) $\phi_{in} = 90°$

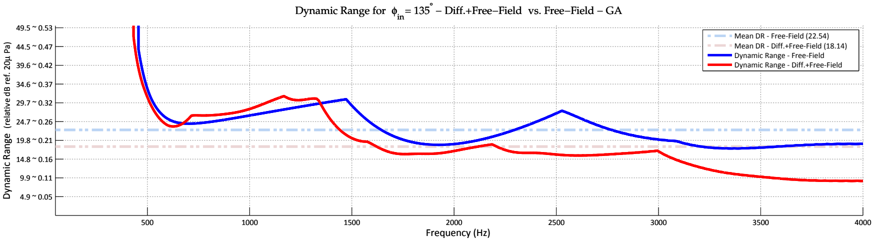

(d) $\phi_{in} = 135°$

Figure 4.24: DR plots of the GA array for $\phi_{in} = 30°, 70°, 90°$ and $135°$ (FvB extraction).

Table 4.1: GA array, DR mean (dB) for frequencies
750 Hz - 2 kHz (PSF extraction).

Type \ Angle	**30°**	**70°**	**90°**	**135°**
Free-Field	19,00 dB	15,89 dB	15,79 dB	16,58 dB
Diff.+Free-Field	20,12 dB	21,99 dB	21,08 dB	19,21 dB
Difference	1,12 dB	6,11 dB	5,29 dB	2,63 dB

On account of the discussed data until this point, new simulations were carried out changing[16] the cylinder radius, but keeping the angle and height of the microphone positions over it. Figure 4.25 depicts the experiment, with each sub-plot containing four pairs of data:

a. the full lines represent the conditions with and without the diffraction;

b. the dotted lines represent the mean for $1,7 \lessapprox kr \lessapprox 4,6$;

c. the dash-dotted lines represent the mean of the equivalent kr range considering $r = 0,1250$ m;

d. the dashed lines represent the mean of the total range, starting from the first measurable DR.

When the radius is doubled the frequency response is inversely proportionally "compressed", an effect consistent with Equation (2.21). This is confirmed by examining items "b" and "c" from the above list in Figures 4.25, 4.26 and 4.27. That is, if the kr relationship is maintained, the discussions made for the $r = 0,1250$ m can be extended to any sized cylinder. Figure 4.26 demonstrates that in kr domain the curves are perfectly superposed. In Table 4.2 it is possible to see that the values are approximately constant for cases "b" and "c".

The DR mean of the total range ("d" case) is degraded as the radius grows, because the effects of shadow start to emerge. For example, in Figure 4.25 (d), at 3,5 kHz the DR(D+F)$\approx$0 dB while DR(F)$\approx$8,4 dB. For the record, compare Figure 4.25 with the polar plots of Figure 4.5, and see that data in the last row of Table 4.2 express the same case and are in accordance.

---

[16] The geometry used was originally optimised for $r = 0,1250$ m and 1 kHz.

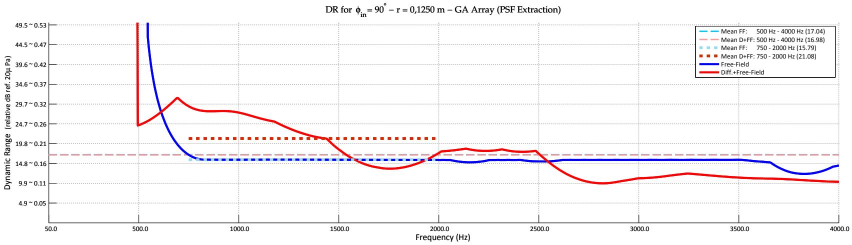

(a) $r = 0{,}1250$ m, $\phi_{in} = 90^\circ$

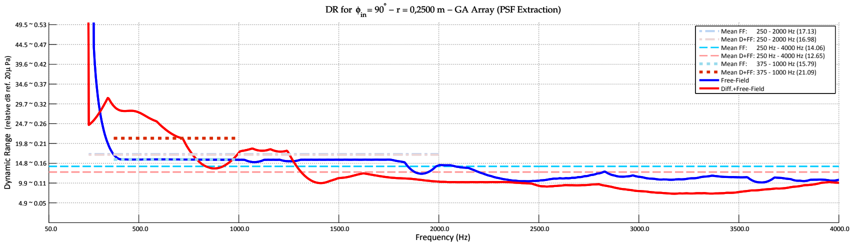

(b) $r = 0{,}2500$ m, $\phi_{in} = 90^\circ$

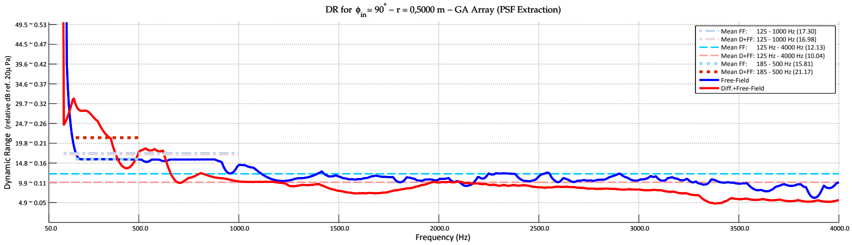

(c) $r = 0{,}5000$ m, $\phi_{in} = 90^\circ$

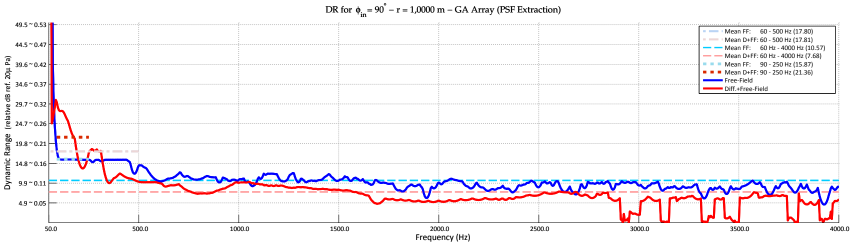

(d) $r = 1{,}0000$ m, $\phi_{in} = 90^\circ$

Figure 4.25: DR plots of the GA array for $\phi_{in} = 90^\circ$ and different radii (PSF extraction).

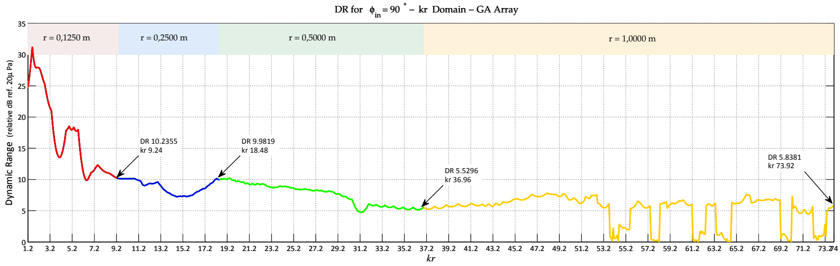

Figure 4.26: Plots for all radii in *kr* domain (DR).

Table 4.2: GA array, DR gain, equivalent and total for $1{,}7 \lessapprox kr \lessapprox 4{,}6$, $\phi_{in} = 90°$ and different radii (PSF extraction).

kr \ **radius**	**0,1250 m**	**0,2500 m**	**0,5000 m**	**1,0000 m**
"b" Case	**Gain for $1{,}7 \lessapprox kr \lessapprox 4{,}6$**			
1,73	750 Hz	375 Hz	185 Hz	90 Hz
4,61	2000 Hz	1000 Hz	500 Hz	250 Hz
Constant for all radii ≈ **5,36 dB**				
"c" Case	**Equivalent freq. ∼ kr range**			
1,15	500 Hz	250 Hz	125 Hz	60 Hz
9,23	4000 Hz	2000 Hz	1000 Hz	500 Hz
Constant for all radii ≈ **17 ±0,25 dB**				
"d" Case	**Total: Diffraction - Free-Field**			
500/250/125/60 Hz ⇒ 4 kHz	-0,1 dB	-1,4 dB	-2,1 dB	-2,9 dB

The Figure 4.27 depicts:

a. the PSFs for different radii at 1 kHz, confirming the behaviour shown in Figure 4.26;

b. Figure 4.27 (a) and Figure 4.27 (e) which demonstrate that for the same $kr = 2{,}3$ the PSFs are equal; and

c. the FvB for the widest radius $r = 1{,}0000$ m. It is possible compare the differences with $r = 0{,}1250$ m by viewing the FvB plot in Figure 4.28 (c).

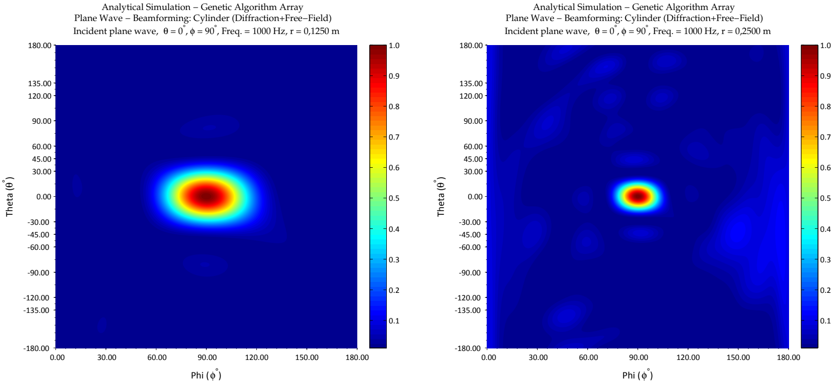

(a) r = 0,1250 m; 1 kHz (b) r = 0,2500 m; 1 kHz

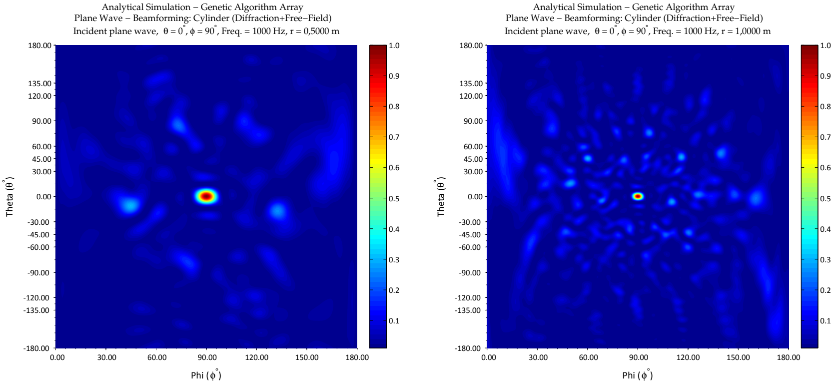

(c) r = 0,5000 m; 1 kHz (d) r = 1,0000 m; 1 kHz

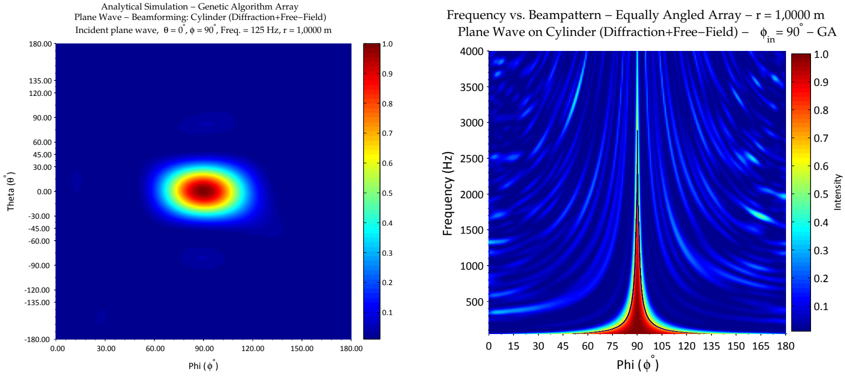

(e) r = 1,0000 m; 125 Hz (f) FvB, r = 1 m, 50 Hz - 4 kHz

Figure 4.27: PSF plots of the GA array for $\phi_{in} = 90^\circ$ at 1 kHz and several radii; and FvB for 50 Hz - 4 kHz.

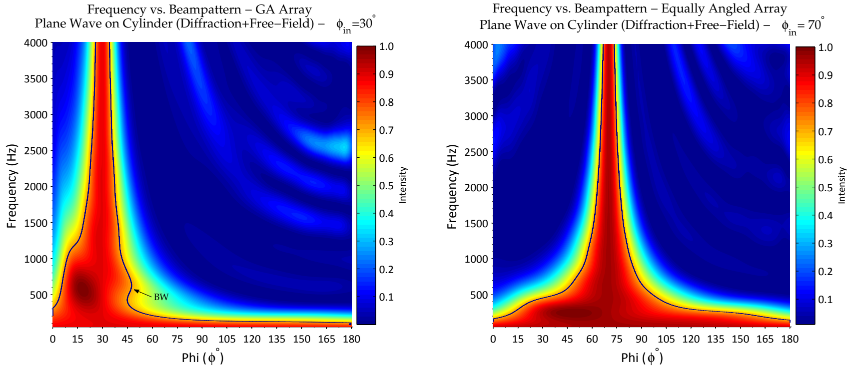

(a) $\phi_{in} = 30°$ (b) $\phi_{in} = 70°$

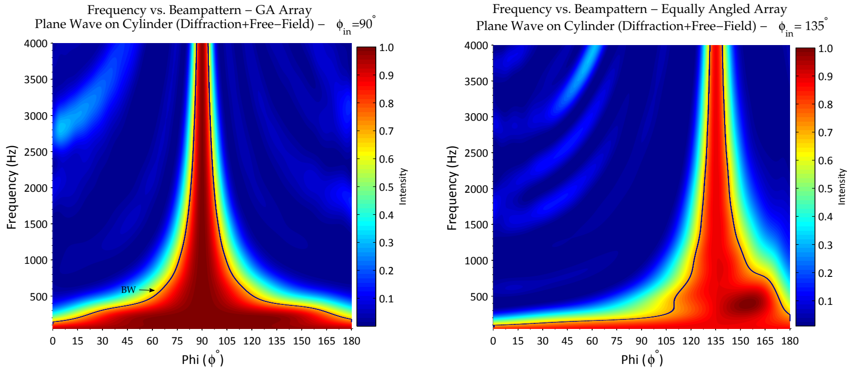

(c) $\phi_{in} = 90°$ (d) $\phi_{in} = 135°$

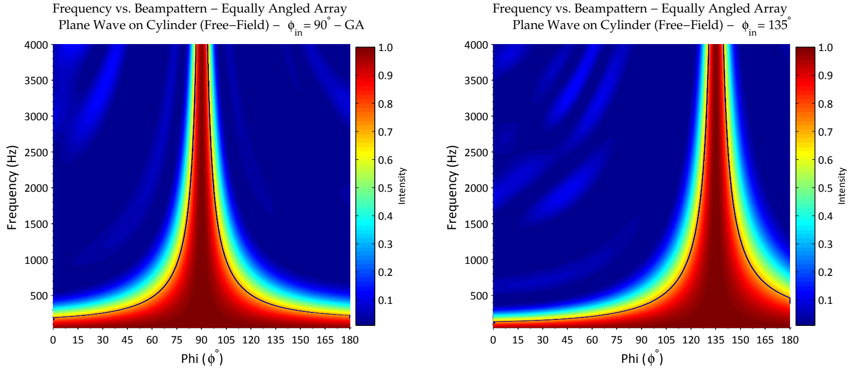

(e) Free-Field, $\phi_{in} = 90°$ (f) Free-Field, $\phi_{in} = 135°$

Figure 4.28: FvB plots of the GA for $\phi_{in} = 30°, 70°, 90°$ and $135°$; 4 kHz> freq. >50 Hz (BW detail in black line).

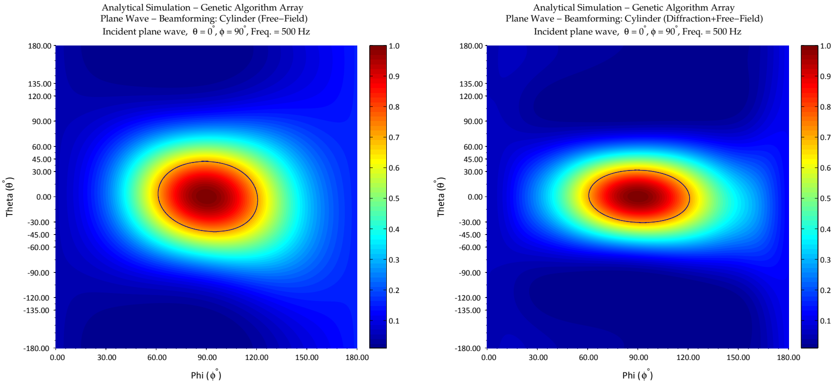

(a) Free-Field, $\phi_{in} = 90^\circ$, 500 Hz

(b) Diffraction, $\phi_{in} = 90^\circ$, 500 Hz

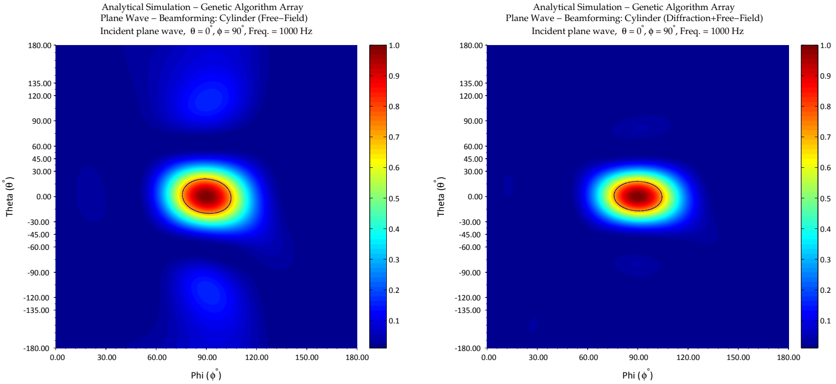

(c) Free-Field, $\phi_{in} = 90^\circ$, 1000 Hz

(d) Diffraction, $\phi_{in} = 90^\circ$, 1000 Hz

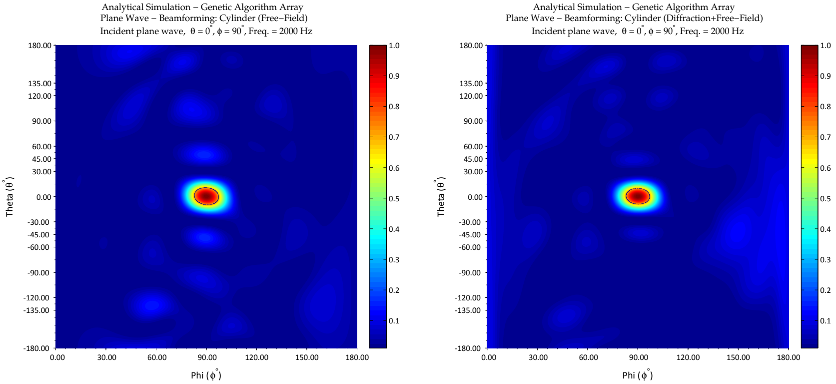

(e) Free-Field, $\phi_{in} = 90^\circ$, 2000 Hz

(f) Diffraction, $\phi_{in} = 90^\circ$, 2000 Hz

Figure 4.29: PSF plots of the GA for $\phi_{in} = 30^\circ, 70^\circ, 90^\circ$ and 135°; 4 kHz$>$ freq. $>$50 Hz (BW detail in black line).

Similarly to that commented on the EAA, through Figure 4.28 one can notice that the curves assume a pattern just after frequencies around 1 kHz, confirming the diffraction effects described earlier in this document.

4.3.2 Considerations

In summary, the inclusion of the diffraction field brought two important aspects

a. DR improvement, enabling better source direction recovery;

b. the sound field is closer to reality since the acoustical free-field is only found in special environments.

To better estimate the contributions of diffraction it is convenient to plot surfaces relating ϕ_{in} and frequency to the performance descriptors DR and BW. After simulating a sweep in frequency, a ϕ_{in} sweep was performed to estimate the complete response along the ϕ-axis. The 2D results[17] for 1 kHz and 2 kHz are shown in Figure 4.31 and the 3D plots are depicted in Figures 4.32 and 4.33.

The "random" shape of the DR shown in the plots are the fruit of the GA optimization algorithm that has generated a controlled random geometry. In Figure 4.32 it is possible to see that the region in green in (b) is filled in with orange-red colours in (a), meaning that the DR has increased. Also, in (a) there two blue lines that express the inability to resolve source directions in those ranges (this effect is clear in Figures 4.31 (a) and (d)). For the BW, Figures 4.31 and 4.33, it is possible to see improvements for angles near to 90° and degradation for angles closer to the limits of the cylinder.

Although the θ-axis is not explicitly discussed, the random nature of the array guarantees that no grating lobes will appear. Figure 4.30 depicts two PSF plots for θ_{in} different than zero. The distortions present are intrinsic of the problem, i.e., geometry related. As the sources approach the limits of the *region of vision*, the PSFs will suffer similar aberrations as to what happens with photographic cameras.

To find a general expression for the gain regarding the geometry strategy and the frequency range of operation further simulations must be carried out to find an empirical model. Underbrink [76], for example,

---

[17] Other frequencies can be found in Appendix F.1, page 280.

stated that for random planar arrays a subtraction of 3 dB from the expression of Equation (3.66) is enough to better estimate the gain (of the array in relation to an unique microphone).

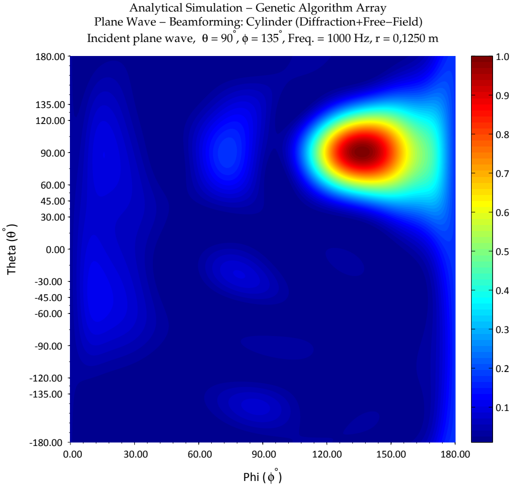

(a) Emitter: $\phi_{in} = 135°$, $\theta_{in} = 90°$

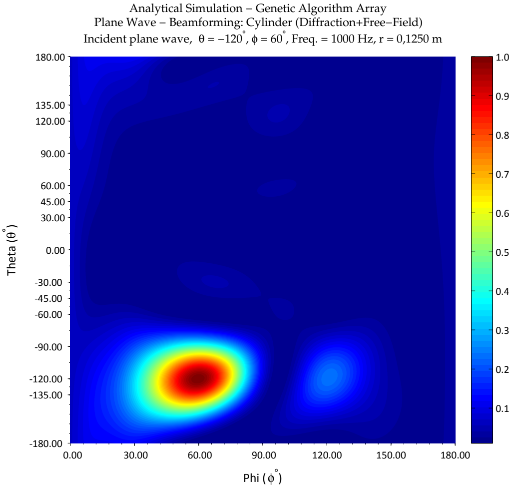

(b) Emitter: $\phi_{in} = 60°$, $\theta_{in} = -120°$

Figure 4.30: PSFs for θ_{in} different than zero.

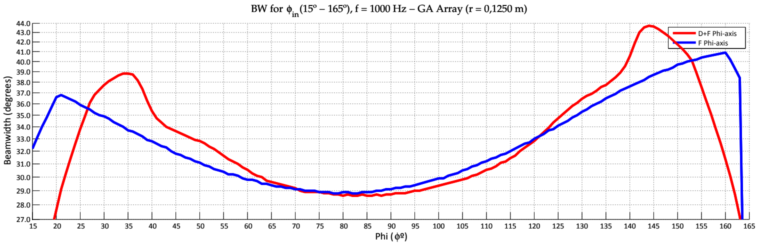

(a) BW, D+FF and FF, 1 kHz, ϕ_{in} sweep

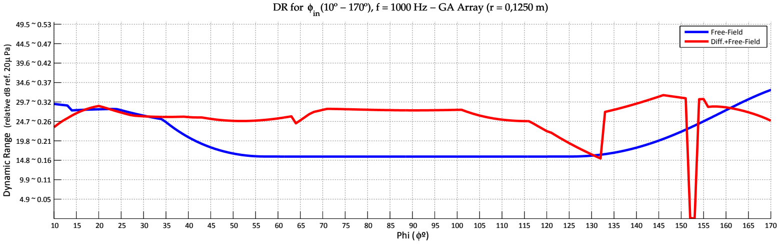

(b) DR, D+FF and FF, 1 kHz, ϕ_{in} sweep

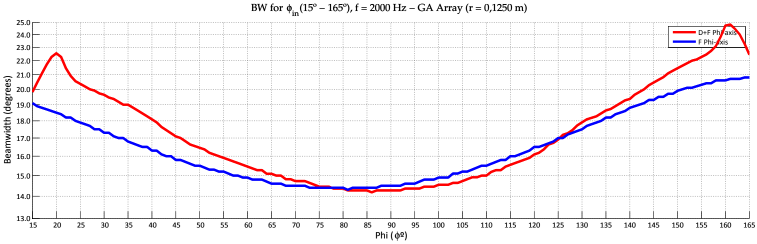

(c) BW, D+FF and FF, 2 kHz, ϕ_{in} sweep

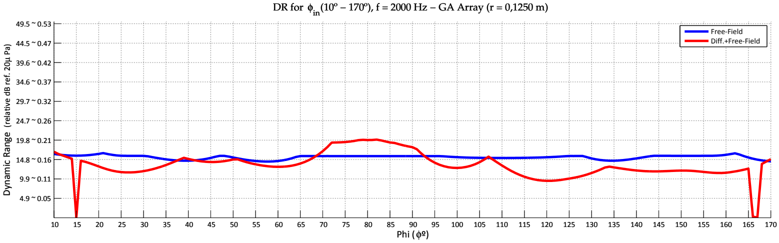

(d) DR, D+FF and FF, 2 kHz, ϕ_{in} sweep

Figure 4.31: BW and DR plots of the GA array for sweep in ϕ_{in} frequencies of 1 kHz and 2 kHz.

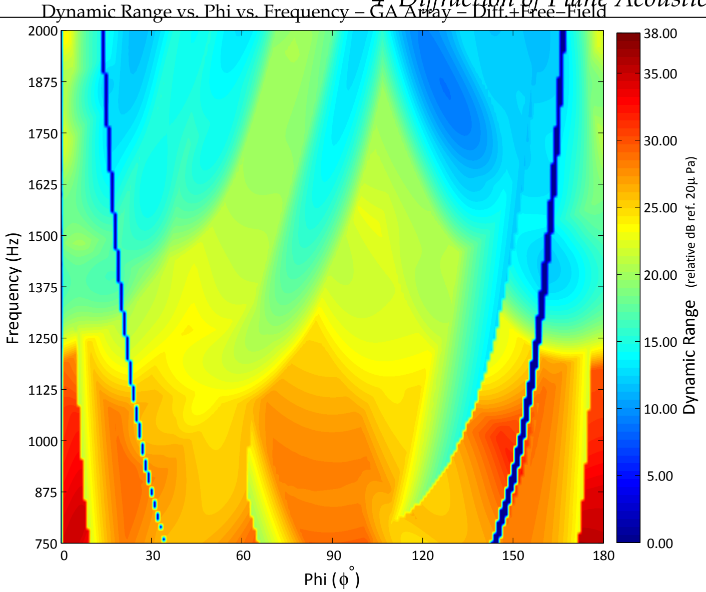

(a) Diffraction + Free-Field, ϕ_{in} vs. Freq. vs. DR

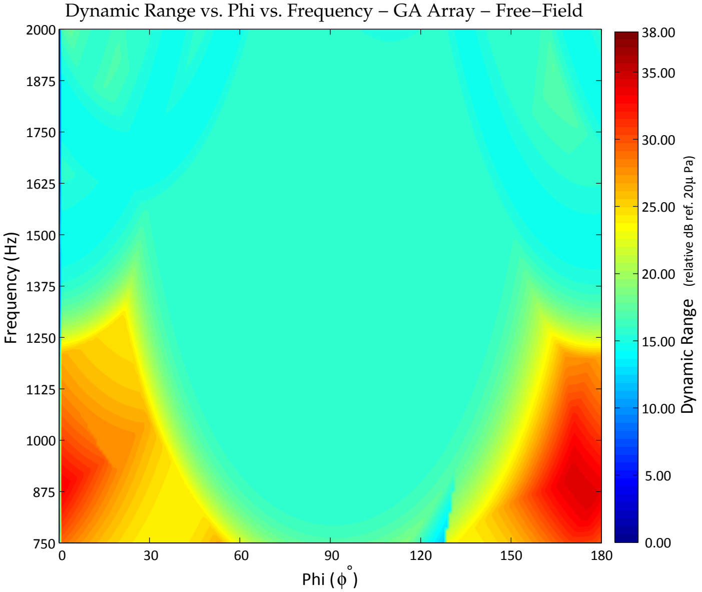

(b) Free-Field, ϕ_{in} vs. Freq. vs. DR

Figure 4.32: Dynamic range (DR), GA array, sweep in frequency (df=5 Hz) and in ϕ_{in} (dϕ=1°).

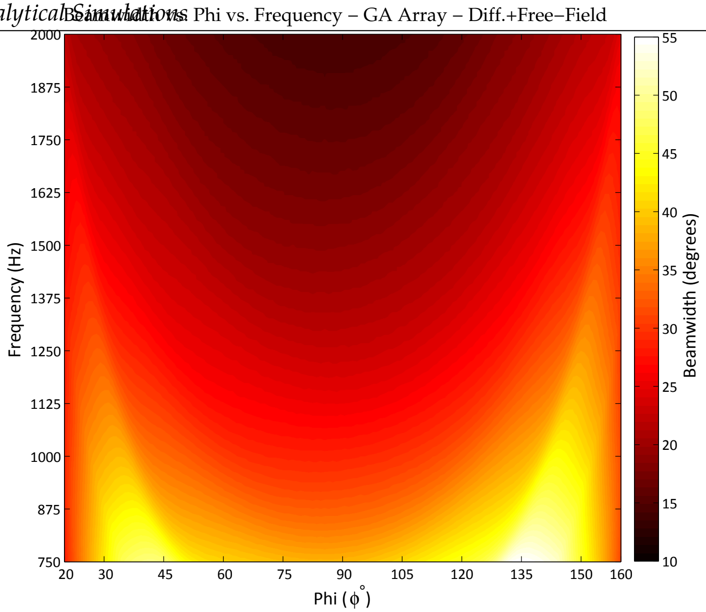

(a) Diffraction + Free-Field, ϕ_{in} vs. Freq. vs. BW

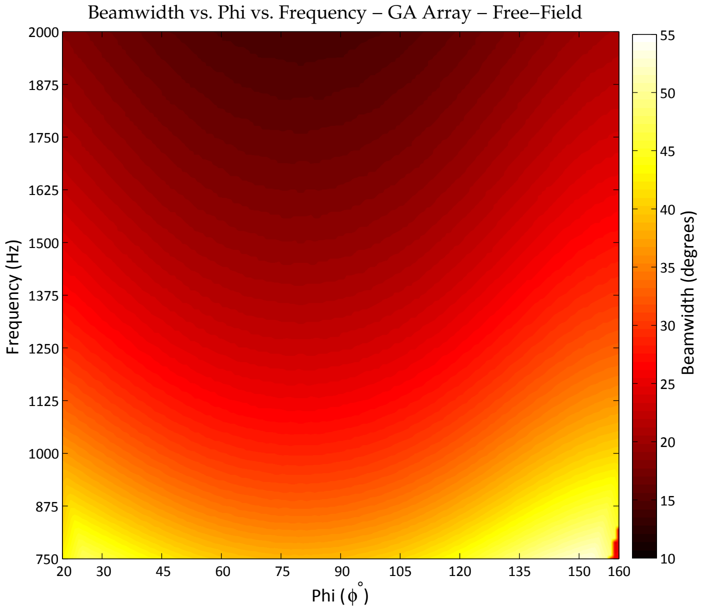

(b) Free-Field, ϕ_{in} vs. Freq. vs. BW

Figure 4.33: Beamwidth (BW), GA array, sweep in frequency (df=5 Hz) and in ϕ_{in} (dϕ=1°).

4.4 Measurements

A set of measurements were carried out in an anechoic environment in order to discuss the resulting agreement between theoretical and practical. A total 244 data points[18] were taken during three days of measurements.

Since the time to use the anechoic room was limited, and the GA simulations were not ready at that time, the measurements were realised only with the EAA.

4.4.1 Measurement Site

The measurements took place in the NLR's Small Anechoic Wind Tunnel KAT[19] (without flow) used as a full anechoic chamber, Figure 4.34. The anechoic room is completely covered with foam wedges, which yields more than 99% of sound absorption above 500 Hz (as stated by Oerlemans in his dissertation [84]).

4.4.2 Setup

The EAA was constructed with a 3,0 m length cylinder. It has a hard surface and wall thickness of 1,5 cm, see Figures 4.34 and 4.35.

The microphones were placed in the cylinder's centre (concerning the length or z-axis). They are flush to the hard surface, listening (or *looking*) outside the cylinder, per Figure 4.35.

The cylinder was sustained by two bars, which are locked to a turntable. This propitiates the rotation around the y-axis, per Figure 4.36. Thus, the measurements were taken at 10° intervals, see Figure 4.38. Such a situation renders the same results as if the sound source were to rotate along the ϕ-axis. Moreover, to avoid sound entering the cylinder, its extremities were filled with foam.

4.4.3 Instrumentation

This section describes the instrumentation used in the measurements. Basically, it comprises the control, generation and acquisition.

---

[18] Since 244 measurements were acquired, they are respectively referred to as "Data Point X" or simply "Dpn$X$", where X is its reference number.

[19] The KAT belongs to the Flevoland NLR base in the Netherlands.

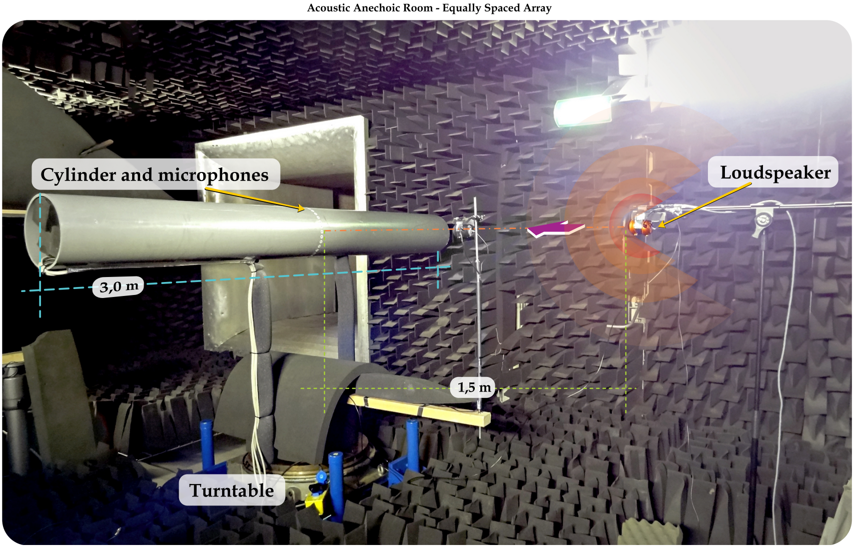

Figure 4.34: Measurement anechoic room with instrumentation.

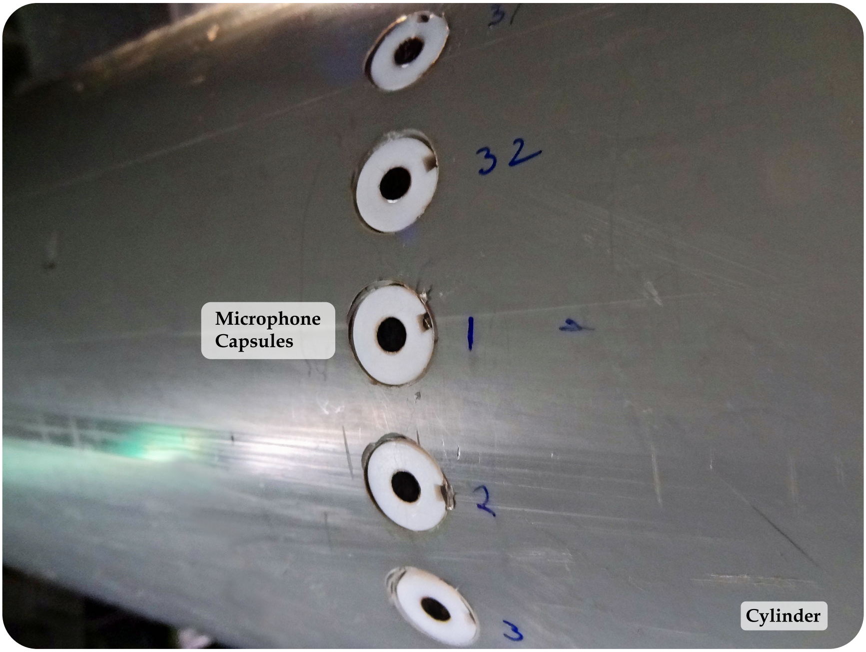

Figure 4.35: Microphones positioned on the cylinder's surface.

The measurement chain is depicted in Figure 4.37. The upper row (in green background) represents the generation of the excitation signal, while the bottom row represents the acquisition of the measured signals. More details of each hardware are described in Section 4.4.3. In addition, the relevant information about the hardwares' technical data is in Annex A.

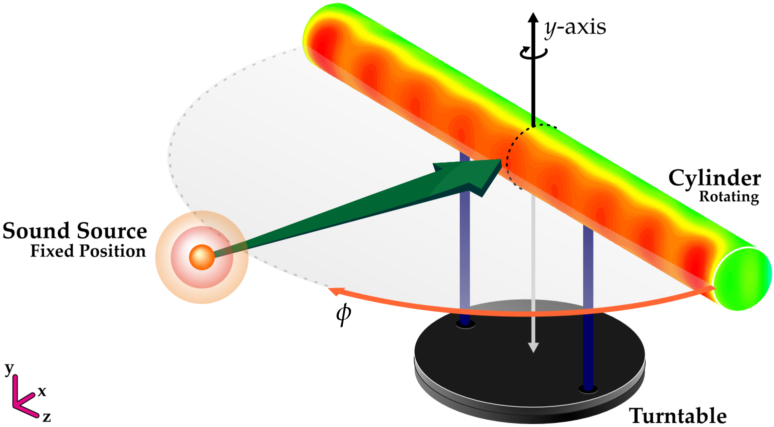

Figure 4.36: Cylinder setup.

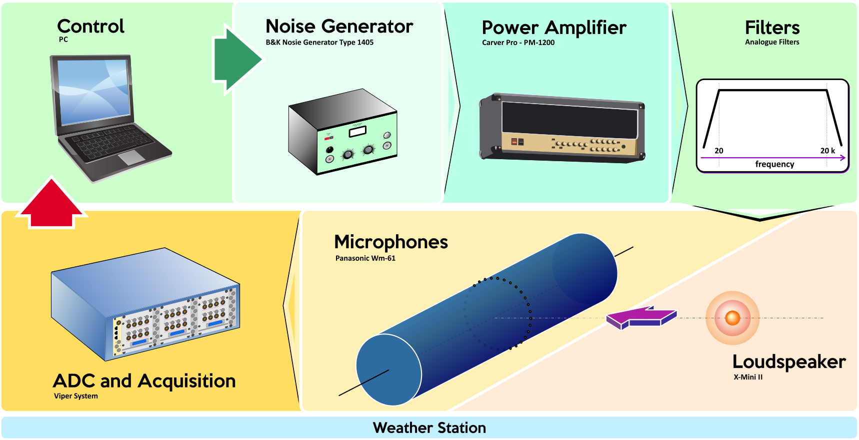

Figure 4.37: Measurement chain scheme.

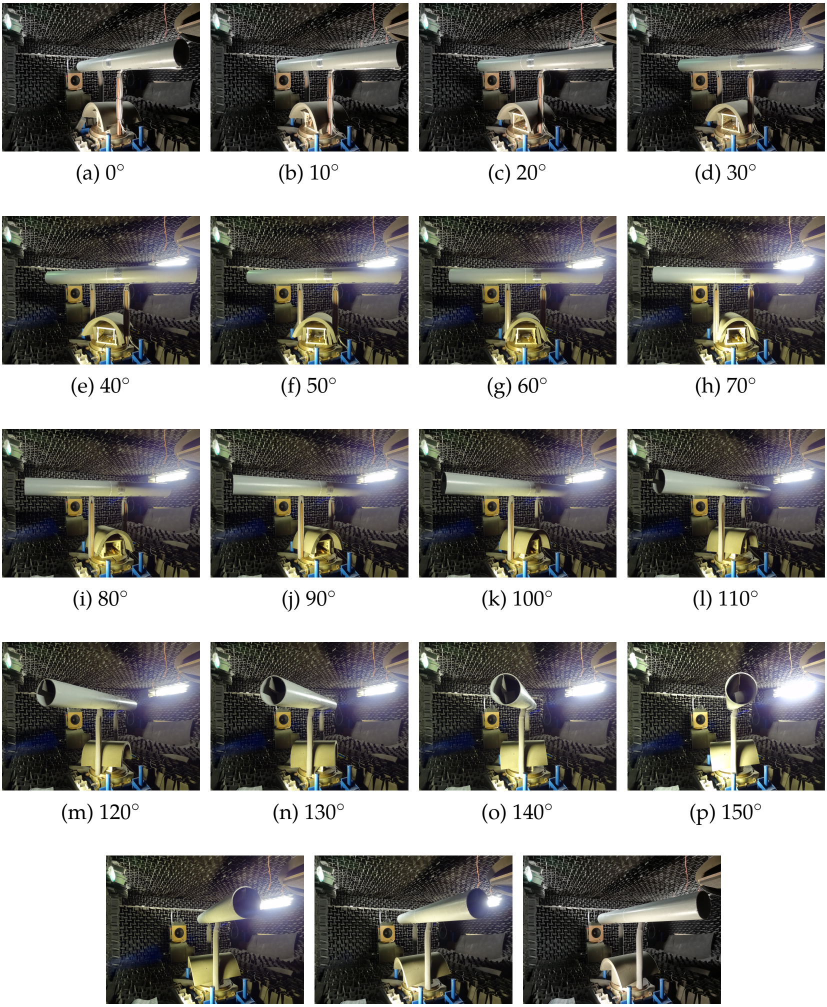

(a) 0°
(b) 10°
(c) 20°
(d) 30°
(e) 40°
(f) 50°
(g) 60°
(h) 70°
(i) 80°
(j) 90°
(k) 100°
(l) 110°
(m) 120°
(n) 130°
(o) 140°
(p) 150°
(q) 160°
(r) 170°
(s) 180°

Figure 4.38: Cylinder rotation at each 10° in relation to y-axis.

4.4.3.1 Control

The control and calibration were performed by a PC machine. Most steps were controlled by codes developed in LabView.

4.4.3.2 Microphones

The microphones are based on the electret Panasonic WM-61A capsules. As can be consulted in Section $A_x.1$, its frequency response is approximately flat in the audible range. This type of microphone has been applied in beamforming since the 90s (in diverse fields) and has presented satisfactory results [104, 105, 61].

The mic housing was designed to be placed flush against the cylinder's surface, see Figure 4.35. Microphone 1 is used as the reference point. It is orthogonal and 1,50 m above the ground. Before enclosing the 32 mics, all of them were calibrated with a *Class 1* acoustical calibrator (1 Pa or 94 dB at 1 kHz, see Section $A_x.3$). The calibration of the microphones (in V/Pa or mV/Pa) enables the recovery of absolute sound pressure values.

Furthermore, a Linear X electret condenser 1/2 inch microphone (model M51) was used closer to the sound source to monitor its reproduction level and spectrum (Section $A_x.2$).

4.4.3.3 Noise Generator

To test different situations, white noise, frequency sweep and tone excitations were applied. For this purpose, three different noise generators were used during the measurements:

1. Brüel & Kjær Noise Generator Type 1405 (Section $A_x.5$), for *white noise*[20] generation;
2. Agilent 33220A Arbitrary Waveform Generator (Section $A_x.6$), for tone and frequency sweep generation;
3. Neutrik Minirator MR1 Analog Audio Generator (Section $A_x.7$), for tone and white noise generation.

For every measurement there is a “level code” which represents its signal type. In Appendix G the codes are described.

---

[20] If the power spectrum is constant, independent of frequency, then the noise is called “white” [106, 14]. Although it has theoretically all frequencies, in this research it is band limited (depending on the case).

4.4.3.4 Power Amplifier and Filters

A power amplifier (Caver Pro PM-1200, Section A_x.9) was used to guarantee the excitation levels to feed the loudspeakers. To exclude undesired frequencies, the output of the amplifier passed through a pass-band filter - it was set up through a SCADAS II LMS-Difa Measuring System. In addition, the output of the filter was also wired to an input channel to certify the excitation frequency span (see the *yellow gold* curve in Figure 4.44).

4.4.3.5 Sound Sources

Since a plane wave generator was not available, loudspeakers were utilised as sound emitters. To minimise the loudspeaker size, small speakers (X-Mini II, Section A_x.4) were used in part of the measurements.

It is known that small sized speakers have poor frequency response in low frequencies. Thus, a second set of loudspeakers were also utilised to extend the experiment to low-mid frequencies.

Basically, four set ups[21] were measured:

1. One X-Mini[22] loudspeaker 1,50 m away from the cylinder surface, 1,50 m above the ground and aligned with microphone 1, see Figures 4.39 and 4.41 (a).

2. Two X-Mini:

   (a) One fixed (orange) 1,50 m away from the cylinder surface; and

   (b) The other (blue) turning with the cylinder and 0,75 m away from the cylinder surface.

   Both loudspeakers were 1,50 m above the ground and aligned with microphone 1, Figure 4.41 (b).

3. Two X-Mini plus synthetical “background noise”, this configuration is identical to the one previously described. The difference is the the addition of white noise through the low-mid speakers on the sideline, see Figures 4.40 and 4.42 (a).

---

[21] These conditions are referred to in the text as “Loudspeaker Set”. For example, Loudspeaker Set #1, or simply LD#1.

[22] Although the X-Mini has a battery, for all the cases the USB charger was connected.

4. The mid and low frequency loudspeakers were also placed 1,50 m away from the cylinder surface. Nevertheless, since there are two (one for low and another for low-mid frequencies) one is 1,50 m above the ground and the other 1,15 m, see Figure 4.42 (b).

In all measurements, the loudspeaker heights were aligned with a rotating laser pointer. This guaranteed a nearly perfect alignment.

The loudspeaker levels were referred to the overall SPL at the microphone 1. The amplitudes are limited to avoid the non-linear speaker response condition.

(a) X-Mini (b) X-Mini mounted with a stand

Figure 4.39: X-Mini loudspeaker.

(a) Low-mid Speaker (b) Low-mid Speaker Set

Figure 4.40: Low-mid loudspeakers.

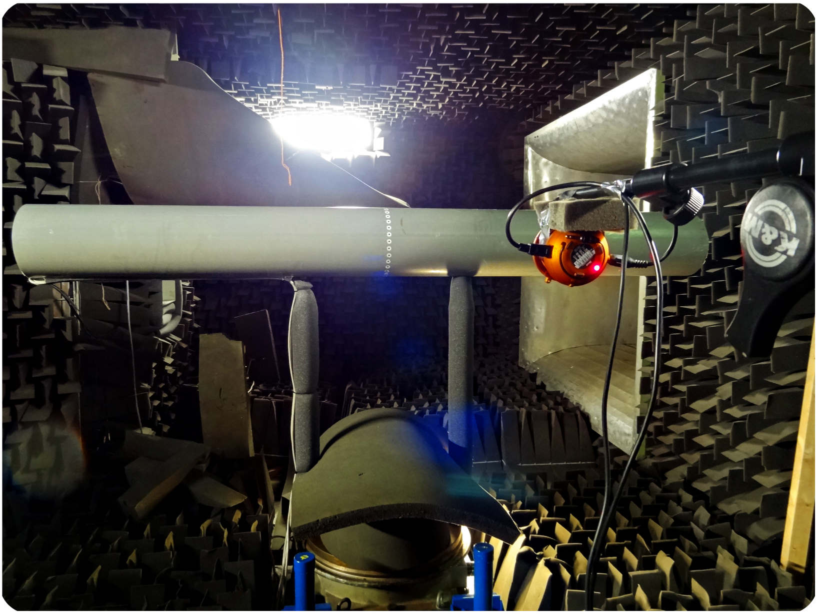

(a) Loudspeaker Set #1

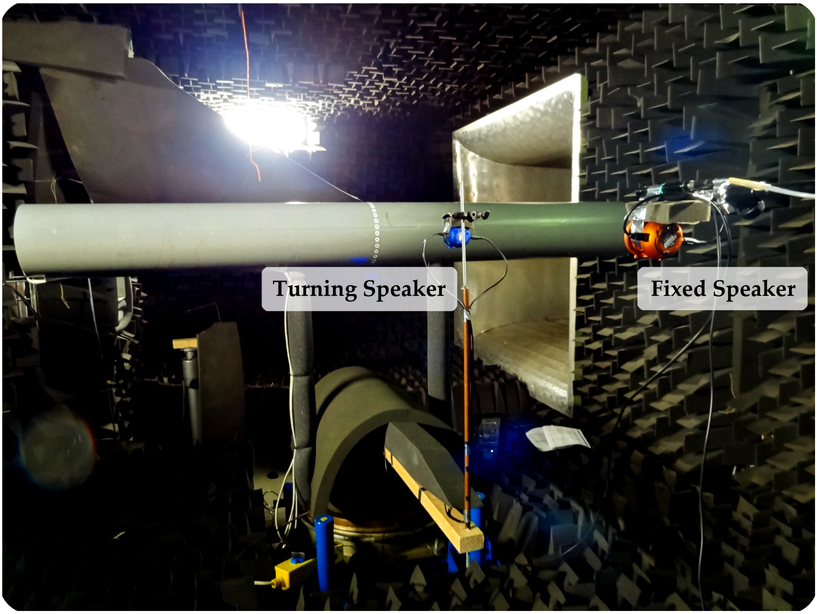

(b) Loudspeaker Set #2

Figure 4.41: Loudspeaker Sets #1 and #2.

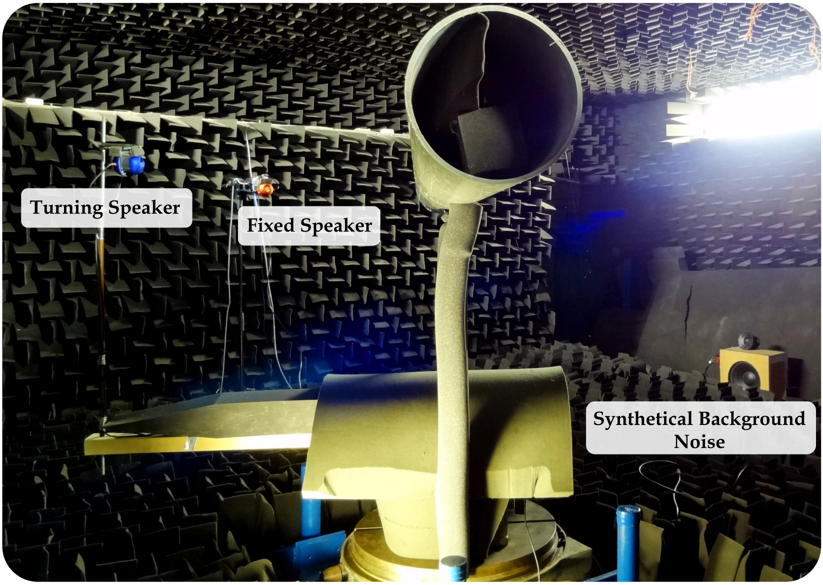

(a) Loudspeaker Set #3

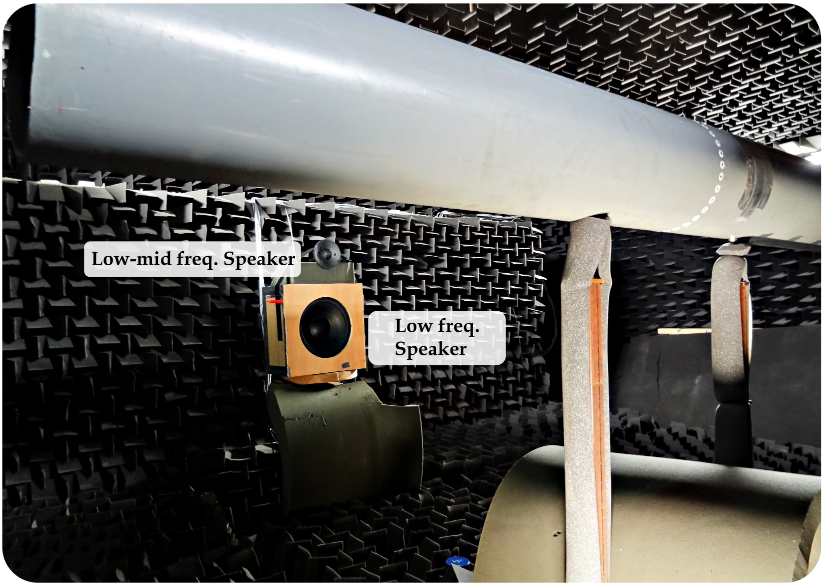

(b) Loudspeaker Set #4

Figure 4.42: Loudspeaker Sets #3 and #4.

X-Mini Frequency Response

The X-Mini frequency response and directivity were measured in an anechoic environment. Figure 4.43 depicts the directivity plot at 1 kHz and 1,5 kHz, and the spectrum (500 Hz - 20 kHz). The complete measurement description and more data can be found in Appendix G, Section G.2.

One can observe that for the frequency range of 500 Hz to 3,5 kHz the response is relatively flat, see Figure 4.43 (c). The minor deviations can be seen in Figure 4.47, where the excitation signal is compared with the sound pressure acquired at microphone 1.

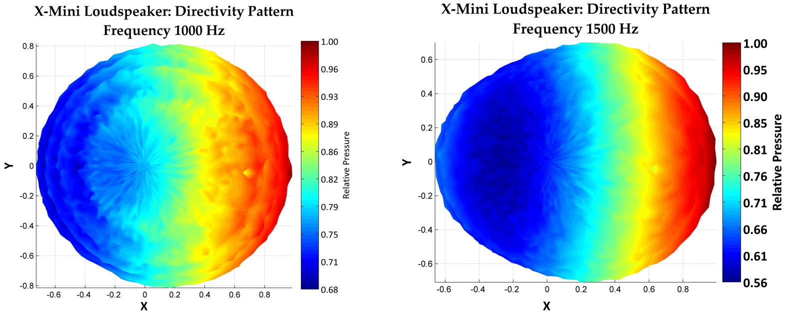

(a) 1 kHz Directivity Pattern (b) 1,5 kHz Directivity Pattern

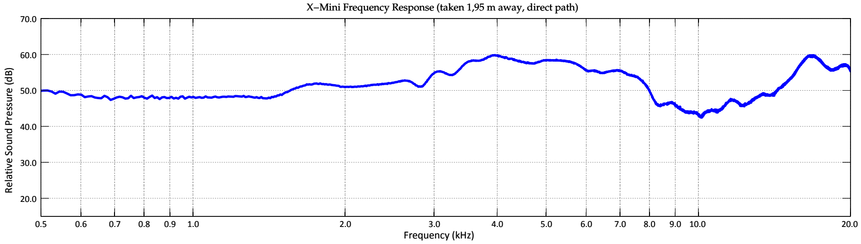

(c) X-Mini II Spectrum

Figure 4.43: The X-Mini frequency response and directivity at 1 kHz and 1,5 kHz.

4.4.3.6 Data Acquisition Hardware

The data was acquired by the GBM Viper Data Acquisition System (Section A_x.8). The system is reliable and has been used in the NLR for diverse kinds of acoustical measurements [107, 108, 109].

4.4.3.7 Weather Station

For the environmental monitoring a very simple weather station was used. The Globaltronics GT-WS-07S Weather Station (Section A_x.10) is capable of measuring temperature, humidity and static pressure. Its range, accuracy and resolution are described in Table 4.3.

Table 4.3: Weather station (WT) range and resolution (Section A_x.10).

Temperature	
Range	0° to +50°
Accuracy	±1° within a measurement range from 0° to +40°
Resolution	0,1°
Humidity	
Range	20% to 90% relative humidity (RH)
Accuracy	±10% RH
Resolution	1%

Although the WT is not very accurate, measuring the environmental conditions provides an impression of the weather conditions instead of a blind situation.

The weather during the measurements ranged as follows: temperature from 11,1° to 14,7°; the humidity from 46% to 73%; and static pressure from 1003 mbar to 1022 mbar. This information may be used later to calculate the correct sound speed [110].

4.4.4 Results and Post-Processing

This section contains a small part of the acquired data. Some results of the four setups are presented as PSFs and spectra. Most of the data points have 25 seconds of recorded data.

The post-processing tools were developed in Fortran, Matlab and LabView. Further details about the software can be consulted in

Appendix D.

Figure 4.44 depicts the fundamental information about one data point:

1. The 32 microphone power spectra of the data point 10 (see the PSFs in Figure 4.46 (a) and 4.46 (b));
2. The background noise measured by
   (a) the array's mics, represented by the mean, and
   (b) by the Linear-X mic;
3. The excitation signal (white noise) used for this data point.

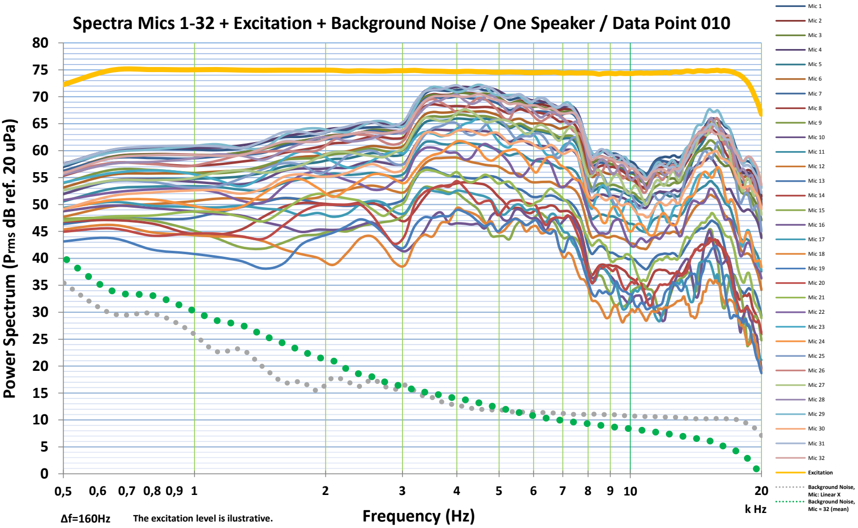

Figure 4.44: Data point 10, emitter at $\theta = 0^\circ$ and $\phi = 90^\circ$. Microphones, excitation signal and background noise spectra.

Concerning the total background noise (anechoic chamber plus electrical), the worst case happens at the lowest frequency. The difference is ≈ 3 dB (dotted green line) and ≈ 8 dB (dotted gray line). For the remaining frequencies this relation increases (as can be seen in Figure 4.44).

4.4.4.1 Loudspeaker Set # 1

The LD#1 comprises the measurements taken from a single speaker (X-Mini orange, Figure 4.41 (a)). As can be seen in Figure 4.46, within this setup several configurations were measured.

1. Different levels: k, l, and m;
2. Different distance: 1,50 m and 0,75 m;
3. Excitation: white noise and frequency sweep.

All these configurations are depicted for 1 kHz and 1,5 kHz. Figures 4.46 (a) to 4.46 (j) can be compared with the analytical modelling in Figures 4.46 (k) and 4.46 (l). In general, they have good accordance. Nevertheless, the differences and/or deformations found in the PSFs may be product of

- Loudspeaker radiation pattern;
- Plane wave assumption; and/or
- Hard wall assumption.

Figure 4.45 depicts the microphone 1 spectra for the different levels k, l and m; and the respective overall levels are 86 dB, 80 dB, and 76 dB. Analysing the Figures 4.46 (a), 4.46 (c) ,4.46 (e), and 4.46 (g) it is possible to confirm that indeed the distance and level have influence over the PSF pattern.

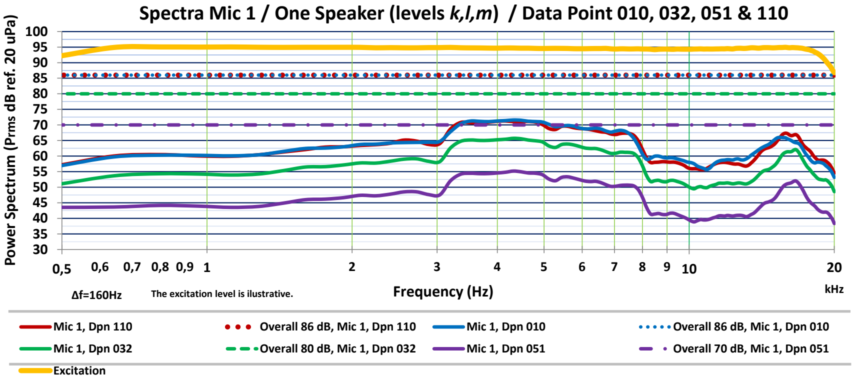

Figure 4.45: Spectra of data points 10, 32, 51, and 110.
One speaker, levels k,l, and m.

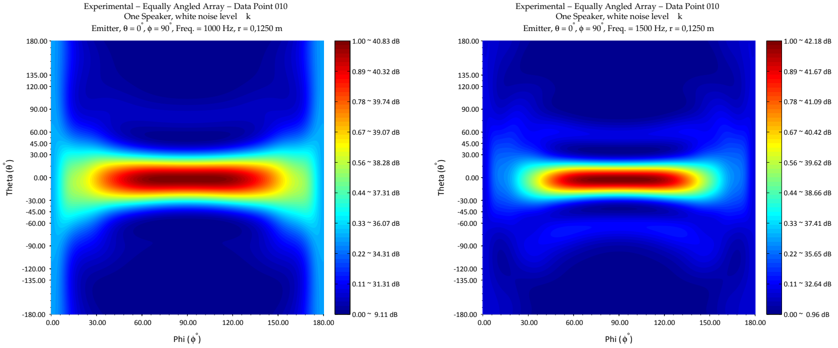

(a) White Noise, Level k at 1 kHz

(b) White Noise, Level k at 1,5 kHz

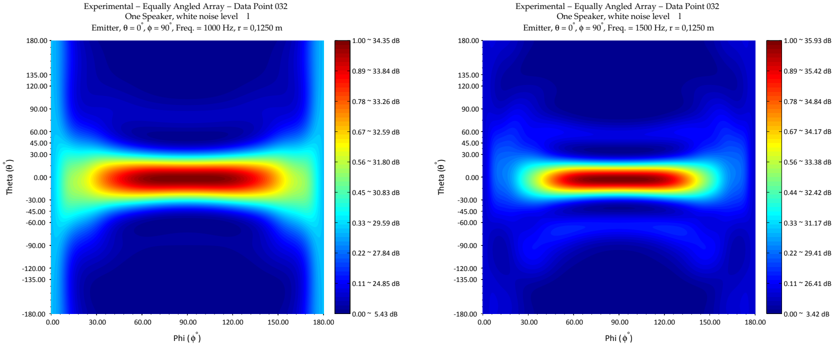

(c) White Noise, Level l at 1 kHz

(d) White Noise, Level l at 1,5 kHz

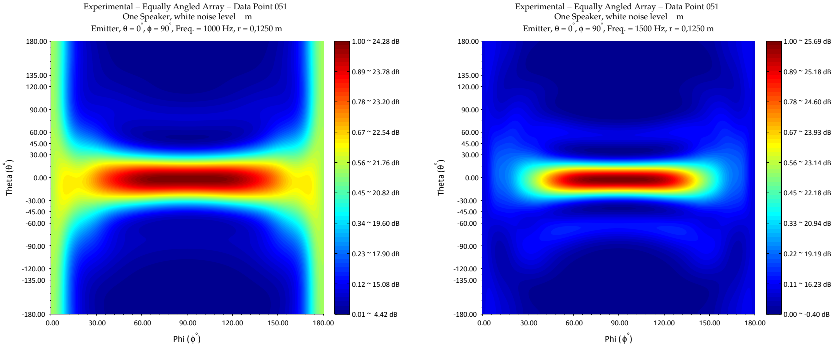

(e) White Noise, Level m at 1 kHz

(f) White Noise, Level m at 1,5 kHz

Figure 4.46: Emitter at $\theta = 0^\circ$ and $\phi = 90^\circ$; 1,50 m distant; levels k, l, and m.

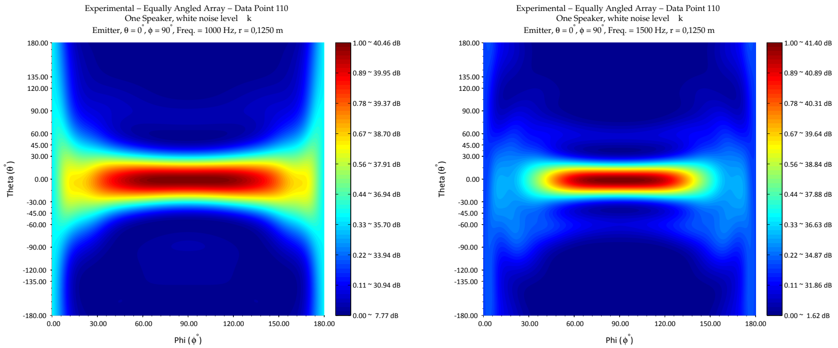

(g) White Noise, Level $\widetilde{k}$ at 1 kHz 0,75 m distant

(h) White Noise, Level $\widetilde{k}$ at 1,5 kHz 0,75 m distant

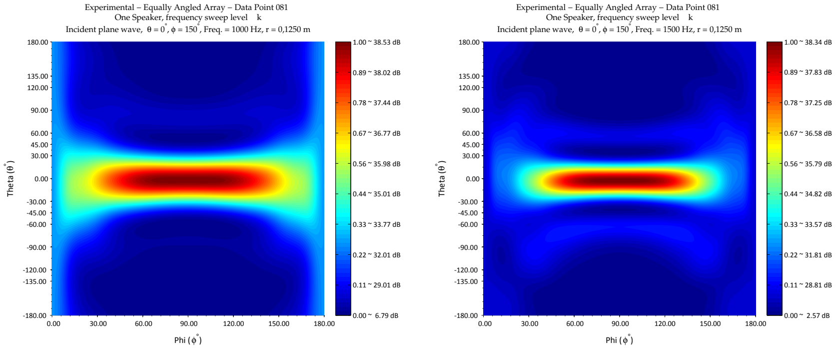

(i) Frequency Sweep at 1 kHz

(j) Frequency Sweep at 1,5 kHz

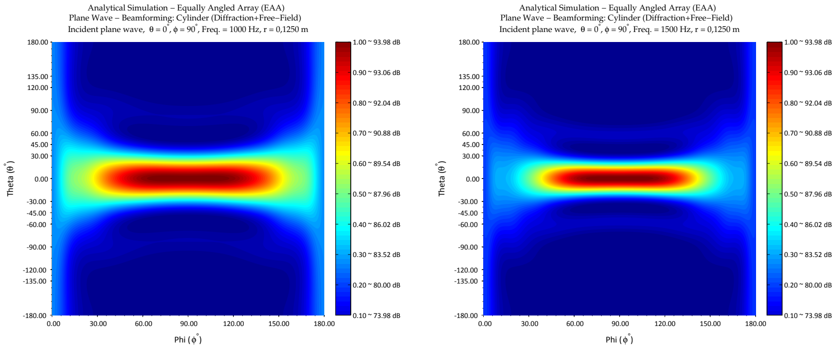

(k) Analytical at 1 kHz

(l) Analytical at 1,5 kHz

Figure 4.46: Emitter at $\theta = 0°$ and $\phi = 90°$; 0,75 m distant; frequency sweep; and analytical.

In the Dpn 110 (Figures 4.46 (g) and 4.46 (h)) the overall level was calibrated to also render 86 dB overall, i.e. $\mathrm{k} \approx \widetilde{\mathrm{k}}$. Thus, comparing Figures 4.46 (a) and 4.46 (g), it is possible to infer that for a 1 kHz (or $kr = 2,31$) emitter, 0,75 m distant, the plane wave assumption is not completely satisfied. Consider $\lambda_{1\mathrm{kHz}} = 0,34$ m; thus,

a) 1,50 m is approximately 4,4 times $\lambda_{1\mathrm{kHz}}$; and

b) 0,75 m is approximately 2,2 times $\lambda_{1\mathrm{kHz}}$.

On the other hand, for 1,5 kHz (or $kr = 3,46$), $\lambda_{1,5\mathrm{kHz}} = 0,22$ m and consequentially

a) 1,50 m is approximately 6,6 times $\lambda_{1,5\mathrm{kHz}}$; and

b) 0,75 m is approximately 3,3 times $\lambda_{1,5\mathrm{kHz}}$.

Accordingly, for 1,5 kHz the wavefield is closer to the plane wave assumption.

Figure 4.47 depicts the microphone 1 spectra for the different ϕ_{in} angles. The shape of the spectra is a consequence of the loudspeaker response. This is confirmed by inspecting its response, see the green line in Figure 4.47.

The logarithmic sine sweep (400-20 kHz, 26 s, Figures 4.46 (i) and 4.46 (j)) has shown satisfactory results. The patterns are similar to the k level white noise measurement and the analytical model.

4.4.4.2 Loudspeaker Set # 2

The LD#2 comprises the measurements with two X-Mini speakers (orange and blue, Figure 4.41 (b)). In this experiment each speaker respectively reproduced a distinct tone (1,6 kHz and 2 kHz), as can be seen in Figure 4.48.

This configuration intends to estimate the recovery of discrete tone components. As shown in Figures 4.48 (a) and 4.48 (b), both speaker positions are well located. In Section G.3 there are the plots for a single loudspeaker at 2 kHz.

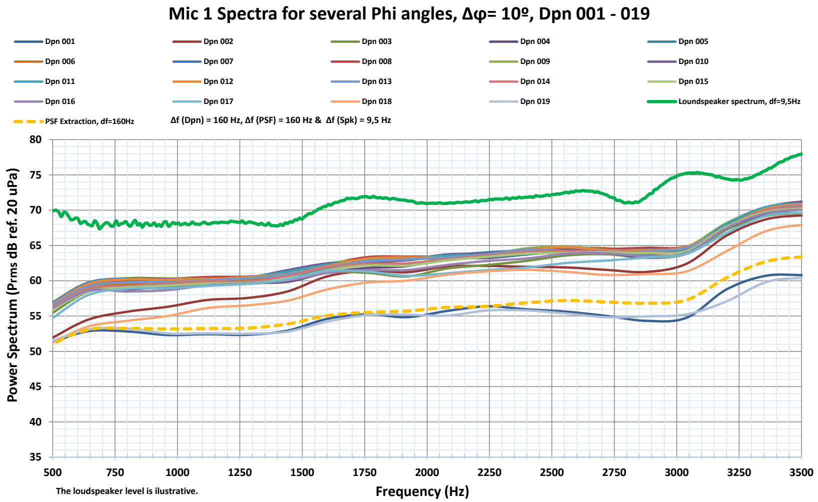

Figure 4.47: Mic 1 spectra for several ϕ_{in} angles, $\Delta\phi = 10^{\circ}$, Dpn 001 - 019.

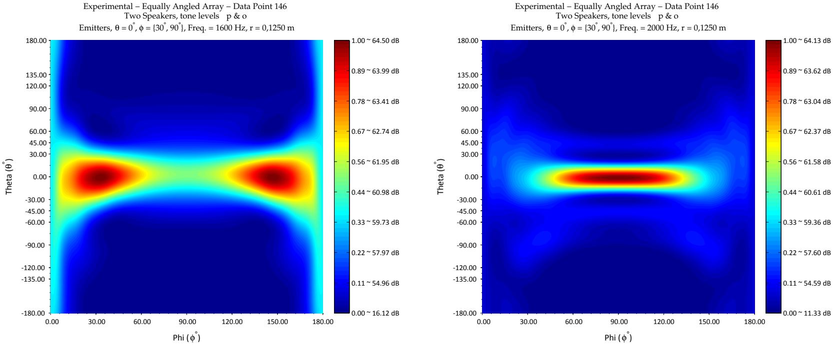

(a) Turning Spk at 1,6 kHz, $\phi_{\text{in}} = 30^{\circ}$ (b) Fixed Spk at 2 kHz, $\phi_{\text{in}} = 90^{\circ}$

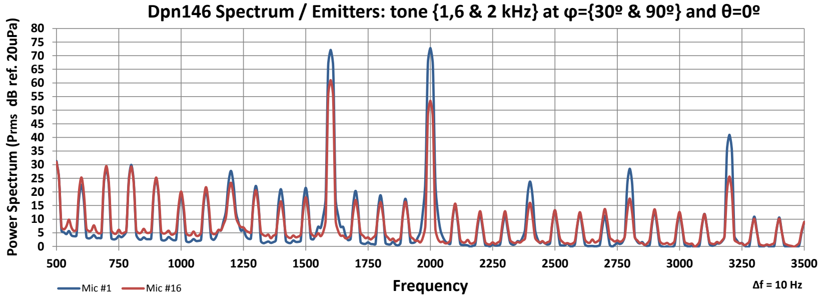

(c) Mic 1 and 16 Spectra

Figure 4.48: Emitters at $\theta = 0^{\circ}$ and $\phi = \{30^{\circ}\ \&\ 90^{\circ}\}$; and 1,50 m and 0,75 m distant.

4.4.4.3 Loudspeaker Set # 3

This configuration is the same as the LD#2 with the addition of "background noise" through the low-mid speakers, see Figure 4.42 (a). The signal used is a white noise (20-6 kHz, level u, Figure 4.49 (g)) and the position of the speakers are theoretically unknown.

At this data point the *fixed speaker* was at the position $\phi_{\text{in Spk1}} = 150°$, and the *turning speaker* was at $\phi_{\text{in Spk3}} = 90°$. The beamforming algorithm then localised the *background noise speakers* at $\phi_{\text{in Bkg}} = 138°$ and $\theta_{\text{in Bkg}} = -159°$. Furthermore, the comparison with the analytical simulations has demonstrated good accordance.

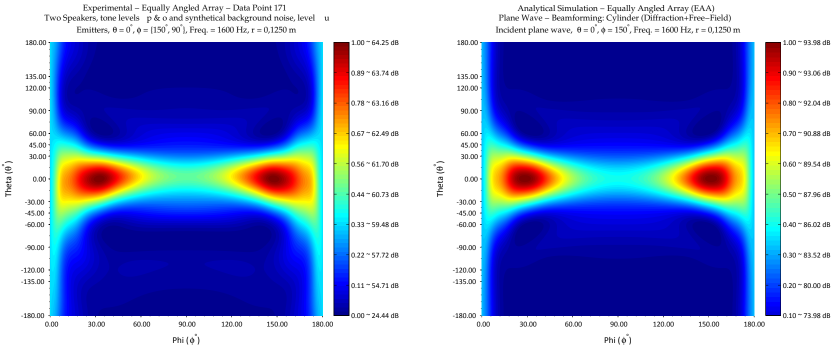

(a) Turning Spk at 1,6 kHz, $\phi_{\text{in}} = 150°$ (b) Analytical at 1,6 kHz, $\phi_{\text{in}} = 150°$

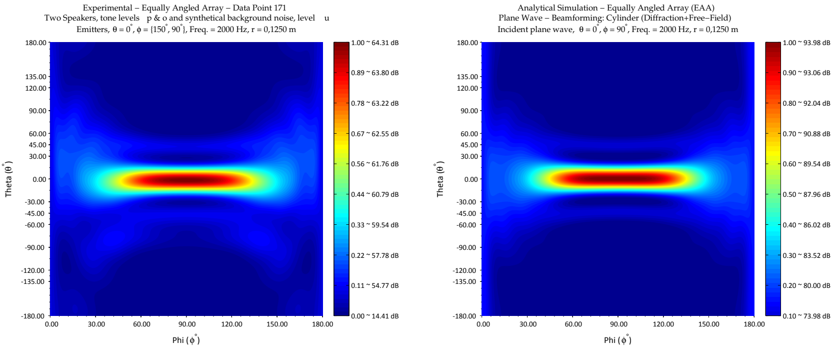

(c) Fixed Spk at 2 kHz, $\phi_{\text{in}} = 90°$ (d) Analytical at 2 kHz, $\phi_{\text{in}} = 90°$

Figure 4.49: Emitters at $\theta = 0°$ and $\phi = \{30° \,\&\, 90°\}$. Fixed speaker 1,50 m distant, turning speaker 0,75 m distant, and background noise speakers on the sideline (PSFs) .

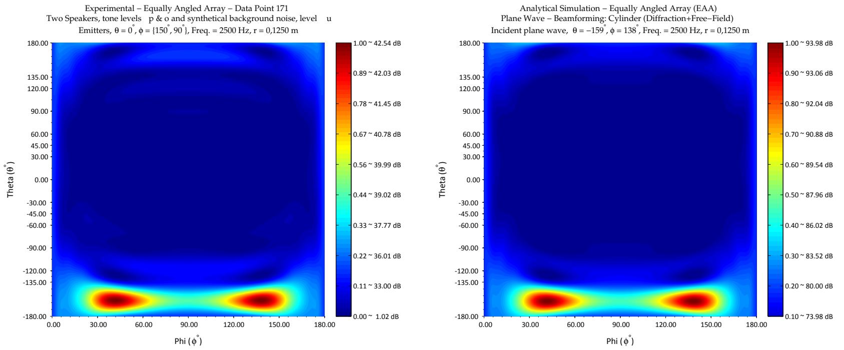

(e) Background Noise at 2,5 kHz, "unknown position" ($\phi_{\text{in Spk1}} = 150^\circ$)

(f) Analytical at 2,5 kHz, $\phi_{\text{in}} = 138^\circ$ and $\theta_{\text{in}} = -159^\circ$

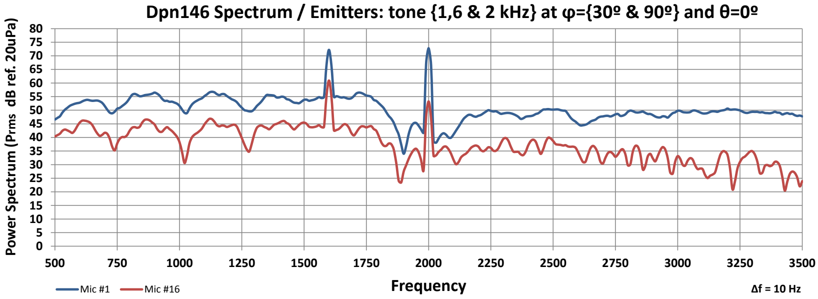

(g) Mic 1 and 16 Spectra

Figure 4.49: Emitters at $\theta = 0^\circ$ and $\phi = \{30^\circ \ \& \ 90^\circ\}$. Fixed speaker 1,50 m distant, turning speaker 0,75 m distant, and background noise speakers on the sideline (PSFs and spectra) .

4.4.4.4 Loudspeaker Set # 4

This setup uses speakers with wider diameters, enabling improved frequency response in low-mid frequencies.

The comparison among LD#4, LD#1, and analytical can be carried out by examining Figure 4.50. One can easily observe that even with distinct levels the PSFs have similar patterns.

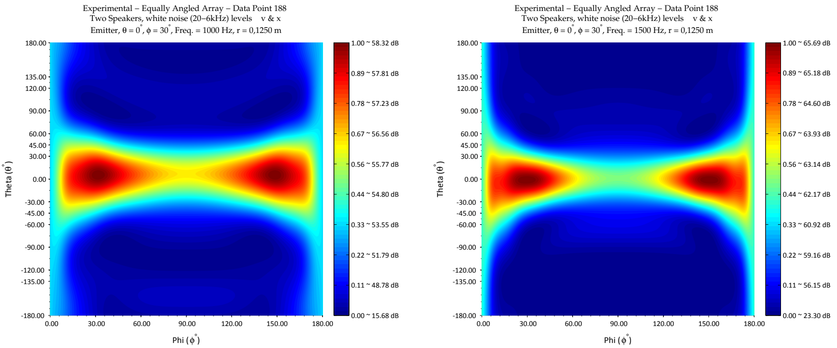
Experimental – Equally Angled Array – Data Point 188
Two Speakers, white noise (20–6kHz) levels v & x
Emitter, θ = 0°, ϕ = 30°, Freq. = 1000 Hz, r = 0,1250 m

Experimental – Equally Angled Array – Data Point 188
Two Speakers, white noise (20–6kHz) levels v & x
Emitter, θ = 0°, ϕ = 30°, Freq. = 1500 Hz, r = 0,1250 m

(h) White Noise, Levels v & x at 1 kHz

(i) White Noise, Levels v & x at 1,5 kHz

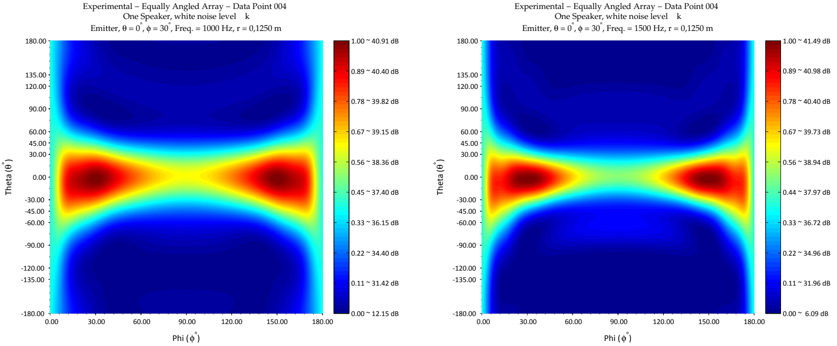
Experimental – Equally Angled Array – Data Point 004
One Speaker, white noise level k
Emitter, θ = 0°, ϕ = 30°, Freq. = 1000 Hz, r = 0,1250 m

Experimental – Equally Angled Array – Data Point 004
One Speaker, white noise level k
Emitter, θ = 0°, ϕ = 30°, Freq. = 1500 Hz, r = 0,1250 m

(j) White Noise, Level k at 1 kHz

(k) White Noise, Level k at 1,5 kHz

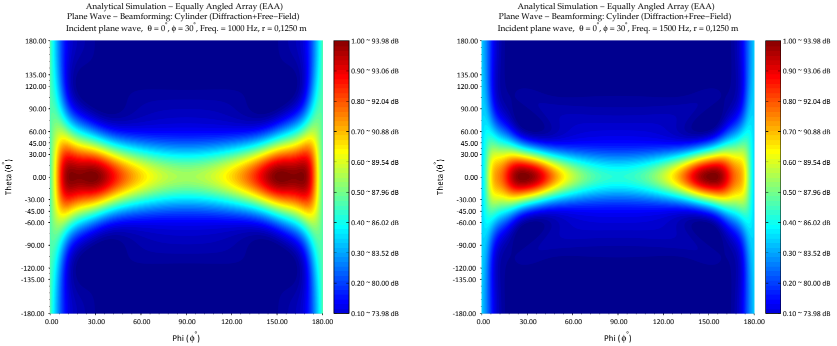
Analytical Simulation – Equally Angled Array (EAA)
Plane Wave – Beamforming: Cylinder (Diffraction+Free–Field)
Incident plane wave, θ = 0°, ϕ = 30°, Freq. = 1000 Hz, r = 0,1250 m

Analytical Simulation – Equally Angled Array (EAA)
Plane Wave – Beamforming: Cylinder (Diffraction+Free–Field)
Incident plane wave, θ = 0°, ϕ = 30°, Freq. = 1500 Hz, r = 0,1250 m

(l) Analytical at 1 kHz

(m) Analytical at 1,5 kHz

Figure 4.50: Emitter at $\theta = 0^\circ$ and $\phi = 90^\circ$; 1,50 m distant; levels k, l, and m.

4.4.5 Considerations

Although only applied for the EAA, the measurements have provided practical details about the applicability of the technique. Further analysis certainly can offer even more information. However, the experimental evaluation of the GA array may help to understand problems not detected in this campaign.

As cited on page 95, for frequencies lower than 1 kHz the ϕ is wrongly detected, this is confirmed here in Figure 4.51. Nevertheless, even below 1 kHz the θ is correctly recovered.

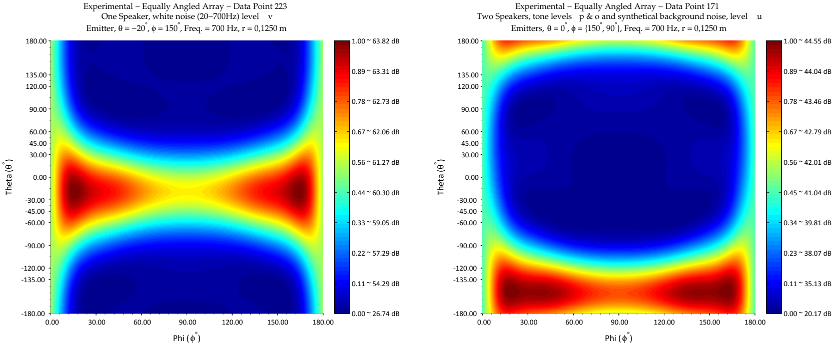

(a) Data point 223, EAA at 700 Hz, $\phi_{\text{in}} = 150^\circ$ and $\theta_{\text{in}} = -20^\circ$

(b) Data point 171, EAA at 700 Hz, detected $\theta_{\text{in Bkg}} = -159^\circ$

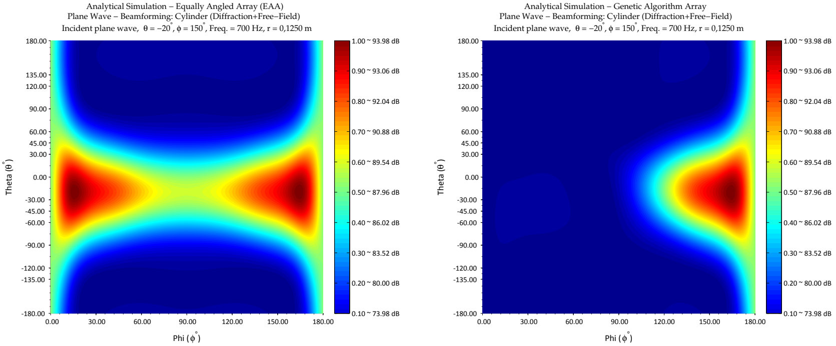

(c) Analytical, EAA at 700 Hz, $\phi_{\text{in}} = 150^\circ$ and $\theta_{\text{in}} = -20^\circ$

(d) Analytical, GA at 700 Hz, $\phi_{\text{in}} = 150^\circ$ and $\theta_{\text{in}} = -20^\circ$

Figure 4.51: Correct recovery of θ; comparison among results.

Since the speaker for low frequencies is 1,15 m above the ground (and not 1,5 m), its θ coordinate is $\theta_{\text{in}} \approx -20^\circ$ instead of $\theta_{\text{in}} = 0^\circ$. This is noticed in Figure 4.51 (a), which has almost the same pattern as the analytical simulation in Figure 4.51 (c). The correct θ estimation can also be observed in Figure 4.51 (c).

Even if the GA array (see Section 5.4.2) is applied, the results will show that: θ is correct, ϕ is wrong, and the grating lobe vanishes, see Figure 4.51 (d). That is, the *blindness* to ϕ in lower frequencies cannot be solved with a geometry change.

5

Numerical Methods

The numerical methods section in this work is comprised of two parts. One is to verify the developments in a more general sense using a Boundary Element Method, meaning the analytical parts are be cross correlated with the methods shown here in this chapter. The second part is the optimization employed to place the microphones over the cylinder. In this case, a Genetic Algorithm was adapted to find an optimal array of microphones. For both topics a basic revision about the theories is given at first and the simulations are discussed thereafter.

In this section only the review about the Boundary Element Method[1] (BEM) and Genetic Algorithm (GA) will be exposed. Even though Beamforming is considered a numerical method, its description is shown in Chapter 3.

5.1 Boundary Element Method

The Boundary Element Method (BEM) is well known among engineers and scientists, as it constitutes a technique for analysing the behaviour of mechanical systems and structures subjected to external loading. The *loading* term here refers to an external source which produces a non-zero field function that describes the response of the system [111].

It is a method for solving boundary-value or initial-value problems formulated by use of *boundary integral equations* (BIEs) [112] on the wave equation, i.e., it is a formulation for the solution of differential equations [113]. Nevertheless, the solution of the partial differential

---

[1] In Portuguese also know as *Método de Elementos de Contorno* (MEC).

equations (PDEs) can only be achieved when the physical problem can be expressed as such [114].

In the numerical implementation of the BEM only the boundary domain needs to be discretized (or meshed), that is, surfaces for three-dimensional (3D) problems or curves for two-dimensional (2D) problems [112], as depicted in Figure 5.1. This is opposed to the Finite Element Method (FEM), which demands the discretization of the whole domain. BEM, if applicable, yields a considerable reduction in the dimensions of the problem (which leads to less computing requirements). Nevertheless, the system matrices are usually densely populated, complex and frequency dependent.

In acoustics, these techniques (BEM and FEM) are usually applied to problems of low and medium frequencies ($k\sigma \lesssim 2\pi$, in acoustics). Other methods, such as Statistical Energy Analysis (SEA) [115] or hybrid approaches are employed for higher frequencies.

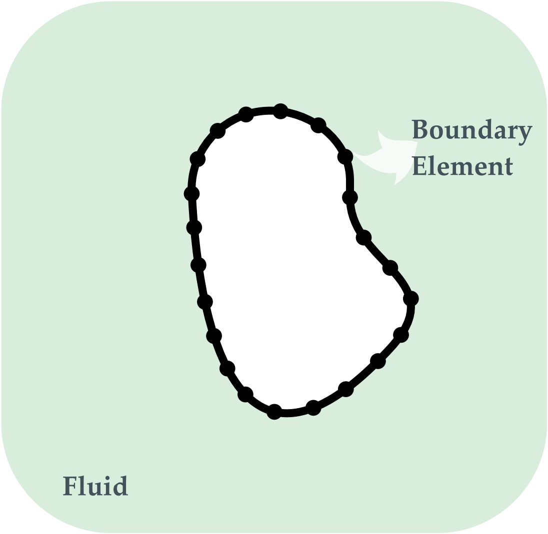

Figure 5.1: Exterior problem, BEM approach, only the boundaries are discretized.

BEM in acoustics is based on expressing the acoustic variables pressure, and particle velocity, within (or outside) the acoustic volume as a surface integral over the boundary acoustic domain [116]. There are two main formulations in BEM: *Direct* (DBEM) [117, 118] and *Indirect* (IBEM) [118, 119]. In DBEM the primary variables are acoustic pressure and particle velocity. The difference in pressure and the difference in the normal gradient on the pressure across the boundary element model constitute the primary variables in IBEM [118] - they are also known as *jump of pressure* and *jump of velocity*. The definition of primary variables is shown in Figure 5.2. In this example, the DBEM calculation is defined as interior since the vector ($\hat{n}$) is pointing inside the model.

In the DBEM approach, the model must be a closed surface. Hence, the primary variables are calculated for just one side, i. e., exterior or interior. On the other hand, in IBEM there is no differentiation; the primary variables and the solution contain information from both sides.

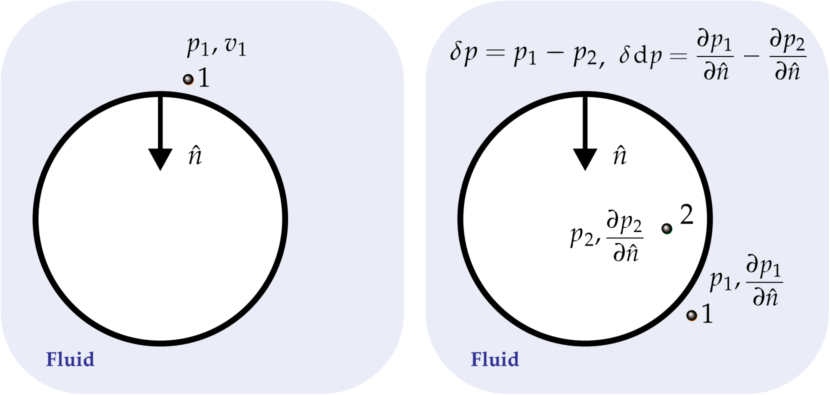

(a) DBEM (b) IBEM

Figure 5.2: Definition of primary variables for DEM and IBEM.

There are three fundamental steps in BEM: pre-processing, in which an equation system is created; evaluation of the boundary values throughout solving the system; and at last but not least, post-processing, in which the pressure field (or field points) is calculated.

In pre-processing a continuous system must be discretized, see Figure 5.3.

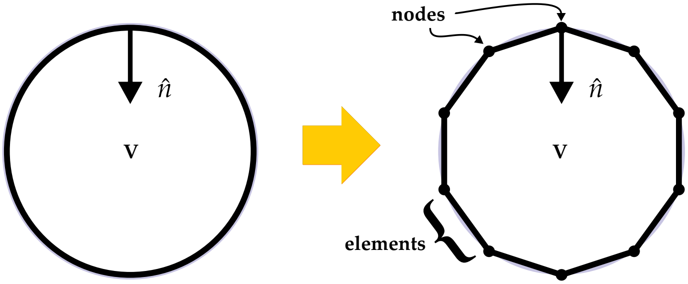

Figure 5.3: Continuous to discrete system.

This process is carried out by discretizing the continuous Helmholtz Integral Equation (HIE). The boundary is split up into n_{total} elements (see Figure 5.4), which will render a system of equations from which the values can then be found.

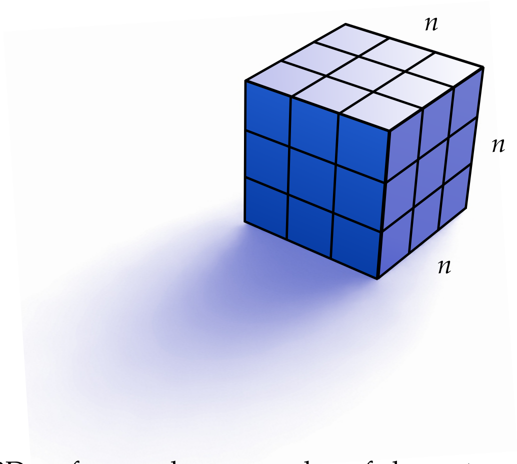

Figure 5.4: 3D surface mesh, $n =$ number of elements per dimension. The sum of the all surfaces gives n_{total}.

5.1.1 Helmholtz Integral Formulation

In order to compute acoustic pressure, the *Helmholtz Differential Equation* (Equation (2.7)), which renders the solution in the fluid domain, is replaced by an integral equation that covers only the boundary surface. To achieve this conversion the Green's second identity must be applied. Further details about this transformation can be consulted in other studies in the literature such as [120, 121, 27].

The resulting equation is known as the *Helmholtz Integral Equation*[2] (HIE). It links the acoustic pressure and normal velocity on the closed boundary surface S of a vibrating body to the radiated pressure field in the fluid domain [123]:

$$\alpha(\vec{x})p(\vec{x}) = \oint_{s} \left\{ \frac{\partial G(r)}{\partial n_y} p(\vec{y}) - G(r)\frac{\partial p(\vec{y})}{\partial n_y} \right\} \mathrm{d}S + p^{\mathrm{in}}(\vec{x}), \tag{5.1}$$

where $\alpha(\vec{x})$ is the geometry related coefficient [124]; $\vec{y}$ is the *data point* located on the boundary surface S; $\vec{x}$ is a *field point* (or *evaluation point*, since the integral has to be evaluated for each point $\vec{x}$); $\vec{n}_y$ is the unit normal to the surface point $\vec{y}$ (pointed into the fluid domain); and r is the length of the vector $\vec{r}$ that is directed from the source point $\vec{y}$ to the field point $\vec{x}$, i.e., $r = \|\vec{x} - \vec{y}\|$; Figure 5.5 illustrates the idea [125]. The term $p^{\mathrm{in}}(\vec{x})$, in the case of scattering analysis, corresponds to the incident acoustic wave. For *free space*, without reflecting objects, the Green's function $G(r)$ reads

$$G(r) = \frac{e^{-jkr}}{4\pi r}\,. \tag{5.2}$$

The Equation (5.2) represents the response of the inhomogeneous Helmholtz Differential Equation to a Dirac pulse in space. The complete subsequent derivations can be found in the references [126, 127, 128].

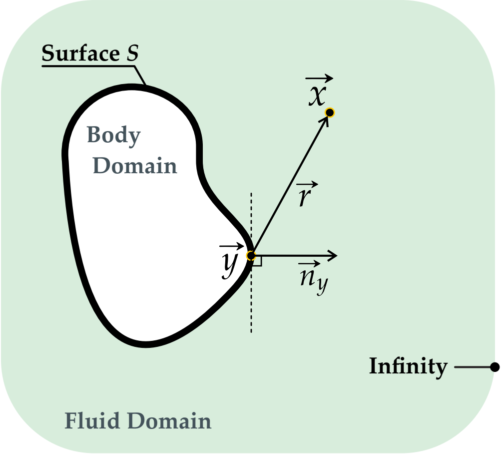

Figure 5.5: Boundary surface for the HIE.

---

[2] Also known as Kirchhoff-Helmholtz Integral Equation (KHIE) [122].

For a review concerning the Boundary Element Method, its recommended a reading in the textbooks Brebbia *et al.* [116] and Wu *et al.* [118]. Also, the complete BEM acoustics formulation can be found in Kirkup [114] and Liu [112].

5.1.2 Direct BEM

After defining the boundary conditions, the following step is to solve for the unknown boundary values. Since the surface pressure is the direct output in DBEM, the model used in this work is closed, with the exterior sound field as the target. All the BEM simulations were carried out using DBEM. In *Direct* BEM the following system of equations is created and solved for each analysis frequency:

$$[A(\omega)]\,\{p\} = [B(\omega)]\,\{v_n\}\,, \tag{5.3}$$

where the influence matrices A and B are non-symmetric, fully populated and frequency-dependant; p is the vector of nodal pressures on the BEM surface; and v_n is the vector of normal velocities on the BEM surface (these last two are also knows as *potentials*). From these *primary surface results*, the field points are directly calculated. The pressure at an arbitrary field point $\vec{x}$ is obtained from surface pressure and normal velocity values by field point post-processing, using the expression [129]:

$$P_{\vec{x}} = \{a\}^t\{p\} + \{b\}^t\{v_n\}\,. \tag{5.4}$$

> *"The calculation of the primary surface results is the most expensive in terms of CPU time because it involves the inversion of a complex and fully-populated matrix. Field point post-processing from these primary surface results is relatively fast."* Excerpt from Sysnoise manual [129].

Even considering the statement above, the DBEM is utilised because the model simulated for this work is relatively simple (see Section 5.2.1). It is understood that more sophisticated processing can accelerate the solving process, such as the High Speed Harmonic BEM, based on the Padé expansion [130] or the Fast Multipole BEM [112].

Different than the other techniques employed in this work, a commercial BEM solver, the LMS Sysnoise [131], was utilised. There are also some other options for BEM simulations on the market such as Open BEM [132], Abaqus [133], Ansys [134] or VA One [135], for example.

5.1.3 Meshing

The meshing in BEM is an important step. It determines the accuracy related to the frequency of analysis. In acoustic computation, the element size is related to the wavelength. It is calculated in order to fit a fixed number of elements per wavelength. Usually, it varies between six and ten [136, 137], which leads to the following rule of thumb

$$\text{Mesh size} = \frac{\lambda}{6} \quad \text{or} \quad \frac{\lambda}{\text{MR}}, \tag{5.5}$$

where λ is the wavelength and "MR" represents a *mesh refinement* coefficient. This ratio is a probable consequence of Shannon's sampling theorem [138] whose discussion is presented in the Chapter 11 of Steffen *et al.* [136]. Equation (5.5) yields

$$\text{Mesh size} = \frac{v_{\text{snd}}}{\text{MR} * f_{\max}}, \tag{5.6}$$

where v_{snd} is the sound speed in the medium and $f_{\max}$ the maximum frequency of analysis. For example, for 3,2 kHz

$$\text{Mesh size} = \frac{\approx 340}{6 * 3200} \approx 0{,}0177\ [\text{m}]\,. \tag{5.7}$$

For the DBEM simulation, there are some important rules to follow concerning the CAD model and the mesh:

1. the model must be closed (Figure 5.7);
2. the element normal vector orientation should reflect the region of interest (Figure 5.8);
3. the mesh refinement must comprise at least 6 element per wavelength (Equation (5.6)).

5.2 DBEM Simulations

Most DBEM simulations[3] were performed considering a basic cylinder model of 3,0 m length, 0,1250 m radius, closed on the limits and rigid, see Figure 5.7. Increasing the radius or length will lead to increased elements per model, and consequently, increased processing time.

Although this model was chosen to compare with other methods. In order to verify sensitivities, some simulations were carried out varying:

1. mesh refinement;
2. cylinder length;
3. cylinder radius; and
4. sound source model:
    (a) plane wave;
    (b) monopole.

One of the intentions of the DBEM-beamforming is to estimate possible issues and compare results with the analytical model. Later, this information then can be used for different models in which the analytical modelling is of difficult or impossible estimation. For example, a cylinder with a hemisphere on top, or more realistic structures.

5.2.1 Model and Mesh

The meshing is the process of creating fine elements for solids or surfaces. For the cylinder of this study the Quad4 Element [139] was chosen for surface meshing, Figure 5.6. At first, a *mesh seed* is placed on the circumference limits of the cylinder, and then all the surface is meshed. Carrying out this way guarantees that all elements over the cylinder will join the edges perfectly. On the major portion of the surface, the Quad4 elements are equally distributed, with irregular elements and a few Tri3 elements only on the extremities (Figure 5.6).

To fulfil the rule explained in Section 5.1.3 with the Sysnoise "minimum 6 elements per wavelength" criterion, the maximum frequencies

---

[3] At the time of the DBEM simulations, the GA simulations were not finished. For this reason the EAA is employed in this section.

are increased by 3%. That means that in the mesh generation process the mesh element size is calculated modifying Equation (5.6) to

$$\text{Mesh size}_{+3\%} = \frac{v_{\text{snd}}}{\text{MR} * f_{\max} * 1{,}03}, \tag{5.8}$$

which, for example, yields

$$\text{Mesh size}_{+3\%} = \frac{\approx 340}{6 * 3200 * 1{,}03} \approx 0{,}0172\ [\text{m}]\,. \tag{5.9}$$

Following Equation (5.9), the three dimension model used has 8320 elements (with 8313 nodes) for simulations up to 3200 Hz, see Figures 5.6 to 5.7.

As previously cited, since this is an exterior problem the acoustic element normal vectors are pointed to the outside of the cylinder (or to the fluid domain), Figure 5.8.

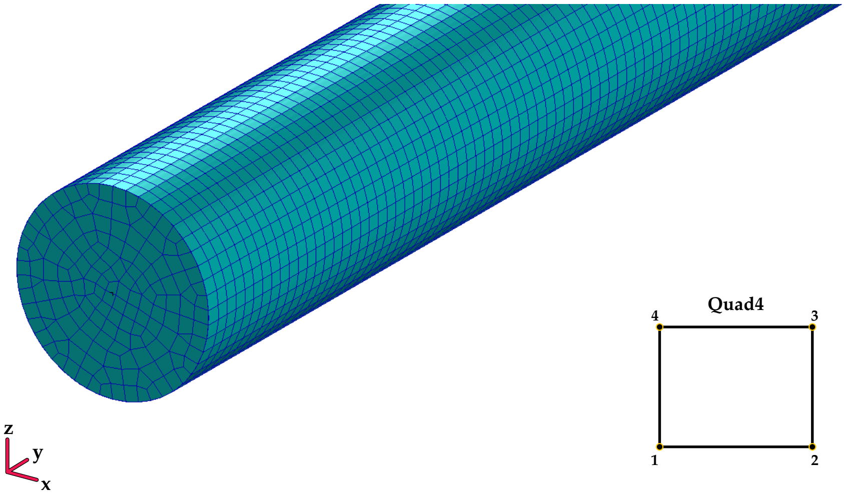

Figure 5.6: Cylinder meshing in detail (and Quad4 element example).

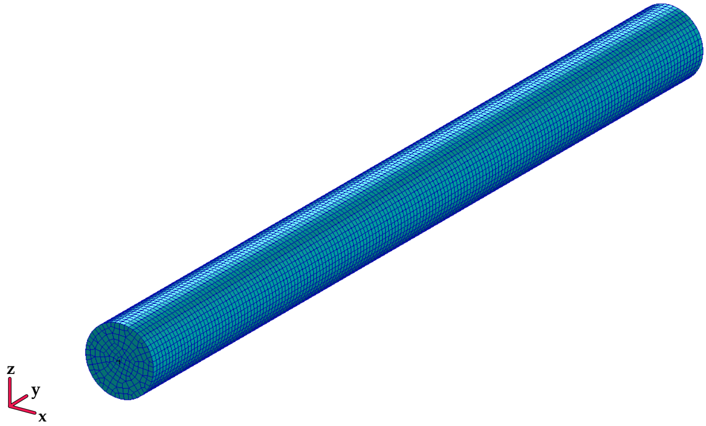

Figure 5.7: Cylinder 3,0 m length; 0,1250 m radius; closed and rigid.

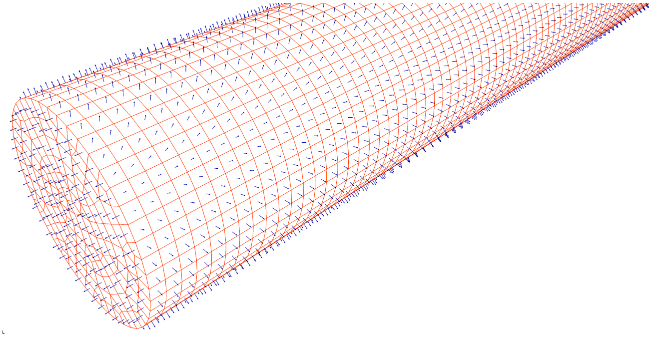

Figure 5.8: Acoustic element normal vector, DBEM exterior problem.

5.2.2 Field Points

At first, the field points are arranged in a circumference with radius of 0,1255 m (0,5 mm above the surface of the cylinder). This is done to avoid singularities on placing the field points directly over the mesh. Figure 5.9 depicts one example, in which the configuration includes a monopole sound source 1,5 m away from the cylinder's surface and 1,5 m in the y direction. The field point circumference is sampled in 32 equally spaced points around the cylinder with the first point aiming towards the sound source (or $(x,y,z)_{1^{st}\text{pt.}} = -0,1255;1,5000;0,0000$).

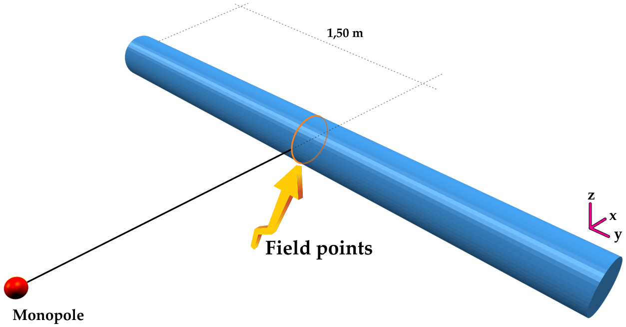

Figure 5.9: EAA *field points* with a monopole sound source.

The outputs of the field points are complex pressures (representing virtual microphones) which will be computed in the post-processing. That is, they are the $\vec{p}_m$ values of the CB in Equation (3.35b).

5.2.3 Mesh Refinement Simulation

Considering the same cylinder dimensions previously described, several *mesh refine coefficients* (MR) were tested. Table 5.1 summarizes the simulated cases.

Table 5.1: Mesh element size and processing time for each MR.

MR	**Mesh Element Size [m]**	**Theoretical Max. Freq. [Hz]**[a]	**Elements**	Process. Time[e]
1,0	0,1032	533,10	240	≈ 1 min.[b]
2,0	0,0516	1066,2	931	≈ 1,5 min.[b]
3,0	0,0344	1599,3	2103	≈ 2,5 min.[b]
4,0	0,0258	2132,4	3623	≈ 13 min.[b]
6,0	**0,0172**	**3198,6**	**8320**	≈ 1h 25 min.[b]
8,0	0,0129	4264,8	14773	≈ 7h 35 min.[b]
10,00	0,0103	5341,4	23000	≈ 50 hours[c]
12,00	0,0086	6397,2	33057	≈ 147 hours.[d]

[a] Considering a minimum of 6 elements per wavelength for $f_{\max} = 3{,}2$ kHz and discounting the 3% described in Section 5.2.1.

[b] Time to process 146 frequencies for one given angle ϕ and θ (for example, $\phi = 30^\circ$ and $\theta = 0^\circ$). Performed in quad core processing with frequency level parallelization.

[c] Same as "b", but dual core processing due to memory limitations.

[d] Same as "b", but single core processing due to memory limitations.

[e] PC computer used: Windows 7 Ut., x64 arch., Intel i7-3939K, 6 Cores , 3,2 GHz, 24,0 Gb RAM. Three dimensional model, Sysnoise solver.

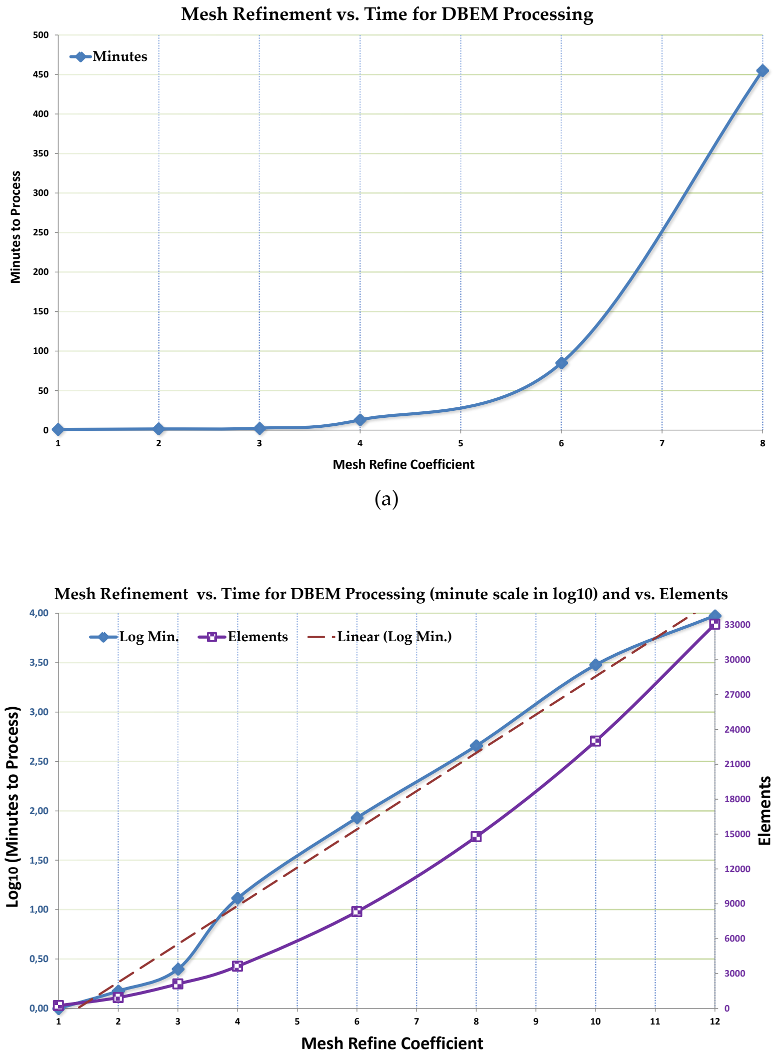

(a)

(b)

Figure 5.10: Mesh Refinement vs. Time to process. (a) for 1 <MR< 8; (b) for 1 <MR< 12 with minutes in log; tendency line in red; and MR vs. Elements (purple line).

The time data of Table 5.1 can be better understood by inspecting Figure 5.10. It possible to notice that the processing time increases similarly to a log function while the number of elements increases almost linearly.

In order to evaluate the differences caused by meshing, graphs relating the maximum peak in the maps (ϕ and θ axis) to frequency were created. Figures 5.11 to 5.13 depict the peak positions for $\phi = 30^\circ$ and $\theta = 0^\circ$ versus frequency. Since the Equally Angle Array (EAA) was used in these simulations, the peak extraction was performed only in the intervals $0^\circ \leq \phi \leq 90^\circ$ and $-180^\circ \leq \theta \leq +180^\circ$. The frequency axis spans

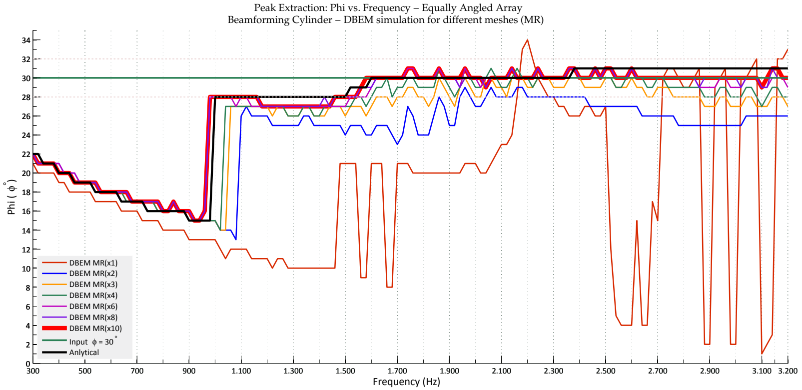

Figure 5.11: Phi vs. Frequency. Peak localization for different mesh refinement (MR), and for $\phi = 30^\circ$ and $\theta = 0^\circ$ (df=20 Hz).

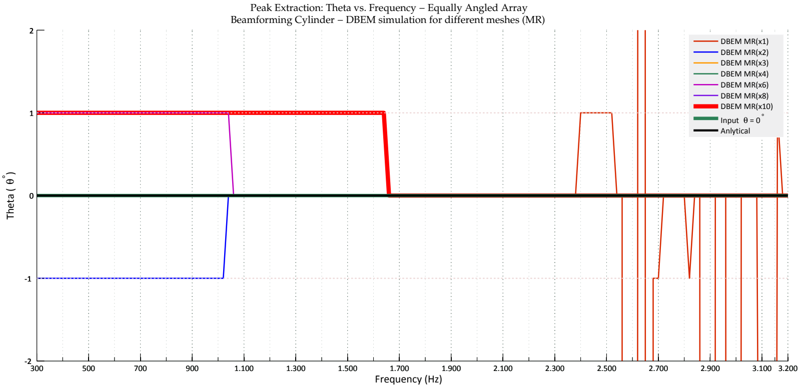

Figure 5.12: Theta vs. Frequency. Peak localization for different mesh refinement (MR), and for $\phi = 30^\circ$ and $\theta = 0^\circ$ (df=20 Hz).

from 300 Hz to 3,2 kHz with a 20 Hz step. Surrounding the input angle (or emitter position, $\phi = 30°$, $\theta = 0°$), there are dashed lines indicating the limits of $\pm 2°$ in ϕ and $\pm 1°$ in θ.

Analysis of Figures 5.11 and 5.12 demonstrates the fact that there is no considerable advantage in using mesh refinements higher than MR $= 4$ for localizing the direction of sound; with MR ≥ 4 almost all lines are superposed. To get an idea how close the differences are, expanded y axis versions of the graphics can be revisited in Figure 5.13.

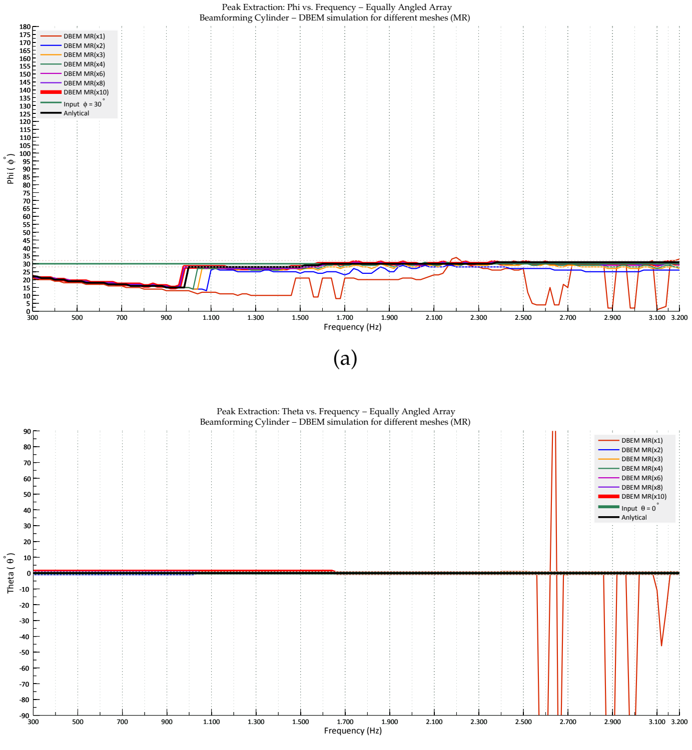

(a)

(b)

Figure 5.13: (a) Phi vs. Frequency and (b) Theta vs. Frequency (expanded angle plot). Peak localization for different mesh refinement (MR), emitter at $\phi = 30°$ and $\theta = 0°$.

Figure 5.14 demonstrates the relation between frequency resolution (df) and the peak localization. As can be seen, a df=20 Hz (blue line) is enough for representing the behaviour in the frequency domain, while with df=100 Hz (lime line) gives the general impression.

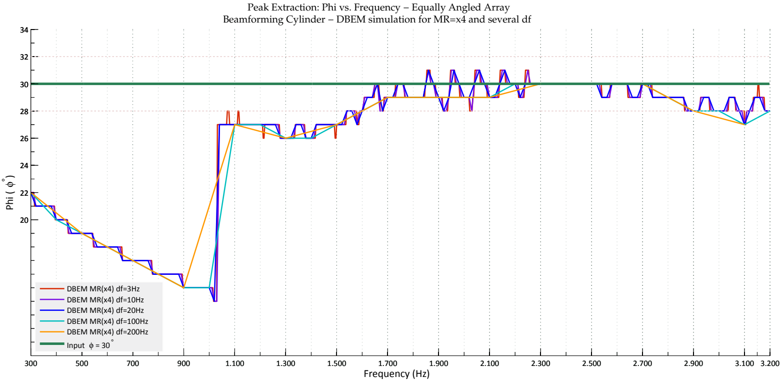

Figure 5.14: Phi vs Frequency for MR=x4 and several frequency resolution (df).

The deviations below 1 kHz are expected and were previously discussed in the Section 4.3.1.1, see Figure 4.18 for the reference. This demonstrates the nature of the problem, where the cylinder tends to be acoustically transparent in lower frequencies.

To evaluate an overall of all frequencies for the relative percentage differences, the following equation is estimated from Figure 5.11 data

$$\text{Diff.}_{\text{R\%}} = \left[\sum_{\substack{f=1 \\ x(\text{MR})}}^{\text{end}} \left| \frac{V(f) - X(f)}{X(f)} \right| \cdot 100 \right] \cdot \frac{1}{\text{size}\ (X)} \,, \tag{5.10}$$

where f is frequency; and V and X are the frequency vectors of *numerical simulations*, *analytical simulations*, and *input angle* depending on the case.

Table 5.2 and Figure 5.15 are the outputs of Equation (5.10). These results demonstrate how similar the simulations are for different values of MR. localization is not improved with a more refined mesh.

Table 5.2: Relative percentage differences for
Phi vs Frequency (Figure 5.11).

	Type / MR	x1	x2	x3	x4	x6	x8	x10
🟪	**Numerical vs Analytical**	31,25%	11,18 %	5,78%	4,09%	2,86%	2,39%	2,40%
🟨	**Numerical vs Input**	40,57%	20,80%	15,59%	13,90%	11,64%	11,30%	11,30%
	Analytical vs Input							
	12,03%							

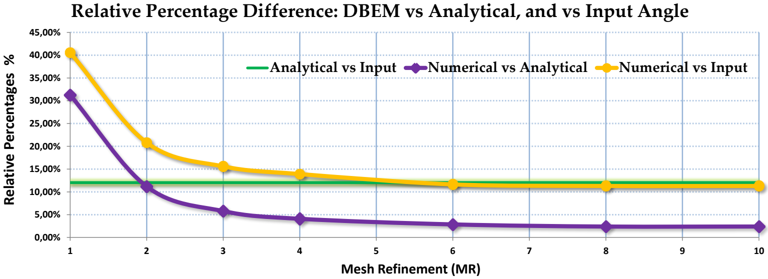

Figure 5.15: Relative percentage differences for
Phi vs Frequency (Table 5.2 and Figure 5.11).

To get a better understanding about the effects on Figure 5.11, a look at the field points spectrum (or *virtual microphones*) offers some new information. A normalization was performed in order to compare the analytical and DBEM spectra. Basically, the *analytical microphone* #1 and *field point* #1 at 1 kHz are the references. Hence, all other microphones and frequencies[4] are rescaled with respect to ratio

$$\text{Scale factor} = \frac{\left|\text{mic}^{\#1}_{\text{Anl}}(1\text{ kHz})\right|}{\left|\text{mic}^{\#1}_{\text{DBEM}}(1\text{ kHz})\right|}\,. \tag{5.11}$$

Figure 5.16 depicts the magnitude spectrum of the analytical simulation; and Figure 5.17 for DBEM simulation with MR = x6. The plots are divided in above and below sections due to the symmetry of the EAA. This is made because instead of 32 lines just 16 would be visible (a least in the analytical simulation).

---

[4] Similar to the indirect calibration usually carried out for acoustical measurements.

In Figure 5.17 it is possible to notice some peaks around 2 kHz. These distortions may be the reason for the peaks in the same frequency on the Phi vs Frequency graph, Figure 5.11. In Appendix H there are the spectrum plots for all MR values, i.e., x1, x2, x3, x4, x6, x8 and x10.

In order to compare the beamforming processing there are a set of PSFs for the following cases:

1. Figure 5.18 depicts maps for several frequencies considering MR = x6. The frequency behaviour is expected, with narrower peaks in the higher frequencies (see Section 3.3.2 for details).

2. Figure 5.19 depicts different MR coefficients for the frequency of 1 kHz. As can be noticed, it is difficult to see differences just with a visual inspection. For this reason the peak extraction was evaluated (Figure 5.11).

3. Figures 5.20 to 5.22 present a comparison between x1 and x10 in contrast to the analytical results. It is possible to observe the distinct behaviour of the sidelobes, specially in Figure 5.22, which shows the effects of a lack of mesh refinement.

It is also important to say that in the simulations of this section the sound source was a plane wave emitter, 10 m away from the centre of the coordinate system. Later in Section 5.2.6 there is a discussion concerning the sound source. All the PSFs maps were normalized with respect to the maximum value of the matrix.

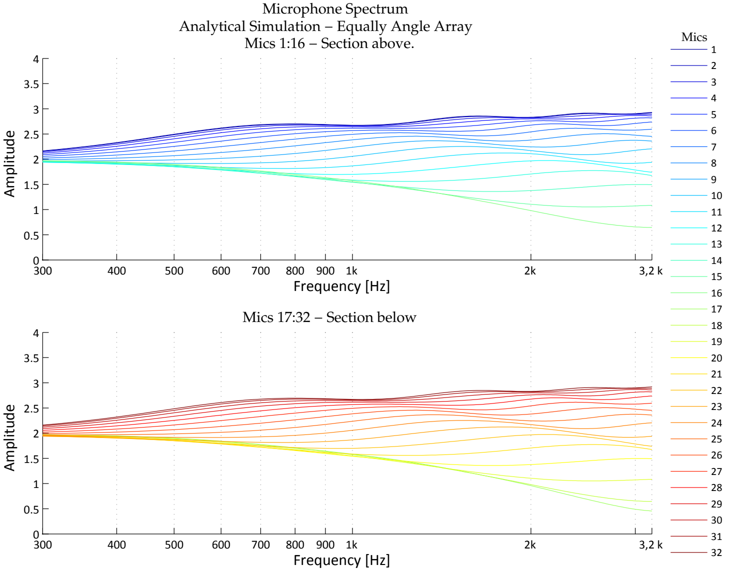

Figure 5.16: Spectrum of 32 microphones. EAA analytical simulation, df=20 Hz and source at $\phi_{in} = 30^\circ$ and $\theta_{in} = 0^\circ$.

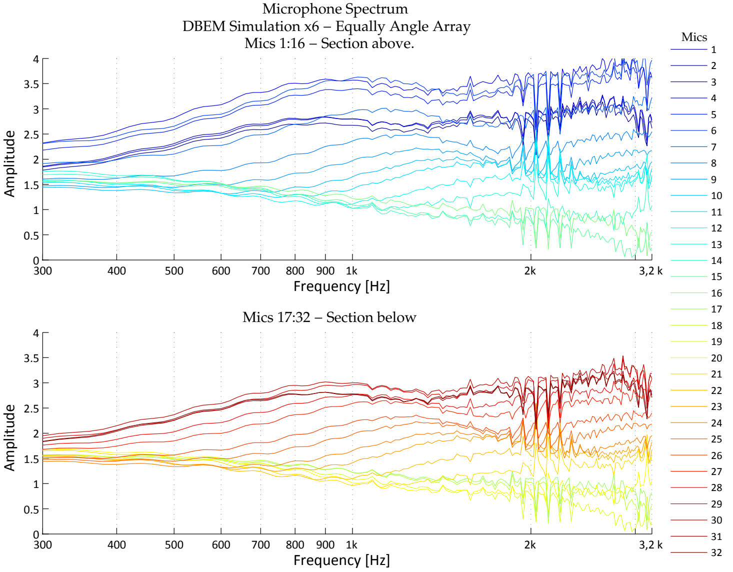

Figure 5.17: Spectrum of 32 microphones. EAA DBEM simulation for x6, df=20 Hz and source at $\phi_{in} = 30^\circ$ and $\theta_{in} = 0^\circ$.

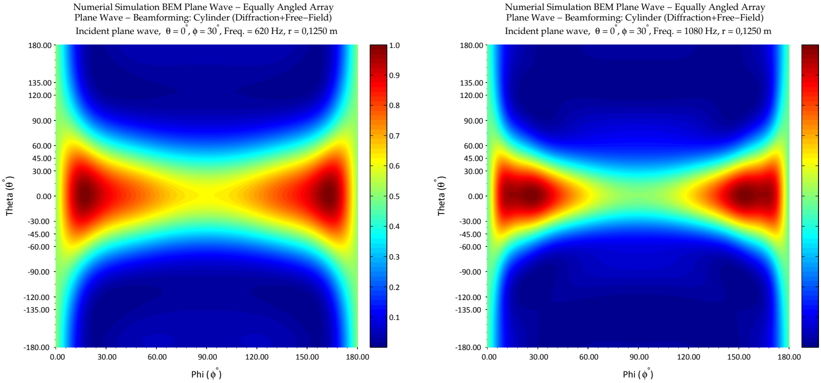

(a) 620 Hz (b) 1080 Hz

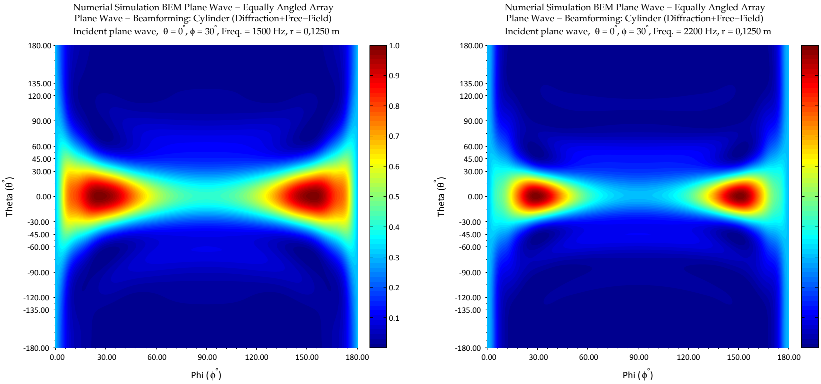

(c) 1500 Hz (d) 2200 Hz

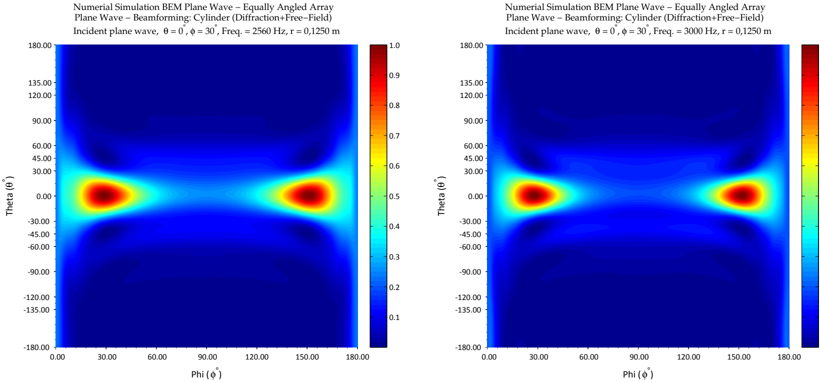

(e) 2560 Hz (f) 3000 Hz

Figure 5.18: Beamforming maps for MR = x6 and for $\phi_{in} = 30^\circ$ and $\theta_{in} = 0^\circ$.

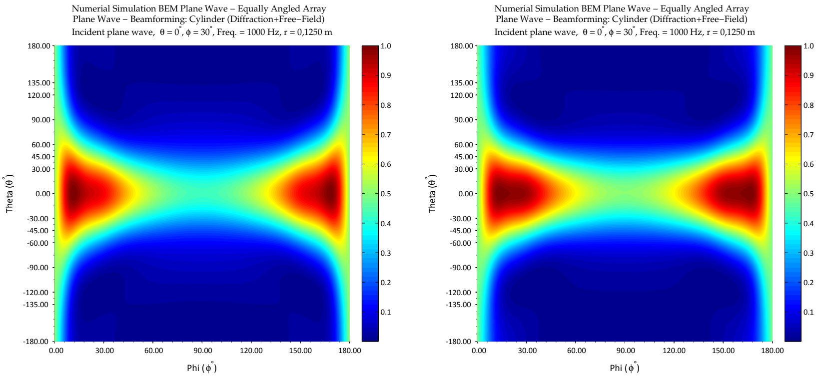

(a) x1 (b) x2

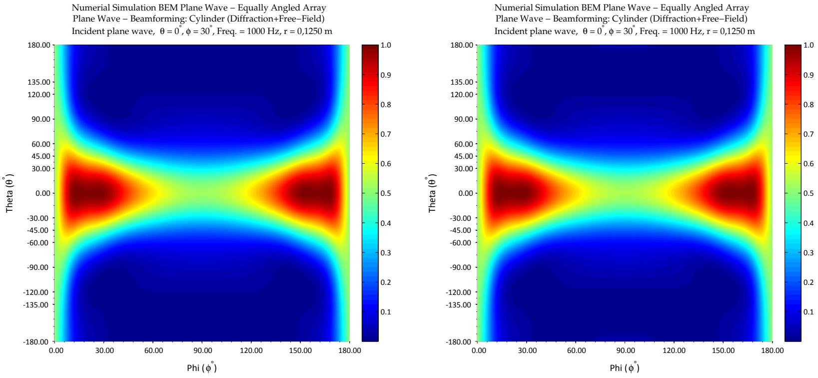

(c) x3 (d) x4

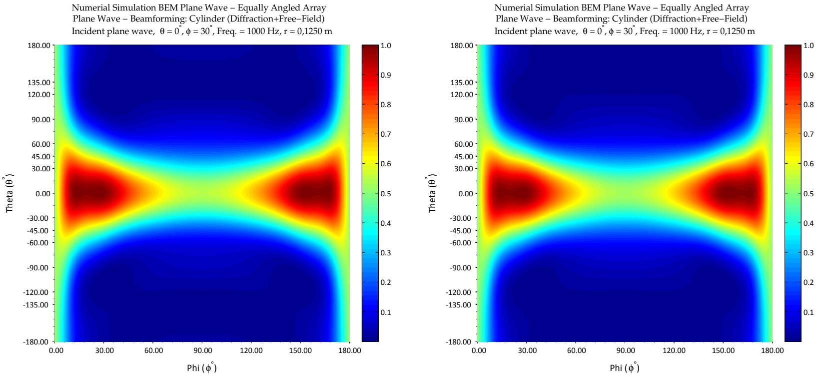

(e) x6 (f) x8

Figure 5.19: Beamforming maps for different MR at 1 kHz and for $\phi_{in} = 30^\circ$ and $\theta_{in} = 0^\circ$.

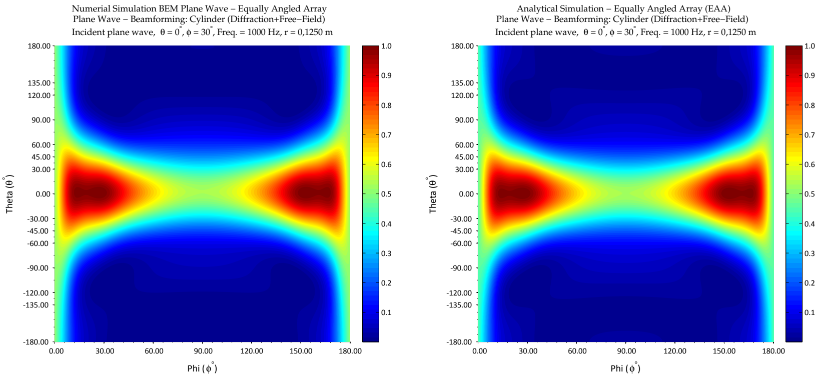

(g) x10

(h) Analytical

Figure 5.19: Beamforming maps for different MR (and analytical) at 1 kHz for $\phi_{in} = 30^\circ$ and $\theta_{in} = 0^\circ$.

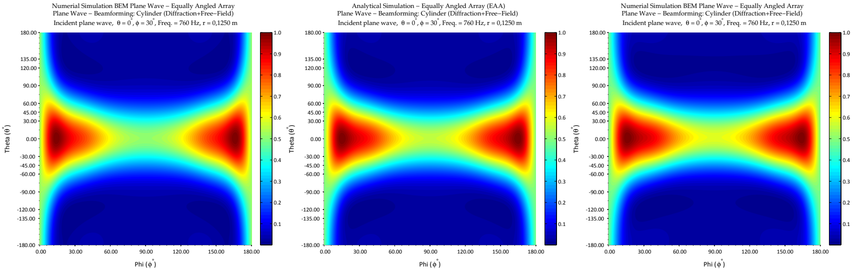

(a) x1 (b) Analytical (c) x10

Figure 5.20: Beamforming maps for MR = {x1 and x10} and for analytical at 760 Hz ($\phi_{in} = 30^\circ$ and $\theta_{in} = 0^\circ$).

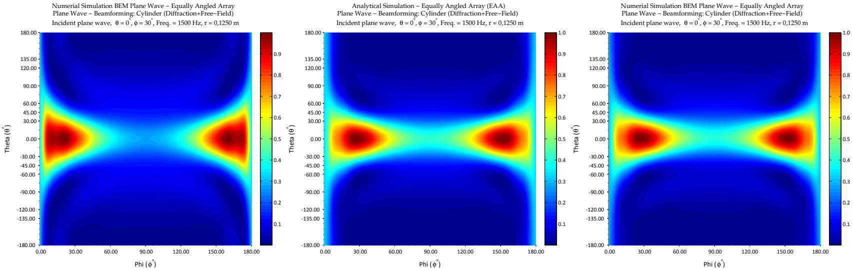

(a) x1 (b) Analytical (c) x10

Figure 5.21: Beamforming maps for MR = {x1 and x10} and for analytical at 1,5 kHz ($\phi_{in} = 30^\circ$ and $\theta_{in} = 0^\circ$).

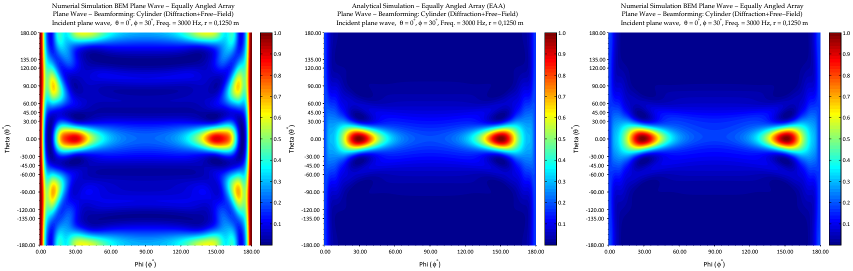

(a) x1 (b) Analytical (c) x10

Figure 5.22: Beamforming maps for MR = {x1 and x10} and for analytical at 3 kHz ($\phi_{in} = 30^\circ$ and $\theta_{in} = 0^\circ$).

5.2.4 Cylinder Length

Some cases were simulated with different cylinder lengths to attempt to detect problems and/or differences in the identification of the sound source.

The lengths tested were: 0,250 m; 0,500 m; 1,000 m; 2,000 m; 3,000 m; 4,000 m; 5,000 m; 8,000 m; and 10,000 m. All the models were built with MR=x6 meshing and the Equally Angled Array (EAA). The field points are at the same positions for all the cases.

It is possible to notice in Figure 5.23[5] that there are no differences or effects (for the EAA) from changing the length of the cylinder, i.e., the main lobe maintains the same characteristics.

5.2.5 Cylinder Radius

Some cases were simulated with different cylinder radii, this change leads to unequal results because

1. the separation among microphones is different (larger or smaller), influencing the spatial aliasing;
2. if a scale model is considered, the proportion scale will be distinct;
3. if a monopole is chosen as the sound source, depending on the distance, some effects could appear due to the change in distance to the mesh points.

All models were meshed considering MR=x6, and the radii tested were 0,0625 m; 0,1250 m; 0,2500 m; and 0,5000 m (length of 3,0 m). Figures 5.24 and 5.25 depict the beamforming maps for the different cases. In all the cases the EAA was considered and the field points were taken 0,5 mm above the 3D model surface.

The behaviour of the main lobe in Figures 5.24 and 5.25 is expected since it is a beamforming resolution issue connected to the microphone positioning. This was previously discussed in Sections 3.3.4.1 and 4.3. The difficulties in increasing the radius arise because doubling the radius also doubles[6] the number of elements.

---

[5] In Appendix H there are the plots for 500 Hz.

[6] There are two modes mainly: the *in-core* and the *out-of-core* processing. If there is enough Random Access Memory (RAM), the in-core is performed (faster), otherwise the problem is split into blocks and the out-of-core calculates the problem in parts (slower).

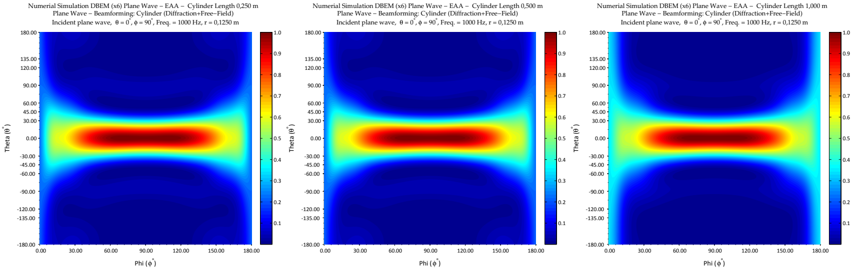

(a) 0,250 m (b) 0,500 m (c) 1,000 m

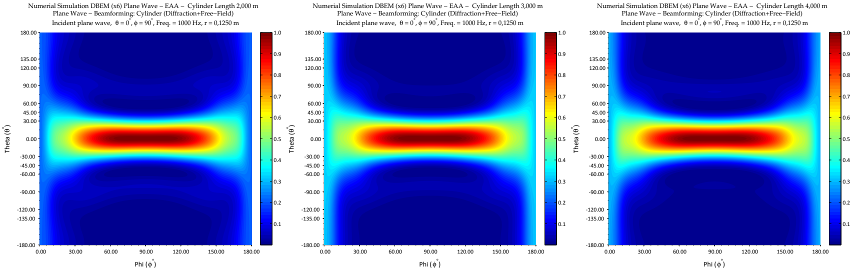

(d) 2,000 m (e) 3,000 m (f) 4,000 m

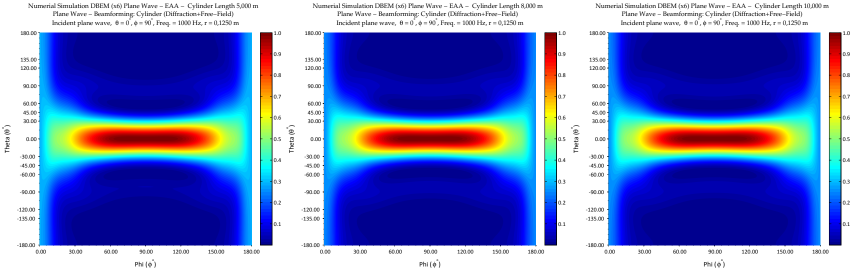

(g) 5,000 m (h) 8,000 m (i) 10,000 m

Figure 5.23: Beamforming maps for several cylinder lengths, at 1 kHz, EAA, $\phi_{in} = 30^\circ$ and $\theta_{in} = 0^\circ$.

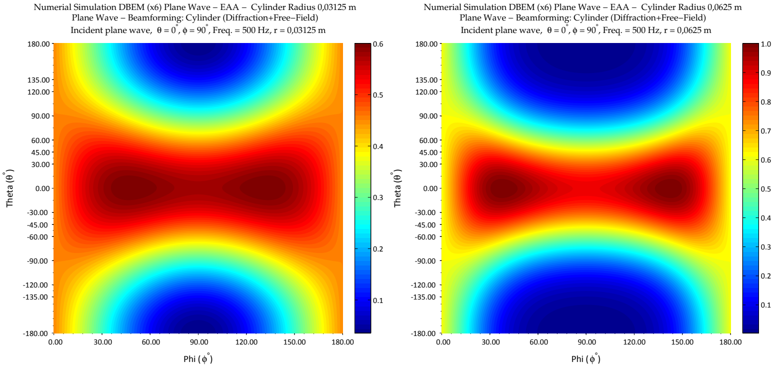

(a) 0,03125 m (b) 0,0625 m

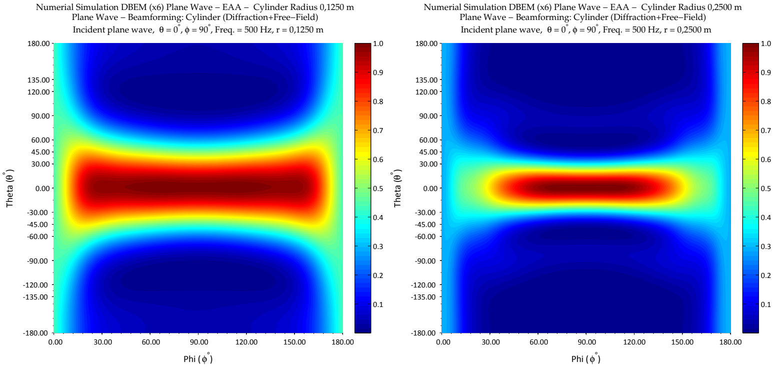

(c) 0,1250 m (d) 0,2500 m

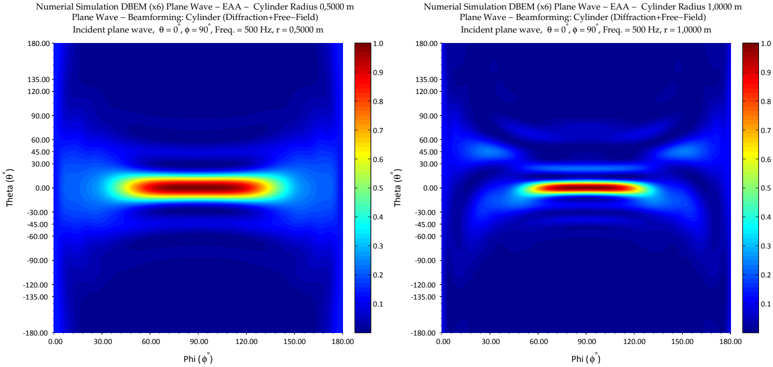

(e) 0,5000 m (f) 1,0000 m

Figure 5.24: Beamforming maps for different cylinder radius at 500 Hz. Tested radii: 0,03125 m; 0,0625 m; 0,1250 m; 0,2500 m; 0,5000 m; and 1,0000 m. Plane wave sound source at $\phi_{in} = 90°$, $\theta_{in} = 0°$.

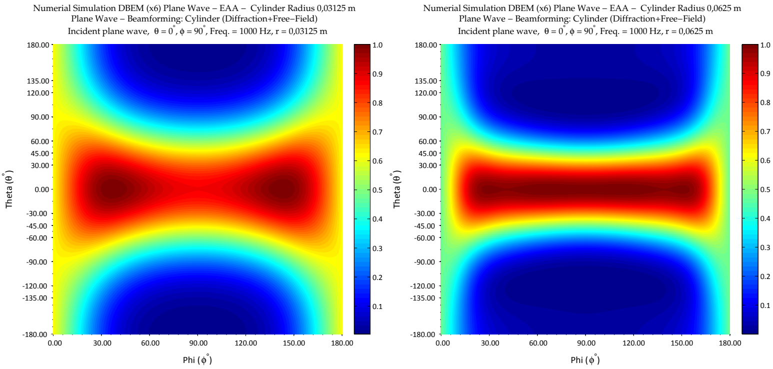

(a) 0,03125 m (b) 0,0625 m

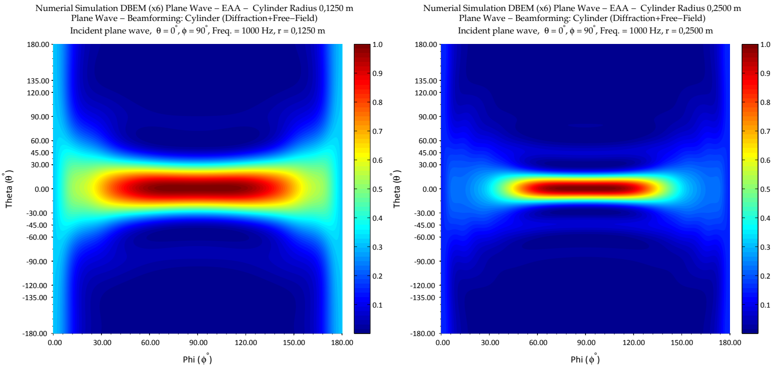

(c) 0,1250 m (d) 0,2500 m

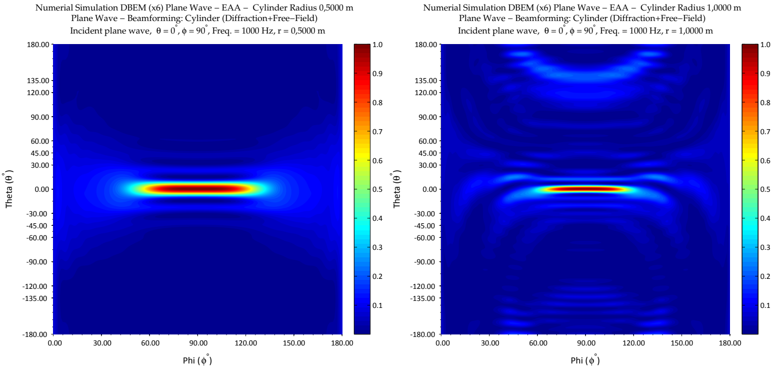

(e) 0,5000 m (f) 1,0000 m

Figure 5.25: Beamforming maps for different cylinder radius at 1000 Hz. Tested radii: 0,03125 m; 0,0625 m; 0,1250 m; 0,2500 m; 0,5000 m; and 1,0000 m. Plane wave sound source at $\phi_{in} = 90^\circ$, $\theta_{in} = 0^\circ$.

5.2.6 Sound Source

Since there are a few models for the sound source simulation, some distances considering the plane wave and the monopole were evaluated. All models were meshed considering MR=x6.

In the DBEM calculation the total sound field p_t is

$$p_{t_{\text{DBEM}}} = p_i + p_s \,, \tag{5.12}$$

where p_i is the incident field (or free-field pressure) and p_s is the scattered field. For all series of simulations the ϕ angle was discretized at each 10°, like in the schema of Figure 5.26[7].

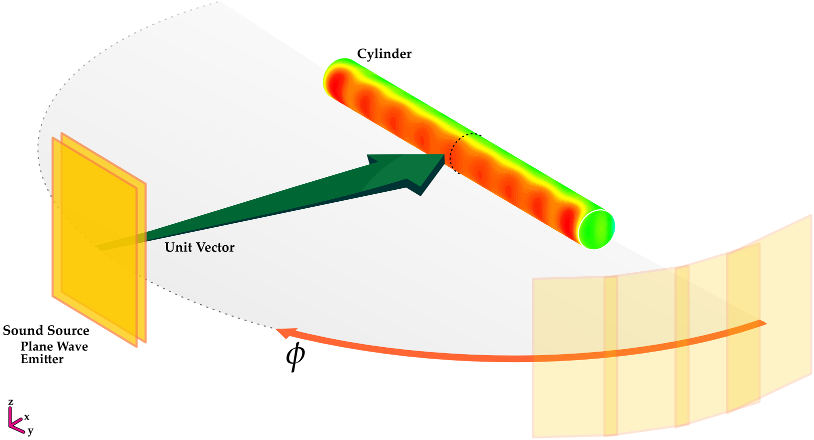

Figure 5.26: Schema of the cylinder simulations. The sound source sweeps the ϕ angle at each 10° (from 0° to 180°).

5.2.6.1 Plane Wave

As described in the Section 2.2 (and in the Sysnoise Manual [129]), for a plane wave, the incident field varies in free space as

$$p = \hat{p}\, \mathrm{e}^{-jkd} \quad \text{in} \;\; \mathrm{N/m^2} \;\; \text{or} \;\; \mathrm{Pa}, \tag{5.13}$$

---

[7] In the example, the surface pressure on the cylinder is 1 kHz and the sound source is a plane wave emitter at $\phi_{in} = 90°$, $\theta_{in} = 0°$ and 10 m away.

where d is the perpendicular distance from the source plane to the point where the incident field is evaluated; k is the wavenumber; and $\hat{p}$ is the incident pressure amplitude, constant throughout space (Figure 5.27), but its phase varies linearly with d. The model used is considered laterally infinite and creates the sound field in just one direction from the emitter, Figure 5.28. The total pressure is depicted in Figure 5.31 (a).

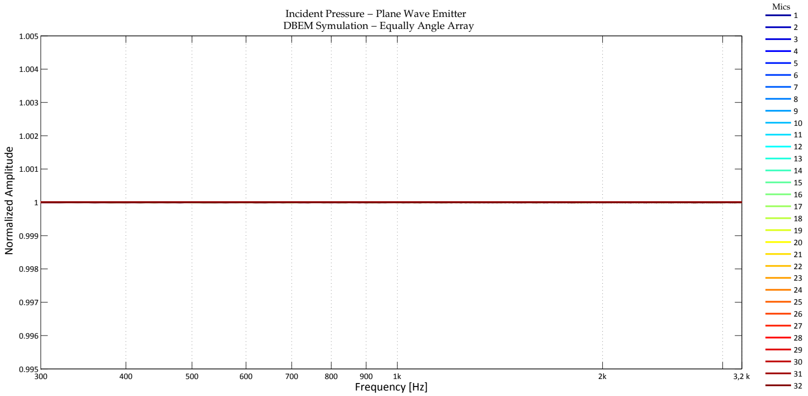

Figure 5.27: Incident pressure at the 32 field points. Plane wave emitter 10 m away from the cylinder and $\phi_{in} = 90°$.

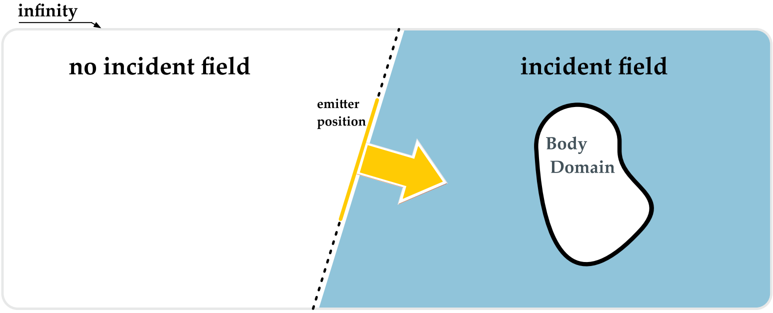

Figure 5.28: Plane wave model used in the DBEM simulations.

5.2.6.2 Monopole

As derived in Section 2.1 the monopole incident field varies in free space as

$$p = \frac{p_{\mathrm{pk}}}{R}\, \mathrm{e}^{-jkR} \quad \text{in} \;\; {}^{\mathrm{N}}/_{\mathrm{m}^2} \;\; \text{or} \;\; \mathrm{Pa}, \tag{5.14}$$

where R is the distance from the source to the point where the incident field is evaluated; k is the wavenumber; and p_{pk} is the *peak* pressure amplitude of the incident wave (in ${}^{\mathrm{N}}/_{\mathrm{m}}$) at a distance away from the source (see Figure 5.29). Figure 5.30 illustrates the simulation setup.

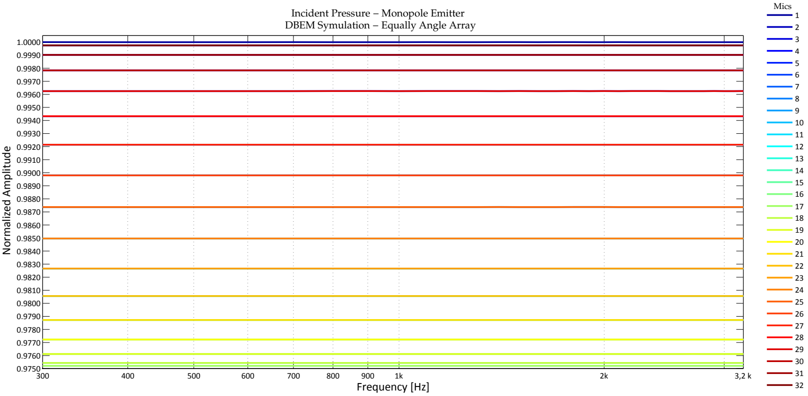

Figure 5.29: Incident pressure at the 32 field points. Monopole emitter 10 m away from the cylinder and $\phi_{in} = 90°$.

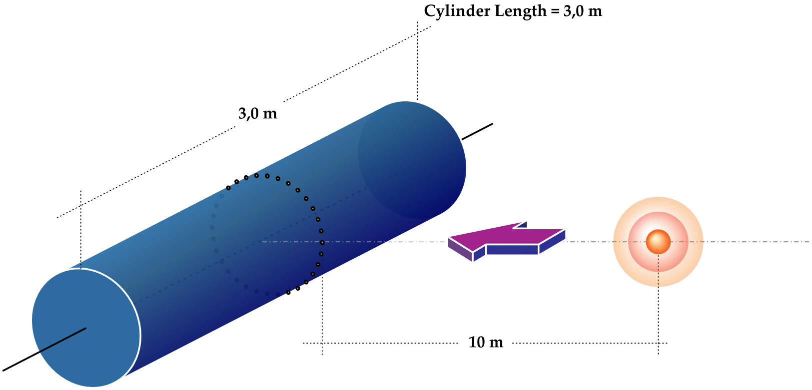

Figure 5.30: DBEM, example of monopole source setup.

It is possible to notice in Figure 5.29 that the amplitudes are distinct[8]. However, since the field points are close to each other these amplitude differences are small.

The plane wave and the monopole "measured" total pressures are depicted in Figures 5.31 (a) and 5.31 (b), respectively. The subtraction of these two graphs yield small differences, as shown in Figure 5.31 (c). For this case study the differences in the incident pressures are small. However, for a monopole source concern must be taken considering its positioning and the model size.

5.2.7 Considerations

For further research combining beamforming with BEM, it is important to estimate the mesh refinement requirement to avoid losing time without advantageous results. Section 5.2.3 shows that even without adequate mesh refinement the main lobe information can be still recovered.

One interesting point in the DBEM simulation is that when the problem is solved, the field points are calculated separately (and faster). That means other array geometries can be estimated without solving the BEM problem again.

Consider the EAA, if the source position is simulated in a different θ angle. Due to the symmetry, the effects would be the same, but virtually with a distinct "microphone #1".

---

[8] See page 14 for a better understanding.

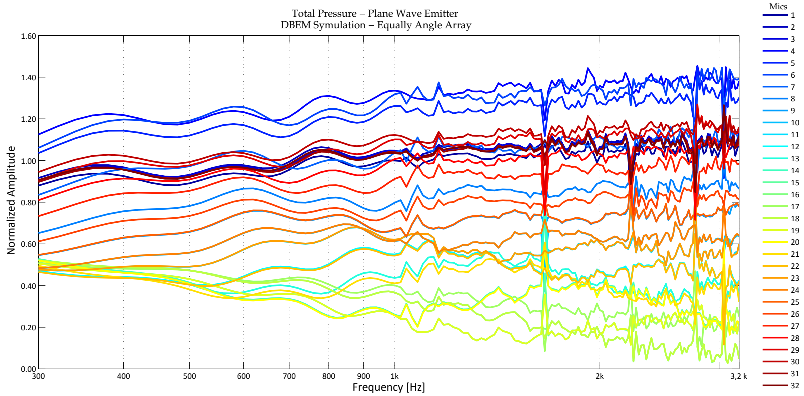

(a) Plane Wave - Total Pressure p_t

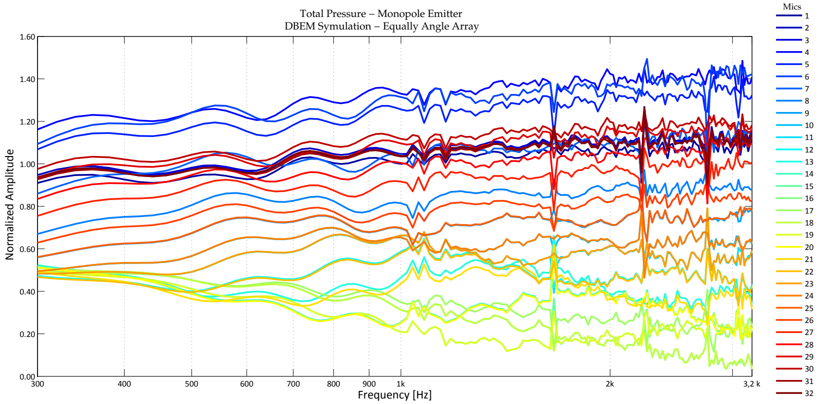

(b) Monopole - Total Pressure p_t

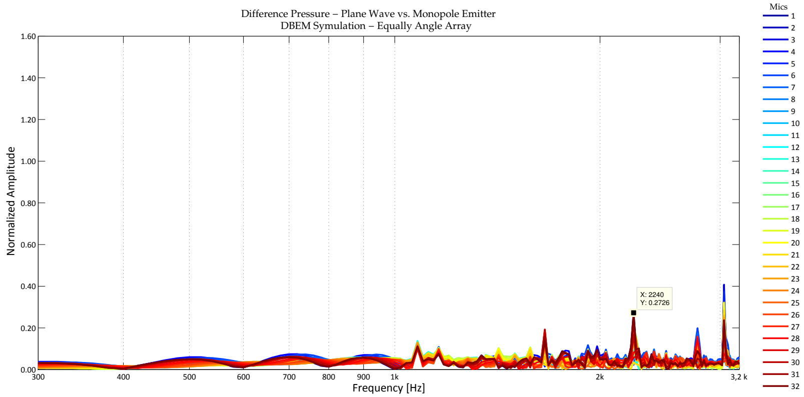

(c) Total Pressure Difference - Plane Wave vs. Monopole

Figure 5.31: Total pressure p_t ($\phi_{in} = 90°$): plane wave, monopole, and the difference between (a) and (b).

5.3 Genetic Algorithm

To circumvent the mirror image problem in the EAA, the genetic algorithm is then proposed as a possible solution already attached to an optimization process. As described in Section 4.3.1.1, the mirror is the effect of the symmetric positioning with respect to the axis of the cylinder. Therefore, the geometry change will result in beamforming maps with different patterns (or PSFs). This section will present the basics about GA and its parameter modelling.

In the pursuit for the best solution the fact arises that the term "best" implies that there are more than one solution and such solutions are not of equal value. Accordingly, this solution will be dependent on the problem's formulation. Fundamentally, optimization is a process which seeks continuous improvement. It consists of trying variations on an initial concept (or problem) and uses the successive information gained with the iterations to improve on the idea.

Genetic Algorithm[9] (GA) [143, 144] is an optimization and search technique for finding approximate solutions. The technique uses the principles of genetics and natural selection such as heredity, mutation, and crossover, as it is considered to be a particular class of evolutionary algorithms.

GA is commonly implemented using genetic programming (GP), it allows a population - composed of individuals that represent abstract solutions for a problem - to evolve under specific selection rules. The process searches for solutions that best fit the given problem. This "survival of the fittest" idea was first introduced by Darwin[10] in his work *On the Origin of Species* (1859) [145]. The whole process can be divided into some basic steps:

a) The evolution begins from a generated randomly set of individuals (solutions) and continues through the cross of these individuals over the generations.

b) In each generation the fitness level of each solution is evaluated; some individuals are selected, crossed, and/or mutated to form the population of the next generation.

---

[9] Originally, the method was developed by John Holland [140] over the course of the 1960s and 1970s and finally made popular by one of his students, David Goldberg [141, 142].

[10] Charles Robert Darwin (1809 - 1882) was an English naturalist/scientist who established the foundations of the theory of evolution. The theory states that all living beings have a common ancestor. He published his work with cogent evidence in the book *On the Origin of Species* [145].

c) The new population is then used as input for the next iteration of the algorithm. This process is repeated for several generations, until they converge to a satisfactory solution.

Figure 5.32 represents the basic cycle of the genetic algorithm. These steps will be described in greater detail in the following sections.

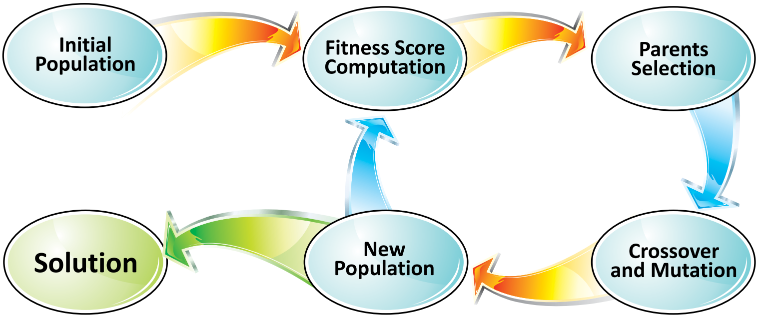

Figure 5.32: Basic cycle of the genetic algorithm.

5.3.1 Simple Genetic Algorithm

The Simple Genetic Algorithm (SGA) is the most common class of genetic algorithms. It uses only simple computational operations like copying strings and swapping partial strings [144]. The basic procedures of SGA are reproduction, crossover and the mutation. The following sections describe each of these items in the context of array modelling.

5.3.1.1 Initial Definitions

Before describing the SGA procedures, it is important to define the basic concepts of the technique and how they are modelled to solve the problem. The most basic concepts in genetic algorithms are genes and chromosomes [146]. The chromosome represents a single solution, or part of it. One individual - the entire solution of the problem - is composed of at least one chromosome, which is subdivided in genes, Figure 5.33. The genes represent the minor factor of control and the encoding of the chromosome information.

To represent the geometry of a microphone array, the chromosomes were defined as matrices with three lines (one for each coordinate axis) and

m columns, where m represents the desired number of microphones. The lines represent the coordinates of each microphone on the r, θ and z axis (in meters and radians), respectively, considering the zero point in Cartesian coordinates as the origin of the coordinate system.

Since the radius of the cylinder is considered constant, the line corresponding to the r axis will remain with the same value. The length is the restriction of the array on the z-axis, hence it needs to be designed for practical situations. Thus, the gene values must be restricted in order to only allow values below the array's maximum length. Also, since real mics have a finite size (like 1/2 inch), they cannot be placed in close proximity. Thus, a grid is proposed to determine the minimum distance among them. Each microphone - or column of the matrix - is considered to be a gene inside the chromosome and each row corresponds to an individual's genotype, Figure 5.33.

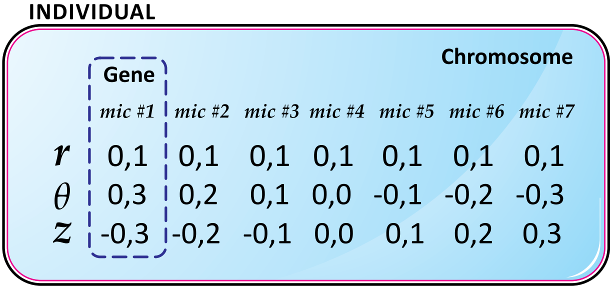

	mic #1	mic #2	mic #3	mic #4	mic #5	mic #6	mic #7
r	0,1	0,1	0,1	0,1	0,1	0,1	0,1
θ	0,3	0,2	0,1	0,0	-0,1	-0,2	-0,3
z	-0,3	-0,2	-0,1	0,0	0,1	0,2	0,3

Figure 5.33: Chromosome, every m^th column corresponds to a gene or a microphone.

To start the algorithm an initial population of individuals which will evolve to the desired solution is needed. In SGAs, the initial population is usually created randomly with the number of individuals chosen by the coder[11]. In this case, each individual has been defined as one chromosome, representing one possible geometry. The population is then created by generating random coordinates for each microphone of each individual (respecting the radius and grid restrictions).

---

[11] The term "coder" refers to the engineer who program/create the software.

5.3.1.2 Reproduction and Fitness Function

The reproduction process involves the selection of the individuals according to their fitness level. It starts with an initial population, and in subsequent iterations it uses the newer generations produced by the algorithm.

The first step in this procedure is to rank the individuals according to their capacity to solve the problem. This is done according to the *fitness score* (FS), which is calculated by the *fitness function* (FF) [147]. The fitness function is an equation that describes how the individuals should evolve and is equivalent to the environment in biological evolution. This equation must take into account the constraints of the problem and must be able to score the individuals fairly.

The fitness function is one of the most important points in GAs, since it defines how the population will evolve. A minor error in its designing can make the algorithm converge to unexpected results. Thus, the formulation of this equation must be a point of concern in modelling the problem.

The implementation of this work considers only one frequency for each score. However, it is possible to extend to multiple (n) frequencies, for example, by performing a weighted average of the fitness scores for the frequencies which the algorithm should maximize,

$$\mathrm{FS}\ (f_1 \cdots f_n) = \frac{\alpha_1 * \mathrm{FS}(f_1) + \alpha_2 * \mathrm{FS}(f_2) + \ \cdots \ + \alpha_n * \mathrm{FS}(f_n)}{(\alpha_1 + \alpha_2 + \cdots + \alpha_n)}, \qquad (5.15)$$

where α_n is the chosen weight for a given frequency f_n.

The fitness function projected in this work has three main parts: dynamic range, beamwidth and symmetry,

$$\mathrm{FS}\ (f) = \frac{S_{\mathrm{DR}}.W_{\mathrm{DR}} + S_{\mathrm{BW}}.W_{\mathrm{BW}} + S_{\mathrm{Sy}}.W_{\mathrm{Sy}}}{W_{\mathrm{DR}} + W_{\mathrm{BW}} + W_{\mathrm{Sy}}}, \qquad (5.16)$$

where S_{DR} is the dynamic range score, S_{BW} is the beamwidth score, and S_{Sy} is the symmetry score; and W_{DR}, W_{BW} and W_{Sy} are the respective weights.

Symmetry Score

The symmetry score calculates the symmetry of the main lobe. In order to calculate it, the position of the main lobe peak (P_k), and an open angle where the symmetry should be evaluated must be known. In total, three angles are evaluated,

- an original open angle (O),
- the open angle divided by two ($O_{.5} = O/2$), and
- the open angle times a constant ($O_{\mathfrak{c}} = O * \mathfrak{c}$).

For each O angle, $a = {}^{O}/_{2}$ and eight points are evaluated around the main lobe peak. Considering P_k a cell position in the PSF matrix, it has two dimensions, $P_k = (\phi, \theta)$, and the selected points are:

$$P_n(O) = \left\{ \begin{array}{l} \left. \begin{array}{l} P_1 = P_k + (a, 0) \\ P_2 = P_k + (-a, 0) \end{array} \right\} \phi \text{ axis} \\ \left. \begin{array}{l} P_3 = P_k + (0, a) \\ P_4 = P_k + (0, -a) \end{array} \right\} \theta \text{ axis} \\ \left. \begin{array}{l} P_5 = P_k + (a/\sqrt{2}, a/\sqrt{2}) \\ P_6 = P_k + (a/\sqrt{2}, -a/\sqrt{2}) \\ P_7 = P_k + (-a/\sqrt{2}, a/\sqrt{2}) \\ P_8 = P_k + (-a/\sqrt{2}, -a/\sqrt{2}) \end{array} \right\} \text{diagonals} \end{array} \right. \tag{5.17}$$

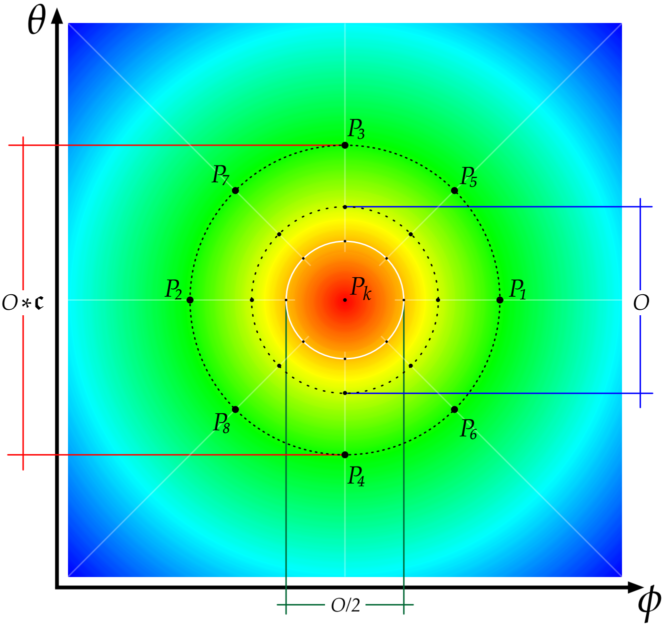

Figure 5.34: Evaluations points $P_n(O)$ around the main lobe.

For each geometrical point $P_n(O)$ the sound pressure[12] is read, then the value is subtracted of P_{pk}, the result is converted to dB, and the final value is stored as P_{pn}. If two squares are circumscribed in one circumference of Figure 5.34, a given point n and a next point (in relation to the square corner) are taken; in the following, the comparison pairs are defined: (P_{p1}, P_{p4}), (P_{p4}, P_{p2}), (P_{p2}, P_{p3}), (P_{p3}, P_{p1}), (P_{p5}, P_{p6}), (P_{p6},P_{p8}), (P_{p8},P_{p7}), and (P_{p7},P_{p5}).

With the pressure points taken, first, a paired comparison is carried out for calculating coherence between the points

$$\mathrm{Co}_i = \frac{\min(P_{pn}, P_{pn}^{nsqc})}{\max(P_{pn}, P_{pn}^{nsqc})} \,, \tag{5.18}$$

where P_{pn} is the pressure at point n and P_{pn}^{nsqc} is the *next square corner* pressure point; $\min(\cdot)$ is a function that returns the element with the minimum value; and $\max(\cdot)$ is a function that returns the element with the maximum value. In the following, the score for one given opening angle O is summed as

$$S_O = \frac{1}{8}\sum_{i=1}^{8} \mathrm{Co}_i \,. \tag{5.19}$$

Finally, the symmetry score is summed and weighted concerning the score for a chosen angle O and constant $\mathfrak{c}$ as

$$S_{\mathrm{Sy}} = \frac{S_O.W_O + S_{O_{.5}}.W_{O_{.5}} + S_{O_\mathfrak{c}}.W_{O_\mathfrak{c}}}{W_O + W_{O_{.5}} + W_{O_\mathfrak{c}}} \,. \tag{5.20}$$

Beamwidth Score

The beamwidth score is calculated based on a vector of values containing ($P_{p1} \cdots P_{p8}$) for only the open angle O (and not for $O_{.5}$ and $O_\mathfrak{c}$). It is defined as

$$S_{\mathrm{BW}} = \frac{\max(P_{p1} \cdots P_{p8})}{\mathrm{Decay}_{\mathrm{exp.}}(\mathrm{dB})} \,, \tag{5.21}$$

where $\mathrm{Decay}_{\mathrm{exp.}}(\mathrm{dB})$ is the expected decay in dB for the open angle O.

---

[12] P_{pk} is the pressure value of the geometrical point P_k, and $P_{pn} = P_n(O) - P_{pk}$ in dB .

This value is empirically defined, for example, for an angle of $O = 12^\circ$ (in the PSF) a decay of 3 dB would be expected.

Dynamic Range Score

The dynamic range score is defined as the relationship between the dynamic range found and the expected DR[13],

$$S_{\mathrm{DR}} = \frac{\mathrm{DR}}{\mathrm{Expec.}_{\approx}(\mathrm{DR})} , \tag{5.22}$$

where $\mathrm{Expec.}_{\approx}(\mathrm{DR})$ is an empirically chosen value. An approximation for the expected DR is usually calculated as $10 * \log(m)$, with m as the total number of microphones (see Section 3.3.3 for details).

5.3.1.3 Evolution Functions

There are three basic instruments in the evolution of individuals: selection of the progenitors, crossover, and mutation [148]. In addition, elitism is one of the possible tools for keeping the best individuals through the next generation. These instruments can be represented in a mathematical form in order to be simulated for the virtual world.

Selection of the Progenitors

There are several ways to select the progenitors, in this work, the *Roulette Wheel* is used. It is one of the most common selection methods [144].

In the roulette wheel, the chances of being selected are proportional to the fitness score of the individual. This ensures that the fittest individuals are selected more frequently, while those with lower scores will be underprivileged, see Figure 5.35. At each crossover operation the roulette is triggered twice in order to select the two parents for the descendants.

The roulette wheel is modelled as a list, with each individual placed within the list according to their fitness score. In this dissertation, the number of times that each individual is put in the list is defined as

---

[13] As described in Section 3.3.2, the DR for each frequency is evaluated as the difference between the mainlobe and the highest sidelobe in the PSF.

$$n_i = \exp\left(\mathrm{FS}_i * \frac{1+\sqrt{5}}{2} * \pi\right), \tag{5.23}$$

where n_i is the number o times rounded up, and FS_i is the fitness score for the i^{th} individual. In order to prevent that the list becomes too large n_i is scaled so that the list size can be determined,

$$n_i' = n_i * \mathrm{L}_{\text{size}} * \underbrace{\left(\sum_{i=1}^{\text{last}} n_i\right)^{-1}}_{\text{old list size}}, \tag{5.24}$$

where L_{size} is the desired length of the new list, and is defined as

$$\mathrm{L}_{\text{size}} = \text{Pop. Size} * V, \tag{5.25}$$

where V is a constant depending on the computer's memory. This ensures that the list size does not affect the proportions, since Equation (5.24) is compressing it.

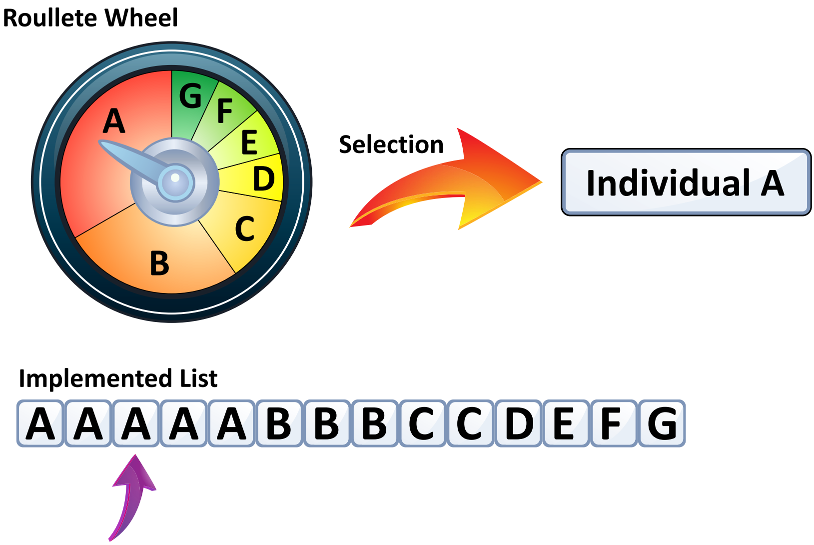

Figure 5.35: Basic idea behind the roulette wheel.

Crossover and Mutation

The crossover operator [149] is the main tool for change and evolution in the genetic algorithm. It performs the recombination between the chromosomes of both parents selected by the roulette wheel in order to find more suitable descendants. There are several crossover techniques, like the single point crossover, the two point crossover, the ordered crossover, and others [144].

In the single point crossover two mating individuals have their chromosomes sliced once and the resulting sections are exchanged. The slice point is defined as $m/2$, where m is the number of microphones, rounded up. The exchange occurs as depicted in Figure 5.36.

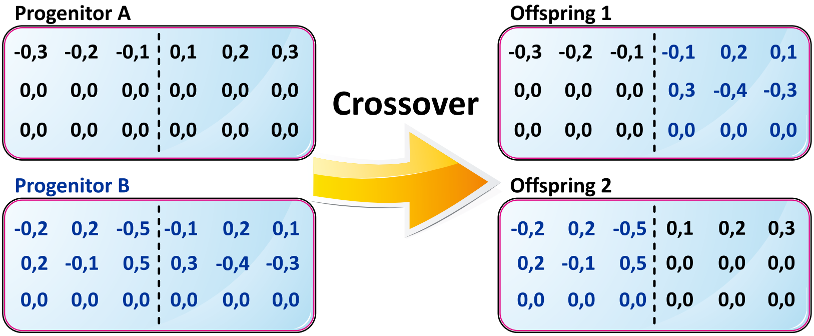

Figure 5.36: Single point crossover procedure.

In the two-point crossover, two mating individuals have their chromosomes sliced twice and the sections are exchanged. The slice points are defined as $m/3$ and $2m/3$, where m is the number of microphones. The exchange occurs as depicted in Figure 5.37.

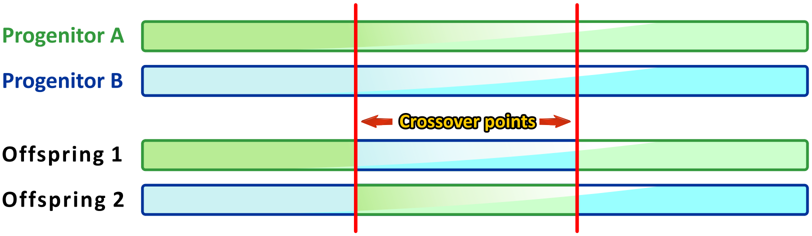

Figure 5.37: Two-point crossover procedure.

Both crossover techniques were implemented, but the two-point was utilised by showing most effective results in the evolution.

After the crossover, the mutation operator is applied. The mutation is responsible for genetic variation and tries to prevent the algorithm from being trapped in a local minimum. It usually occurs only in a small ratio of individuals and causes a random change in one gene of one chromosome, maintaining genetic diversity in the population. The mutation process is the sponsor of the exploration in the algorithm, since the crossover does the exploitation[14].

The mutation operator [150] was modelled like a routine that randomly selects one gene of the chromosome - or array's microphone - and randomly changes the coordinates (respecting the length and grid restrictions), as illustrated in Figure 5.38.

Individual A

-0,3	-0,2	-0,1	0,1	0,2	0,3
0,0	0,0	0,0	0,0	0,0	0,0
0,0	0,0	0,0	0,0	0,0	0,0

New Individual

-0,3	-0,2	-0,1	-0,3	0,2	0,3
0,0	0,0	0,0	0,2	0,0	0,0
0,0	0,0	0,0	0,0	0,0	0,0

Figure 5.38: Mutation procedure.

Elitism

Elitism [151, 152] ensures that at least one copy of the best individuals of a generation is propagated into the next one. It eliminates the chance of any undesired loss of information during the mutation stage and its convergence is guaranteed (that is, once a global optimum has been discovered, the evolutionary algorithm converges to that optimum). Also, it usually boosts the performance of the GA algorithm.

5.3.2 Hybrid Genetic Algorithm

Even finding satisfactory results in a simple and substantially faster way, the use of SGA for microphone array can be still refined. An interesting approach to speed up convergence by avoiding unnecessary calculations is the Hybrid Genetic Algorithm (HGA).

---

[14] Exploration and exploitation are terms usually used in genetic nomenclature.

In SGA the initial population is generated randomly. This generates a vast genetic diversity (which is something good for the algorithm), but also creates a considerable waste of time calculating poor configurations. One way to approach this problem is to input a pre-defined population as the initial population, and, in this case, the genetic variety will be smaller. However, if the initial population is well-chosen the algorithm will need fewer individuals in the population and fewer generations to find a suitable result.

The use of heuristics in the initial population generation is one of the features of the HGA [144]. The HGA emulates a condition where the algorithm would be continuing the evolution from a previous run. There are also other possibilities to use heuristics in other procedures, most usually on improving offspring produced [144], but they will not be used in this work.

5.4 GA Simulations

In this work, the GA simulations have two main parts. The first is the test of the evolution techniques with a simpler fitness function and the second is the proper simulations with beamforming processing.

The size of population (SPOP) defines the variability of the mating pool. Large populations[15] are not convenient since the calculation time grows proportionally. On the other hand, small populations will not have the variability to achieve a great part of the possible distributions, consequently not allowing a deep search.

The number of generations (NGEN) defines the depth of the search. If this number is too small, it can prevent the population from evolving and, thus, compromising the results. On the other hand, a large number of generations is also not convenient due to the calculation time.

The best option then is to use a balanced relationship between size of population and number of generations. It is recommended to iterate the algorithm for a certain number of generations until the population stops evolving (end of exploitation) and then continue a little more to permit the mutation to explore more solutions.

Crossover rate[16] (CSR) specifies the percentage of the next

---

[15] In Section I.1, Appendix I, there is one discussion concerning the attempt to reduce the problem size.

[16] The word *rate* (for crossover and mutation) can also be found as *probability* in the literature.

generation that will be formed by new individuals generated by the crossover operation. This rate is used to allow random individuals to be moved directly to the next generation (without crossover) so that it maintains the mating pool more continuous.

The mutation rate[16] (MUR) specifies the percentage of individuals that will suffer mutation. The higher the rate, the closer to a random search the algorithm will be and a larger variability of the mating pool will arises.

Finally, the elitism rate (ELR) is an advanced parameter that ensures the continuity of the best results. Usually, it is complementary to the crossover rate. For example, if CSR=90% then ELR=10%. It defines the percentage of the best individuals of the mating pool that will be directly moved to the next generation, ensuring that good results will not be lost. The value of this parameter is defined considering the population size and always safeguarding one, two, or three of the best results. If the ELR is not complementary, the new population will be composed by individuals produced by the crossover, individuals selected by the ELR, and random individuals from the previous population passed to the new one, in order to complete the initial SPOP set.

5.4.1 Test of GA Evolution

In order to prove the evolution techniques described in Section 5.3 a simpler *fitness function* is proposed. The goal of the FF is to place all the microphones on the right border of the cylinder, that is

$$\mathrm{FS}_{\mathrm{border}} = \frac{\sum_{i=1}^{m} z_i}{Z_{\mathrm{limit}} * m}, \tag{5.26}$$

where z_i is the coordinate for the i^{th} microphone; Z_{limit} is the border of the cylinder and m is the number of microphones. The simulation is independent of beamforming as it is just a simple minimization problem. The $\mathrm{FS}_{\mathrm{border}}$ will be one when the algorithm achieves the EAA from a random first scene.

5.4.1.1 Parameters Performance

Several parameters of the GA were tested: size of population, number of generations, roulette wheel, crossover rate, mutation rate, and list size ($\mathrm{L}_{\mathrm{size}}$). The simulations and gathering of GA data will serve as the basis for the GA-Beamforming.

The first parameter evaluated was the crossover rate, 9n which two types of tests were carried out, one with fixed ELR (5%) and the other with complementary ELR. The crossover rate values tested were 20%, 40%, 50%, 60%, 80% and 95%. The FS was observed the along 2000 generations, as depicted in Figures 5.39 and 5.40.

The tests with complementary ELR have provided much better results, Figure 5.39. The best result was found for the combination CSR=80% with ELR=20%, which gives 16 new individuals and 4 elite for a given new generation of 20 individuals. For this case, the evolution is faster (purple line) and it also has achieved the maximum FS. It is also possible to notice that the evolution curve is similar to a log function. This means that the evolution occurs more quickly in the early generations. The results of non-complementary ELR (Figure 5.40) have approximately the same behaviour. However, it is important to mention that with a fixed ELR the new generations will have random chromosomes from the previous population. For this last case, a further research must be done as the results are inconclusive.

The mutation rates tested were 20%, 30%, 40%, 60%, 80% and 95%, Figure 5.41. Even with similar evolution behaviour, if the MUR value is high it impacts in the maximum fitness. Thus, an intermediate value keeps the variability and hold the same performance. Since the mutation implemented just changes one gene, a 40% MUR cannot be considered of great impact. The textbooks about GA do not recommend high MUR values because depending on the formulation, it could or slow or confuse the process.

For the parental selection (see page 174), four types of roulette wheels have been tested: linear[17] and exponential (Equation (5.23)), with single point and two-point crossover. It is possible to see in Figure 5.42 that the exponential with two-point crossover has substantially improved the speed and the maximum FS with respect to the linear single point crossover.

To demonstrate that the $\mathrm{L}_{\mathrm{size}}$ do not affect the proportions in GA evolution, a V sweep was carried out (see Equation (5.24)). As can be seen in Figure 5.43, there are only very small differences, which are inherent to the evolutionary process.

---

[17] In the linear roulette wheel, the number of times in the list (n_i) is proportional to the fitness score without applying the exponential operator of Equation (5.23).

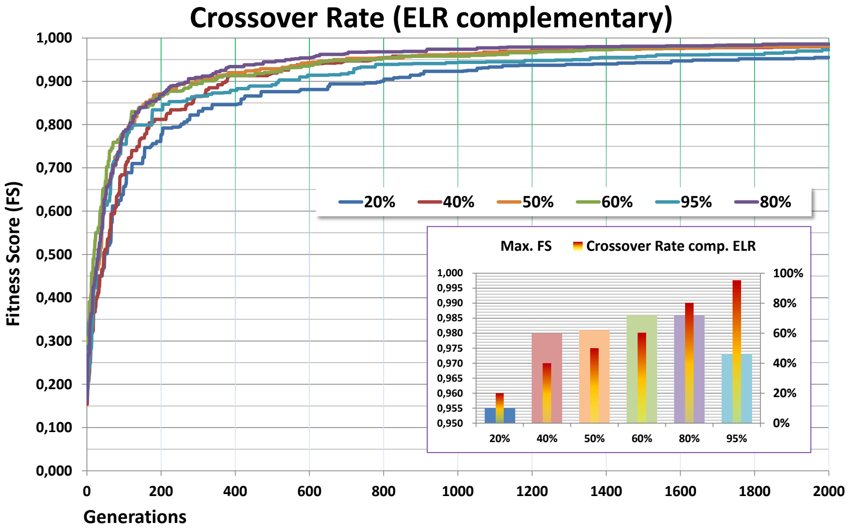

Figure 5.39: Crossover rate evolution for ELR complementary; NGEN=2000; SPOP=20; and MUR=20%

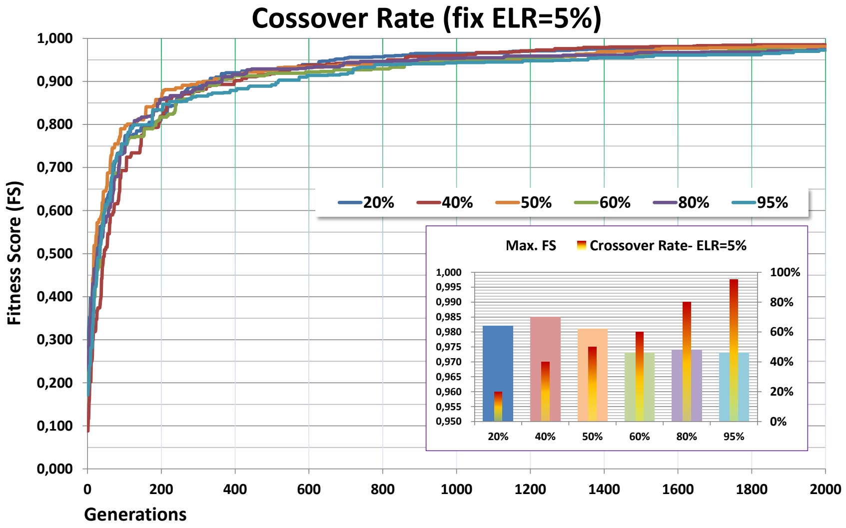

Figure 5.40: Crossover rate, evolution for 5% ELR; NGEN=2000; SPOP=20; and MUR=20%.

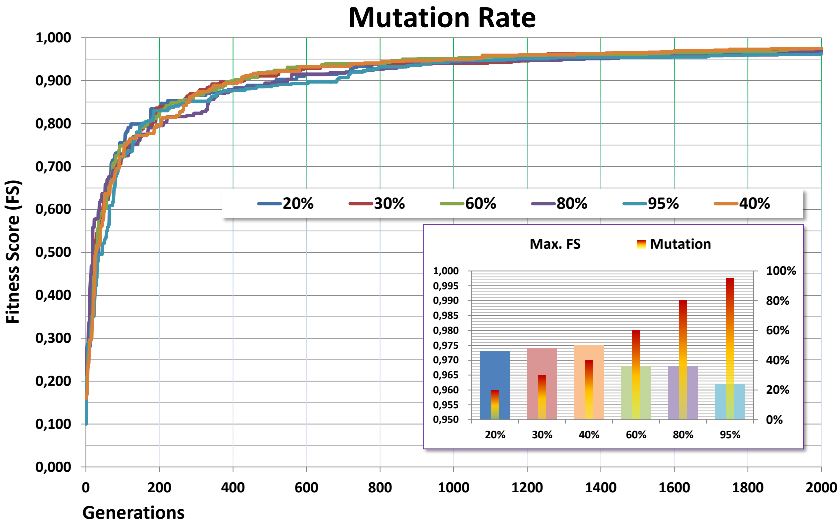

Figure 5.41: Mutation rate, evolution for NGEN=2000; SPOP=20; and CSR=80%.

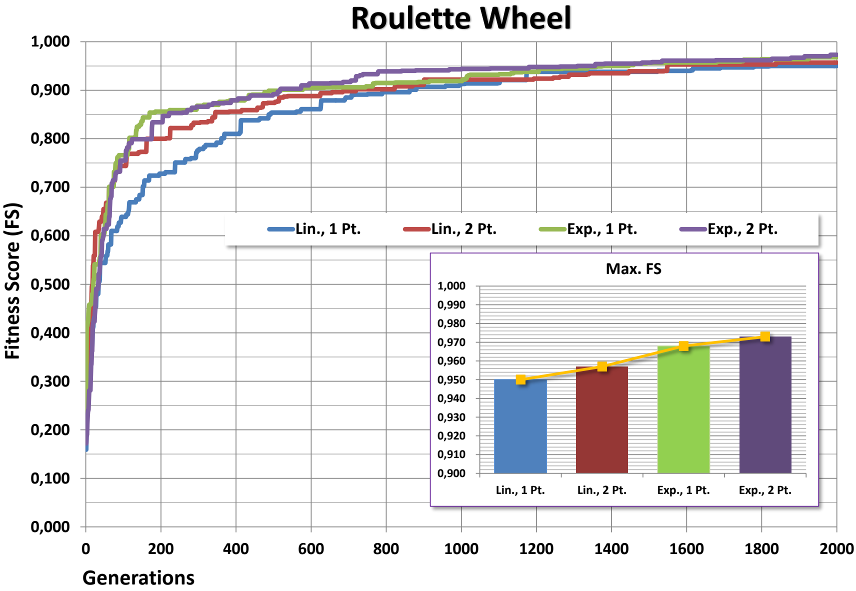

Figure 5.42: Roulette Wheel, linear 1 pt., linear 2 pt., exponential 1 pt., and exponential 2 pt..

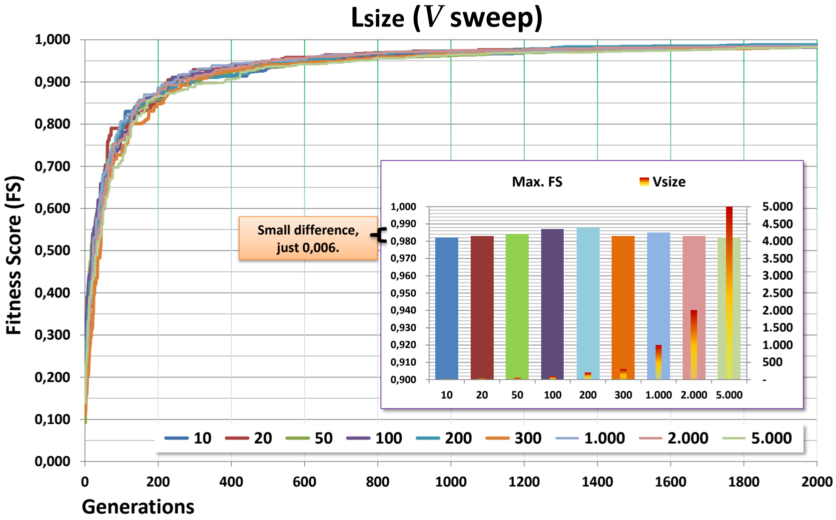

Figure 5.43: L_{size}, V sweep.

Number of Generations vs. Size of Population

Finally, one question still arises, which is better, large number for size of population or number of generations? To solve this issue, two tests are proposed:

Case 1. Fix the size of population and sweep the number of generations; and

Case 2. Fix number of generations and sweep the size of the population.

And to aid analysis, the same vector is used for the fixed values in both cases,

$$\text{Fixed Values} = \{10, 20, 50, 100, 200, 300, 500, 1000\}. \qquad (5.27)$$

For each sweep case[18] a vector of 56 points was used.

---

[18] Sweep values = {10, 20, 30, 40, 50, 60, 70, 80, 90, 100, 110, 120, 130, 140, 150, 160, 170, 180, 190, 200, 220, 240, 260, 280, 300, 320, 340, 360, 380, 400, 420, 440, 460, 480, 500, 600, 700, 800, 900, 1000, 1100, 1200, 1300, 1400, 1500, 2000, 2500, 3000, 3500, 4000, 5000, 6000, 7000, 8000, 9000, 10000}

Figure 5.44 depicts "Case 1", it is possible to observe that for all SPOP the curves show similar behaviour. This offers the information that even for small populations, if enough time is given all SPOPs they will achieve a similar FS value.

Figure 5.45 depicts "Case 2", in which it is possible to infer that even for a large population size the algorithm cannot achieve a high FS without a certain number of generations in order to evolve.

The summary is shown in Figure 5.46 [19], which relates both cases. The evolution of a given population is strongly influenced by the number of generations and not so with the size of the population itself (**red** bars). This dependence is more evident when comparing the NGEN=10 with NGEN=100 (**green** bars), where there is clearly a ramp relation.

In Figure 5.47 there is a comparison for two cases, it is possible to see that with the increased number of generations (blue line), the FS increases; while with an increase in the size of the population (red line), the FS is approximately constant.

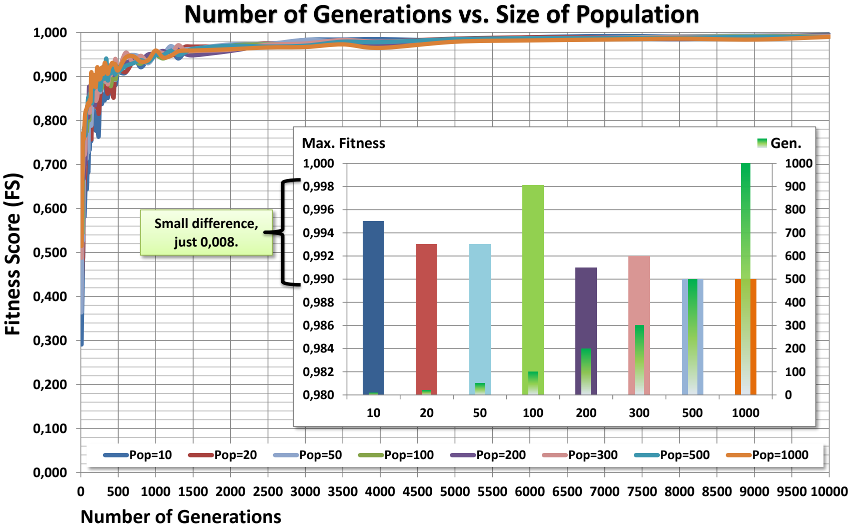

Figure 5.44: Fixed size of population for sweep of number of generations.

---

[19] Figure 5.46 is basically the bar graphics of Figures 5.44 and 5.45 in the same plot.

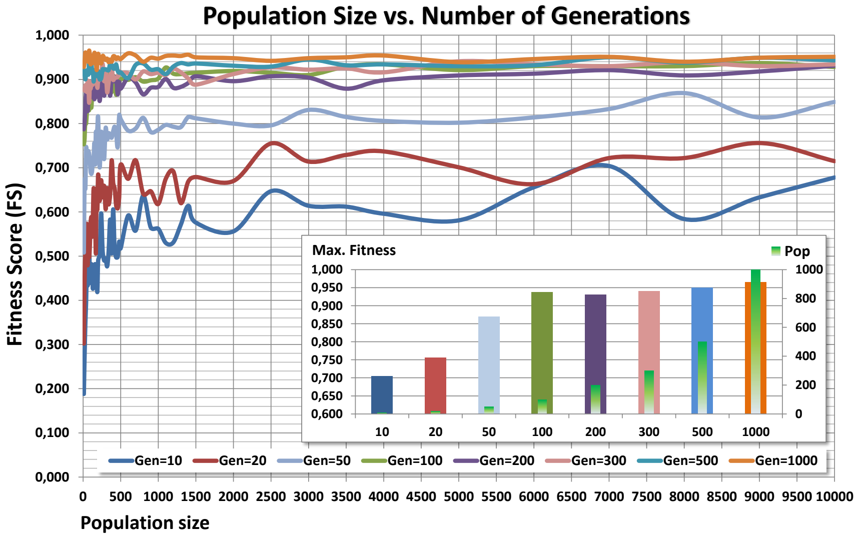

Figure 5.45: Fixed number of generations for sweep of size of the population.

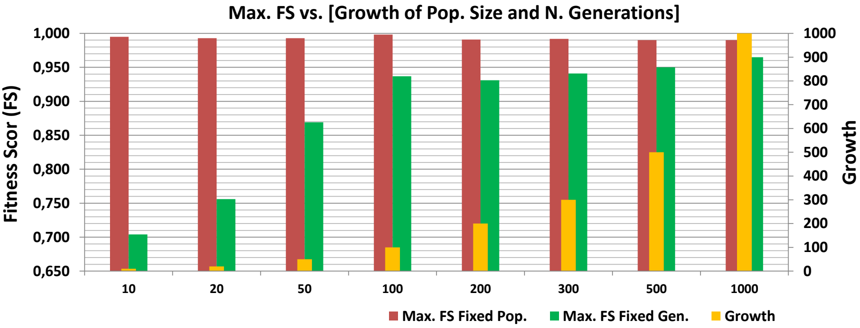

Figure 5.46: Maximum FS vs. Grow of Size of [Population and Number of Generations]

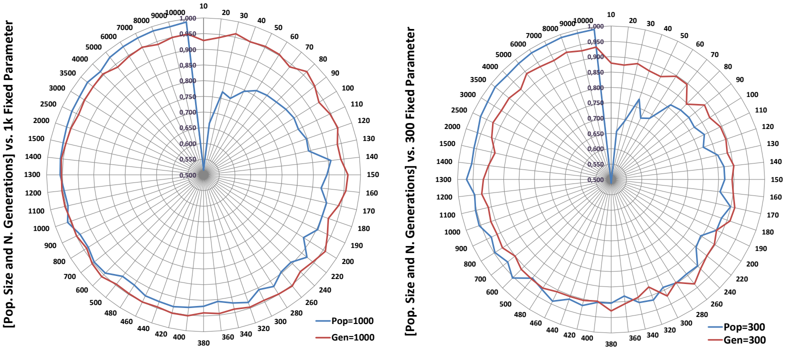

(a) 1k (b) 300

Figure 5.47: Pop. Size and N. Generations vs. Fixed Parameter.

Reproducibility

To estimate the reproducibility of the results out of the evolutions, two tests were carried out.:

a. The run of the same case several times and *standard deviation*[20] evaluation;

b. The run of the same case several times so that the FS achieves one.

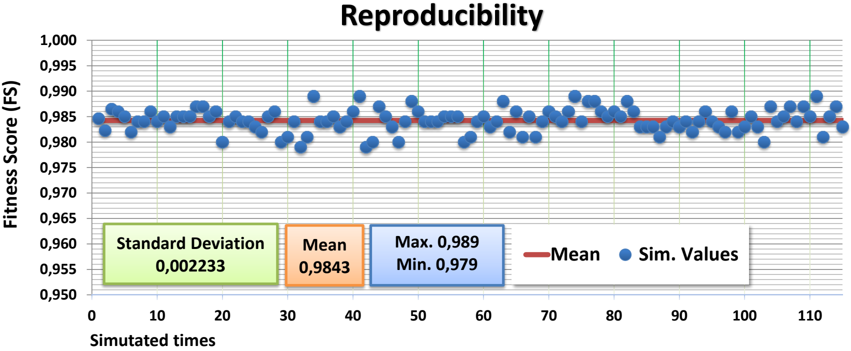

Figure 5.48: Reproducibility, 115 runs for SPOP=20, NGEN=2000, CSR=80%, ELR=20%, and MUR=40%.

---

[20] The *standard deviation* is a positive value and indicates the distance among the measured data and the mean. At least 75% of the measured data is inside the interval $[\mu - 2\sigma , \mu + 2\sigma]$, where μ is the mean and σ is the standard deviation.

As can be verified in Figure 5.48, for a limited number of generations, the process has satisfactory agreement, which is confirmed by the very low standard deviation.

The simulation to obtain the number of generations to achieve FS=1 showed one interesting point about GA. It is difficult to determine precisely, but in some simulations the algorithm falls into a local minimum and this retards the evolution for several generations. Figure 5.49 depicts the simulated data. Minimum and maximum generations found were 26200 and 44697, respectively.

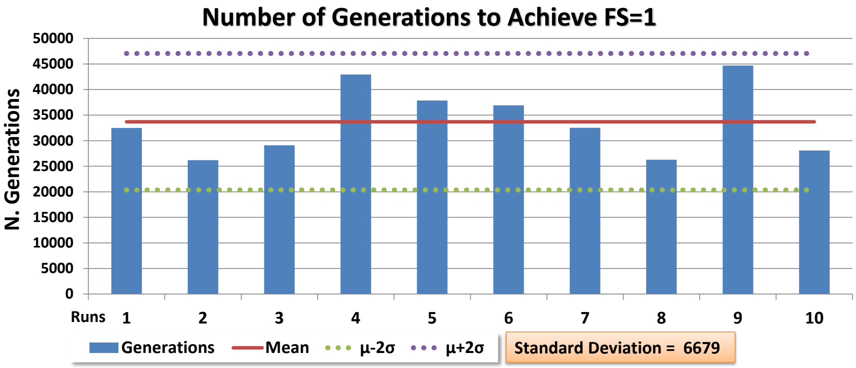

Figure 5.49: Number of Generations to Achieve FS=1. Parameters: SPOP=21, CSR=80%, ELR=20%, and MUR=40%.

In GA it is impossible to determine how close the result is to the optimum. The algorithm ranks the individuals with the FS. However, this value is the consequence of the fitness function modelling. For example, once the parameters are set, a process is initiated to evolve for thousands of generations. If at some point one individual has a FS value of more than one, it means the restrictions imposed in the FF were not "difficult" enough for the process. This is not a problem in GA, but rather a point to remember. This work sought to model the FF so the FS value is kept under one to get an idea of how good the result are.

5.4.2 GA-Beamforming Simulations

Using the knowledge acquired in Section 5.4.1 the GA-Beamforming parameters were determined. The size of the population[21] was set to 21 individuals and the number of generations ranged between 200 and 1000, depending on the simulation. The FF followed the previously described methods in Section 5.3. In all the simulations the frequency considered was 1 kHz, the reasons for which are:

1. it would be a worst case considering it is the "transition frequency" observed in Section 4.3.1.1;
2. it is the same frequency used in the indirect calibration procedures in acoustic measurements;
3. more frequencies would cost more computational time.

Crossover, Mutation and Elitism Rates

In most simulations the CSR was 80% with complementary ELR, i.e., the remaining 20% are the best individuals which are preserved and moved to the next generation without crossover. The MUR was set to 40%, the two-point exponential roulette wheel was selected, and V was set to 50.

GA Weights

The weights of Equation (5.16) (W_{DR}, W_{BW}, W_{Sy}) were empirically chosen to keep the FS less than one and force the algorithm to evolve to an optimal condition.

5.4.2.1 SGA - Phase Zero

In phase zero the SGA was applied to extract the best geometries for each separate angle. On the left site of the ϕ-axis the angles tested were 85°, 70°, 35° and 19°. Each angle was simulated eleven times with 400 generations. Additionally, the simulation for 90° (*centre*) was left indefinitely to evolve, and after about 21 thousand generations the process was stopped. Here, an interesting fact emerged, the geometry found for 90° was slightly similar to two rings on the limits of the cylinder,

---

[21] In phase one of the HGA some simulations used a population of 41 individuals.

Figure 5.50. That is, from a random initial process the algorithm has evolved to a deterministic answer.

Although the geometries of these five angles are the best for each, they are also not optimal if a different angle is processed. The way to escape this situation was to adapt Equation (5.16) to account for more than one ϕ angle. That is,

$$\mathrm{FS}_{\text{total}}(f) = \frac{\mathrm{FS}(f,\phi_1) + \mathrm{FS}(f,\phi_2) + \cdots + \mathrm{FS}(f,\phi_k)}{k} \tag{5.28}$$

where $\mathrm{FS}_{\text{total}}(f)$ is the total *fitness score* for the k processed angles; and k is the total number of angles. This expression is used in both HGA phases.

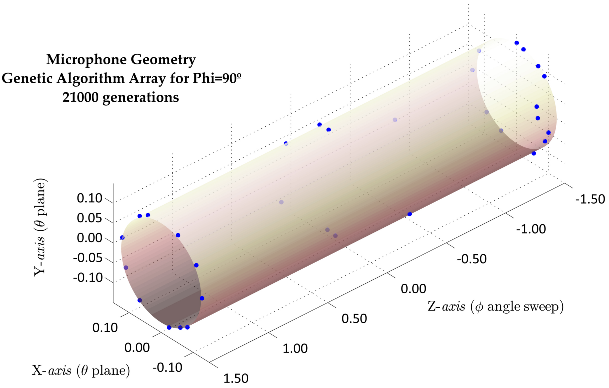

Figure 5.50: GA array for $\phi_{in} = 90°$, 21k generations.

5.4.2.2 HGA - Phase One

The HGA phase one was subdivided in two parts, simulations with three angles (90°, 70°, and 35°) and simulations with five angles (90°, 85°, 70°, 35°, and 19°). As the initial population, the best arrays out of the SGA were loaded. Two types of stop criterion were adopted in this phase: until FS=1 (or indefinitely, once the weights were chosen to maintain FS<1); and fixed number of generations. The simulations were running parallelly in seven different computers[22]. Since the operations in the GA process are

---

[22] GA-Beamforming was developed with Fortran-Labview with the capability to run in x86 and x64 machines, and from 1 to 8 threads. This was extremely useful since these seven machines have very different hardwares.

random, the run in several machines helps to avoid the whole process from getting trapped in a single solution.

After a series of simulations a tendency to the left side of the ϕ-axis was noticed. The simulations were stopped and a new set angles were proposed to the next phase.

5.4.2.3 HGA - Phase Two

The HGA phase two was carried out with five angles, two to the left, one central and two to the right (20°, 70°, 90°, 95°, and 145°). This is proposed to have *one*[23] best geometry that can operate in the full ϕ-axis with the best FF proprieties.

The initial population of arrays was composed of the best arrays from HGA phase one. In phase two, several running configurations were tested. In all of them, at least the best individual of the run was kept for the subsequent run.

After about 60 thousand generations (summing all the runs in all computers) *one* best geometry was found and the simulations were truncated[24] at this point. The selected geometry was then used in the simulations discussed in Section 4.3.1.2, Figure 5.51.

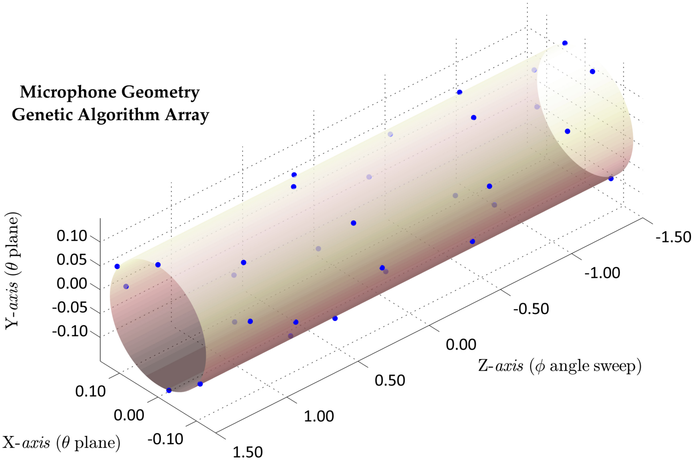

Figure 5.51: GA array, the best geometry found after ≈60 thousand generations.

---

[23] It might exist a different geometry that also would be considered *the best*.

[24] It was a user decision to stop the simulations, the best array (Figure 5.51) got FS=0,933577.

5.4.3 Considerations

Although in GA it is impossible to determine how close the result is to the optimum, PSF analysis can supply information for the researcher to decide to discontinue the run. The methods employed have proved their effectiveness and they can be applied - theoretically - for any shaped array, it is just a matter of adapting the coordinate system.

Figure 5.52 exemplifies a typical GA evolution, and in this specific case it is possible to observe that the process was trapped for about 150 generations (from 100 to 250) and after that the evolution continued. The blue line is the maximum fitness, i.e., the fitness of the best individual. The red line is the average fitness, i.e., the mean of the all FS for one generation.

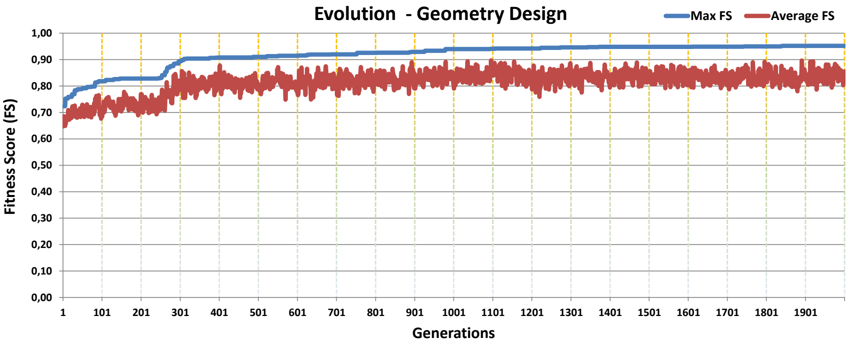

Figure 5.52: GA, example of geometry evolution during 2k generations.

In "regular" processing the problem evolves the most in the early generations, after that a "stable" condition is achieved. In this region the problem is undefined, the evolution becomes less frequent, and the evolving steps are usually the fruit of the mutation operator. For this reason a set of simulations for a fixed number of generations can provide a rich family of arrays to feed the HGA.

In the GA formulation of this work, as the fitness function grows in terms of complexity, the process needs more generations to reach the "stable" region. This means that the increase of angles and frequencies to process will lead to an increase in the processing time - in order to bypass this time issue more computer threads can help.

The length[25] of the cylinder has influence on the symmetry of the mainlobe, see PSF examples in Figure 5.53. Thus, depending on the problem the symmetry weight (W_{Sy}, Equation (5.16)) should be changed.

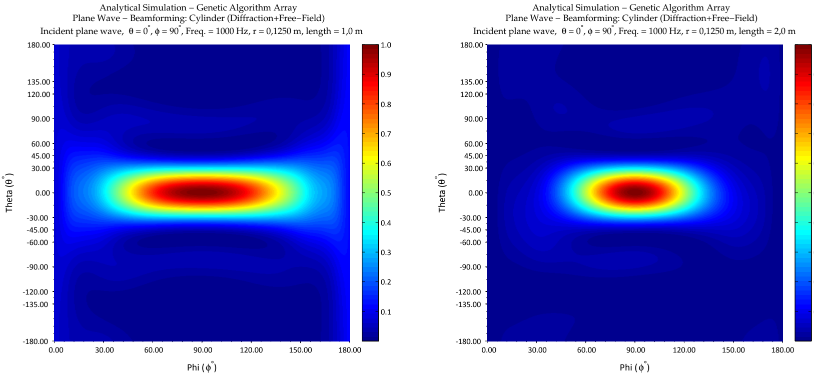

(a) $L = 1{,}0$ m (b) $L = 2{,}0$ m

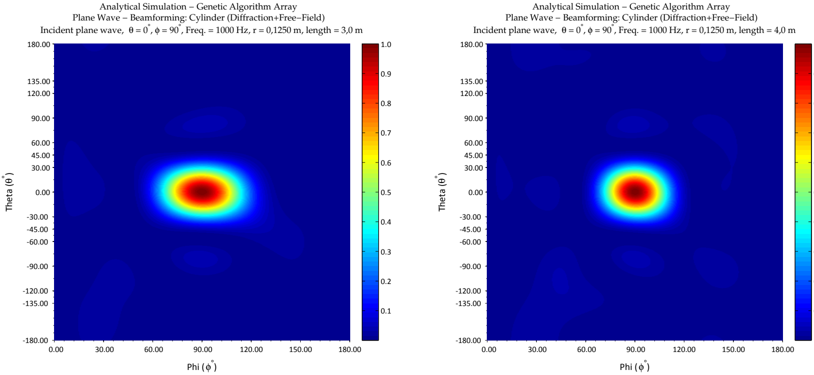

(c) $L = 3{,}0$ m (d) $L = 4{,}0$ m

Figure 5.53: Differences in the PSF for different cylinder length at 1 kHz.

---

[25] GA data for different lengths: $L = 1{,}0$ m, 7072 generations; $L = 2{,}0$ m, 12754 generations; $L = 3{,}0$ m, best array used in the dissertation; and $L = 4{,}0$ m, 5644 generations.

6

Conclusions

This chapter contains a summary of the content discussed throughout this work, as well as some thoughts and recommendations for continued studies. More specific conclusions about each topic covered in this dissertation are found in the "Considerations" sections of the respective topics.

The main theme of this work is beamforming, a technique which enables sound source localisation and mapping. The applied formulation includes the effects of diffraction, instead of just acoustical free-field. The first idea was to bring the results closer to reality, and the second, to estimate if an improvement would be noticeable given this consideration.

The work expands the horizon of the beamforming technique in the sense that other methods are combined to improve results. The use of different concepts as tools made the mash-up of ideas possible, creating new paths for this and future research.

The spark of the work was an open question. What is happening in the acoustic images as a consequence of the diffraction effects? Thus motivated, the cylinder was chosen as the first step (or first object of study) to discuss the possible outcomes.

In Chapter 2, as usual, everything started with a revision of basic wave motion theory focusing on linear acoustics, derived to be used as raw-material to supply the following chapters.

A great deal of information from diverse areas has been published surrounding beamforming. For this reason, descriptions of nomenclatures and approaches present divergences. To avoid misunderstandings, Chapter 3 provides a complete review on the beamforming concepts (for acoustics), highlighting the intricate details involved. After clarifying the *steering theory*, several array parameters are presented and discussed; among them, the most important are Beamwidth (BW) and Dynamic Range (DR). They are products of the geometry design and together are truly a *barometer* in terms of qualifying arrays.

Diffraction is a well-known effect in which waves "bend around" obstacles. This is one of the phenomena that propitiates a receiver outside a room to perceive a sound source from a different one. The free-field is commonly considered in beamforming applications; however, in the *real world* it is known that such a situation is very uncommon. Thus, properly equipped with the beamforming concepts, diffraction is added to the processing (as discussed in Chapter 4). As expected, the diffraction effects offered improvements in the low-mid frequencies; confirmed acoustical transparency in the low frequencies; and exposed the shadow effects for higher frequencies. If the free-field is compared to the diffraction plus free-field, some results seem to be deteriorated and some seem to be refined. However, a more appropriate way to consider this is that only the free-field processing was "overestimating" or "neglecting" the real array response. In Section 4.3 it is possible to consult simulations for two kinds of arrays. One, a circumference array (EAA), is very simple, and the other is the fruit of a genetic algorithm (GA) optimisation.

The Boundary Element Method (BEM) is employed as a tool to estimate the diffraction in a more general sense. Since the cylinder can be analytically modelled, comparison between methods can be consistently carried out. This study aimed to demonstrate whether the BEM can substantiate significantly proximate results with respect to the analytical model. In Section 5.2 there are discussions about the BEM input parameters that can influence the beamforming results. Since a discretization is needed, several *mesh refinement coefficients* were simulated and beamformed to depict the side effects. Considering a simple source, as a plane wave generator, a poor mesh can still recover the direction; however, there are deformations in the PSF. On the other hand, increasing the refinement more than six elements per wavelength does not improve the source localisation. Thus, computationally speaking, it is better to process more frequencies instead of using a mesh with many nodes.

The simulations started with the simplest array geometry: one circumference (or arc) of microphones (see Section 3.4). However, as shown in Section 4.3 this geometry has a mainlobe replica due to its nature. To circumvent this issue and optimise the array response, instead of an analytical modelling, the Genetic Algorithm (GA) was employed in the process to select a new array geometry. To accomplish this optimisation the GA was translated to the *array design domain*, modelling the geometries as chromosomes. First, a simple *fitness function* (FF) was used to identify a better set of inputs concerning the GA and afterwards the complete FF (described in the Section 5.3) was applied. Nevertheless, if just one ϕ_{in} angle is being used, natural selection will guide the geometry to an optimal array for just one angle. Most likely, this configuration would not be so interesting for the other angles. To resolve this issue, the simulated GA has considered five angles on the ϕ-axis, two to the left, one central and two to the right (for each iteration). Although the final array seems to be random, it is optimally random and thus guarantees no mainlobe replicas in the $\theta\phi$-plane.

In order to demonstrate the effects studied and to apply the proposed methods, a set of acoustic measurements was designed and carried out. The EAA was built with a rigid cylinder and the thirty two microphones were placed forming the circumference geometry. The necessary instrumentation was carefully prepared and thus, the measurements took place in an anechoic chamber. As can be consulted in Section 4.4, the experimental results are consistent with theory and confirm the applicability of the technique.

Finally, it is also important to mention that many hours were dedicated to the programming part of the work. The software development includes several theories and proceedings that should be used to avoid a mess of information. Mainly, three programming languages were used to extract the best of each one: Fortran, Matlab, and LabView. Furthermore, they were integrated, making it possible to accelerate the optimisation and calculation procedures. The use of multi-threading dramatically improved the performance in all simulations - about four times faster if one thread is compared to eight.

Elaborating and carrying out each step of the science of this dissertation was fundamental to attain a complete understanding of its capabilities and limitations. The main contributions of this work are the discussion of the diffraction effects over acoustic images; the testing of BEM as an alternative to the diffraction estimation (in the beamforming context); and last but not least, the geometry's optimisation through a genetic algorithm.

Philosophically, the research revealed itself as an amazing journey from the roots of wave motion theory to the sophisticated world of multithreading. The knowledge acquired reflects the maturation of the author concerning scientific work. Since in many occasions measures had to be taken not only to apply the concepts, but to program their foundations. The combination of simple concepts with modern tools has created several innovative directions in moving forward. Some are applied here in this dissertation, and some remain available for the next.

6.1 Future Work

With many ideas for continuing this work, some are presented here. First, concerning beamforming, the use of sophisticated post-processing (as cited in Section 3.2.4) may lead to improvements such as "cleaning" the sidelobes in some PSFs. Even with the optimised geometry, a similar study as shown in Section 5.4 can be carried out to search for weighting factors to enhance the array's gain for special cases of ϕ_{in} or θ_{in}. For the study cases with multiple sound emitters the eigenvalue decomposition technique may also help separating them [54].

For the object of study the following step - considering an aircraft model - would be the addition of a hemisphere on one extremity of the cylinder. In that case, since the diffraction analytical prediction is difficult or impossible, the BEM can help with the task of estimating the diffraction effects. In the case of motion, it will be also important to adapt the equations to include the effects of flow and turbulence. Moreover, the use of weighting factors can help with loss of coherence issues.

For a different problem, but still radial, the use of Circular Harmonics Beamforming (CHB) may be useful. As Sijtsma [153] stated, there is no reason to expect better or worse results. Notwithstanding, its use may lead to a speed improvement in the calculations, which is needed for real-time processing, for example.

Concerning the BEM, the use of more sophisticated techniques such as FMM BEM [112] may be of interest. Instead of being connected to the analytical simulation the GA could be connected to the BEM. Another application for BEM-beamforming is array simulation (of any shape) to create tables in frequency domain. The values of these tables would be then utilized in order to apply corrections, due to diffraction, in the post-processing stage of the measurements taken by the array.

In the GA field, several improvements in the proceedings may accelerate the evolution and/or help to escape local minima. The mutation could be applied at random for more than one gene. This would render increased variability, possibly preventing evolutionary stagnation. Furthermore, if the process spans several generations without evolution, an automatic change in the mutation and/or crossover and/or elitism rates would work to escape this situation. The inclusion of one more frequency for optimisation will raise its respective performance; however, the total processing time will accordingly increase.

The sound speed and atmospheric absorption effects should still be tested against the PSF, BW, and DR in order to estimate and predict deviations. Generically, the sensitivity to the simulation's input values are also worth testing with a statistical method such as Monte Carlo [154].

THESIS SUMMARY IN PORTUGUESE

1

Introdução

O som pode ser entendido como apenas uma onda ou, com regozijo, o adorável soar de uma música. Assim, além de sua natureza, deve-se levar em consideração um importante ponto: os seres vivos que estão sob a sua ação. Tais fenômenos estão presentes constantemente na vida diária, podendo trazer desde informações úteis, como um alarme de incêndio, até consequências indesejáveis do uso, como o ruído da turbina de uma aeronave [1]. Sons de alta intensidade podem danificar os ouvidos humanos, o que irá conduzir à modificação de sua percepção. E, além disso, podem causar efeitos colaterais, como estresse, irritação, entre outros. Esta é uma das razões pelo qual a acústica é um ponto importante de preocupação na vida moderna.

Governos e a comunidades[1] agem para regular e mitigar sons que podem causar problemas de saúde e/ou os que são considerados como pertubações. Entretando, por vezes, a identificação clara das fontes sonoras é de difícil acesso e, é neste ponto que as técnicas de imageamento acústico desempanham um papel importante, pois elas ajudam na localização das fontes e, com uma instrumentação mais sofisticada, podem criar verdadeiros mapas do sonoros (ou *imagens acústicas*).

Os esforços em utilizar tais técnicas se tornam claros quando as limitações humanas (psico-física) são apresentadas [3]. As faixas humanas típicas de visão e audição são na verdade muito restritas, Figura 1.1. Assim, além de recuperar a direção da fonte, a ideia por trás destas técnicas é estender o entendimento de um evento desconhecido

---

[1] O Dia Internacional da Conscientização Sobre o Ruído (INAD) é uma das campanhas que visa ampliar o conhecimento e consciencia sobre o assunto [2]. Mais informações sobre o ramo brasileiro podem ser encontradas em `http://www.inadbrasil.org`.

e/ou fonte sonora por meio do cruzamento de ambos os domínios de informação. É comprovado que uma informação visual pode aclarar mais facilmente uma situação que tomaria pelo menos algumas linhas para ser descrita. Ademais, a análise de uma informação sonora crua, sem a imagem acústica e realizada por uma pessoa, poderia ser influenciada pelo seu conhecimento prévio e/ou por sua criatividade.

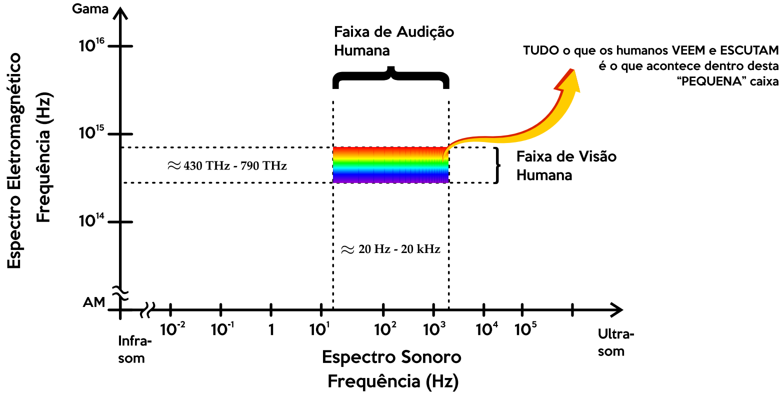

Figura 1.1: Faixa de visão e audição típicas de um humano.

Nesta tese, uma dessas técnicas, o *beamforming*[2], é colocada em prática junto a outros conceitos para aprimorar sua aplicação. É uma técnica conhecida no que concerne ao aperfeiçoamento de sinais, e que tem sido aplicada em diversos campos tais como astronomia, sonar e detecção sísmica. Junto ao pós-processamento, o *array*[3] é a principal ferramenta da técnica. Isto é verdade devido ao fato de que ele - o *array* - é responsável por amostrar o domínio espaço-tempo com um "arranjo" de sensores de modo a extrair os sinais incidentes em si.

No Novo México, EUA, há um dos *arrays* mais conhecidos do último século, o *Very Large Array* (VLA), Figura 1.2. Com o propósito de ver o espaço sideral, ele é uma das importantes ferramentas no campo da radioastronomia [4].

---

[2] *Beamforming* em uma tradução livre e aproximada do inglês seria "conformação de feixe". Como o termo original é amplamente empregado nos meios científicos, de modo a não se alterar este sentido, será mantido em sua forma original.

[3] *Array* em uma tradução livre do inglês seria como "arranjo" ou "matriz". Todavia, o termo original é mantido para preservar o sentido da aplicação.

Figura 1.2: Antenas do *Very Large Array* (VLA), radiotelescópio para beamforming, Novo México, EUA (foto por Kim Jew [5]).

O princípio do *beamforming* é relativamente simples, ele basicamente amostra o campo sonoro com um *array* de sensores e os soma. A correta soma destes sinais irá render um reforço (no som gravado) para uma dada direção no espaço. Adicionalmente, o processamento de uma série de possíveis direções de chegada do som permite a criação de mapas sonoros. A Figura 1.3 exemplifica a diferença entre um *padrão de feixe*[4], ou "padrão de aquisição", omnidirecional (um microfone) para um *padrão de feixe* focado (conjunto de seis microfones).

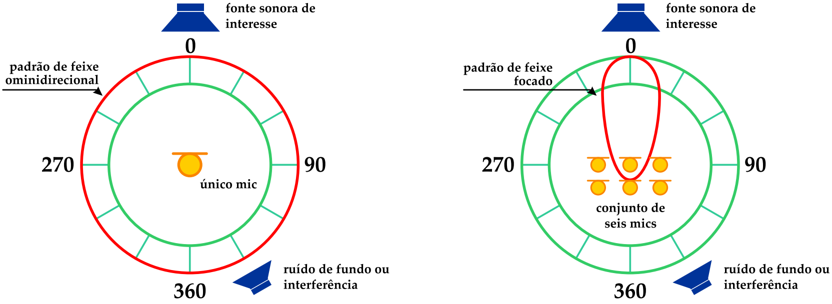

(a) Resposta omnidirecional (b) Resposta direcional

Figura 1.3: Diferença da resposta do *padrão de feixe* entre um e múltiplos sensores.

---

[4] *Padrão de feixe* é a tradução livre do inglês de *beampattern*.

Na prática, o leitor pode imaginar que o funcionamento do *beamforming* é similar ao de uma câmera digital. Dentro deste tipo de câmeras existe um microchip CCD que contém um *array* de pontos sensíveis a fótons – ou de forma geral, luz. Após a aquisição, há um pós-processador que entrega a foto ao usuário. Em acústica, os sensores são os microfones, também dispostos em um *array*, e o resultado do pós-processamento será então o mapa acústico ou a imagem acústica. Estas imagens acústicas (em uma comparação distinta) serão similares às fotos provenientes de câmeras de calor, isto é, há um mapa de cores e, normalmente, os pontos com cores vermelhas representam pontos com alta intensidade e as regiões em azul serão as que contêm menos energia – o Capítulo 3 formalmente descreve toda a física envolvida.

O segundo importante fenômeno considerado nesta tese é a difração do som. Mesmo que a matemática para descrevê-la envolva uma série de conceitos de física, sua natureza é bem intuitiva. Por exemplo, é por causa da difração que uma pessoa pode escutar música fora do recinto onde está a fonte sonora. As ondas ”contornam” as superfícies e propagam-se até o receptor. É também devido à difração (junto com outros efeitos) que os seres humanos localizam a origem das fontes ao seu redor. A sombra acústica que a cabeça cria entre as orelhas ajuda o processamento cérebro a estimar a direção do som – no Capítulo 4 há as descrições sobre o modelo de difração aplicado.

Em suma, em processamento de *arrays*, os pontos importantes são:

a. o posicionamento dos sensores ou geometria do *array*;

b. a técnica de pós-processamento empregada; e

c. a resolução número-de-onda-frequência[5].

Estes três itens estão fortemente conectados, visto que uma mudança em um afetará os outros. A geometria determina a resposta em número-de-onda-frequência, que é basicamente, junto ao pós-processamento, a essência da estratégia tomada. Questões com a geometria podem possivelmente levar a inconvenientes condições de sub-amostragem espacial [71] ou outros imprevistos. Neste documento, duas geometrias são principalmente discutidas. A primeira é a mais básica, é simplesmente uma circunferência. E a segunda é fruto de simulações utilizando algoritmo genético[6] (GA).

---

[5] *Wavenumber frequency response* em inglês.

[6] *Genetic Algorithm* (GA) em inglês.

O GA é parte de uma família de técnicas evolucionárias as quais são baseadas nos conceitos previamente desenvolvidos por Charles Darwin. O princípio é simples: os indivíduos mais adaptados irão sobreviver e perpetuar os genes. Esta técnica de busca e otimização é então adaptada no contexto de design de geometrias para ser aplicável ao problema proposto – os fundamentos estão descritos na Seção 5.3.

Com os métodos esclarecidos, simulações analíticas são realizadas para discutir e comentar os princípios apresentados e, por conseguinte, simulações utilizando o Método de Elementos de Contorno[7] (MEC ou BEM) são confrontadas com o processamento de *beamforming*. O MEC é utilizado como um método numérico adicional para prever os efeitos de difração de casos gerais para o específico.

1.1 Motivação e Descrição do Problema

A busca da ciência em descrever eventos e comportamentos é um processo contínuo. Quando um tema de pesquisa emerge, há sempre uma série de problemas e questões o circundando. É importante organizar as ideias e analisar possíveis passos de um ponto de começo até o ainda desconhecido resultado final. Dado um bloco definido de tempo para execução, o escopo deve ser definido e o trabalho tangível deve prosseguir. A ciência é então o trabalho de recolhimento de informações baseado em observações e o conhecimento prévio, para a extração de novas conclusões.

É comum que engenheiros acústicos declarem que um *array* é acusticamente transparente para uma determinada faixa de frequências. Todavia, como seriam os efeitos da difração que impactam nas medições? Questões como esta são levantadas e o papel do pesquisador é investigar métodos para que se possa chegar ao objetivo. Este trabalho tem uma forte motivação baseada na experiência passada do autor com técnicas relacionadas combinada ao anseio de desvendar questões e dúvidas.

O objeto de estudo em que esta tese é baseada é o cilindro. O estudo acerca de um volume básico pode servir de matéria-prima para uma ampla gama de aplicações. O problema proposto é a contabilização da difração sobre uma superfície cilíndrica, o posicionamento do sensores nesta superfície e o processamento do *beamforming* nos sinais dos sensores.

---

[7] *Boundary Element Method* (BEM) em inglês.

O *beamforming* é uma técnica amplamente aplicada tanto no campo de aeroacústica quanto em diversos de seus ramos, tais como: medições de *fly-over*, em túneis de vento, de ruído de jato e etc. Todavia, os conceitos apresentados nesta tese podem alimentar uma aplicação distinta: o uso do *beamforming* como sistema auxiliar na localização de obstáculos emissores de som. A forma do cilindro é similar a de uma fuselagem, sendo assim o seu comportamento deverá ser semelhante. O Veículo Aéreo Não Tripulado[8] (VANT) - aeronave sem piloto e tripulantes – poderia ser, por exemplo, uma aeronave que teria um aperfeiçoamento em seus sistemas sensoriais (ou de detecção). Claro, para esta aplicação o pesquisador em questão deverá ainda conectar os efeitos de movimento e fluido aos aspectos mostrados aqui.

Outras aplicações também podem ser consideradas em campos como marinha, ruído ambiental, monitoração sonora, entre outros. É uma questão de usar o conhecimento apresentado aqui como conhecimento prévio para esses outros campos. Além da forma do volume estudado, a discussão sobre difração combinada ao beamforming pode inspirar, ou contribuir, para outras áreas de pesquisa e/ou projetos. Embora GA e BEM não sejam o tema principal do trabalho, eles são utilizados como poderosas ferramentas para se alcançar resultados aprimorados.

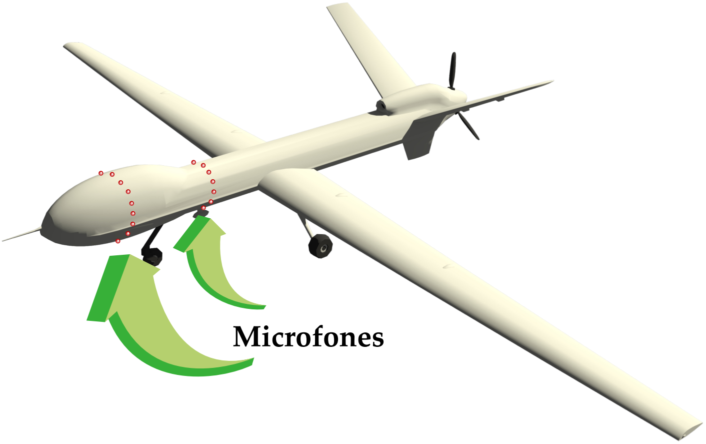

Figura 1.4: Veículo Aéreo Não Tripulado (VANT ou UAV) com sensores na superfície.

---

[8] Em inglês *Unmanned Aerial Vehicle* (UAV).

1.2 Objetivos e Contribuições

Esta tese visa desenvolver a técnica de *beamforming* no campo da acústica. Como contribuição principal, a condição de difração é incluída ao problema proposto. As derivações são demonstradas e a conjectura de que sua adição rende um aperfeiçoamento é apresentada e discutida.

O projeto tem uma natureza multi-disciplinar que pode ser verificada ao longo do documento. Ele lida com: acústica; *beamforming*; difração; processamento de sinais; métodos numérico e analítico; otimização; instrumentação e medição; métodos computacionais; entre outros. Além disso, ele também tem um aspecto conceitual, visto que o problema básico pode ser estendido para outras dimensões, e os resultados discutidos podem ser aplicados a outros problemas de *beamforming*.

De forma objetiva, as metas e contribuições são:

1. Implementação do campo de difração para a técnica de *beamforming* no problema do cilindro acusticamente rígido. Além das derivações analíticas, simulações são realizadas e discussões relativas ao desempenho das duas geometrias consideradas são feitas. Ademais, resultados experimentais são confrontados com os analíticos;

2. Um método de otimização de geometria baseado em algoritmo genético é desenvolvido adaptando-se os conceitos evolucionários para o "domínio dos *arrays*". Nesta aplicação, o *array* é projetado em coordenadas cilíndricas de modo a se ajustar a uma superfície de qualquer raio;

3. O Método de Elementos de Contorno (MEC) é usado como uma ferramenta alternativa para confirmar e discutir os efeitos da difração. Além disso, esta seção lista detalhes acerca da relação entre localização da fonte e o refinamento do modelo 3D;

4. Uma revisão sólida sobre os conceitos de *beamforming*, incluindo equações e figuras, e excluindo possíveis concepções errôneas;

5. Construção de ferramentas computacionais originais (*software*) integrando todos os diferentes aspectos contidos nesta pesquisa.

1.3 Organização do Documento

O documento é organizado em seis capítulos, sendo que os três primeiros introduzem a base para o bom entendimento das discussões dos três capítulos subsequentes. São eles:

Capítulo 1. Introdução

Compreende os primeiros conceitos, objetivos e uma parte introdutória para contextualizar o leitor aos tópicos abordados nesta pesquisa.

Capítulo 2. Formulações Acústicas

Introduz as formalidades matemáticas que sustentam as bases da acústica moderna.

Capítulo 3. Beamforming

Este capítulo inclui uma revisão sólida acerca dos métodos de *beamforming*, e a descrição dos parâmetros para estimar o desempenho no processamento de *arrays*.

Capítulo 4. Difração e Cilindro

Inicia-se com o básico a respeito de difração, e em seguida há as derivações para o caso do cilindro. No final da primeira parte o *beamforming* é contextualizado. As seções subsequentes discutem as simulações para dois tipos de *arrays*. Para um dos *arrays*, medições em ambiente anecoico também foram realizadas. Este capítulo é de fundamental importância, pois ele costura o conhecimento produzido junto às teorias apresentadas.

Capítulo 5. Métodos Numéricos

Este capítulo é separado em duas seções principais, a que lida com MEC e a que lida com GA. Em cada parte há uma revisão básica a respeito das técnicas, e após há discussões sobre os resultados obtidos. Ele contribui no sentido de que aspectos destes temas são mesclados aos de *beamforming*.

Capítulo 6. Conclusões

Incorpora as considerações finais e comentários acerca dos desenvolvimentos desta pesquisa. Ao final, há recomendações para estudos futuros.

Elementos após os capítulos principais:

I. Após os capítulos escritos em inglês, há também os Capítulos 1 e 2 em língua portuguesa.

II. Lista de Referências, com início na página 217.

III. Apêndices complementando os conteúdos dos capítulos principais. Em especial, no Apêndice B se encontram os resumos para as línguas estrangeiras: holandês, alemão, francês, espanhol e italiano.

IV. Anexos com informações adicionais relacionadas à instrumentação usada.

V. Índice Remissivo como ajuda a encontrar termos e seus contextos.

1.3.1 Versão Eletrônica

Além da versão impressa desta tese, no Apêndice A, há a versão eletrônica em PDF. Durante a pesquisa, cuidados foram tomados para se gerar figuras vetoriais de alta definição no maior número de figuras possível. Isto propicia que o leitor possa fazer ampliação (*zoom*) e assim possa observar e compreender melhor os detalhes.

2

Conclusões

Este capítulo contém uma síntese do conteúdo discutido ao longo do documento, bem como reflexões e recomendações para estudos continuados. Conclusões mais específicas acerca de cada tema abordado nesta tese podem ser consultadas nas seções "considerações" dos respectivos tópicos.

O tema principal deste trabalho é o *beamforming*, uma técnica que permite a localização e mapeamento de fontes de sonoras. A formulação aplicada inclui os efeitos de difração em vez de apenas considerar o *campo livre*[1] acústico, como ocorre normalmente nas publicações sobre o tema. A primeira ideia foi trazer os resultados mais próximos à realidade, e, em conseguinte estimar se melhorias surgiriam dada esta consideração.

O trabalho expande o horizonte da técnica *beamforming* no sentido de que outros métodos são combinados para melhorar os resultados. O uso de diferentes conceitos como ferramentas permitiu a mescla de ideias, criando novos caminhos para esta e futuras pesquisas.

O que estaria acontecendo nas imagens acústicas em decorrência dos efeitos de difração? Esta questão em aberto foi a centelha que motivou a pesquisa. Deste modo, o primeiro objeto de estudo escolhido, o cilindro, foi o primeiro passo para discutir os possíveis resultados.

No Capítulo 2, como de costume, tudo começa com uma revisão acerca da teoria ondulatória no que concerne à acústica. Ela é focada na acústica linear, e é derivada de modo a ser utilizada como matéria-prima para os capítulos subsequentes.

---

[1] *Free-field* em inglês, veja Seção 2.4.1.

Existe uma grande quantidade de informações, e em diversas áreas, publicadas sobre *beamforming*. Por esta razão, as descrições de nomenclaturas e abordagens apresentam divergências. Para evitar mal-entendidos, o Capítulo 3 fornece uma revisão completa nos conceitos de *beamforming* (para acústica), destacando os intrincados detalhes envolvidos. Após esclarecida a teoria, vários parâmetros a respeito de *arrays* são apresentados e discutidos, entre eles, os mais importantes são *largura de feixe*[2] (BW) e *faixa dinâmica*[3] (DR). Eles são produtos do projeto da geometria e, juntos, são de fato um *termômetro* em termos de qualificação de *arrays*.

A difração é um efeito bem conhecido em que as ondas "contornam" os obstáculos. Este é um dos fenômenos que propicia que um receptor de fora de um quarto possa perceber uma fonte sonora a partir de um cômodo diferente. O campo livre é geralmente considerado em aplicações de *beamforming*. No entanto, no *mundo real*, sabe-se que tal condição é incomum. Assim, provido dos conceitos de *beamforming*, a difração é adicionada ao pós-processamento (como discutido na Capítulo 4). Se os resultados de campo livre são comparados com os da difração somada ao campo livre, alguns deles parecem estar deteriorados e outros parecem estar refinados. Todavia, a forma mais adequada de avaliar isto é considerar que o processamento de apenas o campo livre "superestimou" ou "negligenciou" a verdadeira resposta do *array*. Na Seção 4.3 é possível consultar simulações para dois tipos de *arrays*. O mais simples possui a forma de uma circunferência (EAA)[4], e o outro é o fruto da otimização pelo algoritmo genético (GA)[5].

O Método de Elementos de Contorno (MEC) é usado como uma ferramenta para estimar a difração em um sentido mais geral. Uma vez que o cilindro pode ser modelado analiticamente, a comparação entre os métodos pode ser realizada de forma consistente. Este estudo teve como objetivo demonstrar se o MEC pode oferecer resultados significantemente próximos ao modelo analítico. Na Seção 5.2 há as discussões a respeito dos parâmetros de entrada do MEC que podem influenciar os resultados de *beamforming*. Uma vez que a discretização do objeto de estudo é

---

[2] *Largura de feixe* é a tradução livre do termo em inglês *Beamwidth*.

[3] *Dynamic Range* em inglês.

[4] *Equally Angled Array*, *array* com ângulos regulares ao redor de uma circunferência, veja Seção 3.4.1 para maiores detalhes.

[5] *Genetic Algorithm*, veja Seções 3.4.2 e 5.3.

necessária, vários coeficientes de refinamento de malha foram simulados e passados pelo processamento de *beamforming*, no intuito de descrever os efeitos colaterais dos coeficientes testados. Considerando uma fonte simples como um gerador de ondas planas, uma malha pobre ainda pode recuperar a direção da fonte, no entanto, há deformações no PSF. Por outro lado, aumentar o refinamento em mais do que seis elementos por comprimento de onda não oferece melhoria na localização da fonte. Assim, computacionalmente falando, é melhor realizar o processamento de mais frequências ao invés de usar uma malha com muitos nós.

As simulações começaram com a geometria mais simples de *array*: uma circunferência (ou arco) de microfones (veja Seção 3.4). No entanto, devido à sua natureza, esta geometria possui uma réplica do seu lóbulo principal, como mostrado na Seção 4.3. Para contornar este problema e otimizar a resposta do *array*, em vez de uma modelagem analítica, o algoritmo genético (GA) foi empregado no processo para selecionar uma nova geometria. Para alcançar esta otimização, o GA foi então traduzido para o domínio de projeto de *arrays* (modelando as geometrias na forma de cromossomos).

Primeiramente, uma *função de fitness* (FF) simples foi utilizada para identificar um melhor conjunto de parâmetros de entrada para o GA. Em conseguinte, a segunda e completa FF (descrita na Seção 5.3) foi aplicada. Entretanto, se apenas um ângulo ϕ_{in} está sendo usado, a seleção natural irá guiar a geometria para um *array* ótimo para apenas um ângulo. Muito provavelmente, essa configuração não será tão vantajosa para outros ângulos. Para resolver esta questão, as simulações de GA consideraram cinco ângulos no eixo ϕ, dois para a esquerda, um central e dois para a direita (para cada iteração). Embora a geometria final se pareça com uma forma aleatória, ela é na verdade uma "aleatória otimizada", garantindo portanto, que não haja nenhuma réplica do lóbulo principal no plano $\theta\phi$.

De modo a comprovar os efeitos estudados e aplicar os métodos propostos, uma bateria de medições acústicas foi projetada e realizada. Com um cilindro rígido o EAA foi construído e os trinta e dois microfones foram posicionados para criar a geometria em forma de circunferência. A instrumentação necessária foi cautelosamente preparada e, assim, as medições foram realizadas em uma câmara anecoica. Como pode ser consultado na Seção 4.4, os resultados experimentais são coerentes com a teoria e confirmam a aplicabilidade da técnica.

Finalmente, é também importante mencionar que muitas horas foram dedicadas para a programação computacional deste trabalho. O desenvolvimento de *software* inclui várias teorias e procedimentos que devem ser usados para evitar a confusão de informações. Sobretudo, três linguagens de programação foram usadas para extrair o melhor de cada uma: Fortran, Matlab e LabView. Além disso, elas foram integradas, tornando possível acelerar os procedimentos de otimização e de cálculo. O uso de *multi-threading* melhorou drasticamente o desempenho em todas as simulações, cerca de quatro vezes mais rápido se um *thread* é comparado com oito.

A elaboração e execução de cada etapa desta tese foi fundamental para alcançar um entendimento completo das capacidades e limitações das ciências estudadas. As principais contribuições deste trabalho são a discussão dos efeitos de difração sobre as imagens acústicas, o teste do MEC como uma alternativa para a estimativa de difração (no contexto de *beamforming*) e, por último, mas não menos importante, a otimização da geometria através de um método de algoritmo genético.

Filosoficamente, a pesquisa revelou-se como uma incrível jornada desde as raízes da teoria ondulatória até o mundo sofisticado do *multi-threading*. O conhecimento adquirido reflete o amadurecimento do autor acerca do trabalho científico. De modo a não somente aplicar os conceitos, mas também para programar suas fundações, em muitas ocasiões medidas tiveram de ser tomadas. As combinações de simples conceitos com ferramentas modernas criaram várias direções inovadoras para se avançar. Algumas estão aplicadas aqui nesta tese, e outras permanecem disponíveis para o próximo.

2.1 Trabalhos Futuros

Há ainda muitas ideias para continuar este trabalho, sendo que algumas delas estão apresentadas nesta seção.

Primeiramente, com respeito ao *beamforming*, o uso de pós-processamento sofisticado (como citado na Seção 3.2.4) poderá trazer melhorias, como a "limpeza" de lóbulos laterais em alguns PSFs.

Mesmo com a geometria otimizada, um estudo similar ao mostrado na Seção 5.4 pode ser realizado para a busca de *fatores de ponderação*[6], com o intuito de aprimorar o ganho do *array* para casos especiais de ϕ_{in} ou

---

[6] *Weighting factor* em inglês.

θ_{in}. Para os casos de estudo com múltiplos emissores sonoros, a técnica de *decomposição de autovalores*[7] pode oferecer auxílio em separá-los [54].

Para o objeto de estudo, o passo seguinte – considerando um modelo aeronáutico – seria a adição de uma semiesfera em uma das extremidades do cilindro. Neste caso, visto que a predição analítica da difração é extremamente complexa ou impossível, o MEC poderá ajudar na tarefa de estimar os efeitos da difração. Para o caso da adição de movimento, ainda será necessário adaptar as equações para incluir os efeitos de fluxo e turbulência. O uso de *fatores de ponderação* poder oferecer ajuda caso haja problemas de perda de coerência entre os sinais.

Para um problema distinto, todavia ainda radial, o uso de *Circular Harmonics Beamforming* (CHB) poderá ser útil. Como Sijtsma afirmou [153], não há motivos para se esperar melhora ou piora nos resultados. Contudo, seu uso pode trazer um aperfeiçoamento na velocidade dos cálculos o qual, por exemplo, é necessário para processamento em tempo real.

No que concerne ao MEC, o uso de técnicas mais sofisticadas como FMM MEC [112] pode ser interessante. Ao invés de estar conectado à simulação analítica, o GA poderia estar conectado ao MEC. Outra aplicação para MEC-*beamforming* é a simulação de um *array* (de qualquer forma) para a criação de tabelas no domínio da frequência. Os valores destas tabelas seriam então utilizados de modo a aplicar correções, devido à difração, na fase de pós-processamento das medições feitas por este *array*.

No campo do GA, algumas melhorias nos procedimentos poderão acelerar a evolução e/ou ajudar a escapar de mínimos locais. A mutação poderia ser aplicada aleatoriamente para mais de um gene. Isto renderia um aumento da variabilidade, possivelmente prevenindo a estagnação da evolução. Além disso, se o processo está diversas gerações sem evolução, uma alteração automática nas taxas de mutação e/ou *crossover* e/ou elitismo poderia ser a saída para escapar desta situação. A inclusão de mais uma frequência para otimização elevará o seu desempenho; todavia o tempo total de processamento irá por conseguinte aumentar.

Os efeitos da velocidade do som e a absorção atmosférica devem ainda ser testados contra o PSF, BW e DR de modo a estimar e prever desvios. Genericamente, vale também a pena testar a sensibilidade às entradas da simulação com um método estatístico como o de Monte Carlo [154].

---

[7] *Eigenvalue decomposition* em inglês.

References

[1] R. M. Schafer. *The Soundscape*. Destiny Books, Oct. 1993.
(Cited on pages 1 and 201)

[2] The International Noise Awareness Day (INAD), Brazilian Branch. `http://www.inadbrasil.org`, Feb. 2013.
(Cited on pages 1 and 201)

[3] H. Fastl and E. Zwicker. *Psychoacoustics: Facts and Models*. Springer, 3rd edition, Dec. 2006.
(Cited on pages 1, 17 and 201)

[4] A. Hewish, editor. *Seeing Beyond the Visible: Electromagnetic Spectrum*. Hodder Arnold H&S, Jan. 1974.
(Cited on pages 2 and 202)

[5] Kim Jew website. http://www.kimjew.com, Feb. 2013.
(Cited on pages 3 and 203)

[6] H. Kuttruff. *Acoustics: An Introduction*. Spon Press, new ed edition, Dec. 2006.
(Cited on pages 11, 12, 13, 15 and 71)

[7] A. R. Frey, A. B. Coppens, J. V. Sanders, and L. E. Kinsler. *Fundamentals of Acoustics*. Wiley, 4 edition, Dec. 1999.
(Cited on pages 11, 13 and 15)

[8] P. S. Laplace. *Théorie analytique des probabilités*. Courcier, 1820.
(Cited on page 11)

[9] T. Rossing, editor. *Springer Handbook of Acoustics*. Springer, 1 edition, Jun. 2007.
(Cited on pages 13, 19, 21 and 73)

[10] H. Helmholtz. *On the Sensations of Tone (Dover Books on Music)*. Number 576. Dover Publications, 2nd edition edition, Jun. 1954.
(Cited on page 13)

[11] N. A. Gumerov and R. Duraiswami. *Fast Multipole Methods for the Helmholtz Equation in Three Dimensions (Elsevier Series in Electromagnetism)*. Elsevier Science, 1 edition, Feb. 2005.
(Cited on page 13)

[12] L. L. Beranek. *Acoustics*. Amer Inst of Physics, Dec. 1986.
(Cited on pages 13 and 16)

[13] J. B. J. Fourier. *Théorie analytique de la chaleur*. Didot, Paris, France, 1822.
(Cited on page 14)

[14] K. Shin and J. Hammond. *Fundamentals of Signal Processing for Sound and Vibration Engineers*. Wiley, 1 edition, Apr. 2008.
(Cited on pages 15 and 118)

[15] D. Cohen. *Performance of Standard Fourier-Transform Spectrometers*. USA, 1 edition, 2007.
(Cited on page 15)

[16] B. P. Lathi. *Linear Systems and Signals*. Oxford University Press, USA, 2 edition, Jul. 2004.
(Cited on page 15)

[17] A. V. Oppenheim, R. W. Schafer, and J. R. Buck. *Discrete-Time Signal Processing*. Prentice Hall, 2 edition, Jan. 1999.
(Cited on pages 15 and 58)

[18] M. Vorländer. *Auralization: Fundamentals of Acoustics, Modelling, Simulation, Algorithms and Acoustic Virtual Reality*. Springer, Berlin, Germany, 1 edition, 2007.
(Cited on pages 17 and 72)

[19] A. V. Oppenheim, A. S. Willsky, and S. Hamid. *Signals and Systems*. Prentice Hall, 2 edition, Aug. 1996.
(Cited on page 18)

[20] S. Oerlemans and P. Sijtsma. Acoustic Array Measurements of a 1:10.6 Scaled Airbus A340 Model. In *10th AIAA/CEAS Aeroacoustics Conference*, number AIAA-2004-2924, Manchester, Great Britain, May 2004.
(Cited on page 19)

[21] Y. Guo; C. Streett R. W. Stoker and N. Burnside. Airframe noise source locations of a 777 aircraft in flight and comparisons with past model scale tests. In *9th AIAA/CEAS Aeroacoustics Conference and Exhibit*, number AIAA-2003-3232, Hilton Head, South Carolina, USA, May 2003.

(Cited on page 19)

[22] H. Kuttruff. *Room Acoustics*. CRC Press, 5 edition, Jun. 2009.

(Cited on page 19)

[23] D. D. Reynolds. *Engineering Principles of Acoustics: Noise and Vibration Control*. Pearson Allyn & Bacon, Jun. 1981.

(Cited on page 19)

[24] B. Kaushik; D. Nance and K. Ahuja. A review of the role of acoustic sensors in the modern battlefield. In *11th AIAA/CEAS Aeroacoustics Conference (26th AIAA Aeroacoustics Conference)*, number AIAA-2005-2997, Monterey, California, USA, May 2008.

(Cited on page 23)

[25] J. Billingsley and R. Kinns. The acoustic telescope. *Journal of Sound and Vibration*, 48(4):485 – 510, 1976.

(Cited on pages 23 and 58)

[26] B. D. Van Veen and K. M. Buckley. Beamforming: a versatile approach to spatial filtering. *ASSP Magazine, IEEE*, 5(2):4–24, April 1988.

(Cited on page 23)

[27] E. G. Williams. *Fourier Acoustics: Sound Radiation and Nearfield Acoustical Holography*. Number 306. Academic Press, Jun. 1999.

(Cited on pages 23 and 140)

[28] F. Fahy. *Sound Intensity*. Taylor & Francis, 1^{st} edition, Oct. 1995.

(Cited on page 23)

[29] U. Michel. History of acoustic beamforming. In *1st Belin Beamforming Conference - BeBeC*, Berlin, Germany, Nov. 2006.

(Cited on page 23)

[30] R. J. Mailloux. *Phased Array Antenna Handbook*. Artech House, 2nd edition, Mar. 2005.

(Cited on page 24)

[31] P. Hacker and H. Schrank. Range distance requirements for measuring low and ultralow sidelobe antenna patterns. In *Antennas and Propagation Society International Symposium, 1981*, volume 19, pages 565 – 568, Jun. 1981.

(Cited on page 24)

[32] R. Hansen. Measurement distance effects on low sidelobe patterns. *Antennas and Propagation, IEEE Transactions on*, 32(6):591 – 594, Jun. 1984.

(Cited on page 24)

[33] P. A. M. Dirac. *The Principles of Quantum Mechanics*. Oxford University Press, USA, 4 edition, Fev. 1982.

(Cited on page 29)

[34] P. Sijtsma. Acoustic array corrections for coherence loss due to the wind tunnel shear layer. Berlin, Germany, Feb. 2008. 2nd Berlin Beamforming Conference - BeBeC.

(Cited on page 32)

[35] P. Sijtsma and R. Stoker. Determination of absolute contributions of aircraft noise components using fly-over array measurements. In *10th AIAA/CEAS Aeroacoustics Conference*, number AIAA-2004-2958, Manchester, United Kingdom, May 2004.

(Cited on pages 32 and 65)

[36] P. Sijtsma. Phased array beamforming applied to wind tunnel and fly-over tests. In *II Sae Brasil International Noise and Vibration Congress*, number SAE-2010-36-0514, page 20, Florianópolis, SC, Brazil, 2010.

(Cited on page 32)

[37] P. Sijtsma. Acoustic beamforming for the ranking of aircraft noise. In *VKI/VALIANT Lecture Series on "Aircraft Noise"*, Brussels, Belgium, Mar. 2012.

(Cited on page 32)

[38] D. H. Johnson and D. E. Dudgeon. *Array Signal Processing: Concepts and Techniques*. Prentice Hall PTR, facsimile edition, Feb. 1993.

(Cited on pages 32, 42, 43, 55, 62, 63 and 65)

[39] A. Hirschberg and S.W. Rienstra. *Notes: An Introduction to Aeroacoustics*. Eindhoven University of Technology, Jul. 2004.

(Cited on page 35)

[40] P. M. Morse and H. Feshbach. *Methods of Theoretical Physics, Part I*. McGraw-Hill Science/Engineering/Math, Jun. 1953.

(Cited on page 35)

[41] G. Elias. Source localization with a two-dimensional focused array: Optimal signal processing for a cross-shaped array. In *International Congress and Exposition on Noise Control Engineering - Internoise 1995*, page 4, Newport Beach, CA, USA, Jul. 1995.

(Cited on page 36)

[42] P. Sijtsma. Experimental Techniques for Identification and Characterisation of Noise Sources. *Advances in Aeroacoustics and Applications, VKI Lecture Series*, 5:15–19, Mar. 2004. Rhode-Saint-Genèse, Belgium.

(Cited on page 39)

[43] J. J. Christensen and J. Hald. Technical review: Beamforming. Technical Report 1, Brüel and Kjær, Nærum, Denmark, 2004.

(Cited on pages 42, 48, 50, 55 and 65)

[44] R. P Dougherty. Advanced time-domain beamforming techniques. In *10th AIAA/CEAS Aeroacoustics Conference*, number AIAA-2004-2955, Manchester, United Kingdom, May 2004.

(Cited on page 42)

[45] P. A. Ravetta. *LORE Approach for Phased Array Measurements and Noise Control of Landing Gears*. PhD thesis, Virginia Tech, Blacksburg,Virginia,USA, Nov. 2005.

(Cited on pages 42 and 48)

[46] S. N. Y. Gerges; W. D. Fonseca and R. P. Dougherty. State of the art beamforming software and hardware for applications (keynote lecture). In *16th International Congress on Sound and Vibration - ICSV2009*, Kraków, Poland, Jul. 2009.

(Cited on page 42)

[47] T. F. Brooks and W. M. Humphreys. A deconvolution approach for the mapping of acoustic sources (damas) determined from phased microphone arrays. *Journal of Sound and Vibration*, 294(4-5):856 – 879, Mar. 2006.

(Cited on page 42)

[48] R. P. Dougherty. Extensions of DAMAS and benefits and limitations of deconvolution in beamforming. In *11th AIAA/CEAS Aeroacoustics*

Conference (26th AIAA Aeroacoustics Conference), number AIAA-2005-2961, Monterey, CA, USA, May 2005.

(Cited on page 42)

[49] K. Ehrenfried and L. Koop. A comparison of iterative deconvolution algorithms for the mapping of acoustic sources. In *12th AIAA/CEAS Aeroacoustics Conference (27th AIAA Aeroacoustics Conference)*, number AIAA-2006-2711, Cambridge, Massachusetts, May 2006.

(Cited on page 42)

[50] P. Sijtsma. Clean based on spatial source coherence. *International Journal of Aeroacoustics*, 6:357–374, Dec. 2007.

(Cited on pages 42 and 45)

[51] R. O. Schmidt. *A Signal Subspace Approach To Multiple Emitter Location And Spectral Estimation*. PhD thesis, Stanford University, 1982.

(Cited on page 42)

[52] R. Schmidt. Multiple emitter location and signal parameter estimation. *Antennas and Propagation, IEEE Transactions on*, 34(3):276–280, Mar. 1986.

(Cited on page 42)

[53] R. Roy, A. Paulraj, and T. Kailath. ESPRIT - a subspace rotation approach to estimation of parameters of cisoids in noise. *Acoustics, Speech and Signal Processing, IEEE Transactions on*, 34(5):1340 – 1342, Oct. 1986.

(Cited on page 42)

[54] E. Sarradj. A fast signal subspace approach for the determination of absolute levels from phased microphone array measurements. *Journal of Sound and Vibration*, 329(9):1553 – 1569, 2010.

(Cited on pages 42, 196 and 215)

[55] E. Sarradj. Improving speed with orthogonal beamforming. In *3rd Berlin Beamforming Conference - BeBeC*, Berlin, Germany, Feb. 2010.

(Cited on page 42)

[56] R. P. Dougherty. Improved Generalized Inverse Beamforming for Jet Noise. In *17th AIAA/CEAS Aeroacoustics Conference (32nd AIAA Aeroacoustics Conference)*, Portland, Oregon, USA, Jun. 2011.

(Cited on page 42)

[57] P. A. G. Zavala. *Aeroacoustic Source and Moving Source Identification*. PhD thesis, University of Campinas, Campinas, Brazil, Mar. 2012.
(Cited on page 42)

[58] M. Brandstein and D. Ward. *Microphone Arrays: Signal Processing Techniques and Applications*. Springer, 1 edition, Jun. 2001.
(Cited on page 42)

[59] H. Cox; R. Zeskind and M. Owen. Robust adaptive beamforming. *Acoustics, Speech and Signal Processing, IEEE Transactions on*, 35(10):1365–1376, Oct. 1987.
(Cited on page 42)

[60] A. K. Bhattacharyya. *Phased Array Antennas : Floquet Analysis, Synthesis, BFNs and Active Array Systems*. Wiley-Interscience, 1 edition, Mar. 2006.
(Cited on page 43)

[61] W. D'A. Fonseca. Development and application of an acoustic imaging system using beamforming technique for moving sources (original: Desenvolvimento e aplicação de sistema para obtenção de imagens acústicas pelo método do beamforming para fontes em movimento). Master's thesis, Federal University of Santa Catarina, Florianópolis, SC, Brazil, Feb. 2009.
(Cited on pages 45, 48, 65 and 118)

[62] A. Öchsner, L. F. M. da Silva, and H. Altenbach, editors. *Materials with Complex Behaviour II: Properties, Non-Classical Materials and New Technologies (Advanced Structured Materials)*. Springer, Jan. 2012.
(Cited on page 48)

[63] Y. A. R. Silva. A system for sound source indentification using the beamforming technique (original: Um sistema de indentificação de fontes de ruído utilizando a técnica de beamforming). Master's thesis, Federal University of Santa Catarina, Florianópolis, SC, Brazil, Dez. 2008.
(Cited on page 48)

[64] W. Song. *Beamforming applied to psychoacoustics*. PhD thesis, Aalborg University, Copenhagen, Denmark, Nov. 2007.
(Cited on pages 49 and 65)

[65] B. D. Steinberg. *Principles of Aperture and Array System Design: Including Random and Adaptive Arrays*. John Wiley & Sons, 1 1976.
(Cited on page 49)

[66] J. S. Bendat and A. G. Piersol. *Random Data: Analysis & Measurement Procedures*. Wiley-Interscience, 4 edition, Feb. 2010.

(Cited on page 55)

[67] R. Boone. *Design and development of a synthetic acoustic antenna for highly directional sound measurements*. PhD thesis, Delft University of Technology, Delft, Netherlands, 1987.

(Cited on page 56)

[68] A. Mast. An experimental microphone antenna array for measuring aircraft noise. Master's thesis, Delft University of Technology, Delft, Netherlands, Mar. 2001.

(Cited on page 56)

[69] A. Wettklo. Tonic strains of a chamber orchestra. In *1st Berlin Beamforming Conference, BeBeC 2006*, Berlin, Germany, Nov. 2006.

(Cited on page 58)

[70] H. Nyquist. Certain topics in telegraph transmission theory. *Proceedings of the IEEE*, 90(2):280–305, Feb. 2002 (Original: Trans. of the AIEE, 47:617-644, Apr. 1928).

(Cited on page 58)

[71] J. Dmochowski, J. Benesty, and S. Affes. On spatial aliasing in microphone arrays. *Signal Processing, IEEE Transactions on*, 57(4):1383 –1395, april 2009.

(Cited on pages 61 and 204)

[72] M. A. Doron and E. Doron. Wavefield modeling and array processing - i. spatial sampling. *Signal Processing, IEEE Transactions on*, 42(10):2549 –2559, oct 1994.

(Cited on page 61)

[73] P. T. Soderman and S. C. Noble. A directional microphone array for acoustic studies of wind tunnel models. In *8th Aerodynamic Testing Conference*, number AIAA-1974-640, Bethesda, Md., USA, Jul. 1974.

(Cited on page 64)

[74] W. H. Kummer. Basic array theory. *Proceedings of the IEEE*, 80(1):127 –140, jan 1992.

(Cited on page 64)

[75] M. Möser, editor. *Messtechnik der Akustik*. Springer, 2010 edition, Nov. 2009.

(Cited on page 64)

[76] J. R. Underbrink. Practical considerations in focused array design for passive broad-band source mapping applications. Master's thesis, Pennsylvavia State University, Pennsylvania, USA, May 1995.

(Cited on pages 65 and 109)

[77] J. R. Underbrink and R. P. Dougherty. Array design for non-intrusive measurement of noise sources. In *Noise-Con*, Seattle, Washington, USA, Sep. 1996.

(Cited on page 65)

[78] H. Kook; G. B. Moebs; P. Davies and J. S. Bolton. An efficient procedure for visualizing the sound field radiated by vehicles during standardized passby tests. *Journal of Sound and Vibration*, 233(1):137 – 156, 2000.

(Cited on page 65)

[79] B. Masiero, W. D. Fonseca, M. Müller-Trapet, and P. Dietrich. Auralization of pass-by beamforming measurements. In *EAA EUROREGIO 2010*, Ljubljana, Slovenia, Set. 2010.

(Cited on page 65)

[80] D. P. Arnold, T. Nishida, L. N. Cattafesta, and M. Sheplak. A directional acoustic array using silicon micromachined piezoresistive microphones. *The Journal of the Acoustical Society of America*, 113(1):289–298, 2003.

(Cited on page 65)

[81] H. Siller, M. Drescher, G. Saueressig, and R. Lange. Fly-over source localisation on a Boeing 747-400. In *3rd Berlin Beamforming Conference*, Berlin, Germany, Feb. 2010.

(Cited on page 65)

[82] R. P. Dougherty; J. Panda and S. S. Lee. Non-intrusive jet noise study combining rayleigh scattering and phased array measurement techniques. In *11th AIAA/CEAS Aeroacoustics Conference (26th AIAA Aeroacoustics Conference)*, number AIAA-2005-2843, Monterey, California, USA, May 2005.

(Cited on page 65)

[83] P. Sijtsma and H. H. Holthusen. Source location by phased measurements in closed wind tunnel test sections. In *5th AIAA/CEAS Aeroacoustics Conference and Exhibit*, number AIAA Paper 1999-1814, NLR-TP-99108, Bellevue, WA, USA, May 1999.

(Cited on page 65)

[84] S. Oerlemans. *Detection of Aeroacoustic Sound Sources on Aircraft and Wind Turbines*. PhD thesis, University of Twente, Enschede, Netherlands, Sep. 2009.

(Cited on pages 65 and 114)

[85] P. Sijtsma. Feasibility of In-Duct Beamforming. In *13th AIAA/CEAS Aeroacoustics Conference (28th AIAA Aeroacoustics Conference)*, number AIAA-2007-3696, Rome, Italy, May 2007.

(Cited on page 65)

[86] R. P. Dougherty, D. Weir, J. Bridges, and F. Agboola. Source identification and location techniques - NASA/CP - 2001-211152. Technical report, NASA Glenn Research Center / Boeing / Honeywell, 2001.

(Cited on page 65)

[87] H. Teutsch and W. Kellermann. Acoustic source detection and localization based on wavefield decomposition using circular microphone arrays. *The Journal of the Acoustical Society of America*, 120(5):2724–2736, 2006.

(Cited on pages 65 and 90)

[88] B. Rafaely. Analysis and design of spherical microphone arrays. *Speech and Audio Processing, IEEE Transactions on*, 13(1):135–143, Jan. 2005.

(Cited on page 66)

[89] E. Tiana-Roig, F. Jacobsen, and E. F. Grande. Beamforming with a circular microphone array for localization of environmental noise sources. *The Journal of the Acoustical Society of America*, 128(6):3535–3542, 2010.

(Cited on pages 66 and 90)

[90] G. Heilmann, A. Meyer, and D. Döbler. Time-domain beamforming using 3D-microphone arrays. In *2nd Berlin Beamforming Conference - BeBeC*, Berlin, Germany, Feb. 2008.

(Cited on page 66)

[91] J. Hald; J. Mørkholt and J. Gomes. Efficient interior NSI based on various beamforming methods for overview and conformal mapping using SONAH holography for details on selected panels. In *SAE Noise and Vibration Conference and Exhibition*, volume SAE-2007-01-2276, St. Charles, IL, USA, May 2007.

(Cited on page 66)

[92] W. G. Neubauer. *Acoustic Reflection from Surfaces and Shapes*. Naval Research Laboratory, Department of the Navy, Nashlinton, D.C, USA, Jun. 1986.

(Cited on page 71)

[93] F. V. Hunt. *Origins in Acoustics: The Science of Sound from Antiquity to the Age of Newton*. Number 196. Yale University Press, first edition edition, Aug. 1978.

(Cited on page 71)

[94] P. Mackensen. *Auditive localization. head movements, an additional cue in localization*. PhD thesis, Technical University Berlin, Berlim, germany, Jan. 2004.

(Cited on page 73)

[95] P. L. Uslenghi, T. B. Senior, and J. J. Bowman, editors. *Electromagnetic And Acoustic Scattering Simple Shapes*. Number 728. Taylor & Francis, revised edition, Set. 1988.

(Cited on page 73)

[96] P. Y. Ufimtsev. *Fundamentals of the Physical Theory of Diffraction*. Wiley-IEEE Press, Feb. 2007.

(Cited on page 73)

[97] E. Kreyszig. *Advanced Engineering Mathematics*. Wiley, 10 edition, Aug. 2011.

(Cited on page 75)

[98] *Mathematische Annalen Journal (Springer)*. `http://www.springer.com/mathematics/journal/208`, Fev. 2013.

(Cited on page 76)

[99] G. B. Arfken, H. J. Weber, and F. E. Harris. *Mathematical Methods for Physicists, Seventh Edition: A Comprehensive Guide*. Academic Press, 7 edition, Jan. 2012.

(Cited on page 76)

[100] T. L. Chow. *Mathematical Methods for Physicists: A Concise Introduction*. Cambridge University Press, Jul. 2000.

(Cited on page 76)

[101] J. L. E. Dreyer and H. H. Turner, editors. *History of the Royal Astronomical Society (v. 1)*. Royal Astronomical Society, London, UK, 1923.

(Cited on page 79)

[102] F. Bowman. *Introduction to Bessel Functions*. Dover Publications, Oct. 2010.

(Cited on page 79)

[103] A. Parthy, N. Epain, A. van Schaik, and C. T. Jin. Comparison of the measured and theoretical performance of a broadband circular microphone array. *The Journal of the Acoustical Society of America*, 130(6):3827–3837, 2011.

(Cited on page 90)

[104] M. Mosher; M. E. Watts; S. Jovic and S. M. Jaeger. Calibration of microphone arrays for phased array processing. In *3rd AIAA/CEAS Aeroacoustics Conference*, number AIAA-1997-1678, Atlanta, GA, USA, May 1997.

(Cited on page 118)

[105] W. H. Humphreys; C. H. Gerhold; A. J. Zuckerwar; G. C. Herring and S. M. Bartram. Performance analysis of a cost-effective electret condenser microphone directional array. In *9th AIAA/CEAS Aeroacoustics Conference and Exhibit*, number AIAA-2003-3195, Hilton Head, SC, USA, May 2003.

(Cited on page 118)

[106] W. M. Hartmann. *Signals, Sound, and Sensation*. American Institute of Physics, Aug. 2004.

(Cited on page 118)

[107] H. Holthusen and H Smit. A new data acquisition system for microphone array measurements in wind tunnels. In *7th AIAA/CEAS Aeroacoustics Conference and Exhibit*, number AIAA-2001-2169, Maastricht, The Netherlands, May 2001.

(Cited on page 124)

[108] E. Rademaker, P. Sijtsma, and B. Tester. Mode detection with an optimised array in a model turbofan engine intake at varying shaft speeds. In *7th AIAA/CEAS Aeroacoustics Conference and Exhibit*, number AIAA-2001-2181, Maastricht, Netherlands, May 2001.

(Cited on page 124)

[109] Z. Sulaiman. Effect of open-jet shear layers on aeroacoustic wind tunnel measurements. Master's thesis, Delft University of Technology, Delft, Netherlands, Nov. 2011.

(Cited on page 124)

[110] American National Standards Institute. ANSI 81.26-1995 - Method for Calculation of the Absorption of Sound by the Atmosphere, Jun. 2009.

(Cited on page 124)

[111] J. T. Katsikadelis. *Boundary Elements: Theory and Applications*. Elsevier Science, 1 edition, Jun. 2002.

(Cited on page 137)

[112] Y. Liu. *Fast Multipole Boundary Element Method: Theory and Applications in Engineering*. Cambridge University Press, 1 edition, Ago. 2009.

(Cited on pages 137, 138, 142, 196 and 215)

[113] R. Ram-Mohan. *Finite Element and Boundary Element Applications in Quantum Mechanics (Oxford Applied and Engineering Mathematics)*. Oxford University Press, USA, Nov. 2002.

(Cited on page 137)

[114] S. Kirkup. *The Boundary Element Method in Acoustics: A Development in Fortran (Integral Equation Methods in Engineering)*. Integrated Sound Software, Oct. 1998.

(Cited on pages 138 and 142)

[115] R. H. Lyon and R. G. DeJong. *Theory and Application of Statistical Energy Analysis*. Butterworth-Heinemann, 2 edition, Dec. 1994.

(Cited on page 138)

[116] C. A. Brebbia, J. C. F. Telles, and L. C. Wrobel. *Boundary Element Techniques: Theory and Applications in Engineering*. Springer, softcover reprint of the original 1st ed. 1984 edition, Jul. 2012.

(Cited on pages 138 and 142)

[117] H. A. Schenck. Improved integral formulation for acoustic radiation problems. *The Journal of the Acoustical Society of America*, 44(1):41–58, 1968.

(Cited on page 139)

[118] T. W. Wu, editor. *Boundary Element Acoustics: Fundamentals and Computer Codes (Advances in Boundary Elements)*. Number 256. WIT Press, Set. 2000.

(Cited on pages 139 and 142)

[119] P. J. T. Filippi. Layer potentials and acoustic diffraction. *Journal of Sound and Vibration*, 54(4):473 – 500, 1977.

(Cited on page 139)

[120] R. D. Ciskowski and C. A. Brebbia. *Boundary Element Methods in Acoustics*. Computational Mechanics Publications, Oct. 1991.

(Cited on page 140)

[121] L. H. Chen and D. G. Schweikert. Sound radiation from an arbitrary body. *The Journal of the Acoustical Society of America*, 35(10):1626–1632, 1963.

(Cited on page 140)

[122] E. Sarradj. Brief comparison of Kirchhoff-Helmholtz-BEM and acoustical energy BEM for exterior domains. In *NAG/DAGA International Conference on Acoustics 2009*, Rotterdam, Netherlands, Mar. 2009.

(Cited on page 141)

[123] A. F. Seybert, B. Soenarko, F. J. Rizzo, and D. J. Shippy. An advanced computational method for radiation and scattering of acoustic waves in three dimensions. *The Journal of the Acoustical Society of America*, 77(2):362–368, 1985.

(Cited on page 141)

[124] V. C. Henríquez. *Numerical Transducer Modeling*. PhD thesis, Technical University of Denmark, Denmark, 2001.

(Cited on page 141)

[125] E. B. Carneiro. *Theoretical and Experimental Analysis of In Situ Measurements of Acoustic Impedance (Original: Análise Teórica e Experimental do Processo de Medição In Situ da Impedância Acústica)*. PhD thesis, Federal University of Santa Catarina, Florianópolis, SC, Brazil, May 2011.

(Cited on page 141)

[126] P. M. Juhl. *The Boundary Element Method for Sound Field Calculations*. PhD thesis, Technical University of Denmark, Denmark, Aug. 1993.

(Cited on page 141)

[127] R. Visser. *A Boundary Element Approach to Acoustic Radiation and Source Identification*. PhD thesis, University of Twente, Enschede, Netherlands, Sep. 2004.

(Cited on page 141)

[128] F. Holmström. Structure-acoustic analysis using BEM/FEM; implementation in matlab. Master's thesis, Lund University, Sweden, May 2001.

(Cited on page 141)

[129] LMS Int. *Sysnoise Revision 5.6 Manual*. LMS International N.V., Leuven, Belgium, 1 st. edition, Mar. 2003.

(Cited on pages 142 and 163)

[130] C. Brezinski. *Padé-type approximation and general orthogonal polynomials*. International series of numerical mathematics. Birkhäuser, 1980.

(Cited on page 142)

[131] LMS Engineering, Website. http://www.lmsintl.com, Feb. 2013.

(Cited on page 142)

[132] P. Juhl and V. C. Henriquez. *Open BEM Project, Website*. http://www.openbem.dk/, Dec. 2012.

(Cited on page 143)

[133] Abaqus (Dassault Systèmes), Website. http://www.3ds.com/pt/products/simulia/portfolio/abaqus, Feb. 2013.

(Cited on page 143)

[134] Ansys, Website. http://www.ansys.com/, Feb. 2013.

(Cited on page 143)

[135] VA One (ESI Group), Website. http://www.esi-group.com/products/vibro-acoustics/va-one, Feb. 2013.

(Cited on page 143)

[136] S. Marburg and B. Nolte, editors. *Computational Acoustics of Noise Propagation in Fluids - Finite and Boundary Element Methods*. Number 578. Springer, Apr. 2008.

(Cited on page 143)

[137] E. J. Sapountzakis. *Recent Developments in Boundary Element Methods: A Volume to Honour John T. Katsikadelis*. Number 416. WIT Press, May 2010.

(Cited on page 143)

[138] A. J. Jerri. The shannon sampling theorem - its various extensions and applications: A tutorial review. *Proceedings of the IEEE*, 65(11):1565 – 1596, nov. 1977.

(Cited on page 143)

[139] R. H. Macneal. A simple quadrilateral shell element. *Computers & Structures*, 8(2):175 – 183, 1978.

(Cited on page 144)

[140] J. H. Holland. *Adaptation in Natural and Artificial Systems: An Introductory Analysis with Applications to Biology, Control, and Artificial Intelligence*. A Bradford Book, Apr. 1992.

(Cited on page 168)

[141] D. E. Goldberg. *Genetic Algorithms in Search, Optimization, and Machine Learning*. Addison-Wesley Professional, 1 edition, Jan. 1989.

(Cited on page 168)

[142] D. E. Goldberg. *The Design of Innovation (Genetic Algorithms and Evolutionary Computation)*. Springer, 1 edition, Jun. 2002.

(Cited on page 168)

[143] R. L. Haupt and S. E. Haupt. *Practica Genetic Algorithms*. Second edition edition, 2004.

(Cited on page 168)

[144] S. N. Sivanandam and S. N. Deepa. *Introduction to Genetic Algorithms*. 2008.

(Cited on pages 168, 169, 174, 176 and 178)

[145] C. R. Darwin. *On the origin of species by means of natural selection, or the preservation of favoured races in the struggle for life*. London: John Murray, 1859.

(Cited on page 168)

[146] R. Lowen and A. Verschoren, editors. *Foundations of Generic Optimization: Volume 2: Applications of Fuzzy Control, Genetic Algorithms and Neural Networks (Mathematical Modelling: Theory and Applications)*. Springer, Nov. 2010.

(Cited on page 169)

[147] P. Ponce-Cruz and F. D. Ramírez-Figueroa. *Intelligent Control Systems with LabVIEW*. Springer, 1st edition. edition, Dec. 2009.

(Cited on page 171)

[148] M. Mitchell. *An Introduction to Genetic Algorithms (Complex Adaptive Systems)*. A Bradford Book, third printing edition, Fev. 1998.

(Cited on page 174)

[149] T. Back. *Evolutionary Algorithms in Theory and Practice: Evolution Strategies, Evolutionary Programming, Genetic Algorithms*. Oxford University Press, USA, Jan. 1996.

(Cited on page 176)

[150] A. E. Eiben and J. E. Smith. *Introduction to Evolutionary Computing*. Springer, Oct. 2008.

(Cited on page 177)

[151] K. A. Jong. *An analysis of the behavior of a class of genetic adaptive systems*. PhD thesis, Computer and Communication Sciences, University of Michigan, Aug. 1975.

(Cited on page 177)

[152] T. Weise. *Global Optimization Algorithms – Theory and Application*. 2 edition, Jun. 2009.

(Cited on page 177)

[153] P. Sijtsma. Circular harmonics beamforming with multiple rings of microphones. In *18th AIAA/CEAS Aeroacoustics Conference (33rd AIAA Aeroacoustics Conference)*, number AIAA-2012-2224, Colorado Springs, CO, USA, Jun. 2012.

(Cited on pages 196 and 215)

[154] J. Hromkovic. *Algorithmics for Hard Problems: Introduction to Combinatorial Optimization, Randomization, Approximation, and Heuristics*. Springer, Dec. 2010.

(Cited on pages 197 and 215)

[155] T. Lentz. *Binaural Technology for Virtual Reality*. PhD thesis, Institut für Technische Akustik, RWTH Aachen, Germany, Nov. 2007.

(Cited on page 282)

[156] F. Zotter. *Analysis and Synthesis of Sound-Radiation with Spherical Arrays*. PhD thesis, Institute of Electronic Music and Acoustics, University of Music and Performing Arts, Austria, Sep. 2009.

(Cited on page 282)

APPENDIX

Appendix A – Electronic Version of the Dissertation

Enclosed here there is the PDF electronic version of this document. The reader may utilize zooming to better see and understand the details.

Appendix B – Abstract in Foreign Language

B.1 Samenvatting

Bundelvorming met Inbegrip van Geluidsdiffractie over Cilinderoppervlakken

Bundelvorming (beamforming) is een bekende signaalverwerkingstechniek die toegepast wordt bij antennes en in de radioastronomie. Het is in wezen een techniek om bronnen te lokaliseren door het afstemmen van golfbundels uit een bepaalde richting of uit een bepaald gebied. De techniek werd voor het eerst, in een rudimentaire vorm, toegepast tijdens de Eerste Wereldoorlog. Maar de ontwikkelingen die hebben geleid tot het maken van geluidsbronnenplaatjes stammen uit de vroege jaren zeventig.

Het onderhavige werk beschouwt de toepassing op sensoren op harde cilindervormige oppervlakken, waarbij gekeken wordt naar geluid dat van buiten de cilinder komt. Aldus kunnen bronnen rondom de cilinder gedetecteerd en geïnspecteerd worden. Daartoe moet er rekening mee worden gehouden dat het geluid zich niet vrij voortplant, maar dat de cilinder zorgt voor afbuiging (diffractie) van geluid. Een analytische benadering hiervoor wordt uitgewerkt en geschikt gemaakt voor toepassing op bundelvormingsalgoritmen. Op deze manier wordt een wezenlijke vernieuwing gerealiseerd, omdat in de meeste andere toepassingen enkel het invallende vrije veld wordt meegenomen in de naverwerking. Daarnaast zijn, in een anechoïsche ruimte, metingen gedaan op een van de bestudeerde geometrieën, ten einde die te vergelijken met analytische en numerieke simulaties.

Op twee fronten worden andere, numerieke methoden ingezet om de fysische betekenis van de resultaten te staven en te bespreken, en om te zoeken naar een meer geschikte geometrie. De randelementenmethode (BEM) wordt gebruikt voor een algemene beoordeling van het probleem, aangezien verreweg de meeste structuren daarmee gemodelleerd kunnen worden. Het doel is om, ter vergelijking, identieke diffractiegevallen door te rekenen, zowel met het analytische model als met BEM. Daarna wordt een studie besproken naar de invloed van het rooster van het 3D-model op de fouten in de bronlokalisatiebepaling in de door bundelvorming gecreëerde geluidsbronnenplaatjes. Verder wordt een optimaliseringsmethode, op basis van Genetische Algoritmen (GA), ontwikkeld voor de plaatsing van sensoren op het cilinderoppervlak, met als doel het verhinderen van zijlobben en pseudo-bronnen, en om het dynamisch bereik zo groot mogelijk te maken.

De toepassing van de bestudeerde methoden heeft, in samenhang met de bundelvormingstechniek, nieuwe gezichtspunten opgeleverd voor het ontwerpen van arrays. Dit document bespreekt vervolgens de verbeteringen en de problemen qua prestaties op het gebied van geluidsbronlokalisatie. Ten slotte is er een samenvatting van de onderzoeksbijdragen en een aantal suggesties voor toekomstig werk.

B.2 Zusammenfassung

Beamforming unter Berücksichtigung von akustischer Beugung an zylindrischen Oberflächen

Beamforming ist eine Methode der Signalverarbeitung, die für ihre Anwendung in der Antennentechnik und der Radioastronomie bekannt ist. Es handelt sich dabei im Wesentlichen um eine Technik der Quelllokalisierung basierend auf der Konformität von Wellenstrahlen aus einer gegebenen Raumrichtung oder -region. Die rudimentäre Anwendung in der Akustik stammt ursprünglich aus dem Ersten Weltkrieg. Allerdings haben die Fortschritte, die zur Erzeugung von akustischen Bildern geführt haben, in den frühen siebziger Jahren begonnen.

Die vorliegende Arbeit behandelt die Anwendung dieser Technik auf Sensoren, die auf einem schallharten Zylinder angebracht sind, wobei das externe Feld gesucht wird. Demzufolge können Schallquellen um den Zylinder bestimmt und visualisiert werden. Zu diesem Zweck wird nicht nur das Freifeld in Betracht gezogen, sondern auch das Beugungsfeld des Zylinders. Ein analytisches Modell des Problems wird entwickelt und angepasst, um Algorithmen des Beamformings anzuwenden. Dies ist ein Beitrag dieser Forschung, da die meisten Anwendungen nur das einfallende Feld in der Nachverarbeitung betrachten. Zusätzlich wurden Messungen in einer reflexionsfreien Umgebung für eine der untersuchten Geometrien durchgeführt, um die Ergebnisse mit den analytischen und numerischen Simulationen zu vergleichen.

Andere numerische Methoden sind an zwei Stellen durchgeführt worden, um die physikalische Bedeutung zu bestätigen und die Ergebnisse zu diskutieren; und um eine geeignetere Geometrie zu suchen. Die Randelementemethode (REM oder BEM) wird benutzt um das Problem allgemein zu lösen, da die große Mehrzahl der Strukturen damit modelliert werden können. Das Ziel dabei ist es, identische Anordnungen und deren Beugung mit dem analytischen Modell und der BEM zu berechnen und zu vergleichen. Die Arbeit zeigt anschließend eine Studie zur Korrelation des Gitters des 3D-Modells mit den Lokalisierungsfehlern der mittels Beamforming erzeugten Karten. Anschließend wird eine Optimierungsmethode basierend auf genetischen Algorithmen (GA) entwickelt um die Sensoren auf der Zylinderoberfläche so zu platzieren, dass Nebenkeulen und sekundäre Hauptkeulen verhindert und der Dynamikbereich maximiert werden.

Die Anwendung dieser untersuchten Methoden in Kombination mit dem Beamforming hat neue Aspekte im Array-Design geschaffen. Diese Arbeit diskutiert und zeigt Verbesserungen und Probleme bezüglich der Effizienz der Schallquellenortung. Abschließend wird die Arbeit bezüglich der Forschungsbeiträge zusammengefasst und einige Gedanken zu zukünftigen Arbeiten gegeben.

B.3 Resumen

Beamforming considerando difracción acústica en superficies cilíndricas

Beamforming es una técnica de procesamiento de señales ya conocida por sus aplicaciones en antenas y radioastronomía. Es esencialmente una técnica de localización de fuentes basada en la conformación de haces de onda de una dada dirección o región en el espacio. Su aplicación en acústica fue iniciada de forma rústica en la Primera Guerra Mundial. Sin embargo, los avances que propiciaron la creación de imágenes acústicas datan desde la década del setenta.

Este trabajo propone la aplicación de esta técnica considerando que los sensores están posicionados en la superficie de una estructura rígida y cilíndrica, siendo que el campo externo es el objeto de interés. De este modo, las fuentes sonoras alrededor del cilindro serán detectables y pasibles de visualización. Para este propósito, diferente del comúnmente aplicado, no solamente el campo libre es considerado, sino también el campo de difracción que es generado por el cilindro. El modelado analítico del problema es desarrollado y adaptado para la aplicación del algoritmo de beamforming. Esta es una de las contribuciones de esta investigación, visto que en la mayoría de las aplicaciones se considera solamente el campo incidente en el post-procesamiento. Además, para una de las geometrías estudiadas, las mediciones fueron realizadas en ambiente anecoico para comparar los resultados con las simulaciones analítica y numérica.

Otros métodos numéricos fueron también empleados en dos frentes, para confirmar el significado físico y discutir resultados, y para encontrar una geometría más adecuada. El Método de Elementos de Contorno (MEC o BEM) es utilizado para la evaluación del problema de manera genérica, visto que casi todos los tipos de estructuras pueden ser modelados en su dominio. El objetivo es calcular las mismas situaciones de difracción con el modelo analítico y con el MEC y compararlas. El trabajo entonces presenta un estudio correlacionando la malla del modelo 3D con los errores de localización en los mapas creados por el beamforming. Por consiguiente, un método de optimización basado en el Algoritmo Genético (GA) es desarrollado para posicionar los sensores en la superficie del cilindro de modo de suprimir lóbulos laterales, lóbulos espejo y maximizar el rango dinámico.

La aplicación de los métodos estudiados junto al beamforming creó nuevos aspectos en el diseño de arrays. A lo largo del documento las discusiones apuntan a las mejoras y problemas relacionados al desempeño en la localización de fuentes sonoras. Al final de este documento se presenta un resumen con las contribuciones de la investigación y algunas ideas para trabajos futuros.

B.4 Résumé

La technique du Beamforming considérant diffraction acoustique sur des surfaces cylindriques

Beamforming (ou formation de faisceaux) est une technique de traitement du signal reconnu pour ses applications dans la télécommunication et la radioastronomie. Il s'agit essentiellement d'une technique permettant de localiser les sources en fonction de la conformation des faisceaux d'ondes à partir d'une direction ou d'une région dans l'espace. Son application en acoustique a commencé de façon rudimentaire pendant la première guerre mondiale. Cependant, les progrès qui ont conduit à la création d'images acoustiques datent des années soixante-dix.

Le présent travail propose l'application de cette technique ayant les capteurs placés sur une surface cylindrique rigide avec le champ externe comme objet d'intérêt. Ainsi, les sources sonores n'importe où autour du cylindre deviennent détectables et peut être visionnées. A cet effet, non seulement le champ libre est considéré, mais aussi le champ acoustique de diffraction créée par le cylindre. Modélisation analytique du problème est développée et adapté pour appliquer l'algorithme de formation de faisceaux. C'est l'une des contributions de cette recherche puisque dans la plupart des applications uniquement le champ incident est considéré en post-traitement. En plus, les mesures ont été effectuées dans une chambre anéchoïque pour l'une des géométries étudiées pour comparer les résultats avec les simulations numériques et analytiques.

D'autres méthodes numériques sont également employés sur deux fronts, pour confirmer le sens physique et de discuter des résultats et pour rechercher une géométrie plus approprié. La méthode des éléments de frontière (BEM) est utilisée pour examiner de façon générique le problème, puisque la grande majorité des structures peut être modélisé dans son domaine. L'objectif est de calculer les mêmes situations de diffraction dans le modèle analytique et le BEM afin de les comparer. Ce travail présent ensuite une étude sur le maillage du modèle 3D utilisé en corrélation avec l'erreur de localisation de la carte des sources des faisceaux sonores. Par la suite, un procédé d'optimisation sur la base d'algorithme génétique (GA) est développée afin de placer les capteurs sur la surface du cylindre, afin d'éviter les lobes latéraux, les lobes de réseau, et d'optimiser la gamme dynamique.

L'application des méthodes étudiées avec la technique de formation de faisceau a créé de nouveaux aspects dans la conception du positionnement. Ce document aborde ensuite et souligne les améliorations et les problèmes relatifs au rendement du placement de la source. Enfin, un résumé est fait concernant les contributions effectuées et quelques réflexions pour des futures travaux.

B.5 Riassunto

Beamforming con l'Applicazione della Diffrazione Acustica su Superfici Cilindriche

Beamforming è una tecnica di processamento di segnali già conosciuta dalle sue applicazioni in antenne e nella radioastronomia. È essenzialmente una tecnica di localizzazione di fonti sonore in base alla conformazione di fasci di onda di una data direzione o regione nello spazio. La sua applicazione in acustica è stata iniziata in modo rudimentale alla prima grande guerra. Tuttavia, gli avanzi che hanno favorito la creazione delle immagini acustiche sono degli anni settanta.

Questo lavoro propone l'applicazione di questa tecnica considerando che i sensori sono posizionati sulla superficie di una struttura rigida e cilindrica, essendo il campo esterno l'oggetto di interesse. In questo modo, fonti sonore intorno al cilindro saranno rilevabili e passibili di visualizzazione. Con questo proposito, diversamente da quanto solitamente realizzato, non soltanto il campo libero sarà considerato, ma anche il campo di diffrazione creato dal cilindro. Il modellaggio analitico del problema si è sviluppato e adattato per l'applicazione dell'algoritmo di *beamforming*. Questo è uno dei contributi di questa ricerca, visto che nella maggioranza delle applicazioni soltanto il campo incidente è considerato nel post-processamento. Oltre a questo, per una delle geometrie studiate sono state fate medizioni in ambiente anecoico per paragonare i risultati con le simulazioni analitica e numerica.

Altri metodi numerici sono stati impiegati con due scopi diversi: per la conferma del significato fisico e la discussione dei risultati, e perché si potessi trovare una geometria più adeguata. Il Metodo degli Elementi di Contorno (MEC o BEM) è utilizzato per la valutazione del problema in modo generico giacché quasi tutti i tipi di strutture possono essere modellati nel suo dominio. L'obbiettivo è quello di calcolare le stesse situazioni di diffrazione con il modello analitico e con il MEC e paragonarli. Il lavoro presenta, dunque, uno studio che relaziona la rete del modello 3D agli errori di localizzazione sulle mappe create dal *beamforming*. Di conseguenza, un metodo di ottimizzazione in base ad un Algoritmo Genetico (GA) è stato sviluppato per il posizionamento dei sensori sulla superficie del cilindro in modo a prevenire lobi laterali, lobi specchio e massimizzare l'intervallo dinamico.

L’applicazione dei metodi studiati assieme al beamforming ha creato nuovi aspetti in design di *arrays*. Lungo il documento le discussioni indicano miglioramenti e problemi legati alla performance nella localizzazione di fonti sonore. Alla fine, c’è un riassunto dei contributi della ricerca e alcune idee per lavori futuri.

Appendix C – Array Geometries

The tables below display the array coordinates used in this research, i.e. EAA and GA array - see Section 3.4 for more details. The centre of the coordinate system coincides with the cylinder centre. In addition, the radius is 0,1250 m for both cases.

Table C.1: EAA coordinates.

Mic	θ (rad)	**Height** (m)
1	0,000	0,000
2	0,196	0,000
3	0,393	0,000
4	0,589	0,000
5	0,785	0,000
6	0,982	0,000
7	1,178	0,000
8	1,374	0,000
9	1,571	0,000
10	1,767	0,000
11	1,963	0,000
12	2,160	0,000
13	2,356	0,000
14	2,553	0,000
15	2,749	0,000
16	2,945	0,000
17	3,142	0,000
18	3,338	0,000
19	3,534	0,000
20	3,731	0,000
21	3,927	0,000
22	4,123	0,000
23	4,320	0,000
24	4,516	0,000
25	4,712	0,000
26	4,909	0,000
27	5,105	0,000
28	5,301	0,000
29	5,498	0,000
30	5,694	0,000
31	5,890	0,000
32	6,087	0,000

Table C.2: GA array coordinates

Mic	θ (rad)	**Height** (m)
1	-3,142	0,270
2	-2,945	0,870
3	-2,749	-0,390
4	-2,553	1,490
5	-2,356	0,500
6	-2,160	-1,490
7	-1,963	0,700
8	-1,767	1,490
9	-1,571	-0,100
10	-1,374	-0,930
11	-1,178	0,830
12	-0,982	-0,780
13	-0,785	0,130
14	-0,589	0,680
15	-0,393	-1,480
16	-0,196	-0,320
17	0,000	1,380
18	0,196	-1,480
19	0,393	-0,450
20	0,589	1,500
21	0,785	0,300
22	0,982	-0,810
23	1,178	-1,490
24	1,374	0,480
25	1,571	1,500
26	1,767	-0,650
27	1,963	-1,420
28	2,160	1,090
29	2,356	0,370
30	2,553	-1,090
31	2,749	-0,510
32	2,945	1,190

Appendix D – Software Development

As stated during the text the software development is an important part of this research. A base software named Wavemap was created with a modular concept. It integrates different programming languages and the different routines required to perform all the processing.

In Figure D.1, one can observe a summary concerning connections and capabilities. From Figure D.2 to D.6 some diagrams describing the flow of information can be consulted.

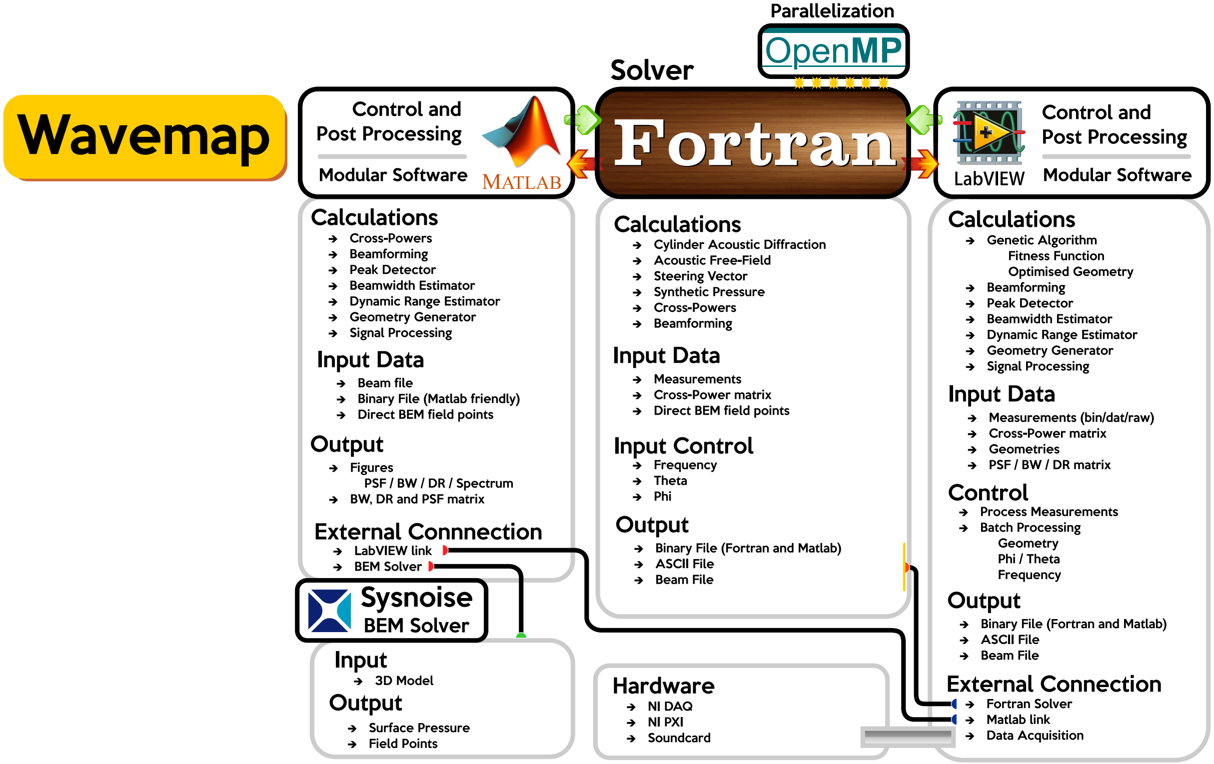

Figure D.1: Wavemap, programming language connections and processing.

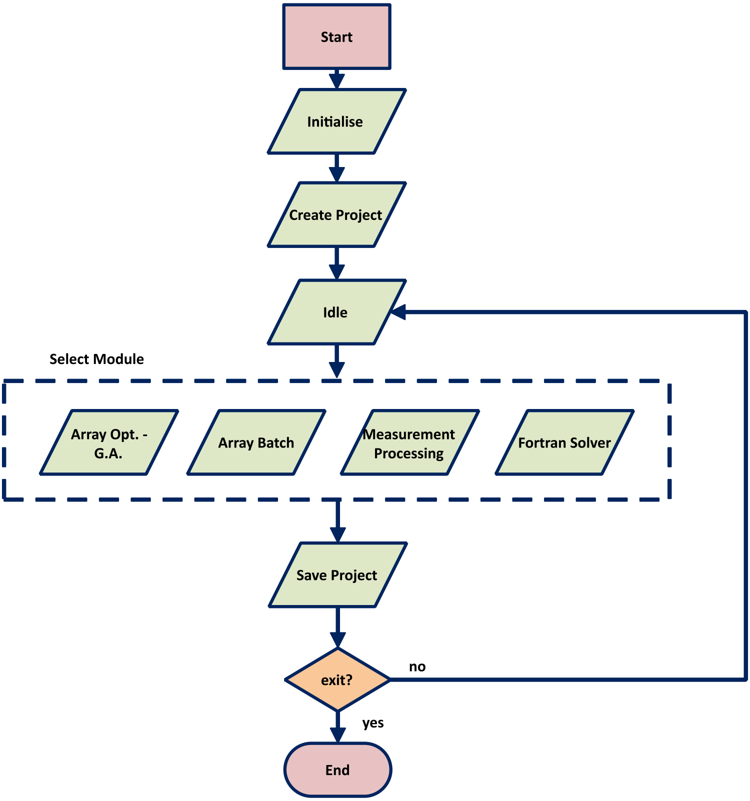

Main routine: control of the modules

Figure D.2: Wavemap, main routine.

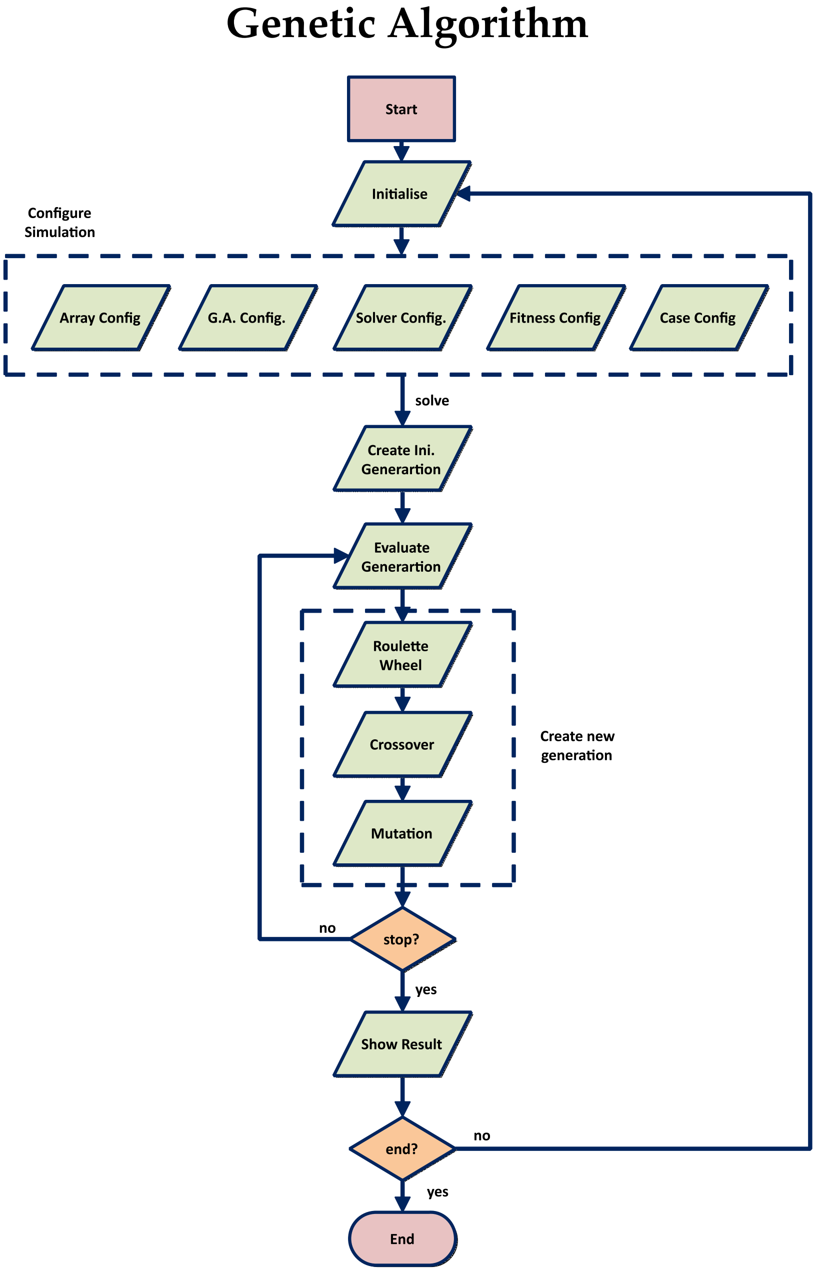

Figure D.3: Wavemap, gentetic algorithm.

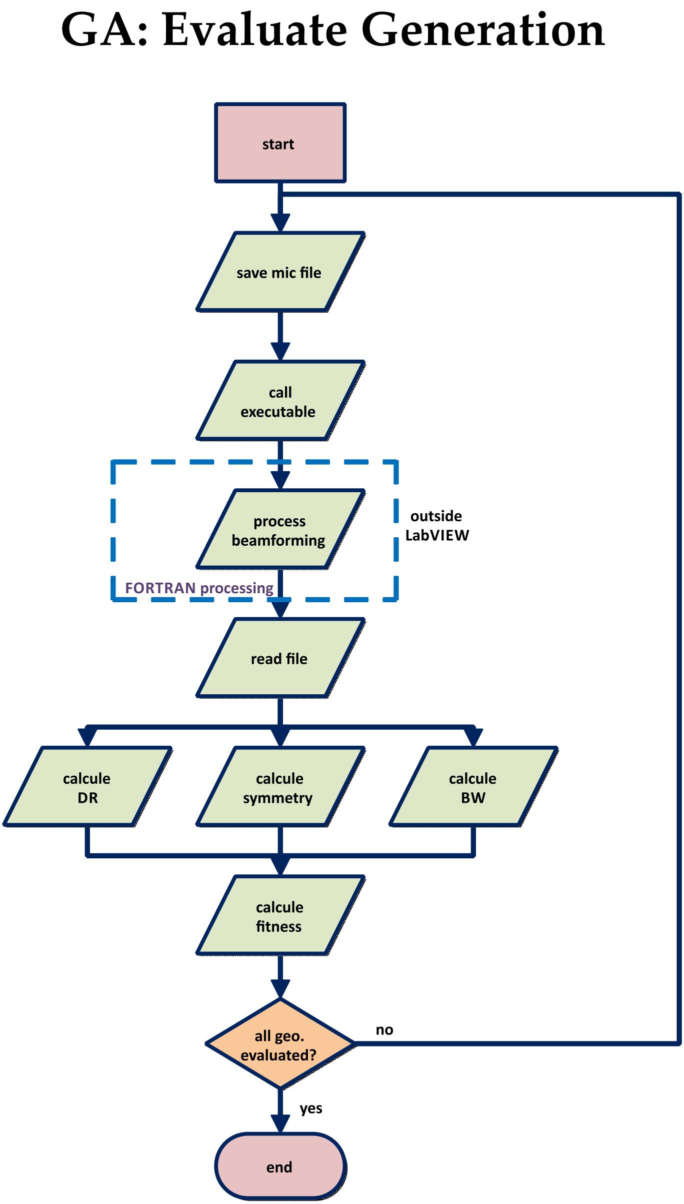

Figure D.4: Wavemap, evolution in gentetic algorithm.

Geometry Batch

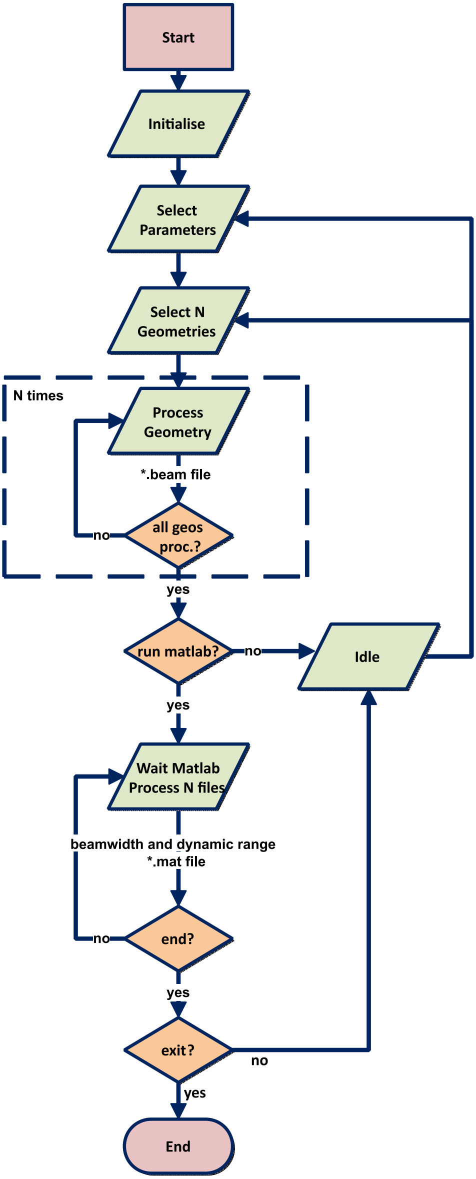

Figure D.5: Wavemap, geometry batch.

Input and Process Measurement

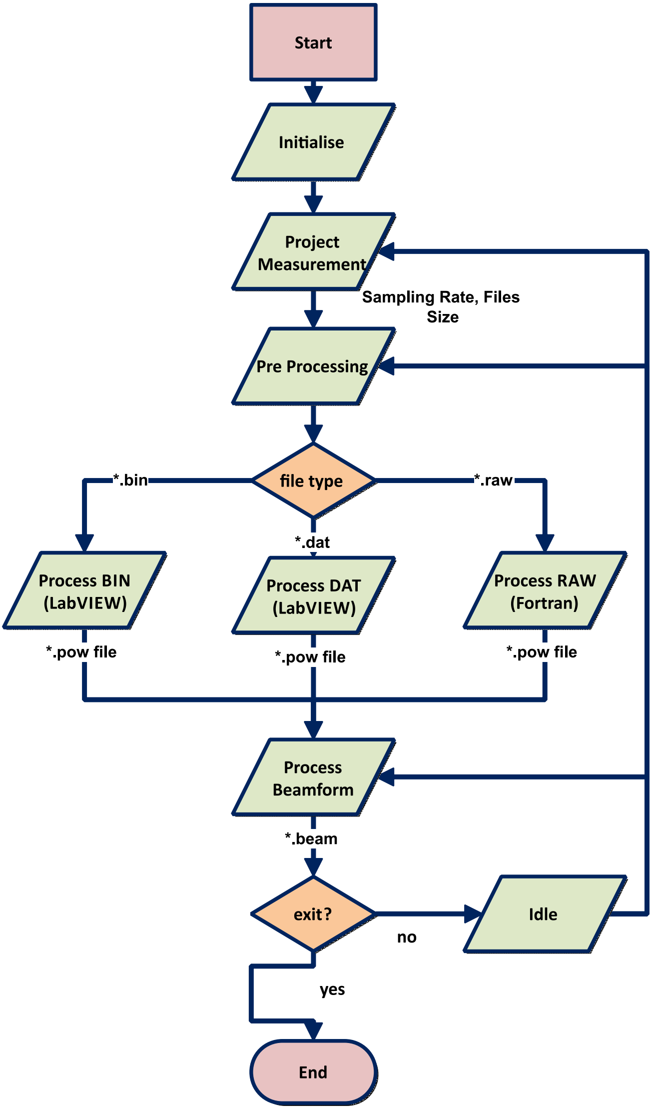

Figure D.6: Wavemap, input and process measurements.

Appendix E – Truncation Criteria for Diffraction

The truncation of the summation in Equation (4.31) (copied below) is based on the Bessel m order derivative[1] function $J'_m(x)$.

$$p(r,\theta,z) = \Bigg\{ -J'_0\left(kr_0\sin(\phi_{\text{in}})\right) \frac{H_0^{(2)}\left(kr_0\sin(\phi_{\text{in}})\right)}{H_0^{(2)'}\left(kr_0\sin(\phi_{\text{in}})\right)} - 2\sum_{m=1}^{\infty} i^m J'_m\left(kr_0\sin(\phi_{\text{in}})\right) \frac{H_m^{(2)}\left(kr_0\sin(\phi_{\text{in}})\right)}{H_m^{(2)'}\left(kr_0\sin(\phi_{\text{in}})\right)} \cos\left(m(\theta-\theta_{\text{in}})\right) \Bigg\} \exp\left(ikz\cos(\phi_{\text{in}})\right) \cdot \tag{E.1}$$

Two stop criteria (STC) were considered:

1. STC$_1$: $m \leq (kr+2)$. In general, the contribution per m increases until $m \approx kr$. After this point it decreases quite rapidly. Hence, in this first criterion, the summation goes at least to kr plus two extra m orders for a secure level of confidence.
2. STC$_2$: $|J'_m(x)| \geq (\eta * |J'_0(x)|)$, where $\eta = 10^{-4}$ is an arbitrary constant. For higher m orders, it stops the *loop*, preventing time lost in computing unimportant orders. For lower m oreders it improves the STC$_1$ results extending the process to higher orders.

To better explain the criteria, consider

$$A_m = J'_m\left(kr\sin(\phi)\right) , \tag{E.2}$$

with

a) $m = \{1,2,\ldots,\text{STC}\}$, where STC is the stop value,

b) $k = \{500:5:5000\} * \frac{2\pi}{340}$,

c) $r = 1$, and

d) $\phi = \{0:1:180\}$.

---

[1] To compute the Bessel derivative in Matlab, the following identity can be used $J'_m(x) = (J_{m-1}(x) - J_{m+1}(x))/2$.

E.1 Stop Criterion #1 (STC_1)

The sub-figures of Figure E.1 depict the processing for

1. STC_1: $m \leq (kr + 2)$,
2. $\mathrm{STC}_{1'}$: $m \leq (kr + 20)$,

exploring the idea of the first criterion. As can be seen, Figures E.1 (a) and E.1 (b) have nearly the same values, except for the differences shown in Figure E.1 (c). Figure E.1 (d) depicts the curves and the difference for one ϕ angle. One can easily deduce that as the frequency increases the differences between STC_1 and $\mathrm{STC}_{1'}$ virtually disappear.

Now consider the subtraction of the absolute values of consecutive m orders,

$$S_m = |\,J'_m(x)\,| - |\,J'_{m-1}(x)\,| \quad \text{with} \quad x = (kr\sin(\phi))\,. \tag{E.3}$$

Figure E.2 depicts the "importance" of m in contrast to kr values (for $\phi = 45°$). One can see that the values out of S_m diminish very fast for $m \geq kr$. In Figure E.2 (a) the m maximum value is 93, while in Figure E.2 (b) it is 113 (as expected). As such, increased kr values result in increased m.

In Figure E.3 it is possible to see the decay of m versus S_m for two ϕ angles and kr values. The graph depicts the processing for STC_1 and $\mathrm{STC}_{1'}$. It confirms that the STC_1 (in red) extracts the $J'_m(x)$ values with a minor loss of information. In both plots the "stop point" of STC_1 is beyond the steep decline and in the descendent part of the last peak.

In Figure E.4 it is possible to compare the calculation[2] time of STC_1 and $\mathrm{STC}_{1'}$. Considering the total time, the STC_1 is ≈26% faster than $\mathrm{STC}_{1'}$.

---

[2] Computer used: Windows 7 Ut., x64 arch., Intel i7-3939K, 6 Cores HT, 3,2 GHz, 24,0 Gb RAM. Matlab script without parallelization.

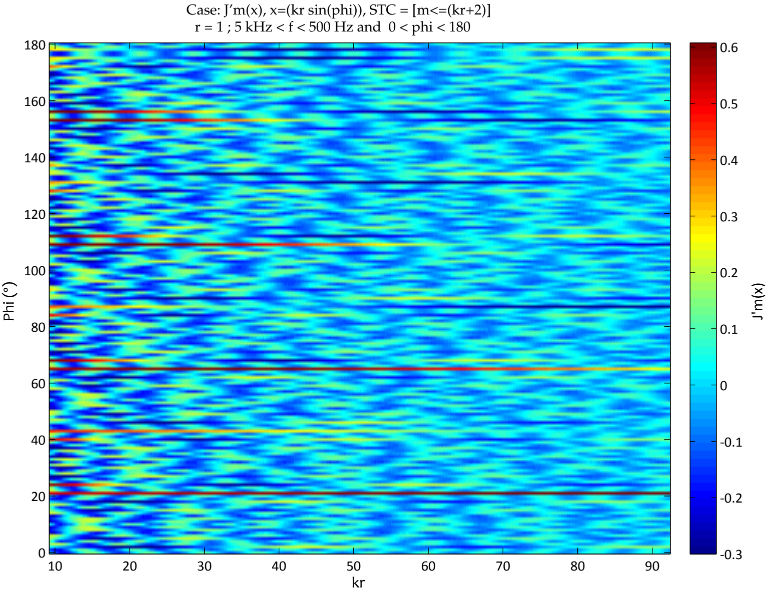

(a) STC$_1$: $m \leq (kr + 2)$

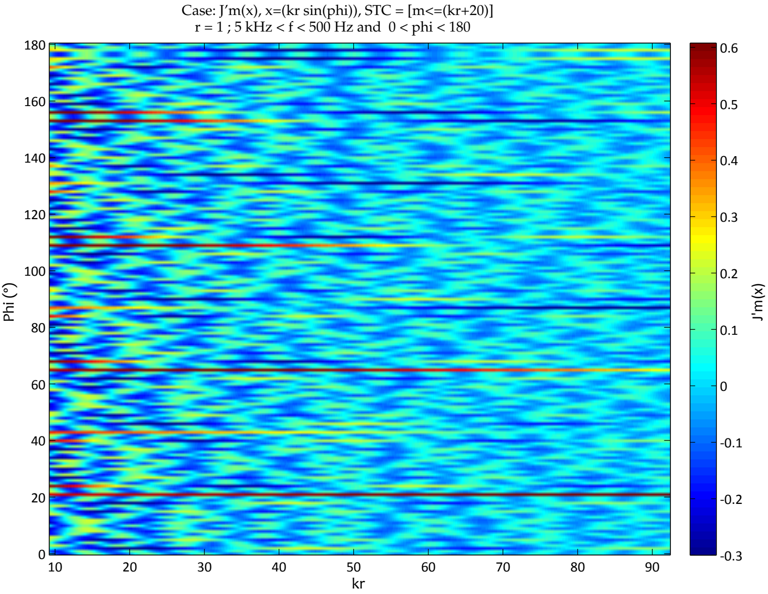

(b) STC$_{1'}$: $m \leq (kr + 20)$

Figure E.1: STC$_1$, $J'_m(kr\sin(\phi))$ for several ϕ and kr (pt.1).

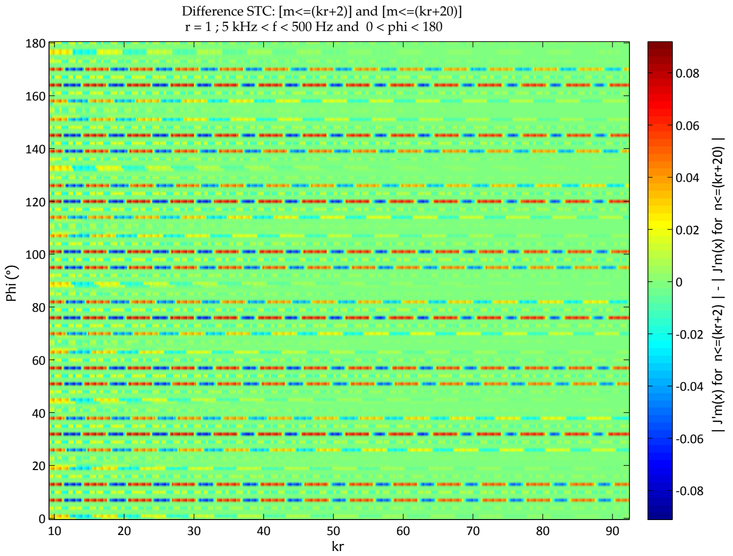

(c) Difference |(a)| - |(b)|

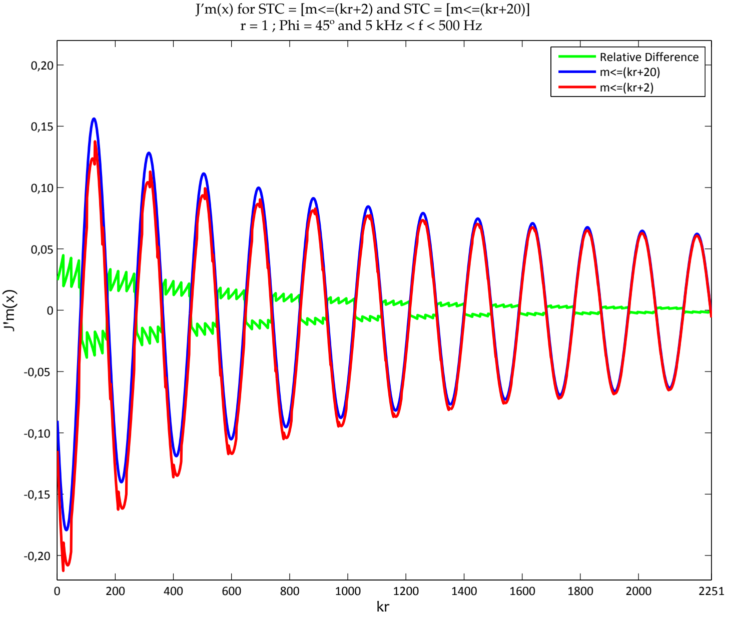

(d) Plot for $\phi = 45^\circ$ (slice from (a) and (b))

Figure E.1: STC$_1$, $J'_m(kr\sin(\phi))$ for several ϕ and kr (pt.2).

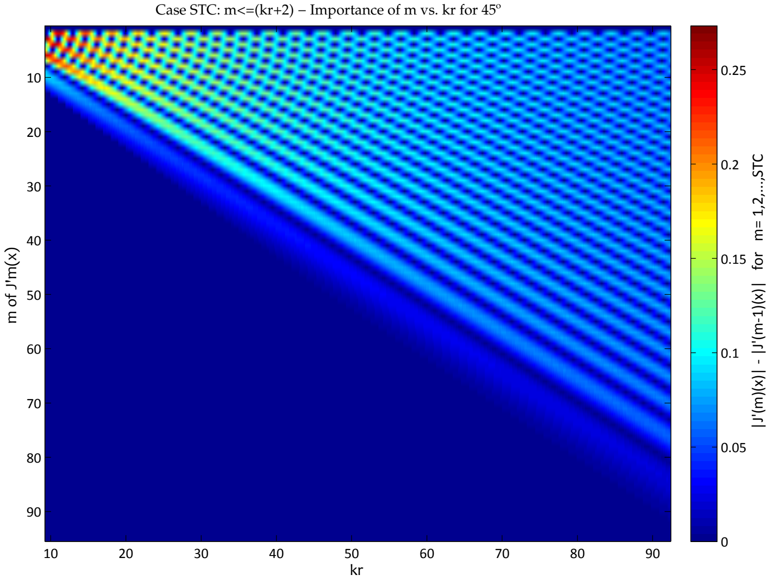

(a) STC_1: $m \leq (kr+2), \phi = 45°, \,|\,J'_m(x)\,| - |\,J'_{m-1}(x)\,|$

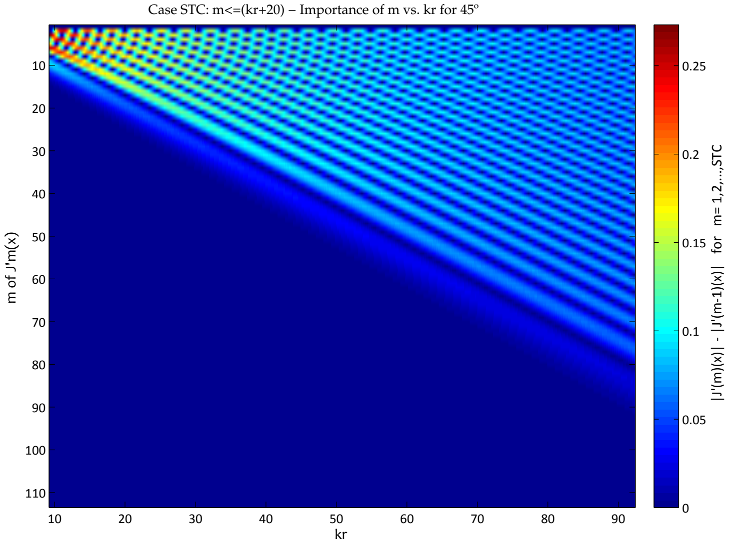

(b) $\text{STC}_{1'}$: $m \leq (kr+20), \phi = 45°, \,|\,J'_m(x)\,| - |\,J'_{m-1}(x)\,|$

Figure E.2: STC_1 , importance of m in contrast to kr values (for $\phi = 45°$).

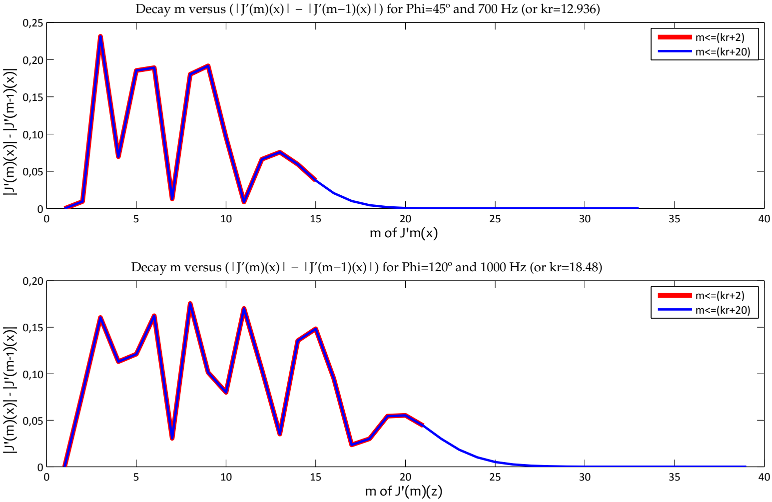

Figure E.3: STC$_1$, decay of m versus $(|J'_m(x)| - |J'_{m-1}(x)|)$ for $\phi = \{45^\circ, 120^\circ\}$.

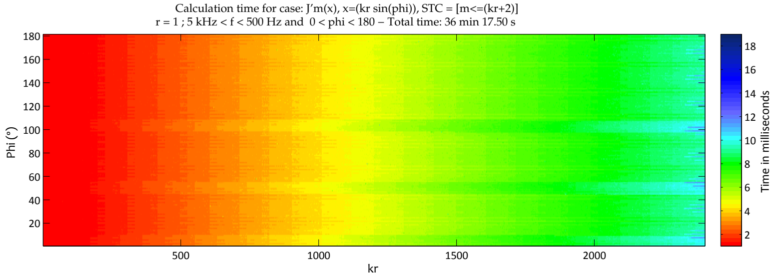

(a) STC$_1$: $m \leq (kr+2)$

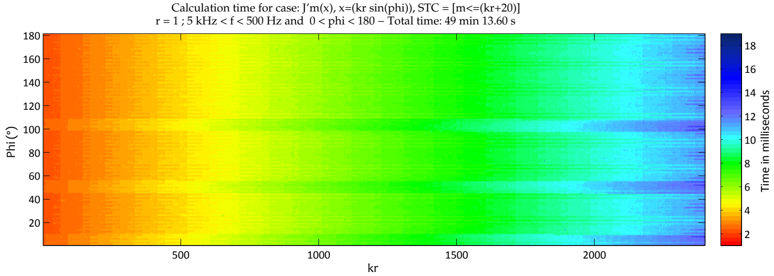

(b) STC$_{1'}$: $m \leq (kr+20)$

Figure E.4: Calculation time for STC$_1$ and STC$_{1'}$.

E.2 Stop Criterion #2 (STC_2)

The STC_2 intends to solve the differences found in Figures E.1 (c) and E.1 (d). Basically it increases the m for lower values and stops the *loop* when the process achieves a $|J_0'(x)|$ percentage.

Consider the conditions

1. STC_2: $m \leq (kr+2)$ or $|J_m'(x)| \geq (\eta * |J_0'(x)|)$,
2. $STC_{2'}$: $m \leq (kr+20)$ or $|J_m'(x)| \geq (\eta * |J_0'(x)|)$,

where $\eta = 10^{-4}$ is an arbitrary constant. Here the STC_2 is combined with STC_1 through an OR operator inside the *while loop* condition. The OR returns logical 1 (or true) if either input or both evaluate to true, and logical 0 (or false) if they do not. That is, if at least one condition is true the process continues.

It is possible to see in Figure E.5 (b) that the differences have an order of 10^{-6}. This magnitude is controlled by the constant η, lower values yield lower differences. In addition, the relevance of m against kr in Figure E.6 has presented the same behaviour of Figure E.2.

Figure E.7 confirms the general improvement showing the reduced m orders rendered by STC_2. As can also be seen in Figure E.8, the time spent to extend m for higher orders offsets the time saved for naturally higher m orders; thus, the total time is similar to the STC_1 criterion. In this case, the STC_2 is ≈19% faster than $STC_{2'}$.

E.2.1 Alternative STC_{2a}

The STC_2 condition can also be used with a slight modification:

- STC_{2a}: $m \leq (kr+2)$ or $|J_m'(x)| \geq \left(\eta * \max\left[\left|J_\mu'(x); \mu < m\right|\right]\right)$,

which implies that inside the *while loop* the code chooses a higher value between a previous iteration $|J_\mu'(x)|$ and $|J_m'(x)|$.

E.3 Parallelization

To improve calculation speed, the *loops* were split into separate *threads*. With an octa-core processing the reduction in the calculation, time was generally a quarter of the original time. Find more parallelization data in Appendix **??**

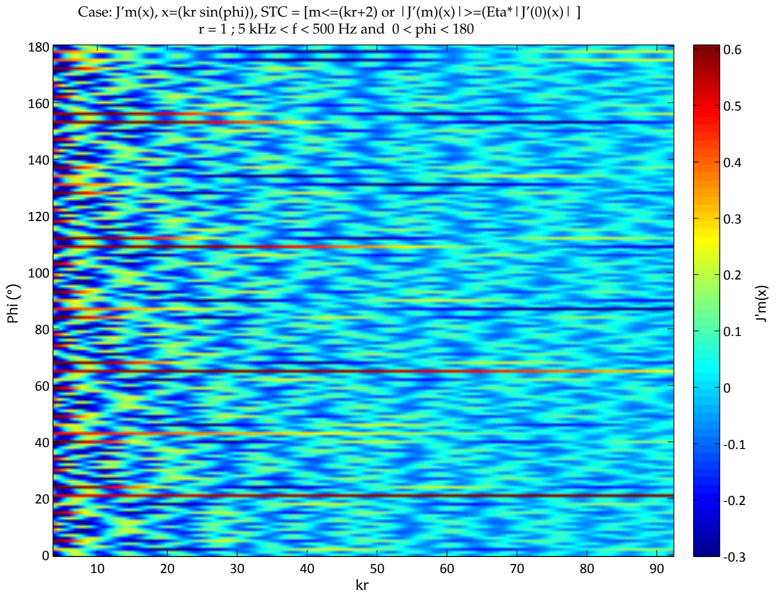

(a) STC_2: $m \le (kr+2)$

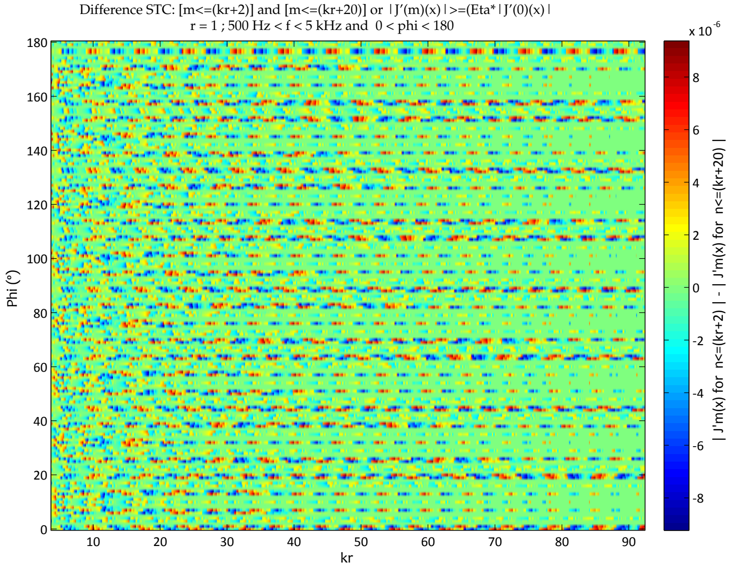

(b) Difference $|\mathrm{STC}_2|$ - $|\mathrm{STC}_{2'}|$

Figure E.5: STC_2 , $J'_m(kr\sin(\phi))$ for several ϕ and kr (pt.1).

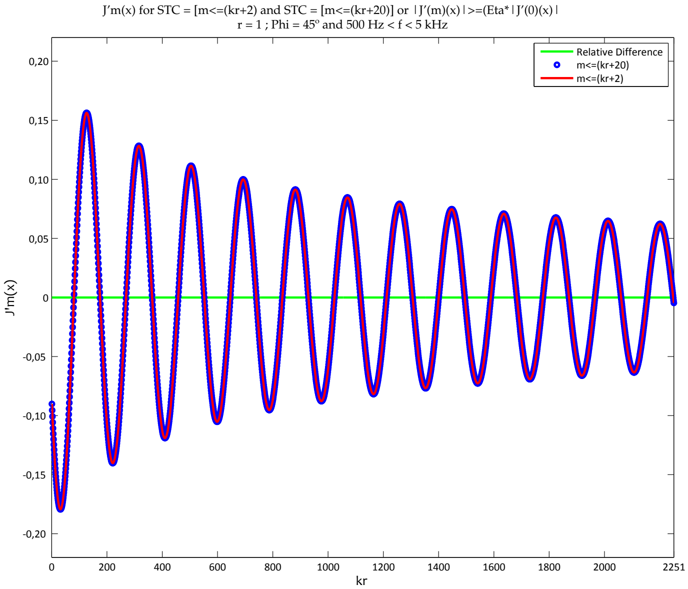

(c) Plot for $\phi = 45^\circ$ (slice from STC_2 and $\mathrm{STC}_{2'}$)

Figure E.5: STC_2 , $J'_m(kr\sin(\phi))$ for several ϕ and kr (pt.2).

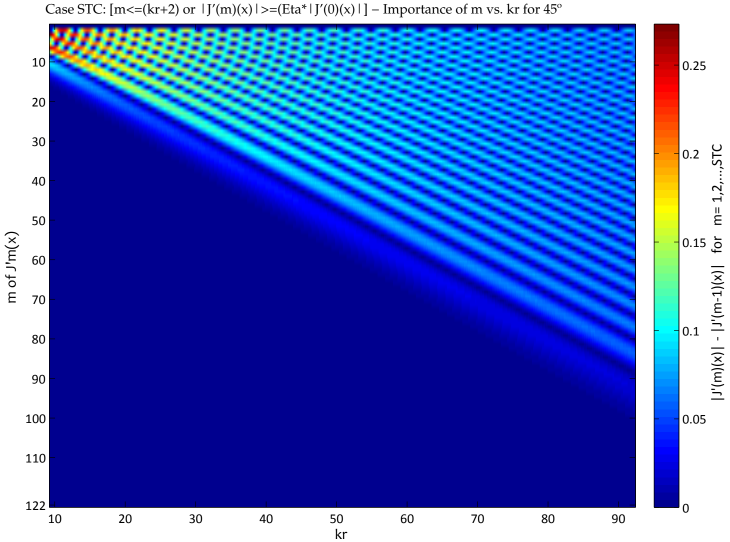

Figure E.6: STC_2 , importance of m in contrast to kr values (for $\phi = 45^\circ$).

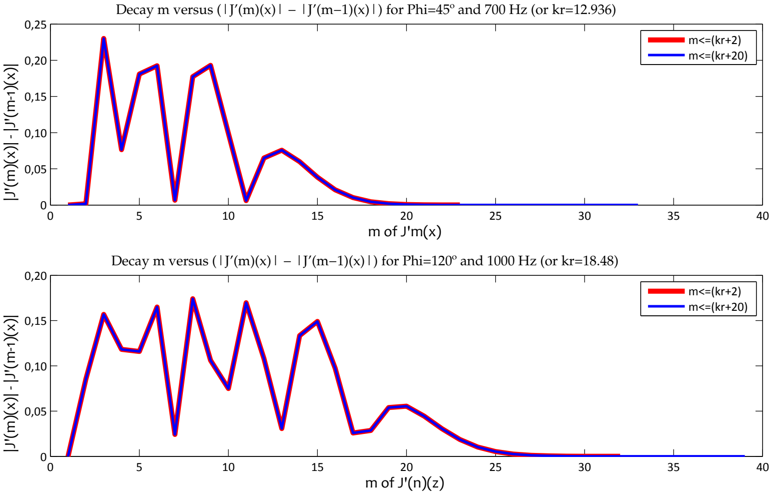

Figure E.7: STC$_2$, decay of m versus $(|J'_m(x)| - |J'_{m-1}(x)|)$ for $\phi = \{45^\circ, 120^\circ\}$.

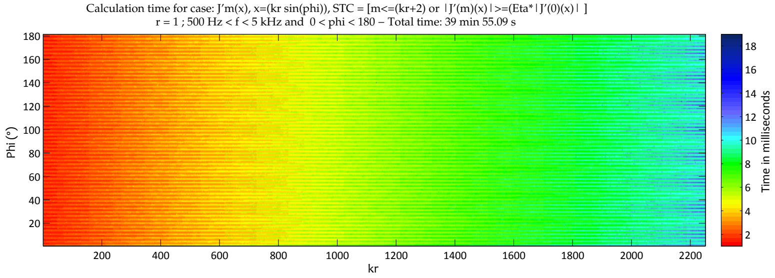

(a) STC$_2$

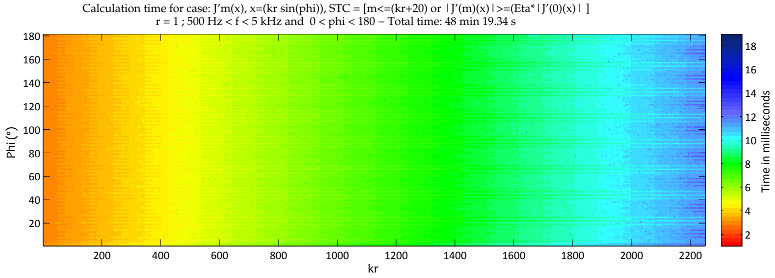

(b) STC$_{2'}$

Figure E.8: Calculation time for STC$_2$ and STC$_{2'}$.

Appendix F – Diffraction - Additional Data

In this appendix there are some extra results to complement the diffraction discussion in Chapter 4.

Figure F.1 depicts the polar plots for different radii with 32 sampling points around the cylinder.

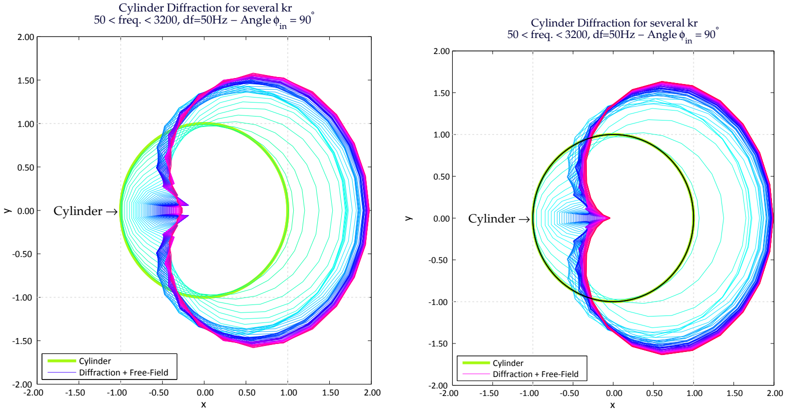

(a) $r = 0,1250$ m

(b) $r = 0,2500$ m

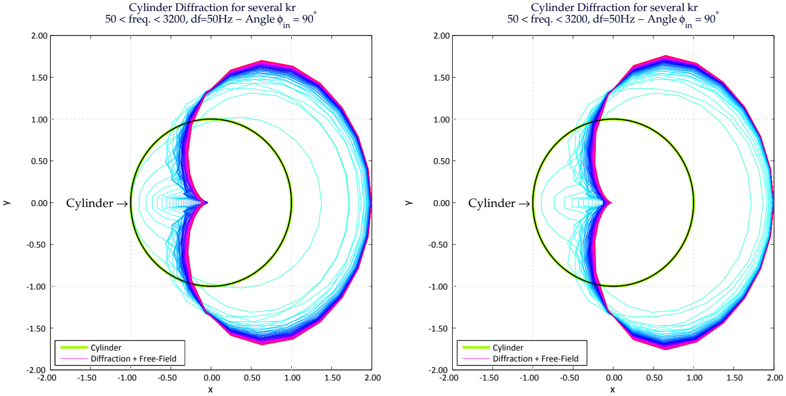

(c) $r = 0,5000$ m

(d) $r = 1,0000$ m

Figure F.1: Polar plots for different radii with 32 sampling points around the cylinder.

Figure F.2 shows polar plots for different sampling points around the cylinder with $r = 0,1250$ m.

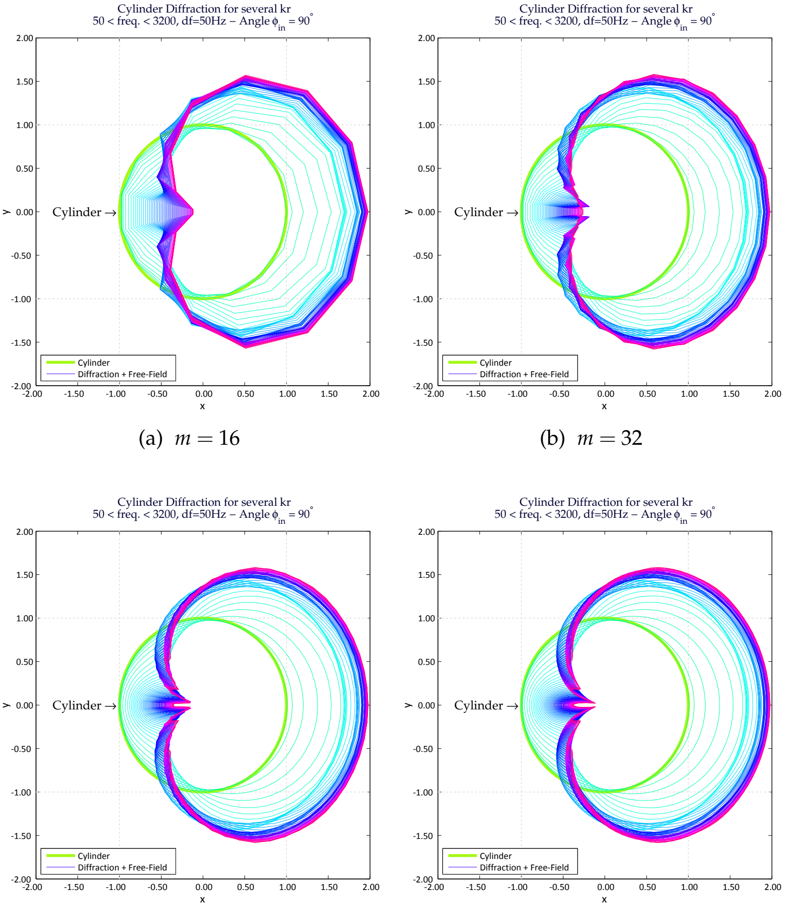

(a) $m = 16$ (b) $m = 32$

(c) $m = 64$ (d) $m = 128$

Figure F.2: Polar plots for different number of sampling points around the cylinder ($r = 0,1250$ m).

Figures F.3 and F.4 depict the diffraction plus the free-field for several angles of ϕ_{in}. As expected, it is possible to observe that there is a symmetry centred on $\phi_{in} = 90°$, this leads to same results for $\phi_{in} = 15°$ or $165°$ (Figure F.3 (b) and F.4 (c)), for example.

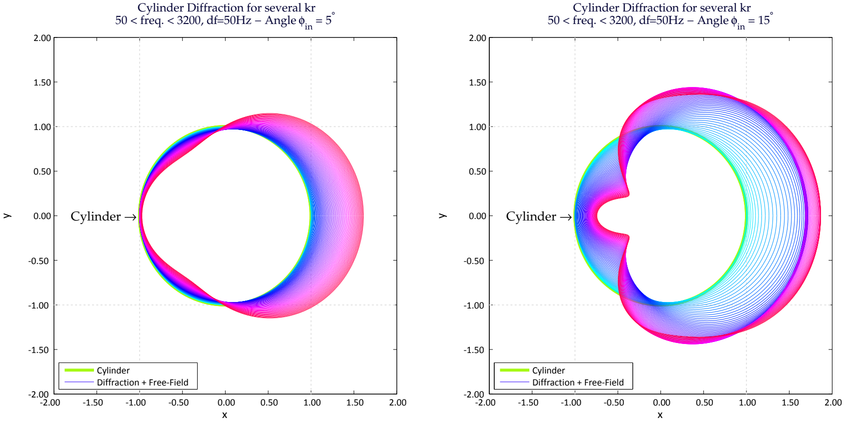

(a) $\phi_{in} = 5°$ (b) $\phi_{in} = 15°$

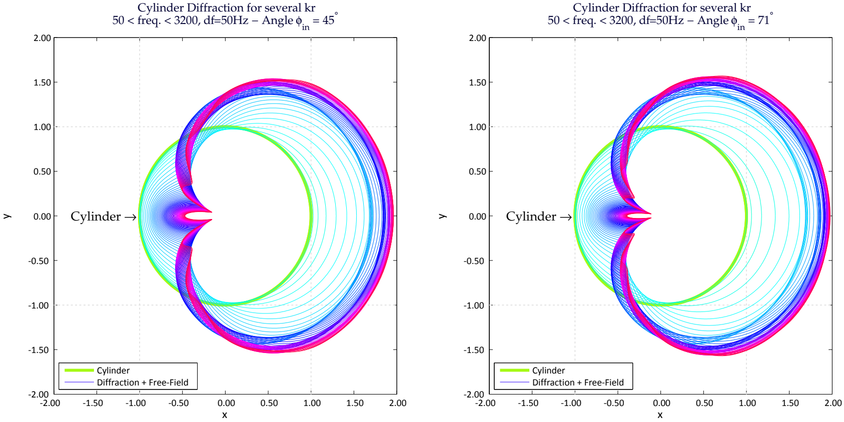

(c) $\phi_{in} = 45°$ (d) $\phi_{in} = 71°$

Figure F.3: Polar plots of acoustic pressure on the cylinder for different $\phi_{in} = \{5°, 15°, 45°, 71°\}$.

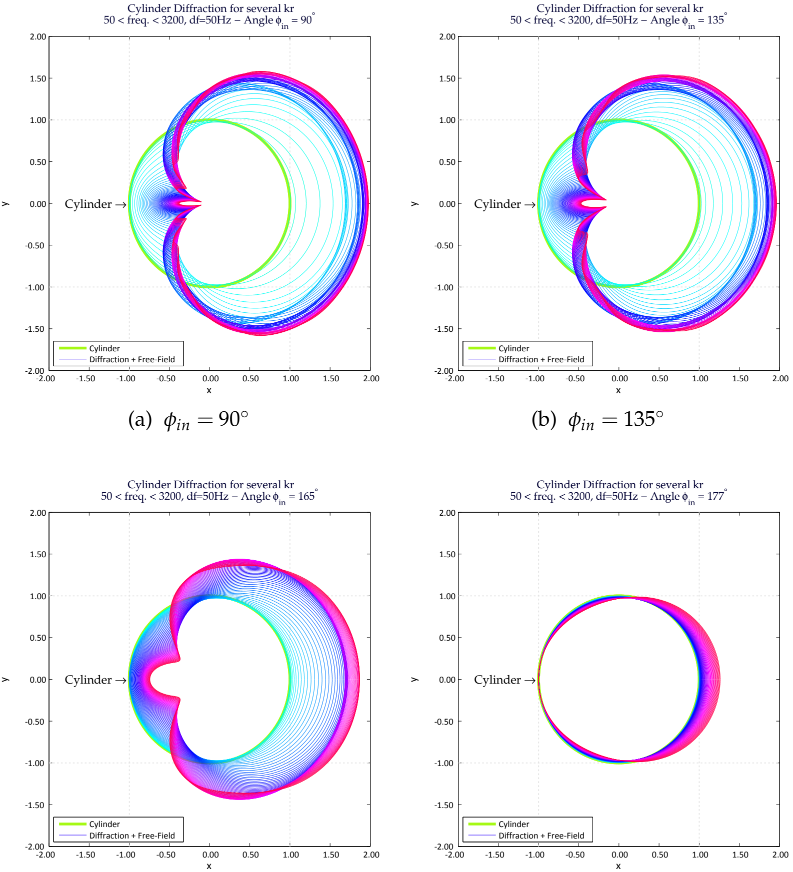

(a) $\phi_{in} = 90°$ (b) $\phi_{in} = 135°$

(c) $\phi_{in} = 165°$ (d) $\phi_{in} = 177°$

Figure F.4: Polar plots of acoustic pressure on the cylinder for different $\phi_{in} = \{90°, 135°, 165°, 177°\}$.

F.1 Analytical Simulations

The figures shown here complement the discussions of Sections 4.3.1.1 and 4.3.1.2 of Chapter 4.

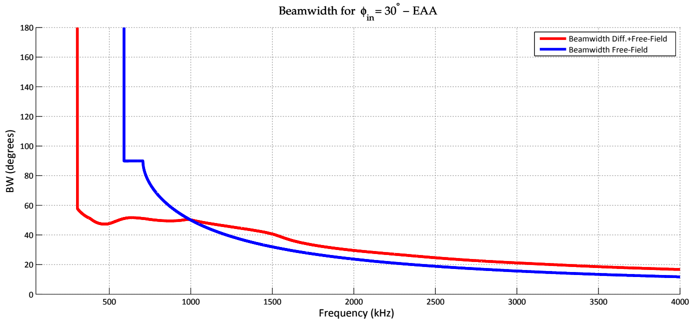

(a) $\phi_{in} = 30^\circ$

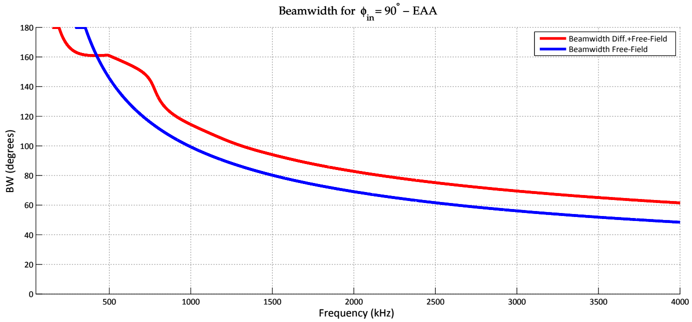

(b) $\phi_{in} = 90^\circ$

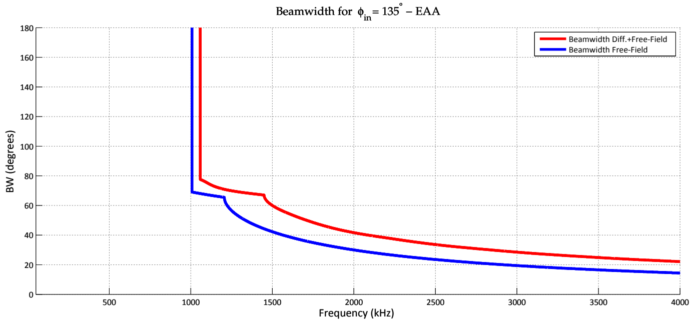

(c) $\phi_{in} = 135^\circ$

Figure F.5: BW plots of the EAA for $\phi_{in} = 30^\circ, 90^\circ$ and 135°, (linear plots, half ϕ-axis, FvB extraction).

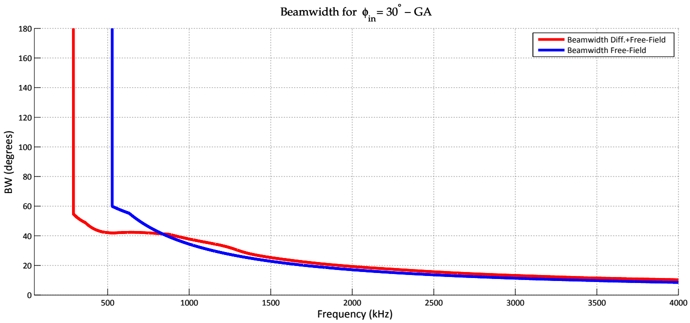

(a) $\phi_{in} = 30°$

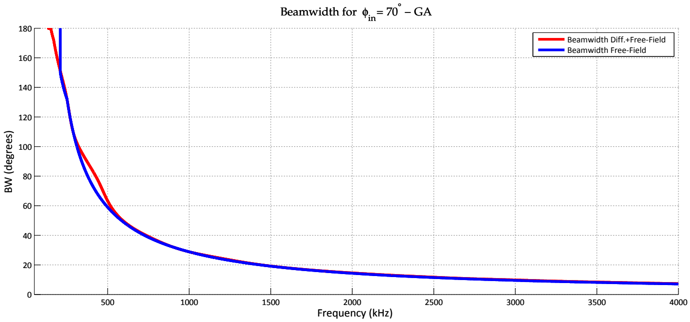

(b) $\phi_{in} = 70°$

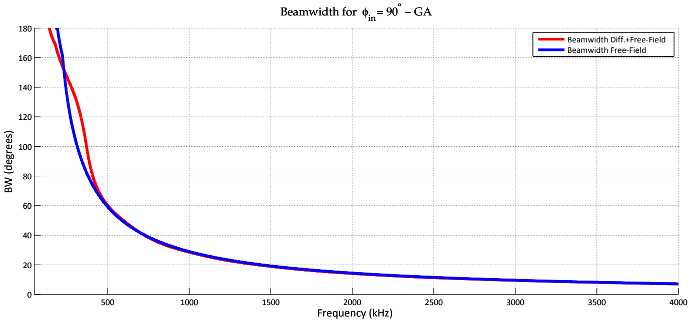

(c) $\phi_{in} = 90°$

Figure F.6: BW plots of the GA array for $\phi_{in} = 30°$, $\phi_{in} = 70°$ and $\phi_{in} = 90°$ (linear plots, FvB extraction).

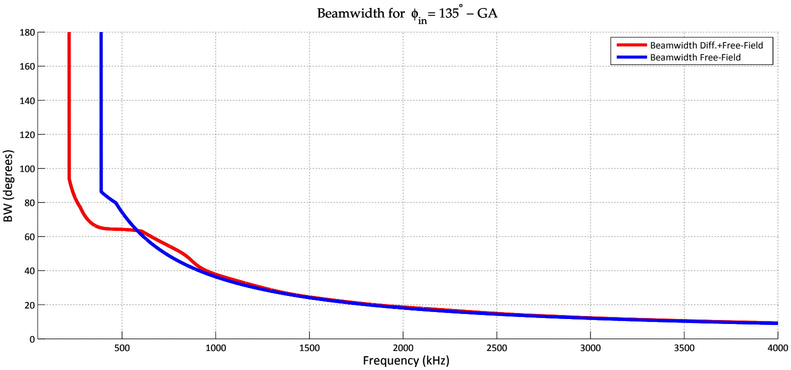

(a) $\phi_{in} = 135°$

Figure F.7: BW plots of the GA array for $\phi_{in} = 135°$ (linear plot, FvB extraction).

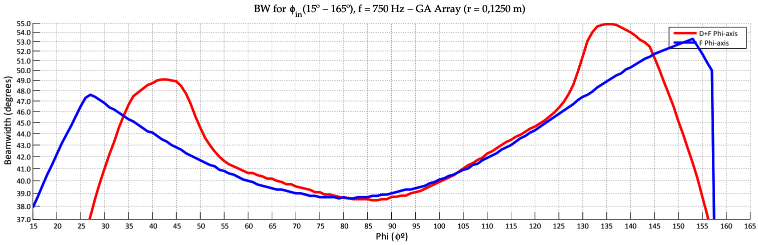

(a) BW, D+F and F, 750 Hz, ϕ_{in} sweep

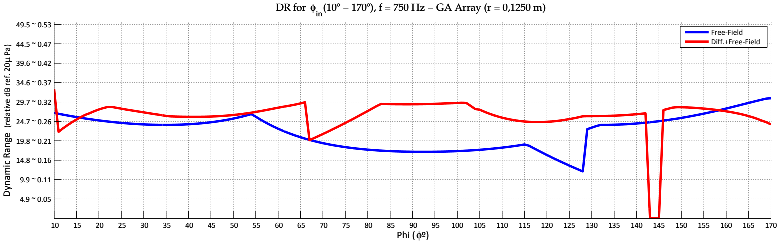

(b) DR, D+F and F, 750 Hz, ϕ_{in} sweep

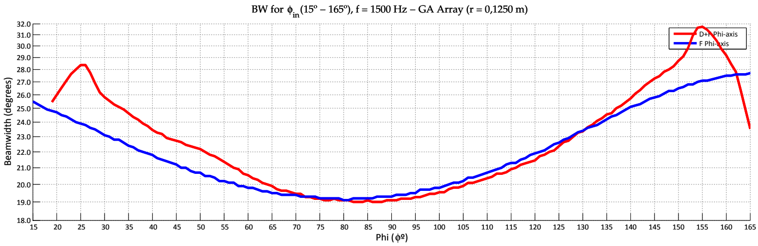

(c) BW, D+F and F, 1,5 kHz, ϕ_{in} sweep

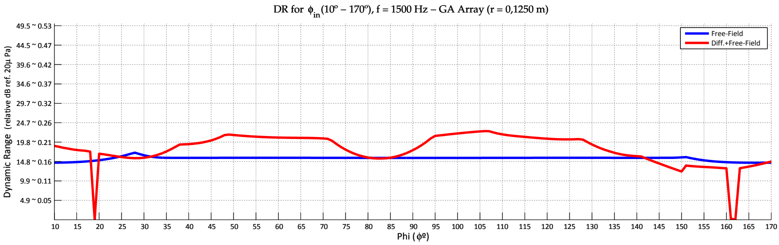

(d) DR, D+F and F, 1,5 kHz, ϕ_{in} sweep

Figure F.8: BW and DR plots of the GA array for sweep in ϕ_{in} frequencies of 750 Hz and 1,5 kHz.

Appendix G – Measurements Additional Data

G.1 Measurement Codes

The PSFs of Section 4.4.4 use the codes of Tables G.1 and G.2 below.

Table G.1: Measurement level codes.

Code	Description
k	≈86 dB overall, mic 01, spk 01, 90°, W. Noise, B&K Gen. 1405, Filter (500-20 kHz), 1,50 m distant
l	≈80 dB overall, mic 01, spk 01, 90°, W. Noise, B&K Gen. 1405, Filter (500-20 kHz), 1,50 m distant
m	≈70 dB overall, mic 01, spk 01, 90°, W. Noise, B&K Gen. 1405, Filter (500-20 kHz), 1,50 m distant
o	Tone 2 kHz, spk 03, Neutrik Minirator MR1, 160 mV, No Filter, 0,75 m distant
p	Tone 1,6 kHz, spk 01, Agilent 33220A, 300mV, No Filter, 1,50 m distant
q	Log Freq. Sweep 400-20k Hz, spk 01, Agilent 33220A, 200 mVpp, Filter (500-20 kHz), 1,50 m distant (*26 s)
u	≈76 dB overall, mic 01, spk 02 + 04, B&K Gen. 1405, Filter (20-6 kHz), 1 Tap Amp., side line
v	spk 04, B&K Gen. 1405, Filter (20-700 Hz), 1 Tap Amp., 1,15 m height
x	spk 02, B&K Gen. 1405, Filter (600-6 kHz), 1 Tap Amp., 1,50 m height

Table G.2: Sound source (speaker codes).

Code	Description
Spk 01	Organge X-Mini II
Spk 02	Low-mid frequency speaker
Spk 03	Blue X-Mini II
Spk 04	Low frequency speaker

G.2 X-Mini Frequency Response

The measurement of the directivity has followed the procedures described by Lentz [155]. The setup took place in the anechoic chamber of the Technical Institute of Acoustics (RWTH Aachen), per Figure G.2. Using a mechanical arm, 2944 measurement points were taken, distributed in a Gaussian grid [156]. The radius was 1,95 m and the azimuth and elevation points can be verified in Figure G.1.

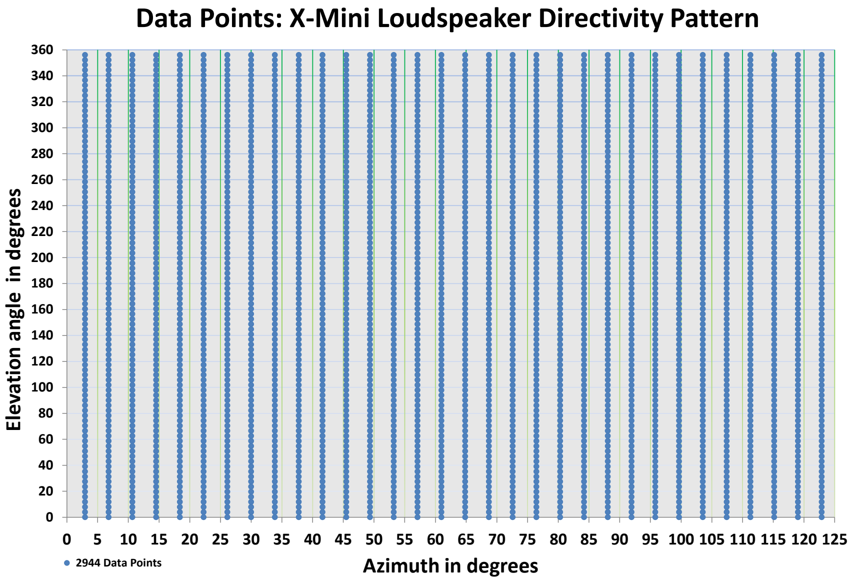

Figure G.1: Azimuth and elevation points.

Figure G.2 depicts

1. The front and side views of the speaker, with the physical support in detail;
2. Two positions of the measuring arm.

The speakers were measured with the *open* and *closed*[1] configurations. The open configuration offers more low frequency content, hence it was used in this research.

---

[1] The closed results are omitted from this document.

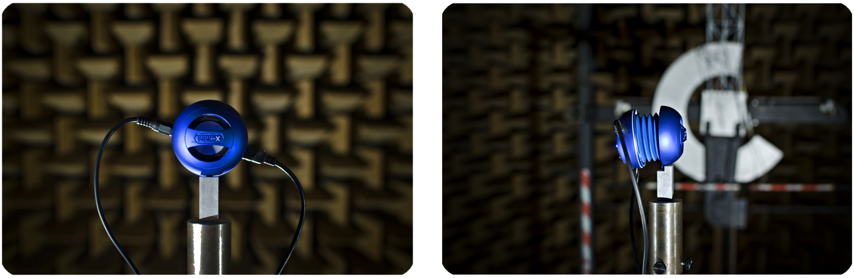

(a) Front view (b) Side view

(c) Measuring Arm (d) Measuring Arm

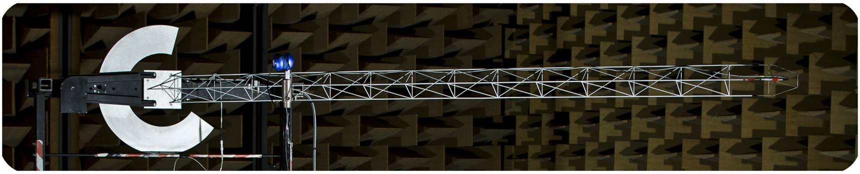

(e) Measuring Arm

Figure G.2: X-Mini directivity measurement.

Figures G.2 to G.6 depict

1. Three views of the balloon plots;
2. The *flat* version of the balloon plot; and
3. The spectrum[2] for the arm position exactly in front of the speaker.

The respective frequencies of the plots are 1 kHz, 1,5 kHz, 2,5 kHz, and 3,5 kHz.

---

[2] The spectrum plots are the same for the four figures. They are repeated to provide an overview with the balloon plots.

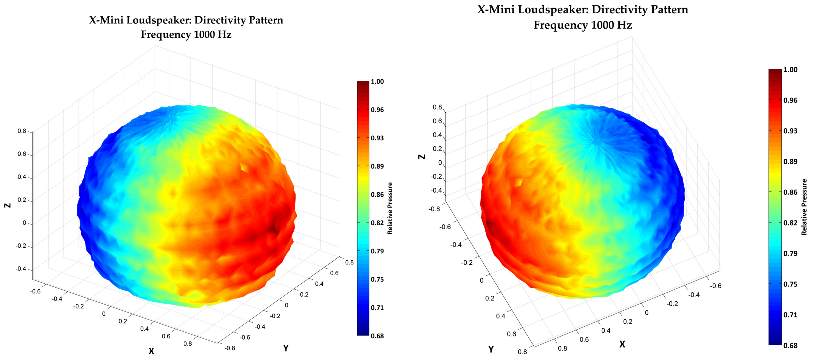

(a) 1 kHz Directivity Pattern,

(b) 1 kHz Directivity Pattern

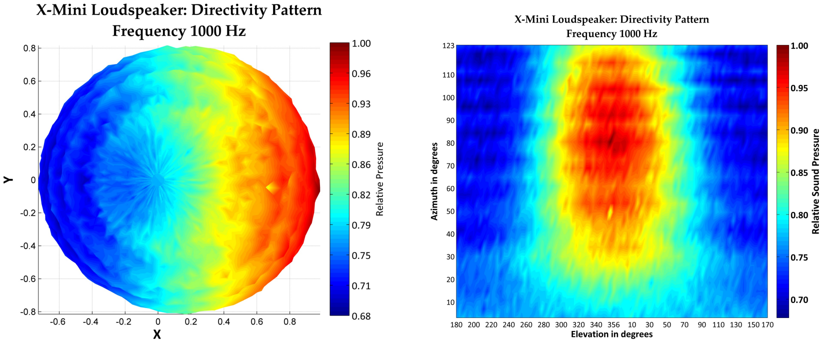

(c) 1 kHz Directivity Pattern

(d) 1 kHz Directivity Pattern

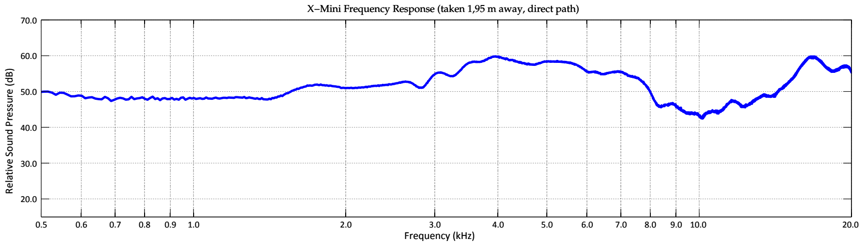

(e) Spectrum (500-20 kHz)

Figure G.3: X-Mini directivity at 1 kHz and frequency response.

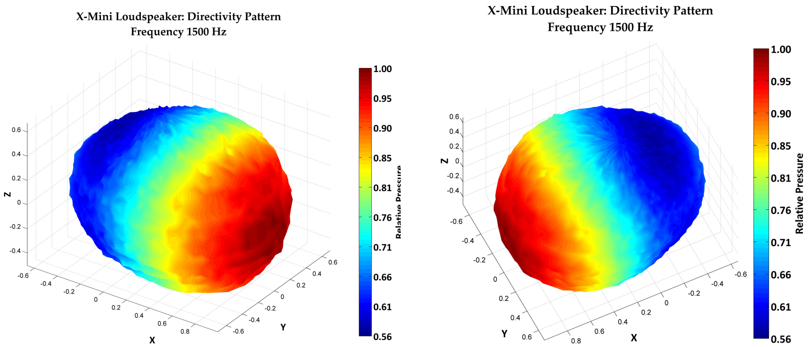

(a) 1,5 kHz Directivity Pattern, (b) 1,5 kHz Directivity Pattern

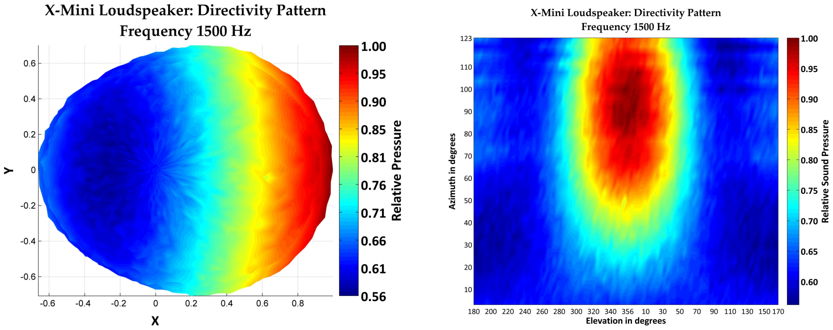

(c) 1,5 kHz Directivity Pattern (d) 1,5 kHz Directivity Pattern

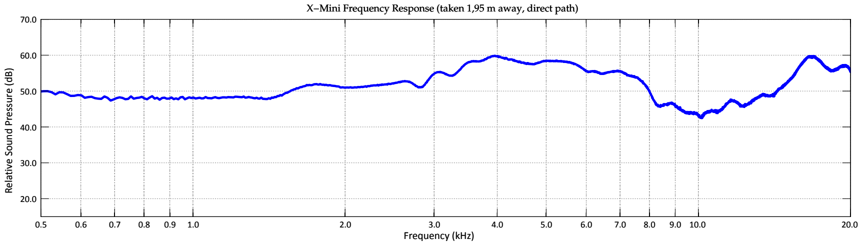

(e) Spectrum (500-20 kHz)

Figure G.4: X-Mini directivity at 1,5 kHz and frequency response.

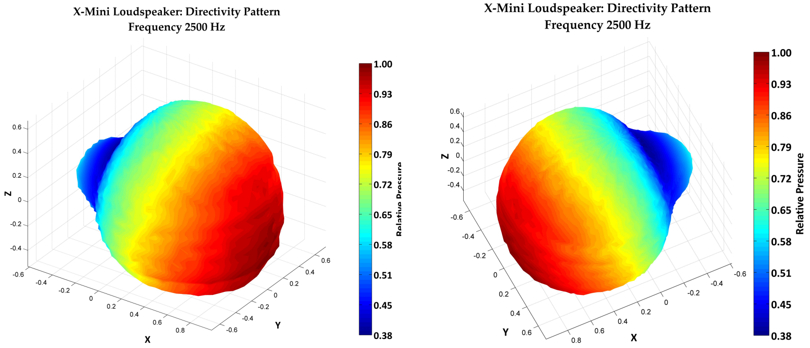

(a) 2,5 kHz Directivity Pattern,

(b) 2,5 kHz Directivity Pattern

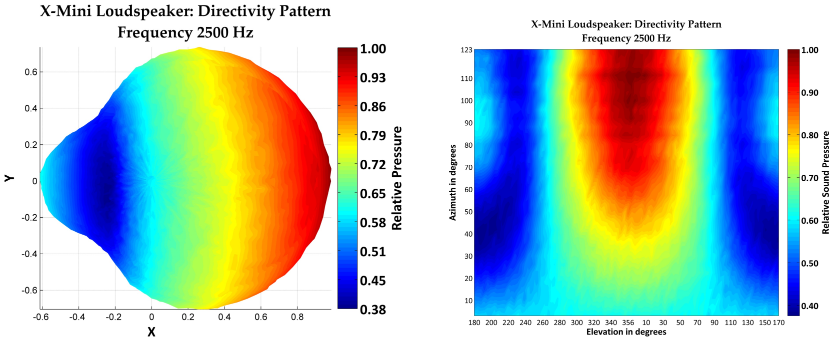

(c) 2,5 kHz Directivity Pattern

(d) 2,5 kHz Directivity Pattern

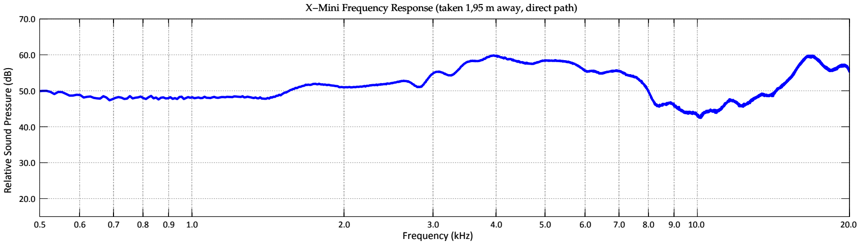

(e) Spectrum (500-20 kHz)

Figure G.5: X-Mini directivity at 2,5 kHz and frequency response.

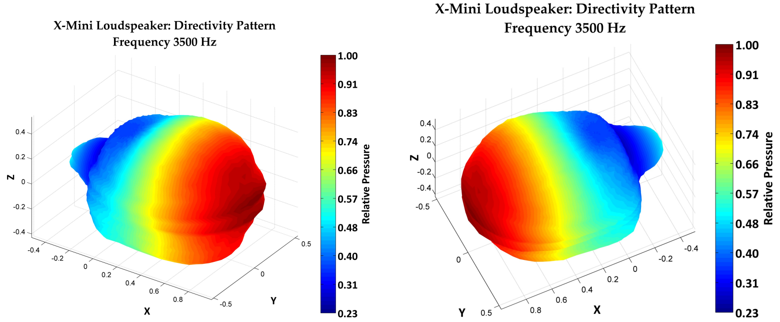

(a) 3,5 kHz Directivity Pattern,

(b) 3,5 kHz Directivity Pattern

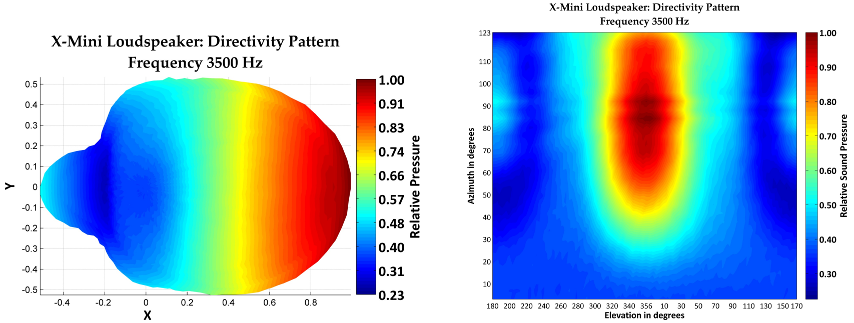

(c) 3,5 kHz Directivity Pattern

(d) 3,5 kHz Directivity Pattern

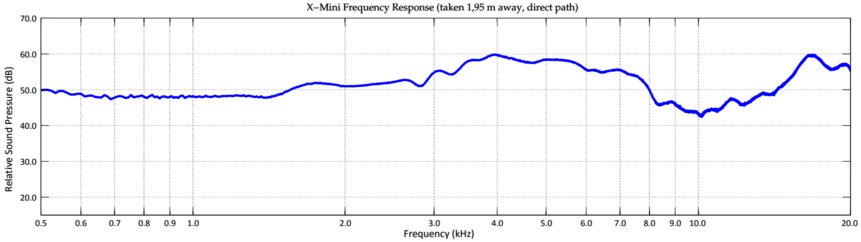

(e) Spectrum (500-20 kHz)

Figure G.6: X-Mini directivity at 3,5 kHz and frequency response.

G.3 Additional PSFs

These are the results that complement Section 4.4.4.2. Figure G.7 depicts the PSFs and the spectrum for one emitter at position $\phi_{\text{in}} = 90^\circ$, $\theta_{\text{in}} = 0^\circ$ with a tone of 2 kHz. In Figure G.7 (a) it is possible to observe that no sources are found in $\phi_{\text{in}} = 90^\circ$ - as expected. On the other hand, in Figure G.7 (b) the source is correctly localised.

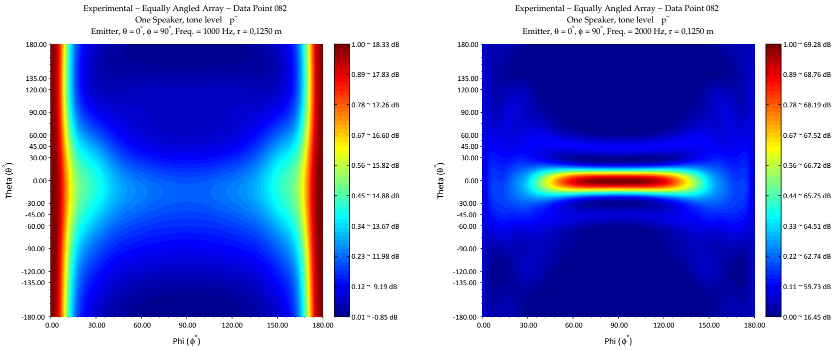

(a) Tone of 2 kHz, Level k at 1 kHz (b) Tone of 2 kHz, Level k at 1,5 kHz

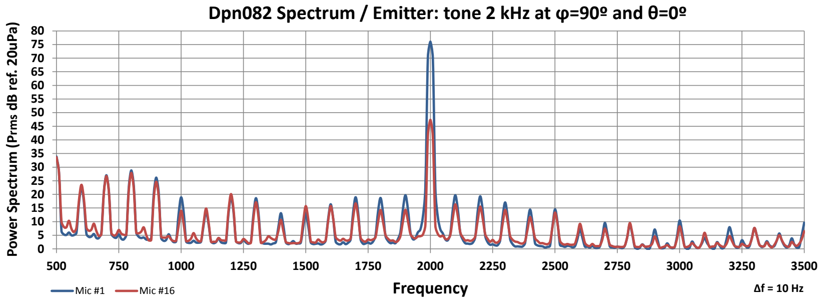

(c) Mic 1 and 16 Spectra

Figure G.7: Emitter at $\theta = 0^\circ$ and $\phi = 90^\circ$; 1,50 m distant; and tone of 2 kHz.

The level is called $\tilde{\text{p}}$ because the same settings of p were used, only the excitation signal was changed to a 2 kHz tone.

Appendix H – DBEM Additional Data

H.1 Mesh Refinement Spectrum Plots

In this section there are the additional spectrum plots for different *mesh refinement* coefficients (MR). Figures H.2 to H.8 are the plots for x1, x2, x3, x4, x6, x8, and x10. Figure H.1 is the product of the analytical simulation and is also here for comparison purposes.

Other discussions can be found in Section 5.2.3.

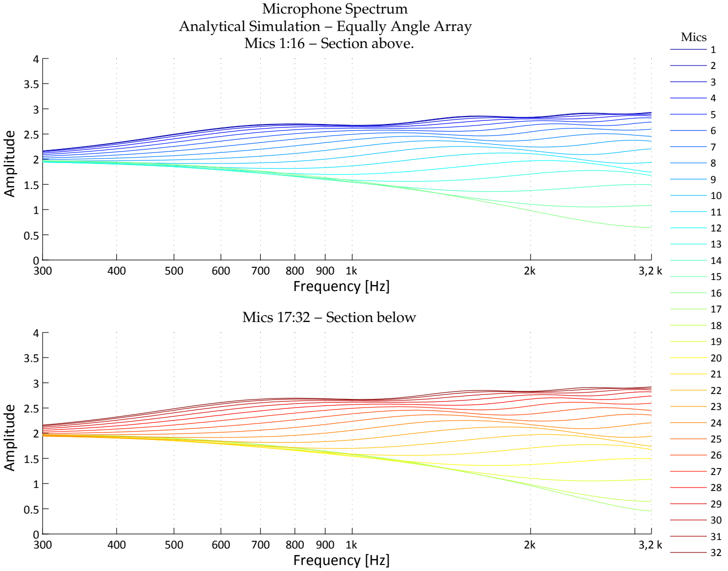

Figure H.1: Spectrum of 32 microphones.
EAA array analytical simulation (df=20 Hz).

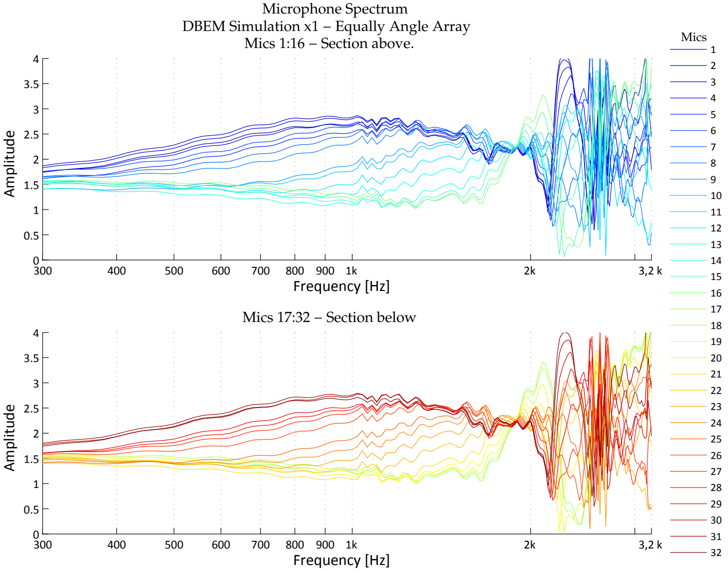

Figure H.2: Spectrum of 32 microphones.
EAA array DBEM simulation for x1 (df=20 Hz).

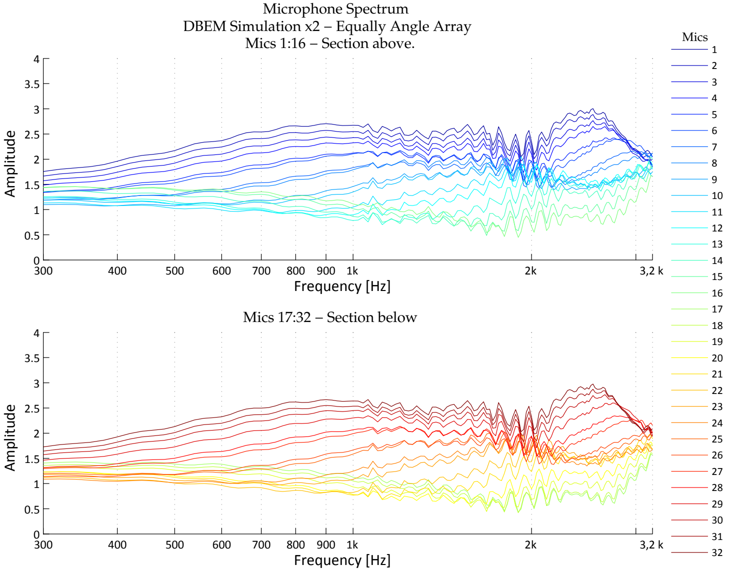

Microphone Spectrum
DBEM Simulation x2 – Equally Angle Array
Mics 1:16 – Section above.

Mics 17:32 – Section below

Figure H.3: Spectrum of 32 microphones.
EAA array DBEM simulation for x2 (df=20 Hz).

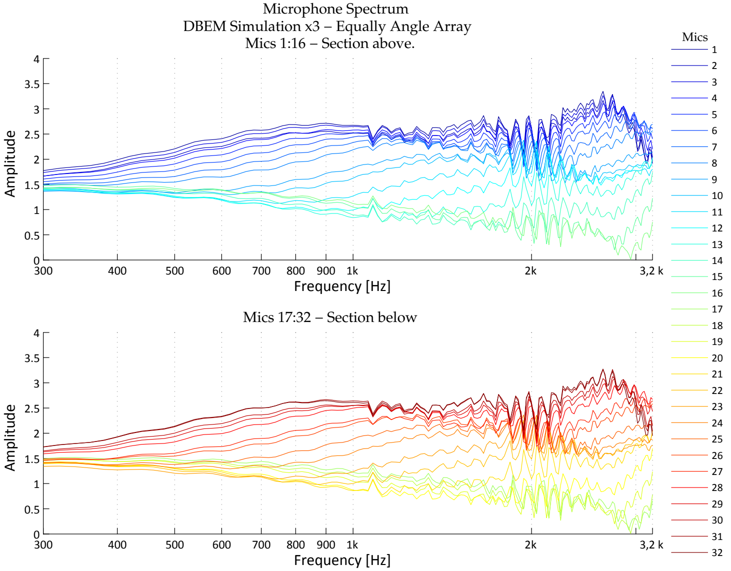

Microphone Spectrum
DBEM Simulation x3 – Equally Angle Array
Mics 1:16 – Section above.

Mics 17:32 – Section below

Figure H.4: Spectrum of 32 microphones.
EAA array DBEM simulation for x3 (df=20 Hz).

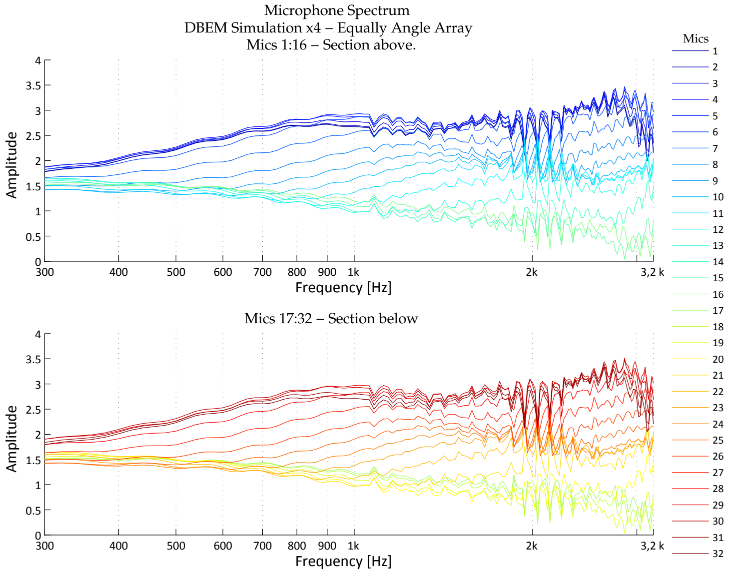

Figure H.5: Spectrum of 32 microphones.
EAA array DBEM simulation for x4 (df=20 Hz).

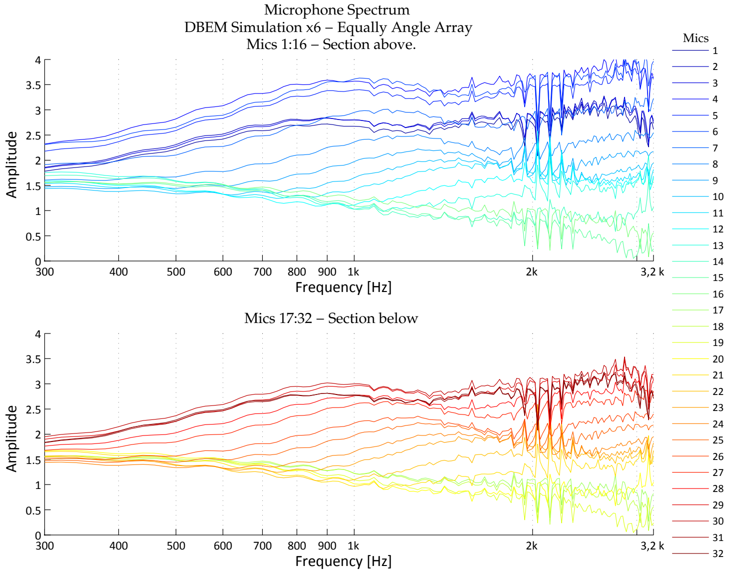

Figure H.6: Spectrum of 32 microphones.
EAA array DBEM simulation for x6 (df=20 Hz).

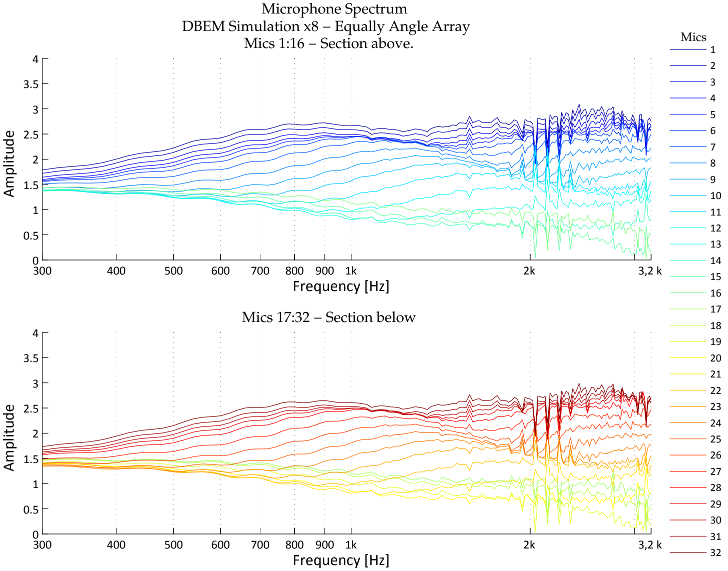

Figure H.7: Spectrum of 32 microphones.
EAA array DBEM simulation for x8 (df=20 Hz).

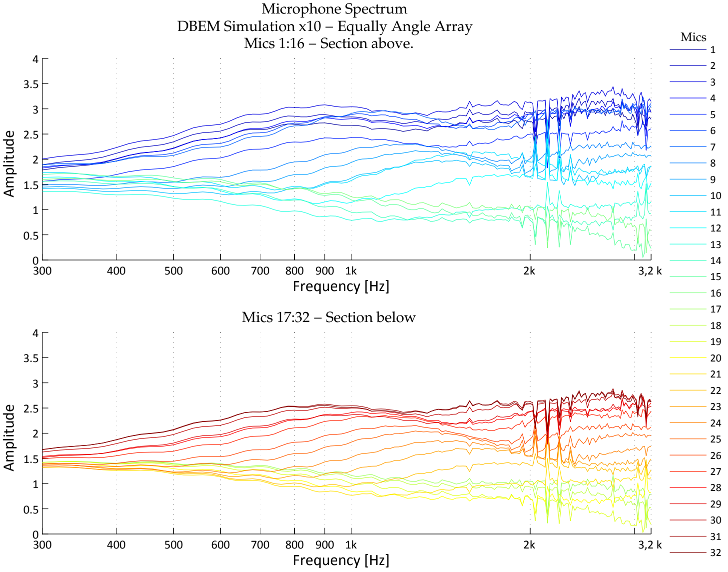

Figure H.8: Spectrum of 32 microphones.
EAA array DBEM simulation for x10 (df=20 Hz).

H.2 Cylinder Length

Here are some additional plots to compare with those in Section 5.2.4. They basically the maps for several cylinder lengths at 500 Hz (EAA).

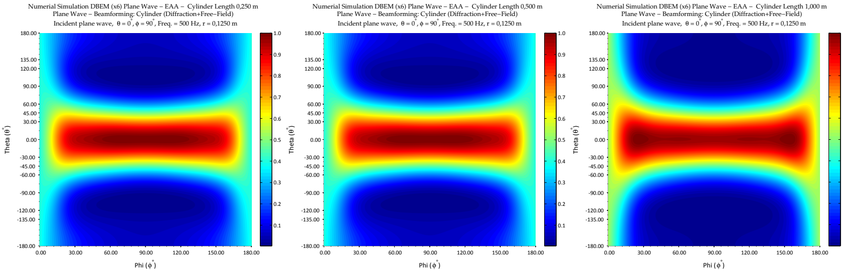

(a) 0,250 m (b) 0,500 m (c) 1,000 m

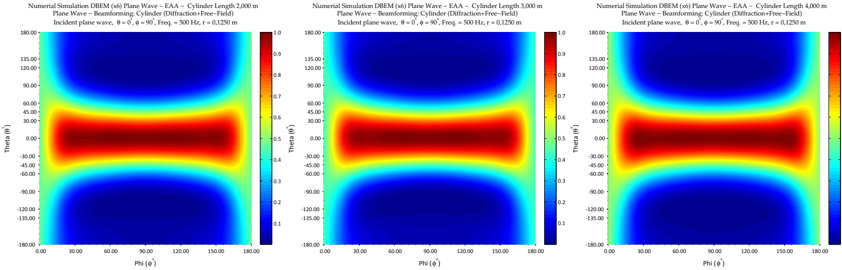

(d) 2,000 m (e) 3,000 m (f) 4,000 m

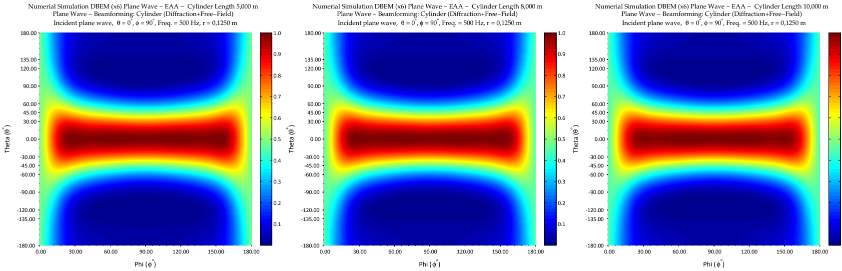

(g) 5,000 m (h) 8,000 m (i) 10,000 m

Figure H.9: Beamforming maps for several cylinder lengths, at 500 Hz, Equally Angled Array, $\phi = 90°$.

Appendix I – GA Additional Data

This appendix complements Sections 5.3 and 5.4 of Chapter 5.

I.1 Reduction of the Cylinder Problem

A reduction of possible distributions is needed to speed up the evolution. There are infinite possible positions for 32 microphones over the cylinder, hence boundary conditions must be determined. Considering that the microphones are equal and occupy an area of 1 cm^2, the cylinder's surface can be meshed, per Figure I.1.

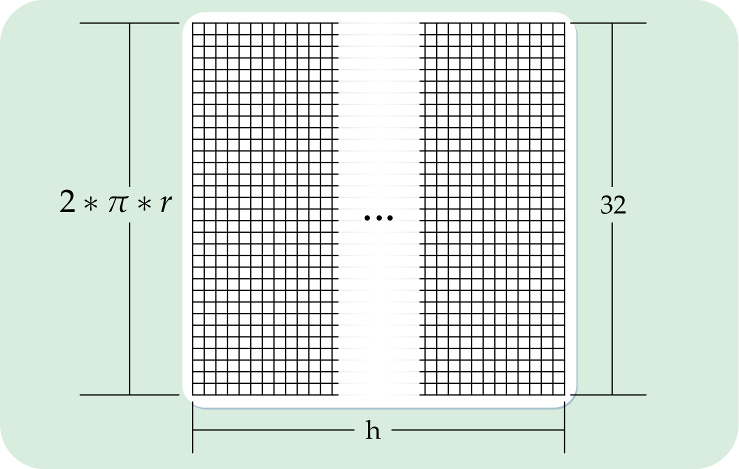

Figure I.1: Meshing the cylinder's surface.

1. The first reduction is to consider the cylinder dimensions. The applicable area with a radius of r =0,1250 m and length of 3 m is $(2 * \pi * 0,1250 * 3,0) \approx 2,3561$ m^2.

   Now, considering 1,0 cm of minimum spacing between the microphones, (for the sake of simplicity, continuity issues are disregarded)

$$C_{32}^{23561} = \binom{23561}{32} = \frac{23561!}{32! \cdot (23561 - 32)!} \approx 3,0261 * 10^{104}, \qquad \text{(I.1)}$$

which is a colossal number of possible distributions.

2. The second reduction is to consider that only 32 slots are possible along the θ axis. This renders

$$C_{32}^{9600} = \binom{9600}{32} = \frac{9600!}{32! \cdot (9600 - 32)!} \approx 9{,}7734 * 10^{91}\,, \tag{I.2}$$

possible distributions.

3. The third reduction is that only one microphone can use a slot in the θ axis. This assumption renders

$$300^{32} \approx 1{,}8530 * 10^{79} \tag{I.3}$$

which is still a huge number of possible distributions. Even with a reduction of $\approx$ 16,331 septillion a number of quinquavigintillion magnitude is impracticable, justifying the use of GA.

ANNEX

Annex A – Hardware Data

Omnidirectional Back Electret Condenser Microphone Cartridge

Series: **WM-61A**
WM-61 B (pin type)

■ Features

- Small microphones for general use
- Back electret type designed for high resistance to vibrations, high signal-to-noise ratio
- High sensitivity type
- Microphone with pins for flexible PCB (WM-61B type)

■ Sensitivity

Vs = 2.0V RL = 2.2kΩ	–35 ± 4dB

■ Specifications

Sensitivity	–35±4dB (0db = 1V/pa, 1kHz)
Impedance	Less than 2.2 kΩ
Directivity	Omnidirectional
Frequency	20–20,000 Hz
Max. operation voltage	10V
Standard operation voltage	2V
Current consumption	Max. 0.5 mA
Sensitivity reduction	Within –3 dB at 1.5V
S/N ratio	More than 62 dB

■ Typical Frequency Response Curve

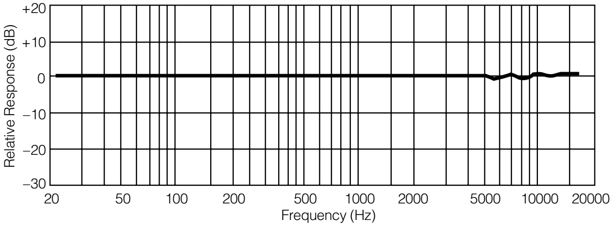

■ Dimensions in mm (not to scale)

WM-61A

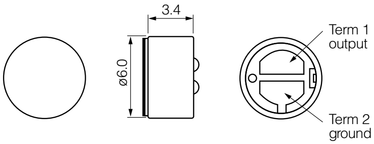

WM-61B

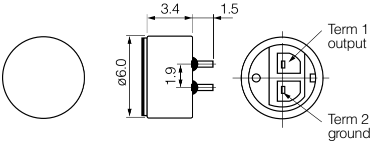

M51

Measurement Microphone

M51 Microphone

The M51 is a high performance low voltage electret condenser microphone. This microphone has wide application for general purpose acoustic measurements, including the measurement of transducers, loudspeaker systems, and room response. The M51 conforms to the external dimensions of industry standard 1/2 inch measurement microphones. This microphone features low cost, low distortion, 150dB SPL capability, wide frequency response, and low voltage power supply requirements.

The M51 incorporates a special element / preamp design which enables performance and capabilities far superior to that of typical electret type microphones, and allows for operation from a single 10 Volt DC supply. A separate detachable cable is provided which converts the TB3M connector of the M51, to a standard 3 pin male XLR type connector.

As with all LinearX microphones, each unit is measured using a comparison free-field calibration procedure with a laboratory grade reference microphone to produce a precision error response curve. This can be used for correcting the response. This data is provided in an ASCII mic data file (MDF) on 3.5”disk.

M51 Technical Specifications

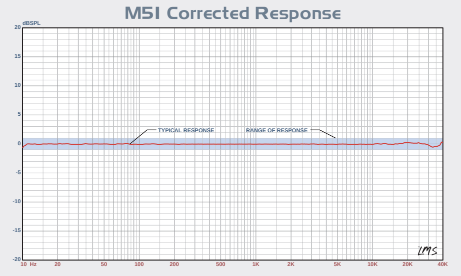

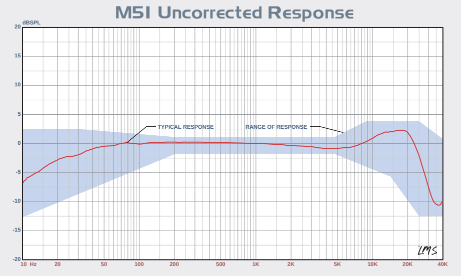

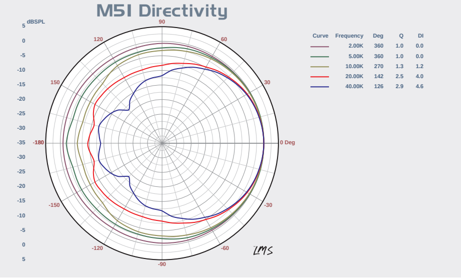

Element Type	Electret Condensor
Preamp / Line Driver	SMT active preamp
Uncorrected Freq Response	±5dB 20Hz-20kHz
Corrected Freq Response	±1dB 10Hz-40kHz
Acoustic Sensitivity	-36dBm/Pa (12mV/94dBspl)
Output Impedance	150 Ohms
Maximum SPL	150 dBspl
1/3 Octave Noise @1kHz	18 dBspl
ANSI-A Weighted Noise	34 dBspl
Temperature Range	0C° to +40C°
Temp Coef @1kHz	-0.01dB/C°
DC Supply Voltage	9-11 Vdc
DC Supply Current	50mA (Max)
Electrical Connector	Switchcraft TB3M
Construction and Finish	Aluminum, Black Anodized
Microphone Dimensions	Dia: 0.52", Length: 4.25"
Weight of Microphone	1 oz (28 grams)
XLR Adapter Cable Length	6 Feet (2 meters)

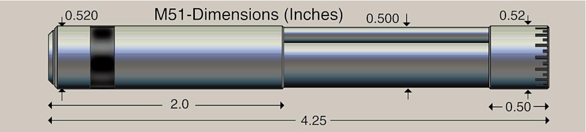

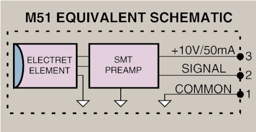

LinearX Systems Inc
9500 SW Tualatin-Sherwood Rd, Tualatin, OR 97062-8586 USA
Tel: (503) 612-9565 - Fax: (503) 612-9344 - Internet: www.linearx.com

LINEARX SYSTEMS

PRODUCT DATA

Sound Calibrator — Type 4231

Sound Calibrator Type 4231 is a handy, portable sound source for calibration of sound level meters and other sound measurement equipment. The calibrator is very robust and stable, and conforms to EN/IEC 60942 Class LS and Class 1, and ANSI S1.40-1984.

050231

USES AND FEATURES

USES

- Calibration of sound level meters and other sound measurement equipment

FEATURES

- Conforms to EN/IEC 60942 (2003) Class LS and Class 1, and ANSI S1.40 – 1984
- Robust, pocket-sized design with highly stable level and frequency
- Calibration accuracy ± 0.2 dB
- 94 dB SPL, or 114 dB SPL for calibration in noisy environments
- Extremely small influence of static pressure and temperature
- Sound pressure independent of microphone equivalent volume
- 1 kHz calibration frequency for correct calibration level independent of weighting networks
- Fits Brüel & Kjær 1″ and 1/2″ microphones (1/4″ and 1/8″ microphones with adaptor)
- Switches off automatically when removed from the microphone

Brüel & Kjær

Sound Calibrator Type 4231

Sound Calibrator Type 4231 is a pocket-sized, battery operated sound source for quick and direct calibration of sound level meters and other sound measuring systems. It fits Brüel & Kjær 1″ microphones and using the removable adaptor, 1/2″ microphones. With optional adaptors, it can be used for 1/4″ and 1/8″ microphones as well.

The calibration frequency is 1000 Hz (the reference frequency for the standardised international weighting networks), so the same calibration value is obtained for all weighting networks (A, B, C, D and Linear). The calibration pressure of 94 ±0.2 dB re 20 μPa is equal to 1 Pa or 1 N/m^2. The +20 dB level step gives 114 dB SPL, which is convenient for calibration in noisy environments, or for checking linearity.

The design of Type 4231 is based on a feed-back arrangement to ensure a highly stable sound pressure level and ease of use. The feed-back loop uses a condenser microphone (see Fig. 1), which is specially developed for this purpose.

Fig. 1
Cross-sectional view of Sound Calibrator Type 4231. The feed-back loop is based on a high-quality condenser microphone to ensure a very stable sound pressure level

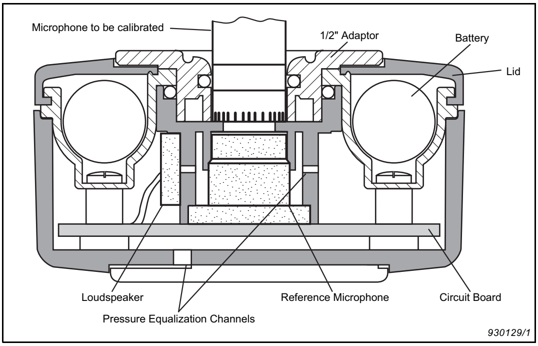

This microphone is optimised to have extremely high stability and independence of variations in static pressure and temperature around the 1 kHz calibration frequency. The result of this is a user-friendly calibrator where exact fitting of the microphone is non critical and the effects of changes in temperature and static pressure are negligible.

Fig. 2
Type 4231 fitted to Hand-held Analyzer Type 2250. The calibrator's centre of gravity is positioned very close to the microphone, giving a stable set-up

The calibrator gives a continuous sound pressure level when fitted on a microphone (see Fig. 2) and activated.

The sensitivity of the sound measuring equipment can then be adjusted until it indicates the correct sound pressure level.

The calibrator is automatically switched off when removed from the microphone.

A leather protecting case, which does not need to be removed to use the calibrator, is supplied.

Compliance with Standards

CE, ✓	CE-mark indicates compliance with: EMC Directive and Low Voltage Directive. C-Tick mark indicates compliance with the EMC requirements of Australia and New Zealand.
Safety	EN/IEC 61010–1: Safety requirements for electrical equipment for measurement, control and laboratory use. ANSI/UL 61010–1: Safety requirements for electrical equipment for measurement, control and laboratory use.
EMC Emission	EN/IEC 61000–6–3: Generic emission standard for residential, commercial and light industrial environments. EN/IEC 61000–6–4: Generic emission standard for industrial environments. CISPR 22: Radio disturbance characteristics of information technology equipment. Class B Limits. FCC Rules, Part 15: Complies with the limits for a Class B digital device. EN/IEC 60942: Instrumentation Standard – Electroacoustics – Sound Calibrators.
EMC Immunity	EN/IEC 61000–6–1: Generic standards – Immunity for residential, commercial and light industrial environments. EN/IEC 61000–6–2: Generic standards – Immunity for industrial environments. EN/IEC 61326: Electrical equipment for measurement, control and laboratory use – EMC requirements. EN/IEC 60942: Instrumentation Standard – Electroacoustics – Sound Calibrators. **Note:** The above is only guaranteed using accessories listed in this Product Data sheet.
Temperature	IEC 60068–2–1 & IEC 60068–2–2: Environmental Testing. Cold and Dry Heat. Operating Temperature: –10 to +50°C (14 to 122°F) Storage Temperature: –25 to +70°C (–13 to +158°F)
Humidity	IEC 60068–2–78: Damp Heat: 90% RH (non-condensing at 40°C (104°F)).
Mechanical	Non-operating: IEC 60068–2–6: Vibration: 0.3 mm (10 to 58 Hz), 20 m/s^2 (58–500 Hz) IEC 60068–2–27: Shock: 1000 m/s^2 IEC 60068–2–29: Bump: 3000 bumps at 400 m/s^2
Enclosure	IEC 60529: Protection provided by enclosures: IP 50 with leather protection case.

Specifications – Sound Calibrator Type 4231

STANDARDS SATISFIED

EN/IEC 60942 (2003), Class LS and Class 1, Sound Calibrators
ANSI S1.40 – 1984, Specification for Acoustic Calibrators

SOUND PRESSURE LEVELS

94.0 dB ±0.2 dB (Principal SPL) or
114.0 dB ±0.2 dB re 20 µPa at reference conditions

FREQUENCY

1 kHz ±0.1%

SPECIFIED MICROPHONE

Size according to IEC 61094-4:

- 1″ without adaptor
- 1/2″ with adaptor UC-0210 (supplied)
- 1/4″ with adaptor DP-0775 (optional)
- 1/8″ with adaptor DP-0774 (optional)

EQUIVALENT FREE-FIELD LEVEL

(0° incidence, re Nominal Sound Pressure Level)
– 0.15 dB for 1/2″ Brüel & Kjær Microphones. See Type 4231 User Manual for other microphones

EQUIVALENT RANDOM INCIDENCE LEVEL

(re Nominal Sound Pressure Level)
+0.0 dB for 1″, 1/2″, 1/4″ and 1/8″ Brüel & Kjær Microphones

NOMINAL EFFECTIVE COUPLER VOLUME

> 200 cm^3 at reference conditions

DISTORTION

< 1%

LEVEL STABILITY

Short-term: Better than 0.02 dB (as specified in IEC 60942)
One Year: Better than 0.05 dB (σ = 96%)
Stabilization Time: <5 s

REFERENCE CONDITIONS

Temperature: 23°C ±3°C (73° ±5°F)
Pressure: 101 ±4 kPa
Humidity: 50%, –10% +15% RH
Effective Load Volume: 0.25 cm^3

ENVIRONMENTAL CONDITIONS

Pressure: 65 to 108 kPa
Humidity: 10 to 90% RH (non-condensing)
Effective Load Volume: 0 to 1.5 cm^3

INFLUENCE OF ENVIRONMENTAL CONDITIONS (Typical)

Temperature Coefficient: ±0.0015 dB/°C
Pressure Coefficient: $+8 \times 10^{-4}$ dB/kPa
Humidity Coefficient: 0.001 dB/% RH

POWER SUPPLY

Batteries: 2 × 1.5 V IEC Type LR6 (“AA” size)
Lifetime: Typically 200 hours continuous operation with alkaline batteries at 23°C (73°F)
Battery Check: When Type 4231 stops working continuously, and only operates when the On/Off button is held in, the batteries should be replaced

DIMENSIONS AND WEIGHT

(Without case)
Height: 40 mm (1.5″)
Width: 72 mm (2.8″)
Depth: 72 mm (2.8″)
Weight: 150 g (0.33 lb.), including batteries

Note: All values are typical at 25°C (77°F), unless measurement uncertainty or tolerance field is specified. All uncertainty values are specified at 2 σ (i.e., expanded uncertainty using a coverage factor of 2)

Audio Revolution In A Box

Instruction Manual English
Manuel d'instruction French
Bedienungsanleitung German
Manual de instrucciones Spanish
설명서 Korean
取扱説明書 Japanese
使用说明书 Chinese
Manual de instruções Portuguese

Introduction

Congratulations on your purchase of X-mini™ product. The X-mini™ II Capsule speaker comes with vastly improved features yet retaining the best characteristics from its first generation, the 2nd generation comes packed with properties that will bring a greater audio experience to its user.

Introducing a larger 40mm driver, the X-mini™ II projects richer and crispier sounds resulting in a greater user experience from its innovative capsule design. Be it for individual or group entertainment, the X-mini™ II is the perfect enhancement to your own music jukebox.

Safety Rules

1) Please follow the rules depicted in this manual closely to ensure your safety. Before using the speaker, we would strongly encourage you to read through this user manual.

2) Be more wary of any edges, uneven surfaces, metal parts, accessories and its packaging so as to prevent any possible injury or damage.

3) Keep this speaker out of reach of children. Take note that this speaker is not edible and should not be placed in your mouth.

4) Do not modify, repair or dismantle the speaker. Doing so may result in fires, electric shocks, complete breakdown of the speaker, etc. All of which, are not covered under warranty.

5) Do not use any diluents or volatile liquid to clean the speaker. Keep in mind that the surface of the speaker should only be wiped with a clean dry cloth.

6) Do not use this speaker in locations whereby there are high-temperatures or high humidity levels

(For instance, bathrooms); ideally, the speaker should be used in a location free of dust and exposure to direct sunlight.

7) Do not insert foreign objects, such as pins, into this speaker.

8) Do not touch this speaker when your hands are wet as this may result in electric shocks.

9) Turn down the volume before/while using this speaker as sudden loud sounds may damage it.

10) Refrain from dropping the speaker as well as any collision with other objects.

11) Do not use this speaker when in hazardous locations.

12) Should any abnormal situations or problems occur while using the speaker, discontinue use of speaker immediately.

Technical Specification

Dimension	:	55mm × 44mm (closed resonator)
Net Weight	:	83g
Speaker	:	Magnetically Shielded 40mm (4Ω)
Loudspeaker Output	:	2W
Frequency Response	:	100 Hz-20 kHz
Signal-to-Noise	:	≥80dB
Distortion	:	≤1.0%
Playback Time	:	up to 12 hours
Battery Voltage/Capacity	:	400mAh
Battery Charging Voltage	:	4.2V±0.05V
Battery Charge Time	:	2.5 hours

Package Contents

The Package will contain the following:

1 x X-mini™ II

1 x User Manual

1 x Input/Audio and Charging Cable

1 x Protection Pouch

Connection Diagram

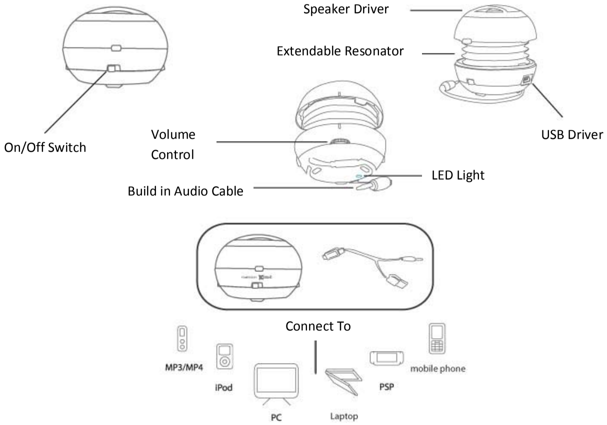

1405

Instruction Manual

Noise Generator Type 1405

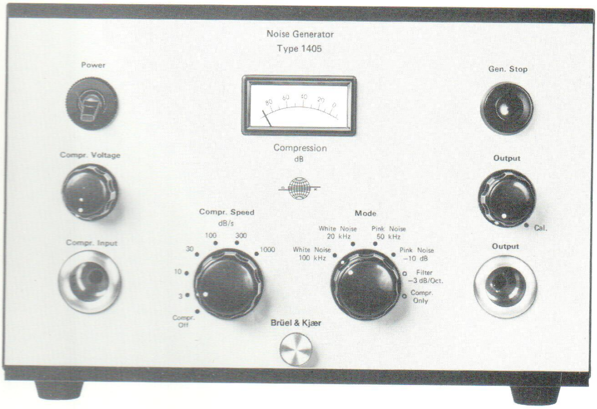

A highly stable random noise generator producing white noise up to 100 kHz, white noise up to 20 kHz (both with a standard spectral density of $10^{-4}\ V^2/Hz$) and pink noise up to 50 kHz. All three random signals can be stopped without extraneous noise either manually or remotely.
The instrument contains a −3 dB/Octave filter and a compressor circuit both of which can be used independently.

Brüel & Kjær

type 1405

Noise Generator

FEATURES:

- White Noise in the frequency range 20 Hz to 100 kHz
- Uniform spectral density 10^{-4} V^2/Hz
- Pink Noise in the frequency range 20 Hz to 50 kHz
- Built-in —3 dB/octave filter can be used separately
- Built-in compressor amplifier with meter
- Six compressor speeds
- Signal/hum ratio better than 90 dB
- Manual and remote generator stop
- Mains or ext. battery operation

USES:

- Sound insulation measurement
- Frequency response measurement
- Vibration testing
- Electro acoustic measurements
- Reverberation measurement
- Sound distribution measurement
- Cross talk measurement
- Signal to noise ratio measurement on communication lines

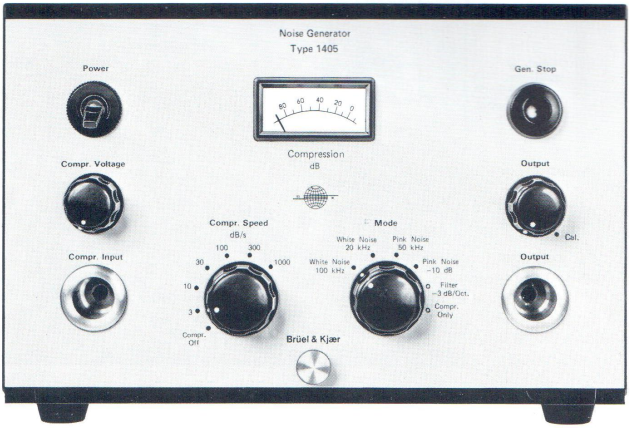

The Noise Generator Type 1405 is designed to supply well defined white noise in the frequency range 20 Hz to 100 kHz. The generator has a built-in —3 dB/octave filter which is used to weight the white noise in order to produce pink noise in the frequency range 20 Hz to 50 kHz. The filter may also be used separately for other weighting purposes such as automatic bandwidth compensation. The generator also contains a compressor amplifier which is useful when performing frequency response measurements in various applications within the fields of sound and vibration. In such cases the noise generator is often combined with a filter in order to obtain a narrow band signal which is then used to control the compressor. Also the compressor amplifier may be used separately.

The Type 1405 is built-into a standard B & K cassette which enables easy combination with other instruments and mounting in racks (for example with Power Amplifier Type 2706 for high output power).

Description

The white noise is made in the generator (see block diagram Fig. 1) which is built up around two zener diodes kept at constant temperature in an oven. It has a uniform spectral density of 10^{-4} V^2/Hz. The signal from the generator is passed on to the first of two filters via an attenuator which sets the output level. The signal from the attenuator can be short-circuited to stop the output, a feature necessary for reverberation measurements. The generator stop can be controlled manually as well as automatically.

The two low pass filter/amplifier sections limit the upper frequency of the white noise signal, the first to 100 kHz and the second to 20 kHz. Both filters are 3 pole filters, the second is of the Chebychev type. The output signals from the filters are available, via the mode switch, at the output of the generator.

The 20 Hz to 100 kHz signal from the output of the first filter is also fed to a −3 dB/Octave weighting network in order to make a pink noise signal in the frequency range 20 Hz to 50 kHz.

The mentioned output signals are also fed to a compressor amplifier system which compresses them according to the signal present at the compressor input. The degree of compression can be seen on the built-in meter.

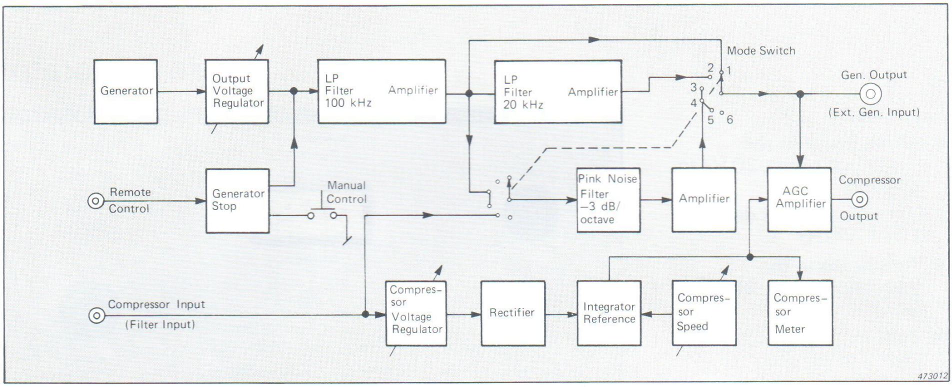

Fig.1. Block diagram of Type 1405

Specifications 1405

Working Modes:

1. Output of white noise in the frequency range 20 Hz to 100 kHz with uniform spectral density of 10^{-4} V^2/Hz (up to 50 kHz)

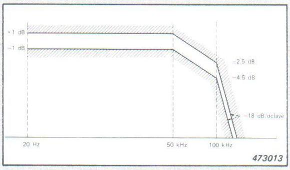

2. Output of white noise in the frequency range 20 Hz to 20 kHz. Level within ± 1 dB in the range. Attenuation slope >18 dB/Octave above 20 kHz
3. Output of pink noise (white noise decreasing 3 dB/Octave) in the frequency range 20 Hz to 50 kHz within ± 1 dB
4. Same as mode 3 but at a 10 dB lower level
5. Use as a −3 dB/Octave filter
6. Use as a compressor amplifier

Amplitude Distribution:
Symmetrical Gaussian with crest factor up to five

Output Level:
Calibrated output 3,16 V RMS, 100 kHz position. Continuously variable down to 0 V

Output Load Impedance:
Output: ⩾5 kΩ
Compressor Output: ⩾5 kΩ

Signal to Hum Ratio:
>90 dB for "white noise" output
>70 dB for "pink noise" output

Stability of Output Level:
Better than ± 0,3 dB in the range −10 ° to 40 °C

Compressor:
Speed: 3; 10; 30; 100; 300; 1000 dB/s
Range: >80 dB
Min. Input Signal: 0,5 V average
Max. Input Signal: 9,5 V average
Input Impedance: >18 kΩ on compressor input
82 kΩ on external generator input
Frequency Range: 20 Hz to 200 kHz
Meter: Calibrated in dB compression (minimum compression at 0 dB)

Distortion: approximately 1% with 3 V RMS on external sine generator

Generator Stop Function:
Operated manually or remotely
Remote Operation: 5 V positive logic, contact or a DC voltage
0 to 2,5 V: Stop. 2,5 to 10 V: Signal

Temperature Range:
−10 to +40°C (+14 to +104°F)

Max. Humidity:
90% RH (non condensing) at 30°C

Power Supply:
100, 115, 127, 220, 240 V AC ± 10%, 50-60 Hz, approx. 5 VA
Complies with safety class 1 of IEC 348
Ext. Batt: 2 × 22 to 30 V, 2 × 2 W

Dimensions:
Height: 132,6 mm (5,2 ″)
Width: 209,5 mm (8,3 ″)
Depth: 200 mm (7,9 ″)
(6/12 of a 19 ″ rack module)

Weight : 2 kg (4,5 lb)

Accessories Included:
1 Power Cable AN 0010
1 100 mA fuse VF 0026
1 50 mA fuse VF 0016

2. CONTROLS

2.1. FRONT PANEL

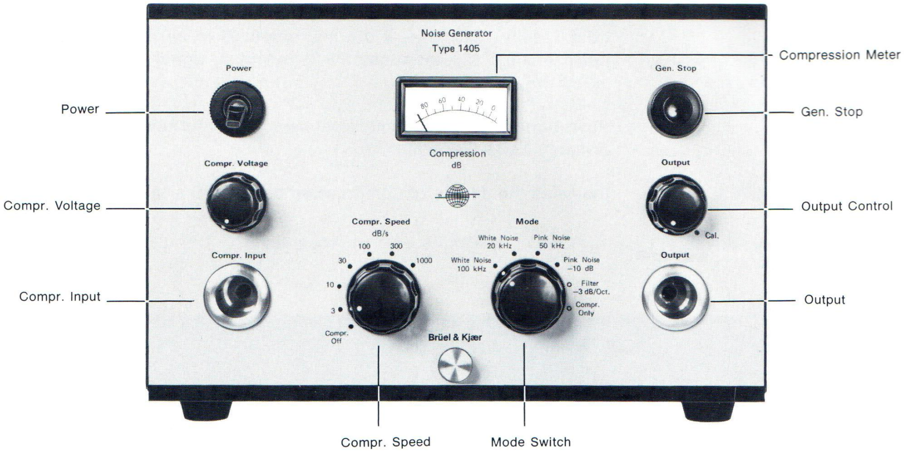

Fig.2.1. Front Panel

POWER:	Toggle switch for turning the instrument on. When the instrument is turned on, the meter lamp should light.
COMPR. VOLTAGE:	Knob for adjustment of the compressor voltage. Turning the knob anti-clockwise will increase the compressor voltage, increase the degree of compression and decrease the output signal level.
COMPR. INPUT:	B & K co-axial socket which accepts plug JP 0101 for input of the compressor control signal. This socket is also used for input to the —3 dB/Octave filter.
COMPR. SPEED:	Knob for adjustment of the compressor speed. In the position "Compr. Off" the compressor voltage is removed from the system.
MODE SWITCH:	Allows selection of the instrument mode, six being available. These are: "White Noise 100 kHz": the instrument outputs a white noise signal from 20 Hz to 100 kHz. "White Noise 20 kHz": the instrument outputs a white noise signal from 20 Hz to 20 kHz.

"Pink Noise 50 kHz": the instrument outputs a pink noise signal (falling at 3 dB/Octave) from 20 Hz to 50 kHz.
"Pink Noise —10 dB": the instrument outputs the pink noise signal as above but decreased in level by 10 dB.
"Filter —3 dB/Oct.": allows the instrument to be used purely as a —3 dB/Octave filter.
"Compr. Only": allows the instrument to act purely as a compressor amplifier.

OUTPUT:	B & K co-axial socket which accepts plug JP 0101 for output of the compressed signal.
OUTPUT CONTROL:	For adjustment of the random noise output level. In the position "Cal.", fully clockwise, if the instrument is in either of the two white noise modes, the instrument will output a signal of spectral density 10^{-4} V^2 /Hz.
GEN. STOP:	Push-button operated noiseless switch for turning the instrument's Random Noise Generator off.
COMPRESSION METER:	Indicates the degree of Compression between 0 and 80 dB.

2.2. REAR PANEL

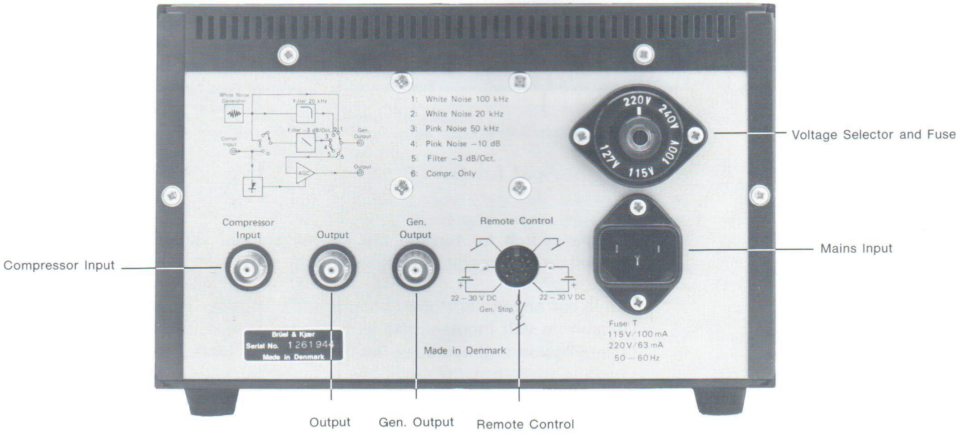

Fig. 2.2. Rear Panel

MAINS INPUT:	For input of the AC mains supply. Before connecting a supply, the mains voltage setting and fuse checks given in section 3.1.3. should be carried out to ensure safe operation of the instrument.
VOLTAGE SELECTOR AND FUSE:	For selection of the correct AC mains supply voltage as described in section 3.1.3. The fuse fits into the centre of the selector.

4. DESCRIPTION

The method of operation of the Noise Generator Type 1405 is described with reference to the block diagram shown in Fig.4.1. This block diagram is a more detailed version of that shown on the rear panel of the instrument. The block diagram on the rear panel is useful as a ready reference for the connections to the instrument in its different modes.

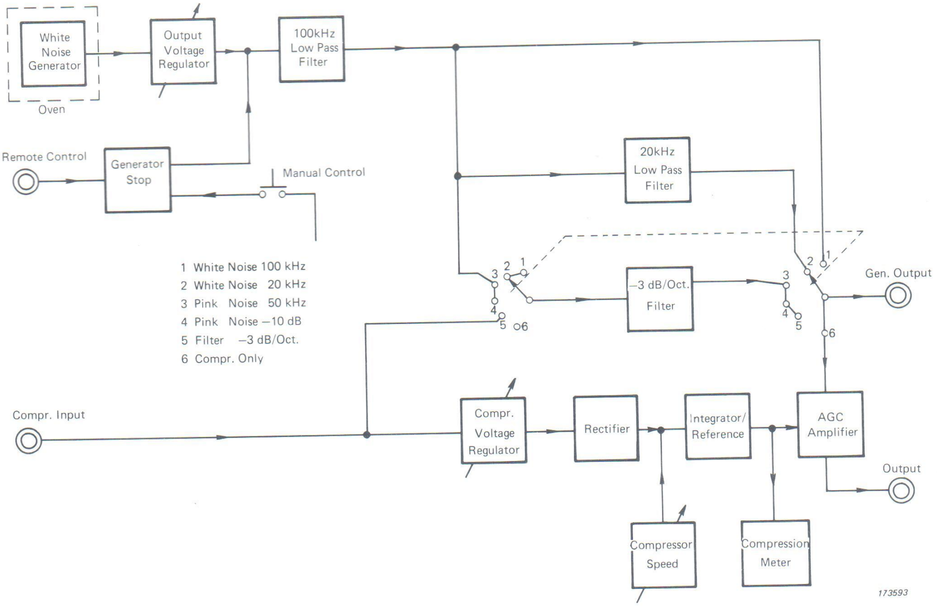

Fig.4.1. Block Diagram

4.1. RANDOM NOISE OUTPUTS

The heart of the 1405 is a White Noise Generator which consists of a matched pair of zener diodes driven by constant current sources. The diodes provide an exceptionally flat spectral density from 20 Hz to 100 kHz. The two zener diodes are housed in a temperature controlled oven which maintains the output of the diodes at 10^{-4} V^2/Hz over the entire operating temperature range of the instrument. This feature allows the use of the 1405 as a high stability standard output random noise generator.

The output from the White Noise Generator is passed to the Output Voltage Regulator, controlled by the OUTPUT knob on the front panel. The output is continuously variable from zero with the knob fully anticlockwise up to 10^{-4} V^2 /Hz with the knob fully clockwise in the "Cal." position.

The White Noise Generator can be stopped (for reverberation measurements etc.) either by pressing the GEN. STOP button on the front panel or using the REMOTE CONTROL socket on the rear panel. Remote control of the generator can be achieved by either simple contact closure or application of 5 V positive logic (or any positive DC voltage between 2,5 and 10 V). Connections and control using this socket are discussed in section 3.2.2. After either remote or manual stopping of the generator it will reach zero output, without extraneous transients, in 10 ms. On restarting the generator will return to full output in approximately the same time.

The noise signal is then passed through a 100 kHz low pass filter to terminal 1 on the instrument MODE SWITCH. If mode 1, "White Noise 100 kHz", is selected then the 100 kHz band limited white noise signal is passed to the GEN. OUTPUT socket. The frequency characteristic of the 100 kHz Low Pass Filter (obtained from a swept sine test) is shown in Fig. 4.2. The spectral density is constant at 10^{-4} V^2/Hz (within ± 1 dB) up to 50 Hz. The effective noise bandwidth of 100 kHz for the Low Pass Filter results in a 3,16 V RMS output in this mode.

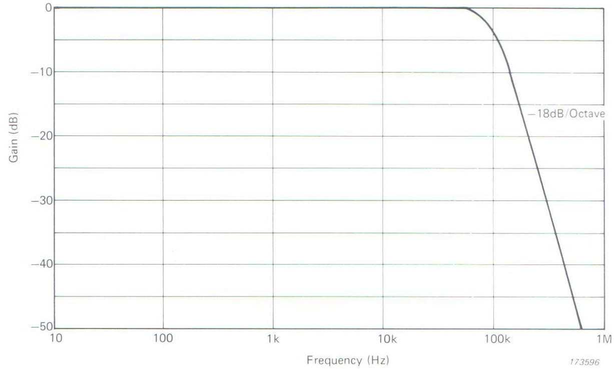

Fig.4.2. Frequency Characteristic of the 100 kHz Low Pass Filter

The 100 kHz band limited white noise signal is also passed via a 20 kHz Low Pass Filter to terminal 2 on the instrument MODE SWITCH. If mode 2, "White Noise 20 kHz", is selected then the white noise signal in the audio range from 20 Hz to 20 kHz is passed to the GEN. OUTPUT socket. The frequency response of the 20 kHz Low Pass Filter (obtained from a swept sine test) is shown in Fig. 4.3. It can be seen that the frequency characteristic is flat to within ± 0,5 dB up to 19 kHz, and within $^{+0,5}_{-1,0}$ to 20 kHz. The fall-off above 20 kHz is greater than 18 dB/Octave. The effective noise bandwidth of this Low Pass Filter is 21,7 kHz which, combined with the spectral density of 10^{-4} V^2/Hz, results in an output of 1,47 V RMS in this mode.

Finally the 100 kHz band limited white noise signal is passed to terminal 3 on the MODE SWITCH. When mode 3, "Pink Noise 50 kHz" is selected this signal is passed via a —3 dB/Octave Filter to the GEN. OUTPUT socket. The frequency characteristic of the —3 dB/Octave filter is given in Fig.4.4.

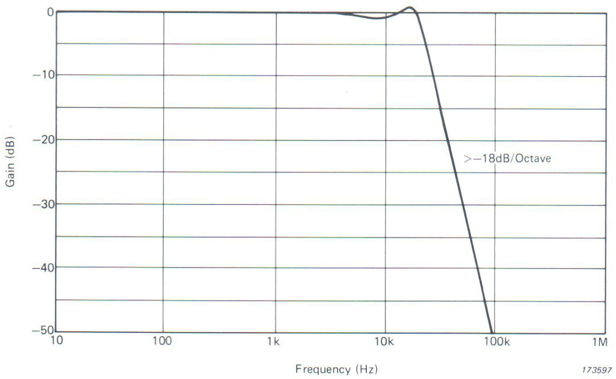

Fig. 4.3. Frequency Characteristic of the 20 kHz Low Pass Filter

With the OUTPUT knob in the "Cal." position, the spectral density S(f) in this mode will follow the formula

$$[S(f)]^{\frac{1}{2}} = \frac{0{,}256}{\sqrt{f}} \quad V/Hz^{\frac{1}{2}}$$

or

$$S(f) = \frac{0{,}0656}{f} \quad V^2/Hz \tag{1}$$

Selection of mode 4, "Pink Noise —10 dB" will result in a signal 10 dB lower than that described above being fed to the GEN. OUTPUT socket. With the OUTPUT knob in the "Cal." position, the spectral density S(f) in this mode will follow the formula

$$[S(f)]^{\frac{1}{2}} = \frac{0{,}0810}{\sqrt{f}} \quad V/Hz^{\frac{1}{2}}$$

or

$$S(f) = \frac{0{,}00656}{f} \quad V^2/Hz \tag{2}$$

4.2. THE —3 dB/OCTAVE FILTER

The —3 dB/Octave filter can be isolated from the rest of the instrument and used separately by setting the MODE SWITCH to mode 5, "Filter —3 dB/Oct.". This mode is useful for converting a constant percentage bandwidth analysis of a noise signal into a constant bandwidth analysis, and hence to power spectral density form.

The gain of the filter A(f) is given by the expression

$$A(f) = \frac{25{,}6}{\sqrt{f}} \tag{3}$$

and shown graphically in Fig. 4.4.

The filter has unity gain at a frequency of 656 Hz.

Agilent 33220A
20 MHz Waveform Generator

User's Guide

Agilent Technologies

Agilent 33220A at a Glance

The Agilent Technologies 33220A is a 20 MHz synthesized function generator with built-in arbitrary waveform and pulse capabilities. Its combination of bench-top and system features makes this function generator a versatile solution for your testing requirements now and in the future.

Convenient bench-top features

- 10 standard waveforms
- Built-in 14-bit 50 MSa/s arbitrary waveform capability
- Precise pulse waveform capabilities with adjustable edge time
- LCD display provides numeric and graphical views
- Easy-to-use knob and numeric keypad
- Instrument state storage with user-defined names
- Portable, ruggedized case with non-skid feet

Flexible system features

- Four downloadable 64K-point arbitrary waveform memories
- GPIB (IEEE-488), USB, and LAN remote interfaces are standard
- LXI Class C Compliant
- SCPI (Standard Commands for Programmable Instruments) compatibility

Note: *Unless otherwise indicated, this manual applies to all Serial Numbers.*

The Front Panel at a Glance

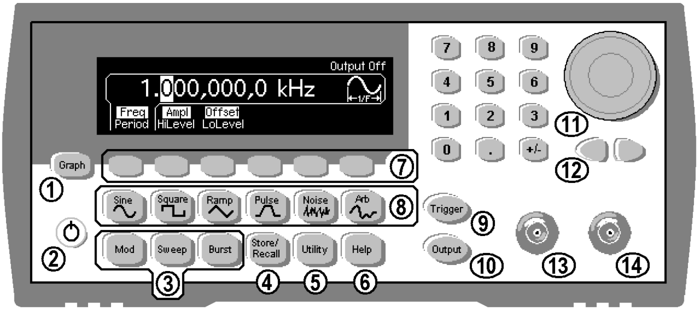

1 Graph Mode/Local Key
2 On/Off Switch
3 Modulation/Sweep/Burst Keys
4 State Storage Menu Key
5 Utility Menu Key
6 Help Menu Key
7 Menu Operation Softkeys
8 Waveform Selection Keys
9 Manual Trigger Key (*used for Sweep and Burst only*)
10 Output Enable/Disable Key
11 Knob
12 Cursor Keys
13 Sync Connector
14 Output Connector

Note: *To get context-sensitive help on any front-panel key or menu softkey, press and hold down that key.*

Output Frequency

As shown below, the output frequency range depends on the function currently selected. *The default frequency is 1 kHz for all functions.*

Function	Minimum Frequency	Maximum Frequency
Sine	1 µHz	20 MHz
Square	1 µHz	20 MHz
Ramp	1 µHz	200 kHz
Pulse	500 µHz	5 MHz
Noise, DC	Not Applicable	Not Applicable
Arbs	1 µHz	6 MHz

- *Function Limitations*: If you change to a function whose maximum frequency is less than that of the current function, the frequency is adjusted to the maximum value for the new function. For example, if you are currently outputting a 20 MHz sine wave and then change to the ramp function, the function generator will automatically adjust the output frequency to 200 kHz (the upper limit for ramps).
- *Burst Limitation*: For internally-triggered bursts, the minimum frequency is 2.001 mHz. For sine and square waveforms, frequencies above 6 MHz are allowed only with an “infinite” burst count.
- *Duty Cycle Limitations*: For square waveforms, the function generator may not be able to use the full range of duty cycle values at higher frequencies as shown below.

  20% to 80% (*frequency* $\leq$ 10 MHz)
  40% to 60% (*frequency* > 10 MHz)

  If you change to a frequency that cannot produce the current duty cycle, the duty cycle is automatically adjusted to the maximum value for the new frequency. For example, if you currently have the duty cycle set to 70% and then change the frequency to 12 MHz, the function generator will automatically adjust the duty cycle to 60% (the upper limit for this frequency).

Waveforms

Standard:	Sine, Square, Ramp, Triangle, Pulse, Noise, DC
Built-in Arbitrary:	Exponential rise, Exponential fall, Negative ramp, Sin(x)/x, Cardiac.

Waveform Characteristics

Sine

Frequency:	1 µHz to 20 MHz, 1 µHz resolution

Amplitude Flatness: [1], [2]

	(Relative to 1 kHz)
< 100 kHz	0.1 dB
100 kHz to 5 MHz	0.15 dB
5 MHz to 20 MHz	0.3 dB

Harmonic Distortion: [2], [3]

	< 1 Vpp	≥ 1 Vpp
DC to 20 kHz	-70 dBc	-70 dBc
20 kHz to 100 kHz	-65 dBc	-60 dBc
100 kHz to 1 MHz	-50 dBc	-45 dBc
1 MHz to 20 MHz	-40 dBc	-35 dBc

Total Harmonic Distortion: [2], [3]

DC to 20 kHz	0.04%

Spurious (Non-Harmonic) Output: [2], [4]

DC to 1 MHz	-70 dBc
1 MHz to 20 MHz	-70 dBc +6 dB/octave
Phase Noise (10 kHz offset):	-115 dBc / Hz, typical

Square

Frequency:	1 µHz to 20 MHz, 1 µHz resolution
Rise/Fall Time:	< 13 ns
Overshoot:	< 2%
Variable Duty Cycle:	20% - 80% (to 10 MHz) 40% - 60% (to 20 MHz)
Asymmetry (@ 50% Duty):	1% of period + 5 ns
Jitter (RMS):	1 ns + 100 ppm of period

Ramp, Triangle

Frequency:	1 µHz to 200 kHz, 1 µHz resolution
Linearity:	< 0.1% of peak output
Variable Symmetry:	0.0% to 100.0%

Pulse

Frequency:	500 µHz to 5 MHz, 1 µHz resolution
Pulse Width (period ≤ 10 s):	20 ns minimum, 10 ns resolution
Variable Edge Time:	< 13 ns to 100 ns
Overshoot:	< 2%
Jitter (RMS):	300 ps + 0.1 ppm of period

Noise

Bandwidth:	10 MHz, typical

Arbitrary

Frequency:	1 µHz to 6 MHz, 1 µHz resolution
Waveform Length:	2 to 64 K points
Amplitude Resolution:	14 bits (including sign)
Sample Rate:	50 MSa/s
Minimum Rise/Fall Time:	35 ns, typical
Linearity:	< 0.1% of peak output
Settling Time:	< 250 ns to 0.5% of final value
Jitter (RMS):	6 ns + 30 ppm
Non-volatile Memory:	Four waveforms

Common Characteristics

Frequency Accuracy:

90 days:	± (10 ppm + 3 pHz)
1 year:	± (20 ppm + 3 pHz)

Amplitude

Range:	
Into 50 Ω	10 mVpp to 10 Vpp
Into open circuit:	20 mVpp to 20 Vpp
Accuracy (at 1 kHz): [1], [2]	± (1% of setting + 1 mVpp)
Units:	Vpp, Vrms, dBm
Resolution:	
10.00 to 20.00 Vpp:	10 mVpp
1.000 to 9.999 Vpp:	1 mVpp
<999.9 mVpp:	0.1 mVpp

DC Offset

Range (peak AC + DC):	± 5 V into 50 Ω ±10 V into open circuit
Accuracy: [1], [2]	± 2% of offset setting ± 0.5% of ampl. ± 2 mV
Resolution:	4 digits

Main Output

Impedance:	50 Ω typical
Isolation:	42 Vpk maximum to earth
Protection:	Short-circuit protected, overload automatically disables main output

Internal Frequency Reference

Accuracy: [5]	± 10 ppm in 90 days, ± 20 ppm in 1 year

External Frequency Reference (Option 001)

Rear Panel Input:	
Lock Range:	10 MHz ± 500 Hz
Level:	100 mVpp to 5 Vpp
Impedance:	1 kΩ typical, AC coupled
Lock Time:	< 2 seconds
Rear Panel Output:	
Frequency:	10 MHz
Level:	632 mVpp (0 dBm), typical
Impedance:	50 Ω typical, AC coupled
Phase Offset:	
Range:	+360 to -360 degrees
Resolution:	0.001 degrees
Accuracy:	20 ns

Modulation

AM

Carrier Waveforms:	Sine, Square, Ramp, Arb
Source:	Internal/External
Internal Modulation:	Sine, Square, Ramp, Triangle, Noise, Arb (2 mHz to 20 kHz)
Depth:	0.0% to 120.0%

FM

Carrier Waveforms:	Sine, Square, Ramp, Arb
Source:	Internal/External
Internal Modulation:	Sine, Square, Ramp, Triangle, Noise, Arb (2 mHz to 20 kHz)
Deviation:	DC to 10 MHz

PM

Carrier Waveforms:	Sine, Square, Ramp, Arb
Source:	Internal/External
Internal Modulation:	Sine, Square, Ramp, Triangle, Noise, Arb (2 mHz to 20 kHz)
Deviation:	0.0 to 360.0 degrees

PWM

Carrier Waveforms:	Pulse
Source:	Internal/External
Internal Modulation:	Sine, Square, Ramp, Triangle, Noise, Arb (2 mHz to 20 kHz)
Deviation:	0% to 100% of pulse width

FSK

Carrier Waveforms:	Sine, Square, Ramp, Arb
Source:	Internal/External
Internal Modulation:	50% duty cycle square (2 mHz to 100 kHz)

External Modulation Input [6] (for AM, FM, PM, PWM)

Voltage Range:	± 5 V full scale
Input Resistance:	5 kΩ typical
Bandwidth:	DC to 20 kHz

Sweep

Waveforms:	Sine, Square, Ramp, Arb
Type:	Linear or Logarithmic
Direction:	Up or Down
Sweep Time:	1 ms to 500 s
Trigger:	Single, External or Internal
Marker	Falling edge of Sync signal (programmable frequency)

Burst [7]

Waveforms:	Sine, Square, Ramp, Triangle, Pulse, Noise, Arb
Type:	Counted (1 to 50,000 cycles), Infinite, Gated
Start/Stop Phase:	-360 to +360 degrees
Internal Period:	1 µs to 500 s
Gate Source:	External Trigger
Trigger Source:	Single, External, or Internal

Trigger Characteristics

Trigger Input:	
Input Level:	TTL compatible
Slope:	Rising or falling, selectable
Pulse Width:	> 100 ns
Input Impedance:	> 10 kΩ, DC coupled
Latency:	< 500 ns
Jitter (RMS)	6 ns (3.5 ns for Pulse)
Trigger Output:	
Level:	TTL compatible into ≥ 1 kΩ
Pulse Width:	> 400 ns
Output Impedance:	50 Ω, typical
Maximum Rate:	1 MHz
Fanout:	≤ 4 Agilent 33220As

Programming Times (typical)

Configuration Times

	USB 2.0	LAN (VXI-11)	GPIB
Function Change	111 ms	111 ms	111 ms
Frequency Change	1.5 ms	2.7 ms	1.2 ms
Amplitude Change	30 ms	30 ms	30 ms
Select User Arb	124 ms	124 ms	123 ms

Arb Download Times (binary transfer)

	USB 2.0	LAN (VXI-11)	GPIB
64 K points	96.9 ms	191.7 ms	336.5 ms
16 K points	24.5 ms	48.4 ms	80.7 ms
4 K points	7.3 ms	14.6 ms	19.8 ms

Download times do not include setup or output time.

General

Power Supply:	CAT II
	100 to 240 V @ 50/60 Hz (-5%, +10%)
	100 to 120 V @ 400 Hz (± 10%)
Power Consumption:	50 VA maximum
Operating Environment:	IEC 61010 Pollution Degree 2 Indoor Location
Operating Temperature:	0 °C to 55 °C
Operating Humidity:	5% to 80% RH, non-condensing
Operating Altitude:	Up to 3000 meters
Storage Temperature:	-30 °C to 70 °C
Floating Connector Shields (**Output**, **Sync**, and **Modulation In** only):	Shields may float at ± 42 V (peak) relative to earth ground.[8]
State Storage Memory:	Power off state automatically saved. Four user-configurable stored states.
Interface:	GPIB, USB, and LAN standard
Language:	SCPI - 1993, IEEE-488.2
Dimensions (W x H x D):	
Bench Top:	261.1 mm by 103.8 mm by 303.2 mm
Rack Mount:	212.8 mm by 88.3 mm by 272.3 mm
Weight:	3.4 kg (7.5 lbs)
Safety Designed to:	UL-1244, CSA 1010, EN61010
EMC Tested to:	MIL-461C, EN55011, EN50082-1
Vibration and Shock:	MIL-T-28800, Type III, Class 5
Acoustic Noise:	30 dBa
Warm-up Time:	1 hour
LXI Compliance:	LXI Class C, Version 1.0

Note: *Specifications are subject to change without notice. For the latest specifications, go to the Agilent 33220A product page and find the 33220A Datasheet.*

www.agilent.com/find/33220A

This ISM device complies with Canadian ICES-001.

Cet appareil ISM est conforme à la norme NMB-001 du Canada.

N10149

Footnotes:

[1] Add 1/10th of output amplitude and offset specification per °C for operation outside the range of 18 °C to 28 °C.

[2] Autorange enabled.

[3] DC offset set to 0 V.

[4] Spurious output at low amplitude is -75 dBm (typical).

[5] Add 1 ppm / °C (average) for operation outside the range of 18 °C to 28 °C.

[6] FSK uses trigger input (1 MHz maximum).

[7] Sine and square waveforms above 6 MHz are allowed only with an “infinite” burst count.

[8] These shields must all float at the same potential to avoid instrument damage.

MINIRATOR MR1

Analog Audio Generator

Less noise • More sound

User Manual

Overview

The Minirator MR1 is the first member of a family of miniaturized battery powered audio instruments, called Minstruments. It is a professional, multifunctional analog audio signal generator that fits in the palm of your hand.

It covers most of the typical test signals used in a professional audio environment:

- **Sinusoidal Signal, 20 Hz - 20 kHz,**
- **Frequency Sweep, 20 Hz - 20 kHz**
- **Square Signal, 20 Hz - 5 kHz**
- **White Noise**
- **Pink Noise**
- **Polarity Test Signal**

Over the entire audio band the output level ranges from the lowest microphone levels in the microvolts range up to studio reference levels.
The user interface is simple and intuitive with three buttons only. A short instruction of the Minirator control can also be found on the rear side of the instrument.

Test Certificate

The Minirator MR1 is fully tested to the manufacturer's specifications. We recommend to calibrate and adjust the Minirator MR1 in one (1) yearly intervals.

---

2. BASIC OPERATION

LC Display

RCA (Cinch) output, unbalanced

Down-button for parameter settings

Up-button for parameter settings

Retractable XLR output connector, balanced. Push the release button and turn to fold out. Push and turn to retract.

MODE button, push once to switch on. Press to toggle to the next parameter. Press and hold for 2 sec to switch off.

Fig 2 Instrument overview

Choose Waveform

Select the S-sign with the MODE-key and toggle through the available waveforms using the UP- or DOWN-key. The available waveforms are listed in below Table 1.

Waveform	Frequency	Description
Sine	20 Hz - 20 kHz	Pure, low distortion sinusoidal waveform defined by frequency and level (RMS) in the display. This is the most common waveform in the audio world for measurements of frequency response, distortion, etc.
Sweep		The output signal is sequentially stepped through all the available frequencies. Step duration can be adjusted. Actual frequency is displayed. Sweep starts automatically indicated by the rotating bar .
W. Noise		White noise signal with 20 kHz bandwidth. Use this signal in conjunction with a spectrum analyzer (FFT analyzer).
P. Noise		Pink Noise signal with 20kHz bandwidth. Signal level decreases with 10 dB/decade (3 dB/octave). Use this waveform in conjunction with swept narrow band filters for auditive (aural) testing.
Square	20 Hz - 5 kHz	Square wave signal with 50% duty cycle and no DC offset.
Pol Test	20 Hz	Proprietary polarity test fix frequency of 20Hz.

Change Frequency

The frequency range of the instrument covers the entire audio range from 20Hz to 20kHz in 31 1/3rd octave steps.

20 Hz	25 Hz	30 Hz	40 Hz	50 Hz	65 Hz	80 Hz	100 Hz
125 Hz	160 Hz	200 Hz	250 Hz	315 Hz	400 Hz	500 Hz	630 Hz
800 Hz	1 kHz	1.25 kHz	1.60 kHz	2.00 kHz	2.5 kHz	3.15 kHz	4.00 kHz
5.00 kHz	6.30 kHz	8.00 kHz	10.0 kHz	12.5 kHz	16.0 kHz	20.0 kHz	

Table 2 Frequency table for sinusoidal signals

Select the F -sign with the MODE-key and toggle through the frequencies using the UP- or DOWN-key.

Note • **The frequency may not be altered in waveforms Sweep, Pink Noise, White Noise and PolTest.**

Change RMS Level

To change the level of the generated signal, toggle with the MODE-key, until the A-character is flashing and increase or decrease the level with the UP- or DOWN-key.

Waveform	Unit	Range	Increment
Sine, Square, White Noise, Sweep	dBu dBV Volts	-76 dBu - +6 dBu -78 dBV - +4 dBV 0.13 mV - 1.6 V	2 dBu 2 dBV ~±23%
Pol Test	dBu dBV Volts	-76 dBu - +4 dBu -78 dBV - +2 dBV 0.13 mV - 1.25 V	2 dBu 2 dBV ~±23%
Pink Noise	dBu dBV Volts	-56 dBu - -4 dBu -58 dBV - -6 dBV 1.25 mV - 500 mV	2 dBu 2 dBV ~±23%

Table 3 Level ranges and increments for signals and units

b. RCA Output

The RCA, also called phono connector or cinch connector, is located on the top of the instrument, see Fig 9. It provides the selected output signal in an unbalanced mode with a nominal output impedance of 200 ohm. The center pin carries the signal (hot), and the screen is the ground. The RCA output is always active regardless of the XLR connectors position.

Fig 9 RCA output

c. XLR Output

The XLR output is a balanced signal output with nominal 200 ohm output impedance, see Fig 10. The XLR pins are retractable in order to protect the pins from inadvertent connections and short circuits. To flip the connector out, push the release button and turn the XLR output whilst pressing. For example press a finger into the notch on the rotator, see Fig 11. To retract the pins, simply press again the release button and turn the pins back.

Fig 10 XLR output

Fig 11 Open the XLR output

3. TECHNICAL SPECIFICATION

Outputs	Balanced XLR, unbalanced RCA, phantom power resistant
Waveforms	Sinusoidal, Square, White Noise, Pink Noise, Polarity
Frequency Range	20 Hz - 20 kHz in 31 steps (Sine) 20 Hz - 5 kHz in 25 steps (Square)
Frequency Sweep	20 Hz ... 20 kHz with sinusoidal signals
Sweep Speed	0.05, 0.5, 1, 2, 3, 4, 5 sec. per step
Units	dBu, dBV, V selectable

Level Ranges	Waveform	Range	Inc
	Sine, Square	-76 dBu to +6 dBu	2 dBu
	White Noise	-78 dBV to +4 dBV	2 dBV
	Sweep	0.13 mV to 1.6 V	±23%
	Pol Test	-76 dBu to +4 dBu	2 dBu
		-78 dBV to +2 dBV	2 dBV
		0.13 mV to 1.25 V	±23%
	Pink Noise	-56 dBu to -4 dBu	2 dBu
		-58 dBV to -6 dBV	2 dBV
		1.25 mV to 0.5 V	±23%

Flatness	±0.5 dB
Accuracy	±0.5 dB
THD+N	<-72 dB (0.025%) typical @ 6 dBu, 1 kHz <-55 dB (0.18%) or 0.1mV, 20 Hz - 20kHz
White Noise	20 Hz - 20 kHz, Crest factor = 2.12
Pink Noise	20 Hz - 20 kHz, Crest factor = 3.27
Output Impedance	200 ohm balanced & unbalanced
Auto Power Off	10, 30, 60 minutes or OFF
Batteries	2 x 1.5 V Dry or NiCd type cell, LR 6, AA, AM3 types
Lifetime	Typical battery lifetime >20 hours
Temp. Range	0° to +45 °C (32 °F to +113 °F)
Humidity	< 90% R.H., non condensing
Dimensions	140 x 74 x 25 mm (5.5" x 2.9" x 1")
Weight	170 g (6 oz) including batteries

Quick Guide Minirator MR1

MODE
On / Off (2 sec)

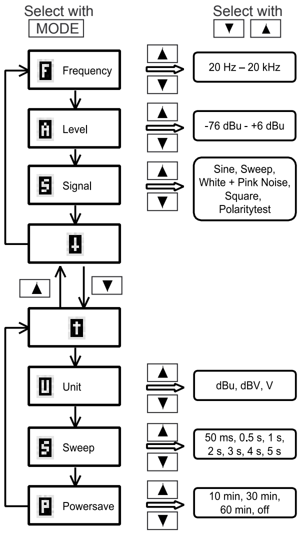

VIPER

User Manual

Revision 2.005 B
September 13, 2006

1 Using the Viper System

This section assumes that the Viper system is properly installed and configured. The chapter 'System Configuration' below describes how to configure the system before the first use.

1.1 General Overview

The GBM Viper system is a modular multi channel high speed data acquisition system with online processing based on DSP technology.

The system consists of:

- A Master PC controlling the whole system through a software programming interface (API)
- One or more Data Acquisition Units with integrated signal conditioning for up to 48 channels
- Synchronisation connections (clock signal distribution) between all different Data Acquisition Units
- TCP/IP network connection between all the Master PC and all Data Acquisition Units

Each Data Acquisition Unit contains a complete PC running Windows XP. Therefore it is optionally possible to use one of the units as the Master PC. This is especially useful for using a Data Acquisition Unit as a stand-alone system.

The system comes with a graphical user interface that can control many features of the API. It may serve as a stand-alone application for simple tasks or where API programming is not wanted. To exploit the full features of the system however direct API programming is required.

6.2 Technical Specification

GBM Viper is a multichannel data acquisition system. It can acquire an unlimited number of channels at a rate of up to 250 kHz (100 kHz bandwidth) for each channel. (Currently tested up to 256 channels total.)

The system can capture all channels simultaneously at full speed with continuous gap-free acquisition. The built-in data storage of 240 GB per 48 channel unit can hold up to 2.5 hours of data when recording all channels at full speed.

A Viper system typically consists of a master PC and one or more Viper-48 units. They are connected via Ethernet and in addition through a clock synchronisation cable. Operating the units stand alone is also possible by using the unit's built-in PC as master PC.

6.2.1 Data acquisition units

Data Acquisition Unit Specification:
- Capture up to 48 channels per unit, supports multiple units.
- Controlled via TCP/IP from Master PC.
- Stand-alone operation without Master PC also possible. This requires connecting keyboard, mouse, and VGA monitor.
- Ethernet connection for control and offline data transfer.
- Sampling rate up to 250 kHz per channel (bandwidth 100 kHz).
- All channels are captured simultaneously. Units synchronize by hardware via clock synchronisation cable.
- Captured data are stored locally on each unit. So the network bandwidth does not limit on the total sum sampling rate.
- Sum sampling rate on each channel limited only by the speed of the unit's internal hard disk.
- Each unit contains up to six TMS320C6701 150 MHz, 900 MFlops floating point DSP's for data capture and online processing.
- Sophisticated autorange procedures can handle non-standard situations.
- External clocking for rotating objects with 1 pulse per revolution (1P). Can interpolate up to 8192 samples per revolution and operates up to 1 kHz 1P rate (60000 RPM) and 85 kHz interpolated sampling rate.
- Optional: Separate channel groups and individual 1P signal per channel group (Multi-1P).
- Optional (obsolete): External clocking for rotating objects with multiple pulses per revolution (NP). Operates up to 85 kHz = 10000 RPM at 512 pulses per revolution.

Built-In PC in each Unit:
- Pentium-4 CPU with 2.8 GHz clock, 1 GB RAM
- 10/100/1000 MBit Ethernet Port.
- 240 GB built-in data storage
- Windows XP Professional operating system

6.2.2 Analog inputs

Analog Signal Conditioning (ASC) Specification:
- Input range +/- 14.142 Volts (10 Volts RMS) at gain 1.
- Input impedance around 1 Mega-Ohm
- Three stage gain amplification with filtering in between.
- Level indicatores and overload detection separate for each channel
- Sensor supply: 5 or 10 or 12 or 15 Volt up to 100 mA per channel, separate selection for each channel
- Current source 4 mA, separate selection for each channel
- 120 and 200 Volt supplies for B&K microphones
- Route a calibration signal (voltage) into a channel's input (Cal) or into a channel's sensor (Cal-Ins)
- Monitor a selectable channel at the common monitor output (BNC+Headphones).

Each channel's signal conditioning contains the following stages (in order):

- Connection: SE/DIFF
- Signal source: Normal/GND/Cal/Cal-Ins
- Coupling: AC/DC
- Pre-Gain: 0.5/1/5/10
- AC highpass filter: OFF / 1.5 Hz 2-pole / 500 Hz 2-pole (curve like HP of A-Filter) / 6000 Hz 2-pole or optional: OFF / 1 Hz 2-pole / 650 Hz 2-pole / 5000 Hz 2-pole
- Mid-Gain: 1/10/100/1000
- Alti-Aliasing lowpass filter fixed at 103 kHz, 6-pole Butterworth
- Post-Gain: 1/2/5/10/20/50

Analog/Digital conversion specification:

- Synchronized acquisition: One Analog Devices AD9260 A/D converter per channel, all A/D converters (not only within a unit) driven from one common clock source.
- 16 Bits A/D converter resolution.
- 8 times oversampling A/D converter with integrated anti aliasing filter (FS = Sampling Frequency):
  - Passband (<= 0.00125 dB) from DC up to 0.242 * FS
  - Stopband (>= 82.5 dB) from 0.748 * FS up to 7.252 * FS
  - -0.1 dB Point at 0.3228 * FS = 80 kHz for the maximum FS of 250 kHz
  - -3.0 dB Point at 0.4544 * FS = 113 kHz for the maximum FS of 250 kHz
- DSP based digital low pass anti aliasing filter for slower sampling rates.

Analog input performance:

- Sampling rate up to 250 kHz per channel (bandwidth 100 kHz) independent from the number of channels.
- Capture 48 channels per unit at 250 kHz each for up to 2.5 hours.
- SNR 80 dB typically at gain 1
- SNR 70 dB typically at gain 1000 (equivalent 130 dB total dynamic range)
- Crosstalk -70 dB typically

6.2.3 Programming API

The Viper system is controlled via an API that comes in the form of a 32-Bit Windows DLL. It can be accessed from any programming environment that can handle DLL calls to standard 32-Bit Windows DLL's. An example program for Microsoft Visual Basic 6 is included.

The programming API provides the following general functionality:

- Detect all Viper stations connected to the local network segment
- Access Viper Units via internet name or IP address
- Select a random set of channels for acquisition
- Assign logical channel numbers and channel names
- Distribute logical channel numbers randomly over the physically installed units
- Select clocking mode: internal / external NP / external 1P
- Set sampling rate for internal clocking
- Set start and stop trigger conditions
- Perform Autorange on those channels where it was selected
- Automatic zero offset calibration at start of measurement
- Select file name for data storage (relative to each station's data store root directory)
- Arm measurement after all settings are specified. This allows a faster start later on.
- Start measurement
- Query measurement status
- Retrieve non-continuous online ("oscilloscope") data during measurement.
- Retrieving online data does not disturb the data storage in the background.
- Stop a running measurement at any time
- Retrieve overload statistics during and after measurement
- API function parameter checking and feedback via error codes
- Convert error codes into ASCII strings explaining the error
- Merge captured data files from different units into one file

The following functionality is provided independent for each channel:

- Select connection: SE / DIFF
- Select mode: Normal / GND / CAL / CAL-INS
- Select coupling: DC / AC
- Select AC highpass filter: 1.5 / 500 / 6000 Hz or optional: 1 / 650 / 5000 Hz
- Select PreGain: Auto / 0.5 / 1 / 5 / 10
- Select MidGain: Auto / 1 / 10 / 100 / 1000
- Select PostGain: Auto / 1 / 2 / 5 / 10 / 20 / 50
- Enable/Disable overload checking
- Exclude DC reference channels from octave analysis

The following functionality is provided for the octave analysis option:

- Select 1/1, 1/3 or 1/12 octave analysis mode
- Select mean computation mode: None / Running average / Exponential average
- Select filter type for 1/3 octaves: 6-pole Butterworth / 12-pole Chebyshev
- Specify range (in Hz) for octave analysis computations.

6.2.4 Octave analysis option

Optionally the Viper System can perform a quasi-online octave analysis. The octave analysis is computed non-continuously by each DSP that acquires the capture data.
Depending on the number of channels, the selected octave analysis range, filter types, etc. the gap in the acquired data and the number of octave spectra computed per second will vary.

Octave analysis specification:

- Supports 1/1, 1/3, and 1/12 octave analysis modes.
- 1/1 octave filters: 12-pole Chebyshev filters with centre frequencies at 1 kHz * 2^k, k = -5 .. +6
- 1/3 octave filters: 6-pole Butterworth and 12-pole Chebyshev filters with centre frequencies at 1 kHz * $2^{k/3}$, k = -16 .. +19
- 1/12 octave filters: 6-pole Butterworth filters with centre frequencies at 1 kHz * $2^{(k+0.5)/12}$ where k = -66 .. +77
- Maximum octave analysis range = 20 .. 80000 Hz, independent from the mode and the number of channels
- Non-continuous operation. Gaps in the data depend on the computation power consumed.
- Quasi-online presentation of results.
- Linear and exponential averaging

Typical octave analysis performance:

- 1/3 octave analysis from 200 .. 20000 Hz using 12-pole Chebyshev filters and all 48 channels computes about one octave spectrum per second

6.2.5 Viper-View application

Viper-View an example of an application using the Viper API. It may serve as a tool for simple tasks, but it does not fully exploit the features of the API.

Viper-View specification:

- Fully interactive application. No batch operation.
- Supports the most commonly used features of the Viper API.
- Fully supports logical channel definitions and analog signal conditioning setup.
- Supports online display of the captured data
- Performs FFT and statistical calculation
- Can store/load complete setups

CARVER

PROFESSIONAL

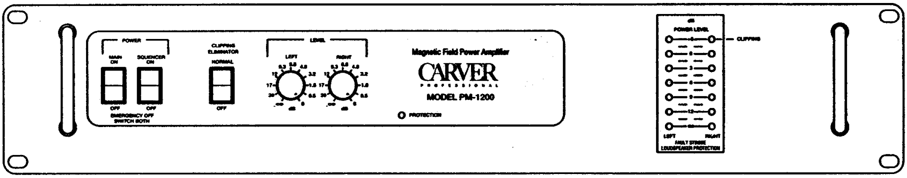

PM-1200
Magnetic Field Power Amplifier
Owner's Manual

CARVER
PROFESSIONAL

Clipping Eliminator

In addition to sounding bad, clipped waveforms kill loudspeakers. This fact of life is made more true by the practice of using large amplifiers for increased headroom. When an amplifier clips, the output waveform contains large amounts of harmonics which extend both above and below the fundamental frequency. This can be potentially destructive to any high-frequency driver.

The clipping eliminator works by sensing amplifier clipping and reducing the input signal level to limit the distortion in the output signal to less than one percent THD with up to 8 dB of overdrive. The action is similar to that of a limiter. The clipping eliminator is sensitive to clipping, regardless of cause: excessive input drive, power line sag, lower load impedances, etc.

Protection Circuitry

The PM-1200 has specially designed protection circuitry that protects the amplifier from abnormal load conditions, as well as protecting the load from an abnormal amplifier. The amplifier includes the following protective measures:

- Input RFI filtering.
- Power line filtering.
- Load protection from excessive low-frequency or DC output.
- Amplifier protection from sustained current limiting caused by severe overdrive or abnor mally low load impedances.
- Thermal overload protection. Activated when the amplifier chassis reaches 90 degrees Centigrade.

The red protect LED indicator on the front panel is illuminated when any of the protection circuits are activated. The two top yellow clipping LED's on the "ladder " display light when the amplifier clips, or when the clipping-eliminator circuit is activated.

Specifications

Power Output, FTC, 20-20kHz, 0.1% THD:

16 ohms, both ch driven	300
8 ohms, both ch driven	450
4 ohms, both ch driven	600
8 ohms mono bridge	1200W
16 ohms mono bridge	1000W

Frequency Bandwidth:
-3, +0 dB, 3Hz-80kHz

IM Distortion (SMPTE):
Less than 0.1%

Gain:
32 dB

Input Sensitivity (full output):
1.5V RMS

Input Impedance:
30 Kilohms balanced, 15 Kilohms unbalanced

Input Overload:
+19 dBu

Slew Rate:
25 V/uSec

Damping Factor:
200 @ 1 KHz

Output Noise (A weighted):
-115 dB, ref 450W output, A-weighted

Inputs (balanced, differential):
XLR, 1/4 inch tip-ring-sleeve

Power-up sequencing:
Barrier strip,
Receive accepts +5 to +15V to signal power on;
Send provides delayed +11.4V output to signal on next unit

Output::
5-way binding posts

Dimensions (HWD inches):
3.5 x 19 x 10.19, 2U rack space

Weight::
21 pounds

Power Requirements:
120 V, 60 Hz, 12A, 1500 Watts
230 V, 50 Hz, 6.25A, 1500 Watts

Note

Carver Corporation reserves the right to improve its products at any time. Therefore, specifications are subject to change without notice.

3. Front and Rear Panel Features

Figure 1

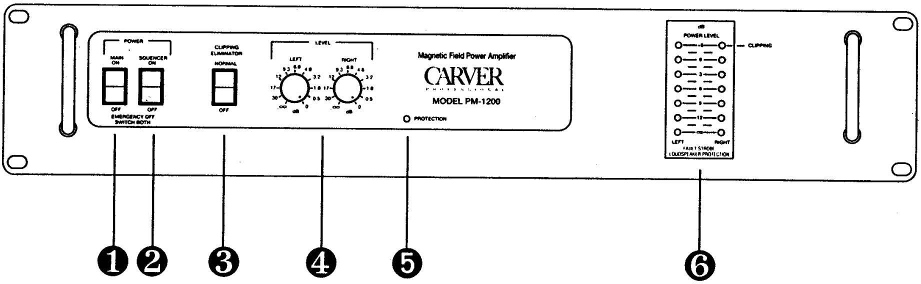

Front Panel

The following paragraphs describe the controls, switches, jacks, and displays found on the front panel of the PM-1200. Refer to Figure 1.

1. POWER switch. Local power switch. Use this switch when you are not using the remote power-up sequencer feature. Having the sequencing switch on will not affect turning on the amplifier with this switch; it will, however, not allow the amplifier to be turned off unless both switches are off. If the POWER switch is turned off, with the sequencing switch still on, the amplifier will remain on.

2. SEQUENCER switch. Rocker switch that enables remote power-up sequencing. The amplifier's POWER switch should be set to the OFF position when using this feature.

3. PUSH CLIPPING ELIMINATOR. Pressing this switch turns on the clipping eliminator circuit. In this mode, the amplifier output remains undistorted even when overdriven by up to 8 dB.

4. LEFT and RIGHT level Controls. 11-step attenuators that adjust the relative output level of the PM-1200. The amount of attenuation corresponds to the front-panel marking, in dB.

5. PROTECTION LED. A red LED that illuminates during fault conditions within the amplifier. This condition may be caused by improper or faulty load wiring. A fault condition causes this LED to light, and a soft popping sound will come from the speakers. Check all wiring, especially the speaker wiring, and the amplifier temperature.

6. Output Status Display. 7 LED's (per channel) indicating the status of the amplifier. The bottom, green LEDs indicate power-on. The five, red LEDs indicate the output power level of the amplifier in dB relative to maximum output. The top, yellow LED's indicate the onset of clipping or the activation of either the clipping-eliminator circuitry (if the clipping-eliminator switch is depressed).

Rear Panel

The following paragraphs describe the various rear panel features of the PM-1200. Refer to Figure 2.

1. PUSH MONO. Pressing this switch sets the PM-1200 for bridged mono operation. Use this mode for 8 ohm or greater loads.

2. INPUTS. Each channel has parallel connected female XLR connectors (2a) and 1/4 inch tip-ring-sleeve phone jacks (2b). These are the input connectors for the amplifier. Since the jacks are connected in parallel, the remaining jack can be used as an output when daisy-chaining several amplifier inputs.

3. AMPLIFIER/CHASSIS. Removing this jumper isolates the amplifier's power supply ground from the amplifier chassis. This may be necessary to eliminate ground loops in some systems. The amplifier chassis is always connected to the safety ground (line plug ground or green wire) of the power cord. With the jumper removed, the amplifier's circuit ground is connected to the amplifier's chassis ground via a 27-kilohm resistor in parallel with a 0.1-mfd capacitor.

Figure 2

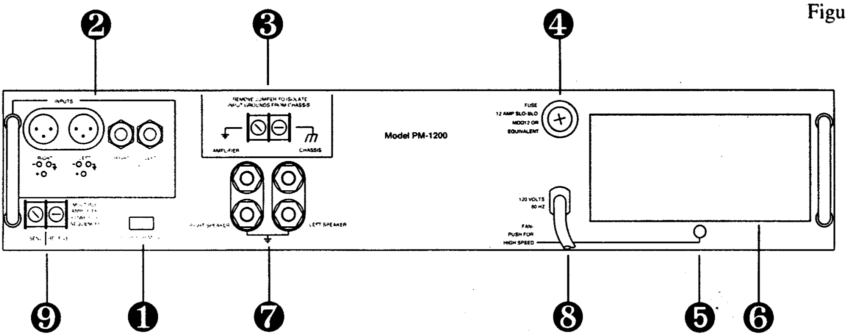

4. FUSE. AC power line fuse for the PM-1200. *Use only one of the following fuses for 120-volt models of the PM-1200*:

Bussman MDQ 12-amp
Little Fuse 3AB 12-amp
Schurter SPT (001.2535) 12.5-amp

For 230-volt models of the PM-1200 use:

Bussman MDQ 6.25-amp
Little Fuse 3AB 6.25-amp
Schurter SPT (001.2532) 6.3-amp

Repeated fuse blowing is a sign of internal distress. Have an authorized Carver service technician examine the amplifier.

5. QUIET/NORMALswitch. Push switch that controls the idle speed of the fan. Use the quiet position in applications that require low acoustic noise output.

6. FAN FILTER. Expanded foam filter that keeps dust and airborne debris out of the amplifier's cooling system. The filter should be washed whenever it shows signs of dust buildup. It is not a good idea to operate the amplifier without the filter in place. Replacement filters can be ordered from Carver; part number 000753.

7. LEFT/RIGHT SPEAKER OUTPUT . 5-way binding posts used to connect the loudspeakers to the amplifier outputs. The red terminal is the signal connection, the black terminal is the signal return connection. The black terminals are internally connected together.

8. Power Cord.

9. SEND/RECEIVE Barrier strip. Barrier strip terminals used to link multiple amplifiers for sequenced turn-on. Connect the SEND connection of the first amplifier to the RECEIVE connection of the second PM-1200. Connect the SEND connection of the second amplifier to the RECEIVE connection of the third power amplifier, and so on.

Basisstation:
GT-WS-06s
GT-WS-06w
GT-WS-07s
GT-WS-07w
Funksensor:
GT-WT-01

Digitale Funkwetterstation

- **Bedienung**
- **Garantie**

07/29/12

Technische Daten

Basisstation:	GT-WS-06s/ GT-WS-06w GT-WS-07s/ GT-WS-07w
Stromversorgung:	3 V ⎓ / 3-5 mA / (2x 1,5 V Typ LR6 AA)
Messbereich der Temperatur:	0 °C bis +50 °C
Messgenauigkeit:	max. +/- 1°C innerhalb eines Messbereichs von 0 bis 40 °C
Auflösung:	0,1 °C
Messbereich der Luftfeuchtigkeit:	20 % bis 90 % relative Luftfeuchtigkeit
Messgenauigkeit:	+/- 10 % relative Luftfeuchtigkeit
Auflösung:	1 %
Sensor:	GT-WT-01
Stromversorgung:	3 V ⎓ / 3-5 mA / (2 x Typ R03 AAA)
Messbereich der Temperatur:	- 15 °C bis +50 °C
Spritzwasserschutz:	IP31
Sendefrequenz:	433 MHz
Reichweite:	max. 100 Meter (in offenem Gelände)

Da unsere Produkte ständig weiterentwickelt und verbessert werden, sind Design- und technische Änderungen möglich.

Alphabetical Index